Development of a Portable Triple Silicon Detector Telescope for Beta Spectroscopy and Skin Dosimetry

Helt-Hansen, Jakob

Publication date:
2000

Document Version
Publisher's PDF, also known as Version of record

Risø-R-1216(EN)

RISØ

Development of a Portable Triple Silicon Detector Telescope for Beta Spectroscopy and Skin Dosimetry

Jakob Helt-Hansen

Risø National Laboratory, Roskilde, Denmark
November 2000

Abstract

It is now recognized that beta radiation can be a significant radiation problem for exposure of the skin. There is thus a need for a portable and rugged active beta dosemeter-spectrometer to carry out immediate measurements of doses and energies of beta particles even in the presence of photon radiation. The main objective of this report is to describe the development of such an instrument.

A beta-spectrometer has been developed consisting of three silicon surface barrier detectors with the thickness: 50μm/150μm/7000μm covered by a 2 μm thick titanium window. The spectrometer is capable of measuring electron energies from 50 keV to 3.5 MeV.

The spectrometer is characterized by a compact low weight design, achieved by digital signal processing beginning at an early stage in the signal chain. 255 channels are available for each of the three detectors. The spectrometer is controlled by a laptop computer, which also handles all subsequent data analysis. The LabView™ software distributed by National Instruments was used for all program developments for the spectrometer.

By use of coincidence/anti-coincidence considerations of the absorbed energy in the three detector elements, counts caused by electrons are separated from those originating from photons. The electron energy distribution is folded by a set of conversion coefficients to obtain the dose at 0.07 mm tissue.

Monte Carlo calculations has been used to derive the conversion coefficients and to investigate the influence of noise and the design of detector assembly on the performance of the spectrometer.

This report describes the development of the spectrometer and its mode of operation, followed by a description of the Monte Carlo calculations carried out to obtain the conversion coefficients. Finally is the capability of the telescope spectrometer to measure beta and photon spectra as well as beta dose rates in pure beta and mixed beta/photon radiation fields described.

This work was funded by The Danish Research Agency, Risø National Laboratory and University of Copenhagen and has been supported by EU under Contract FI4PCT960037.

CPU time for the Monte Carlo calculations presented in this report was kindly provided by Ionizing Radiation Standards, National Research Council of Canada.

This thesis is submitted in partial fulfillment of the requirements for the Ph.D. degree at the University of Copenhagen, Denmark.

Jakob Helt-Hansen
Department of Nuclear Safety Research
P.O. Box 49, DK-4000 Roskilde, Denmark
Phone: +45 4677 4908, Fax: +45 4677 4959
E-mail: jakob.helt-hansen@risoe.dk

ISBN 87-550-2769-5; 87-550-2770-9 (Internet)
ISSN 0106-2840

Information Service Department · Risø · 2000

Contents

1 Introduction

It is now recognized that beta radiation can be significant radiation problem for exposure of the skin [51]. For many decades photon dosimetry has been in focus partly because adequate instrumentation for beta dosimetry has not been available, partly because beta radiation has been thought of as a minor problem due to its limited range.

But beta radiation can be a serious problem. In step with the growing number of applications where beta radiation contribute to the risk scenario (in physics, biology, chemistry, medicine and technology) the awareness for beta dosimetry in radiation protection increased. Today 1 000 000 workers are occupationally monitored with personal dosemeters within the EU. To know the means for proper shielding against beta radiation, or to identify beta radio-isotopes, it is necessary to have information about the energy distribution of the source.

In accident situations where it may be necessary to work in intense beta radiation fields, the need for beta dosimetry is obvious. A recent example is the Chernobyl accident where workers received significant beta doses to the skin. Skin burns due to exposure from beta radiation often contributed to or caused their death [49].

Two problems often accompany measurements of beta radiation fields: the dose rate can be very uneven in space compared to strongly penetrating radiation [20] and the beta radiation is often accompanied by a photon radiation field, which can make an accurate dose rate measurement impossible. Some types of beta radiation are not accompanied by a photon radiation field, and are therefore invisible to detector systems, which can only measure photons.

There is thus a need for a portable and rugged active beta dosemeter-spectrometer to carry out immediate measurements of doses and energies of beta particles even in the presence of photon radiation.

Such an instrument did not exist, and the main objective of this Ph.D. project has been to complete the construction of an operational beta dosemeter-spectrometer.

The spectrometer is based on a telescope configuration, to enable the discrimination of electrons and photons. A couple of thin dE detectors is placed in front of a detector thick enough to absorb any remaining energy of an electron passing through. The determination of particle type is based on simple coincidence/anti-coincidence considerations, utilizing that beta particles will leave energy in all detectors they pass, while photons most likely only will interact with one detector.

The telescope construction is not new, and it has been exploited in many beta spectrometers using different types of detectors [24][25][27].

The skin dose at 0.07 mm tissue ($H_{\mathrm{p}}(0.07)$) is calculated by folding the measured electron energy distribution with a suitable set of conversion coefficients. This technique is not new either [27].

What is unique about the spectrometer developed at Risø, is the use of digital signal processing at a very early stage implying a portable, compact and low weight design, the use of spectrometer specific conversion coefficients which incorporate the detector noise, and the flexibility in the data processing made possible by modern programming technology.

During the project period, the leakage currents of the spectrometer have increased steadily, due to poor intrinsic properties of the silicon surface barrier detectors, malfunctioning ohmic contacts and properly also heat conduction paste seeping into the detector assembly. This have resulted in an enhanced noise level

rendering any serious use of the spectrometer. A new detector assembly was ordered six month before the closing of the Ph.D. project, but the delivery has been postponed several times. The number of experimental results is therefore limited.

The report is structured in three parts: The equipment is described in chapter 3 to 5, chapter 6 to 8 deals with the theory of the Monte Carlo method and the way the calculations are carried out and finally are the results from Monte Carlo calculations and measurements presented in chapter 9 to 12.

2 Basic quantities in skin dosimetry

The fundamental physical quantity in dosimetry is absorbed dose, D, measured as absorbed radiant energy, E, per unit mass, m, in the limit when the volume of interest goes to zero. The unit is Gy, [J/kg].

$$D = \lim_{\Delta m \to 0} \frac{\Delta E}{\Delta m} \tag{1}$$

2.1 Dose equivalent

Two operational quantities are formed from the physical quantity, D: directional dose equivalent, $H'(d, \overrightarrow{\Omega})$, and personal dose equivalent $H_{\mathrm{p}}(d, \overrightarrow{\Omega})$. Both have the unit Sievert, Sv [J/kg]. The former is used for the characterization of radiation fields, and the later for individual monitoring. The term 'equivalent' is used when the dose is weighted with a radiation quality factor, which is one for electrons of all energies. An overview of the quantities are given in [11][35].

Directional dose equivalent

$H'(d, \overrightarrow{\Omega})$ at a point in a radiation field, free-in-air, is the dose equivalent that would be present in an ICRU sphere at depth d, on a radius in a specified direction, $\overrightarrow{\Omega}$, when the radiation field at the point is expanded over the whole sphere. The ICRU sphere is made of tissue equivalent material, 30 cm in diameter. The composition is listed in Table 24 on page 100. By expansion is meant that the fluence and angular- and energy distributions are the same over the volume of interest as at the point of reference.

If the radiation field only has one direction, i.e. its direction can be specified by an angle, α, to the radius pointing to the reference point in the ICRU sphere, the notation $H'(d, \alpha)$ can be used. $H'(d)$ is used in the special case where $\alpha = 0$.

$H'(d, \overrightarrow{\Omega})$ characterizes a radiation field, and conversion factors are calculated using this quantity. $H'(d, \overrightarrow{\Omega})$ is also suitable for calibration purposes.

Personal dose equivalent

$H_{\mathrm{p}}(d, \overrightarrow{\Omega})$ is the dose equivalent at depth d, in the radiation field with direction $\overrightarrow{\Omega}$ relative to the body surface, at a specific point on the body. Again the notation $H_{\mathrm{p}}(d, \alpha)$ can be used when the radiation field is unidirectional, but $H_{\mathrm{p}}(d)$ just specifies the personal dose equivalent at the depth d regardless of $\overrightarrow{\Omega}$.

The quantity measured by personal dosemeters should be close to $H_{\mathrm{p}}(d)$.

To evaluate personal dose equivalent on the trunk of the body, it is recomended that $H_{\mathrm{p}}(d)$ is measured on a 30×30×15 cm phantom of ICRU tissue [34]. For dosemeters worn on extremities two rod-shaped phantoms are defined [44]. Different phantoms are needed because $H_{\mathrm{p}}(d)$ is specific to the point on the body where it is measured.

Tissue depth of interest

Considering stochastic effects, the cells of interest are located in the basal layer, placed under the epidermis, typically in a depth of 20-100 μm depending on the location on the body [12][32]. The basal layer is one cell thick, and it is here the

generation of new skin takes place. The creation of new skin involves an enhanced rate of cell divisions where the DNA is more susceptible for radiation damage.

Considering deterministic effects, some of these also occur at 20-100 μm depth, but the most serious effects arise in deeper layers (300-500 μm).

ICRP recommends that the dose equivalent is determined at a nominal depth of 0.07 mm (7 mg/cm^2), averaged over an area of 1 cm^2, regardless of the area exposed. The effective dose limits provides sufficient protection for the skin against stochastic effects [32].

3 Equipment

The spectrometer consists of three separate parts: a handhold detector probe, a base unit and a host computer. The spectrometer is shown in Figure 1. The total weight of the spectrometer is less than 10 kg.

Figure 1. Photo of the Risø telescope spectrometer. The hand held detector probe is connected to the base unit in which batteries and electronics are located. The spectrometer is controlled by the laptop computer. [22] Photo: I. Gjerløv-Christensen

3.1 Detector probe

The detector probe consists of a 12 cm × 22 cm × 8 cm aluminum box containing a detector assembly consisting of three silicon detectors, a thermoelectric cooling element.

Detector assembly

Figure 2 shows a cross-section of the detector assembly. It consists of three silicon semiconductor detectors with dimensions specified in Table 1. The detector assembly is manufactured by Q-Par Angus Ltd., UK.

The thick detector at the back consists of two detectors mounted very close together with a common electrical connection. The two detectors are thus in parallel.

The total thickness of the detectors in the telescope arrangement is 7341 μm, which enables the spectrometer to measure electron energies up to about 3.5 MeV. This energy is also the decay energy of the ruthenium/rhodium-106 fission product, which can be present at nuclear power stations. The lower detection limit is about 50 keV. 70 keV is the minimum energy an electron needs to reach 0.07 mm tissue depth.

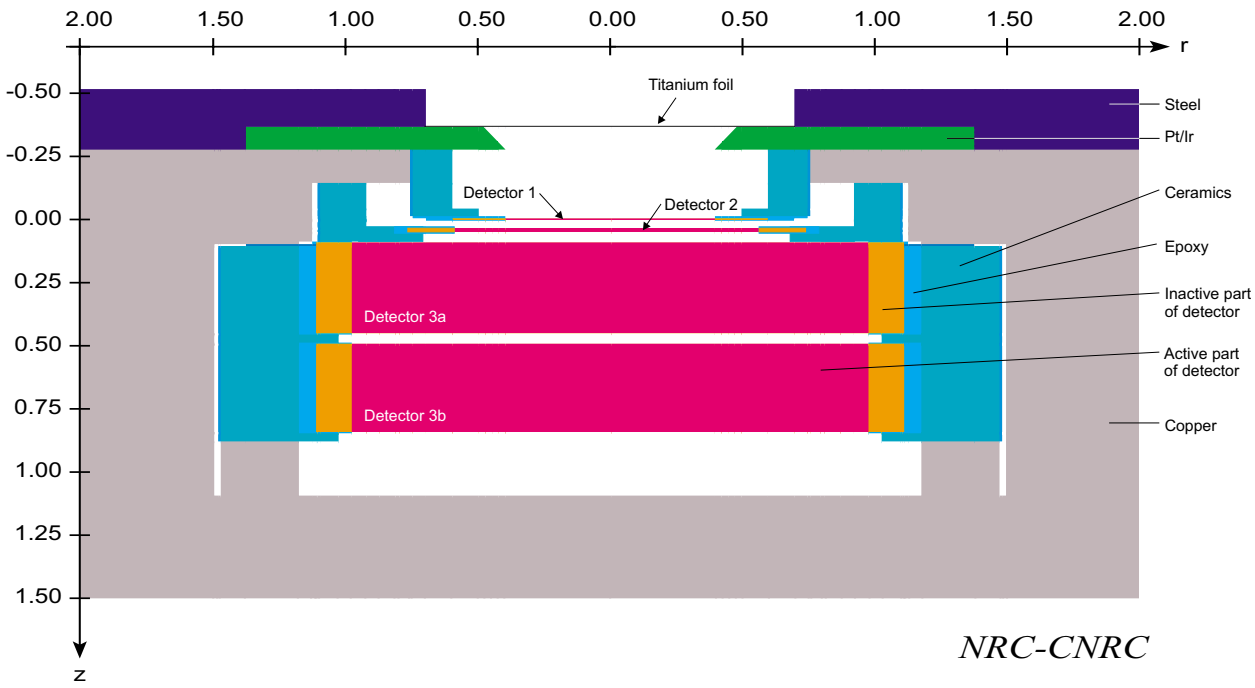

Figure 2. Cross-section of the detector assembly. All lengths in cm. Based on graphics by IRS/NRC (Ionizing Radiation Standards. National Research Council of Canada).

Table 1. Dimensions of the silicon detectors used in this work, as specified by the manufacturer.

Position	Name	Thickness [μm]	Area [mm^2]
Front	Detector 1	52	50
Middle	Detector 2	157	100
Back	Detector 3	7132	300
Upper-back	Detector 3a	3590	300
Lower-back	Detector 3b	3542	300

The detectors are mounted on holders made of ceramics, using conducting epoxy as glue. The whole detector construction is kept together in copper cylinder, 4 cm in diameter and with a wall thickness of 5 mm, assuring that no electrons enters from the side.

At the front side the detectors are shielded by a 0.9 mm thick platinum/iridium (Pt/Ir) diaphragm with a 50 mm^2 hole, which is covered by a light-tight 2 μm thick (0.91 mg/cm^2) titanium foil. In Figure 2 is the Pt/Ir diaphragm shown to have a 45° conical shape with its largest diameter to the top. It has later been revealed that the diaphragm has its largest diameter to the bottom.

Figure 3 shows two photographs of the detector assembly. The copper cylinder with connectors is shown to the left, and to the right a view of the interior of the cylinder.

The copper cylinder is attached by means of screws to a steel flange, which is mounted on the wall of the probe box.

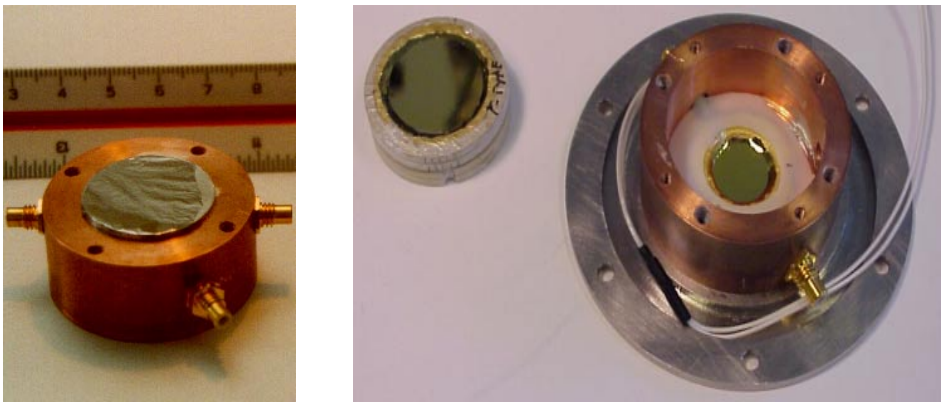

Figure 3. Photos of the detector assembly. Left: The copper cylinder containing the three detectors. The Pt/Ir diaphragm is covered by a titanium foil. The connectors to the detectors can be seen on the side of the cylinder. Right: The detector assembly turned around and opened. Detector 3, consisting of to detector elements, is taken out. Inside the copper cylinder an insulating teflon sheet is seen, and in the center the back side of detector 2. The wire around the cylinder is a thermoelement for measuring the temperature of the assembly. The copper cylinder is mounted on a steel flange.

To reduce the production of bremsstrahlung from high-energy electrons, a 10 mm thick PMMA plate with a 45° conical hole can be attached to the front side of the detector probe. The PMMA plate can be seen in Figure 1.

Thermoelectric element

On the back side of the detector assembly a thermoelectric element (Peltier element) is located. The thermoelectric element cools the detector assembly down to a constant temperature (11°C under normal conditions). Heat-conducting paste is used on the contact surface between the thermoelectric element and the detector assembly.

A solid copper cylinder leads the heat surplus to heat sink placed on the back of the probe.

3.2 Base unit

The base unit is also called a processing and support unit. It holds the batteries for the detector bias supply and the power for the signal processing. A major part of the signal processing takes place in a programmable logic device placed in the base unit (further described in chapter 5). The base unit also hosts a temperature controller, a micro controller for general control with a IEEE488 (GPIB) interface, and a battery charger.

3.3 Host computer

The host computer communicates with the base unit via the IEEE488 interface. Normally a laptop computer will be the host, but also a stationary PC.

Operating program

The spectrometer is operated by a custom build software package. The software is developed in the graphical programing environment 'G' using LabView™ 4.1, 5.0 and 5.1 from National Instruments.

LabView is a graphical programming language contrary to a text and line based language. It is designed for development of computer based instruments i.e. graphical user interfaces, and contains predefined functions for communication with external devices and graphical display of data.

The mathematical treatment of the received pulse heights are described in the next chapter.

The software package consists of three different programs:

Bias- and temperature settings The detector bias can be set either manually or by servo-control, the latter facilitating the use of the instrument by non-experts. In applications where silicon detectors are used, it can be difficult to apply the right detector voltage, since there is a temperature dependent voltage drop over the output resistance of the preamplifier due to the leakage current of the detector.

The leakage current from the three detectors are frequently monitored.

The program includes an automatic test-sequence to plot the relationship between leakage current and detector bias. The test provides a tool to check the quality of the detectors.

Acquisition and detector parameter settings Before an acquisition can start parameters such as acquisition time, threshold settings etc. must be specified. A file name for data storing must be selected. All commands can be executed by a batch-file.

Pulse height data generated by the detectors and relevant information on detector settings and leakage currents can be stored on disc for later analysis.

Each event recorded by the detector array is analyzed by a simple software routine and characterized as an electron or photon event, following the scheme in Table 2. An electron will certainly deliver some of its energy in detector 1, and also in detector 2 and 3 depending on its energy. On the other hand will photons most likely only interact with one detector and then probably with detector 3 which makes up to 99% of the total detector volume.

Monte Carlo calculations shows that the event where energy is absorbed in detector 1 and 3 at the same time is very unlikely, and coincidence pattern 5 is therefore classified as a 'not defined' event. Coincidence pattern 3 [−++] could be caused by a photon creating a Compton electron in detector 2, followed by an interaction in detector 3 either by the photon or the Compton electron. Monte Carlo calculations predicts that this will happen in about 2% of the events where a photon is registered by the spectrometer, but the calculations also foresee that electrons are even more likely to generate this coincidence pattern - it is therefore decided also to classify coincidence pattern 3 as an undefined event.

The total energy distribution in the spectrometer and the energy distributions for electron and photon events are displayed together with the energy absorption in the three detectors, respectively.

The digital pulse heights are received from the base unit (values from 0 to 255), and can be stored as a binary file like this or in a calibrated format, where the pulse heights are expressed in keV. It is also possible to store the pulse height values in an ASCII-file.

Since the pulse height distributions cannot be displayed before the computer has received and analyzed the data, an acquisition is usually broken into smaller sub-acquisitions with a duration of e.g. one second, thereby enabling immediate information on the measurement results.

On the basis of the measured electron energy distribution an estimate for the dose rate from electrons at 0.07 mm tissue depth ($\dot{H}_p(0.07)$) is calculated and displayed.

Table 2. Coincidence patterns. Coincidence and anti-coincidence conditions of the three detectors used to classify electron and photon events. '•' indicates a registered energy absorption above the noise threshold of the detector.

Detector 1	Detector 2	Detector 3	Classification	Coincidence pattern number†	Label‡
-	-	•	Photon	1	[−−+]
-	•	-	Photon	2	[−+−]
-	•	•	Not defined	3	[−++]
•	-	-	Electron (low energy)	4	[+−−]
•	-	•	Not defined	5	[+−+]
•	•	-	Electron (medium energy)	6	[++−]
•	•	•	Electron (high energy)	7	[+++]

† The number is based on a binary interpretation of the detectors entering the pattern.

‡ The label is used later to ease the interpretation of the coincidence pattern number.

In the following will the expression 'dose at 0.07 mm tissue' only be used about dose caused by electron irradiation.

Log-files with relevant data about the acquisition - e.g. count- and dose rates, threshold values, leakage currents and detector temperature - are written at the start and end of an acquisition or at regular time intervals. These data are also written in a global log file documenting the history of the spectrometer.

Figure 4 shows the user interface of the acquisition program.

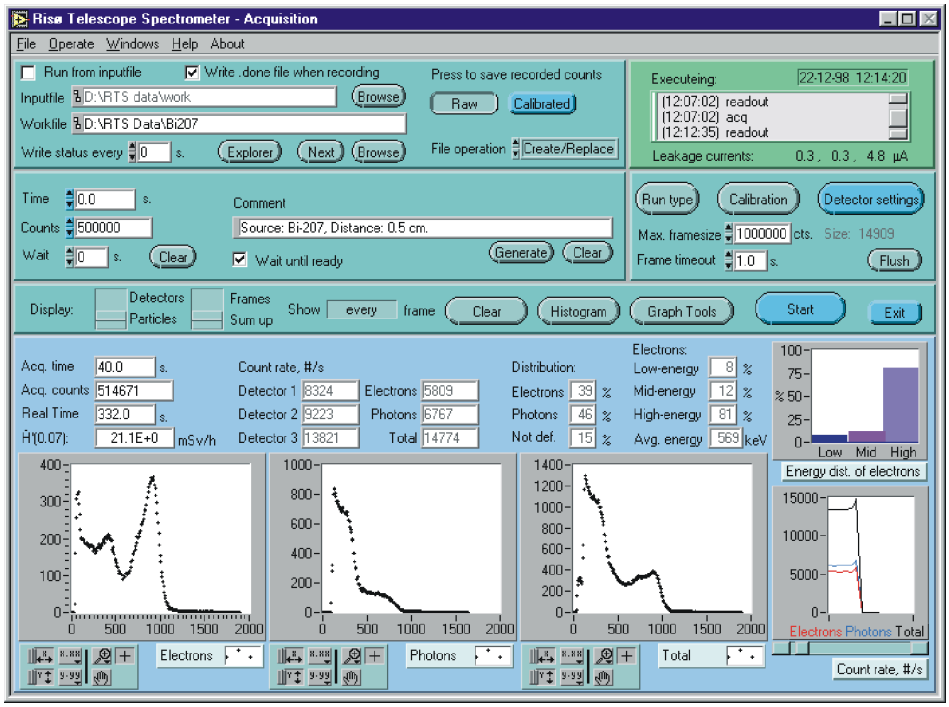

Figure 4. An example of an LabView user interface used in the data acquisition program. The histograms shows the separated electron and photon energy spectra as well as the total spectrum from a Bi-207 source. [22]

Analysis of data stored on disc This program has the functionality of the acquisition program, except that data is read from a file.

Extra analysis tools are available. Histograms of the pulse height distribution for any combination of detectors and coincidence patterns, in a given energy interval, can be presented. It is possible to specify new noise thresholds as long as they exceed those used in the original measurement.

Acquisition time and other information is automatically extracted form the log-files belonging to the pulse height data.

Further documentation of the operating program is found in appendix E.

4 Properties of silicon semiconductor detectors

This section describes some of the properties of silicon surface barrier detectors which are used in the spectrometer.

4.1 Intrinsic properties

A silicon surface barrier detector typically consists of an n-type silicon wafer coated with a thin gold or aluminum layer. The silicon is usually doped with phosphorus to form an n-type material while the gold/aluminum interplay with silicon oxide on the wafer to act as p-type material. The band gab, E_g, between the to materials is in the order of 1 eV.

The n-p conjunction acts as a semiconductor. If a potential is applied in the n-p direction (reverse bias) no current will flow, but the electric potential will result in a region where all free charges (electrons and holes) are swept away, due to build up in the contact potential between the n- an p-type material. This region of the silicon wafer is called the depletion layer, and the size is determined by the specific resistance of the doped silicon and the applied bias voltage [48][43].

The n-p conjunctions used in the detectors for the spectrometer are of a type called England-Hammer Au-Ge-Si contacts. The contacts are special since the Ge-Si layer is constructed in a way so it acts as a barrier for both holes and electrons. When reverse biased the contact behaves as a normal n-p conjunction, and forward biased it acts as a non-injecting ohmic contact. The silicon wafer has the same England-Hammer contacts on both sides, and can be operated with the bias going either way. A thin gold layer is applied on top of the Ge-Si contact to reduce surface resistance [15][16].

Information about the bias voltage needed to totally deplete a specific detector is supplied by the detector manufacturer. If this bias is exceeded a dielectric break through can cause permanently damage to the detector.

When electrons interacts with matter atoms will be ionized, i.e. electron-hole pairs are created. This is also true when photons interacts with matter, since the end-product is electrons in motion.

When an electron-hole pair is created they will usually re-combine, but subjugated to the electric field in the depletion layer, they will be swept apart in opposite directions, and contribute to a small current across the semiconductor. The lifetime of a free electron-hole pair is about 10^{-5} s.

The ionization energy needed to create an electron-hole pair, ϵ, is 3.62 eV in silicon at room temperature. As a comparison it will require about 1 keV to create a photo-electron in a scintillation counter. The low ionization energy gives a good energy resolution compared to other detection systems, since more information carriers are created and the statistical uncertainty therefore less.

The ionization energy is decreasing with decreasing temperature, but this does not play a significant role when the temperature differences are in the order of tens of kelvins. A temperature drop from 20°C to 5°C has been measured to give a 0.3% change in the energy calibration of a silicon semiconductor [21].

Unless otherwise mentioned the word *detector* will only be used meaning the depleted part of the silicon wafer.

Effectiveness

The intrinsic efficiency, i.e. the number of particles registered compared to the number of particles striking the detector with an energy above the noise threshold, is essentially 100% [48].

Fano facor

Not all the absorbed energy is going to the creation of electron-hole pairs. A small part of the energy is used to excitation of fonons, i.e. lattice vibrations, and this may influence on the resolution of the detector.

If energy absorption through ionization and creation of fonons are uncorrelated the variance in the number of electron-hole pairs would be governed by Poisson statistics and equal the number of produced electron-hole pairs equal E/ϵ, where E is the absorbed energy. The Fano factor is defined as the ratio between the observed variance and the Poisson statistic variance [43]

$$F \equiv \frac{\text{observed statistical variance}}{E/\epsilon} \tag{2}$$

To have a good resolution the fano factor should be as low as possible. The fano factor for silicon at 77 K is 0.084 to 0.143 [43]. It is not surprising that the fano factor is fairly small, since the ionization energy is far less than the absorbed energy.

Collection of charge carriers

As mentioned above the life time of a free electron-hole pair is about 10^{-5} seconds, so the mobility of electrons and holes is a key issue.

The transit time in an n-type material, i.e. the time for an electron to cross the entire width of the depletion layer, can for detection of electron radiation be described by the following equation [43]

$$t_c = \frac{0.53 d^2}{\mu V} \tag{3}$$

where
t_c: Transit time in seconds
d: Depletion widths in cm
μ: Electron mobility for electrons in cm^2/V-s
V: Bias voltage in volts

For silicon at room temperature μ=1350 cm^2/V-s. Table 3 shows the transit times for electrons in the three detectors used in this work.

It is seen that the transit times for electrons are at least two orders of magnitude less than the life time of an electron-hole pair. The transit time for holes are about tree times slower than for electrons, but this does not affect the assumption that all created pairs are expected to be collected.

Impurities in the silicon can cause electron and hole traps which can prolong the transit time and annihilate some of the charge carriers.

4.2 Noise considerations

A 100 keV electron totally absorbed in a silicon detector will give rise to about 28 000 electron-hole pairs, which, with a collecting time of 100 ns, would result in

Table 3. Transit times for electrons in the detectors used in the Risø Telescope Spectrometer

Detector	Thickness of depletion layer†	Bias	Electrical field strength	Transit time, t_c (eq. 3)
	[cm]	[V]	[V/cm]	[s]
1	$5.1950{\cdot}10^{-3}$	7	1347	$1.5{\cdot}10^{-9}$
2	$1.5695{\cdot}10^{-2}$	47	2995	$2.1{\cdot}10^{-9}$
3a	$3.5899{\cdot}10^{-1}$	350	975	$1.5{\cdot}10^{-7}$
3b	$3.5420{\cdot}10^{-1}$	350	988	$1.4{\cdot}10^{-7}$

† The two 30 nm thick germanium layers in the England-Hammer contacts are treated as silicon, since they only make up less than 1 per mille of the total thickness.

a current across the detector of $5 \cdot 10^{-8}$ A. A silicon detector is thus very sensitive to noise.

The term 'noise' refers to the factors that leads to a broadening of a measured signal, i.e. that an energy absorption of a single energy is not registered as a Dirac-delta function but rather as a peak characterized by a full-width-half-maximum value.

The noise can be split into several sources which add in quadrature to form the total noise [43]

$$(\Delta E_{\text{total}})^2 = (\Delta E_1)^2 + (\Delta E_2)^2 + \ldots + (\Delta E_n)^2 \tag{4}$$

where ΔE represents the peak broadening due to each source term.

Below some of the major contributions to the total noise are described.

Fluctuations in leakage currents

The two most important contributions to the leakage current are: Thermal generation of electron-hole pairs (bulk leakage current) and surface leakage current.

Thermal generation of electron-hole pairs Electron-hole pairs will continuously be created in the depletion layer due to thermal excitation. The probability per unit time for generation of an electron hole pair is [43]

$$p(T) = CT^{3/2} \exp(-E_g/2kT) \tag{5}$$

where
C: Constant (dependent on the material)
T: Temperature in kelvin
E_g: Band gab matching the units of the Boltzmann constant
k: Boltzmann constant [$1.28{\cdot}10^{-23}$ J/K, $8.62{\cdot}10^{-5}$ eV/K]

The bulk leakage current is proportional to the volume of the detector, and the only way to reduce it is by cooling.

The Risø telescope spectrometer is usually operated at 11°C. Compared to operation at 20°C this gives a reduction factor in the bulk leakage current of about[1]

$$\frac{p(20°\text{C})}{p(11°\text{C})} = \left(\frac{293}{284}\right)^{3/2} \frac{\exp(-1.117 \text{ eV}/(2 \cdot 8.62 \cdot 10^{-5} \text{ eV/K} \cdot 293 \text{ K}))}{\exp(-1.120 \text{ eV}/(2 \cdot 8.62 \cdot 10^{-5} \text{ eV/K} \cdot 284 \text{ K}))} = 2.2 \tag{6}$$

[1]The energy band gab at 11°C and 20°C is calculated using a linear interpolation on values given in [43] and [2].

Cooling the detector assembly has shown to be an efficient and necessary tool to reduce the leakage current and thereby the noise level.

The temperature dependence of the bulk leakage current is discussed in [48][25][2].

Surface leakage current The surface leakage current originates from the edges of the junctions to the detector, where there is a large voltage gradient. The surface leakage currents are among other things dependent on the specific way the detector is manufactured, and if the detector surface is contaminated with dirt or humidity [43].

The detector should therefore be kept clean, and special care should be taken if the detector is cooled, that humidity from the air is not condensed on the surface. Condensed vapor may also cause extra energy absorption of low energy beta radiation at the protection foil.

Electronic noise

The noise originating from the preamplifiers depends among other things on the capacitive load, which should be minimized.

The capacitance of the detector is proportional to the area and inverse proportional to the thickness of the detector.

Capacitance from cables, connectors etc. must be included in the total capacitive load, and cables between detector and preamplifier should therefore be as short as possible.

It is important that the properties of the preamplifier match the capacitive load.

Johnson noise is associated with series resistance and poor electrical contacts. If a detector is not totally depleted, the undepleted region will add to the Johnson noise.

Miscellaneous noise

- Pick up of electro-magnetic noise can be a significant problem, and special emphasis should be taken to shield cables in the vicinity of the detector.
- Surface barrier detectors show an increase in noise and leakage current if subjected to light. The detector should therefore be shielded from light.
- Fluctuations in the energy absorption in the dead layer may add to the total noise, but this is not significant for beta-radiation [43].
- Since the fano factor is small the resolution is not believed to be affected by fonon production in the silicon lattice.

4.3 Noise properties of the Risø telescope spectrometer

The detector elements are manufactured by Q-Par Angus Ltd. Herefordshire, UK, in the spring of 1997. The pulser resolution FWHM was at 18°C specified to 17/17/40 keV (detector 1, 2 and 3 respectively), and the leakage current was specified to 0.40/0.56/5.69 μA. Preliminary measurements showed agreement with these values for detector 1 and 3, and about 0.3 μA for detector 2.

Leakage current of detector 3

Placed in the detector probe the detectors showed similar leakage currents as those specified by the manufacture, but it became clear that the leakage current

of detector 3 was rising with 4 μA per hour at 18°C and 2 μA per hour at 15°C. After the detector had been turned off for several hours the original magnitude of the leakage current was restored.

As times has passed on the lowest leakage current achievable has raised, and it has been necessary to cool the detector assembly to 11°C to keep the leakage current in the range of 5 to 6 μA. Even at this level the pulser resolution full-with-half-maximum value is 130 keV.

The electronics of the detector probe has been thorough investigated to make sure that no component other than the detector causes the rising leakage current.

The rise in leakage current is believed to be caused by intrinsic solid state properties of the silicon wafer, e.g. mobile impurities. Heating the detector assembly at 60°C for 5 hours, as proposed by Q-Par Angus, did not lower the leakage current.

In the spring of 2000 the large leakage current of detector 3 was localized to detector 3b, which is now detached. The measurements presented in this work were all done prior to the detachment.

Noise properties of detector 1

The noise limit for detector 1 has increased to about 45 keV. Some of the noise is believed to originate from the electronics. It has been noted that the surface of detector 1 has been contaminated with a dried-up liquid, as seen in Figure 5, and this may have led to an increased noise level. It is possible that the liquid is heat conduction paste which has seeped in.

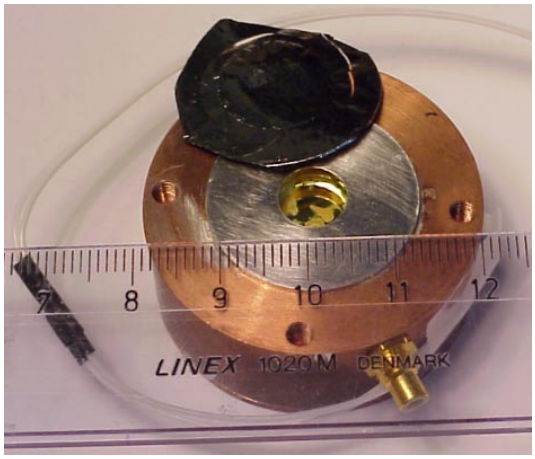

Figure 5. The detector assembly with the titanium foil removed. Beneath the foil is the Pt/Ir diaphragm seen. Dried-up liquid can be seen on surface of detector 1.

5 Signal trace

This chapter gives an overview of how the initial signal registered by a detector is digitized, and how the digital pulse height values are manipulated by the laptop computer, and finally displayed as energy histograms together with a calculated value of the skin dose at 0.07 mm tissue.

The electronics is designed and build by Henning E. Larsen, Optics and Fluid Dynamics Department, Risø.

For a comprehensive description of the electronics used in the Risø Telescope Spectrometer see H.E. Larsen [45] or J. Helt-Hansen *et. al.* [22]. Figure 6 to 10 includes graphics by H.E. Larsen.

5.1 Analogue front end

The signal from a detector is first amplified by a preamplifier with a high signal-to-noise ratio to bring the signal into the dynamic range of the analogue-to-digital converter (ADC), which is 255 levels over 1 V. Next the signal is shaped by a CR, RC pre-shaper to give the pulse a quasi-Gaussian shape of the form $v(t) = \frac{1}{\tau}\exp(-t/\tau)$, where t is time and τ a characteristic time constant.

5.2 Digital signal processing

The digital signal processing takes place in the base unit. The amplified pre-shaped pulse is sampled by the ADC at a rate of 12 million samples per second. The length of the quasi-Gaussian pulse is about 2 μs, and it is thus sampled in 15 to 25 points.

The 255 levels of the ADC results in a reduced energy resolution of the spectrometer compared to conventional analogue systems.

The signal is processed in a general-purpose programmable logic device (PLD). The program code needed for the data processing is uploaded to the PLD when the connection between the base unit and the host computer is established. This takes about 30 seconds.

Digital pulse shaping

In the PLD the digitized pulse from the ADC is folded by a finite impulse response (FIR) filter, which transform the quasi-Gaussian pulse into almost any desired shape called a weighting function. Figure 6 shows as an example how two different FIR filters transform a quasi-Gaussian pulse into a singular or a bi-polar weighting function.

The FIR filter works like an running average, except that the numbers have different weights, as illustrated in Figure 6. A FIR filter gives a weighting function of a finite length, contrary to a infinite impulse response filter, which gives a weighting function, that goes to zero over a long period of time.

It is important to realize that the transformation is a purely mathematical manipulation of the output from the ADC, and that the outcome of the FIR filter also is an array of numbers.

The FIR filter used in the spectrometer is similar to the one giving a singular pulse with a flat top and straight slopes shown in Figure 6. The height of the weighting function is proportional to the energy absorbed in the detector, and the FIR filter is optimized for best amplitude resolution. The length of the weighting function, called the shaping time (τ_s), is 15 sample periods, i.e. $15 \cdot 82$ ns $= 1.25\mu$s.

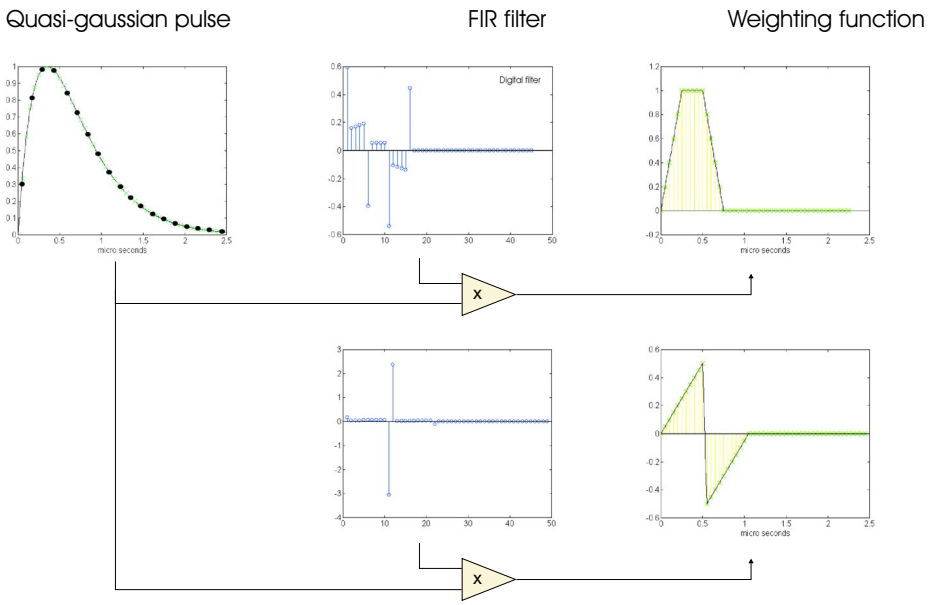

Figure 6. Examples of how different FIR filters can transform a quasi-Gaussian pulse into different weighting functions.

Threshold detection

The weighting function is compared against a user defined noise threshold. The time the weighting function is above the threshold is recorded, and the middle of the time span is used as a time stamp for the event. Figure 7 illustrates the time-over-threshold and the time stamp.

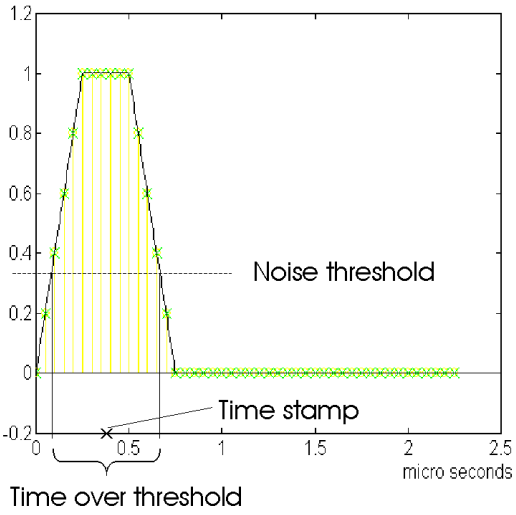

Figure 7. Illustration of 'time-over-threshold' and the position of the time stamp.

The pulse is rejected if the time-over-threshold is not within a predefined time range. If the time over threshold is too long it is a sign of pile-up, and a dead-time counter is incremented.

5.3 Dead-time estimation

The calculation of $\dot{H}_p(0.07)$ depend on three things: The measured energy spectrum of electrons, an algorithm to convert the measured spectrum to $H_{\mathrm{p}}(0.07)$ and finally a measurement of the time used to collect the measured spectrum in order to calculate the dose rate, $\dot{H}_p(0.07)$.

The time, T_m, used in a measurement is

$$T_m = T_{acq} - T_{dead} \tag{7}$$

where T_{acq} is the acquisition time and T_{dead} the dead-time[2].

Each accepted event above the threshold will give rise to a dead time equal to the length of the weighting function, τ_s.

A rejected event, which usually is a superposition of two events, will give a dead-time between 1 and 2 times τ_s. The precise value is statistical and as an approximation $1.5 \cdot \tau_s$ is used [45].

The dead-time counter is incremented for each detector every time the time-over-threshold is to long. For high energy electrons interacting with all three detectors the number of rejected nuclear events is set to $N_{rej} \approx \frac{1}{3} N_{dt}$, where N_{dt} is the value of the dead-time counter. For low energy electrons or photons which are likely only to interact with one detector $N_{rej} \approx N_{dt}$.

The dead-time for medium to high energy electrons is approximated by

$$T_{dead,electron} \approx (0.5 \cdot N_{dt} + N_{event})\tau_s \tag{8}$$

and for low energy electrons and photons

$$T_{dead,photon} \approx (1.5 \cdot N_{dt} + N_{event})\tau_s \tag{9}$$

where
N_{dt}: number of rejected counts read from the base unit
N_{event}: number of registered nuclear events
τ_s: shaping time, 1.25 μs

Figure 8 shows the number of pulses rejected as a function of count rate for a number of electron sources (Pm-147, Tl-204, Sr-90/Y-90) and photon sources (Cs-137, Co-60, Rn-226).

It is evident that the number of rejected pulses per count rate is dependent on the type of radiation measured, but instead of the expected factor of three in the ratio of dead-time counts per count rate, there is a factor of ten in difference. Further investigations are needed to explain this difference.

Fortunately the ratio of rejected pulses over count rate is very small, and the difference in the pulse rejection rate does not influence much on the total dead-time. Figure 9 shows the calculated dead-time for electron and photon sources using both equation 8 and 9 in each case.

For electron count rates up to 35 000 counts/s and photon count rates up to 60 000 counts/s there is no significant difference whether equation 8 or 9 is used to calculate the dead-time.

For electron counts rates well above 35 000 counts/s a notable difference probably will be seen. In such cases the spectrometer could as a future development

[2]Since the detector signal is continuously digitized and likewise continuously evaluated after the FIR filter, the dead-time of the spectrometer is not strictly equivalent to the term dead-time used about a multi-channel analyzer, in which a certain amount of dead-time is associated to each registered count. Then considering dead-time the spectrometer should be regarded as a pile-up detector. Therefore equation 8 and 9 does not truly describe the way to calculate the dead-time, but the uncertainty of the dose rate measurements presented later in this report is not affected notably by this observation, since the effect is small.

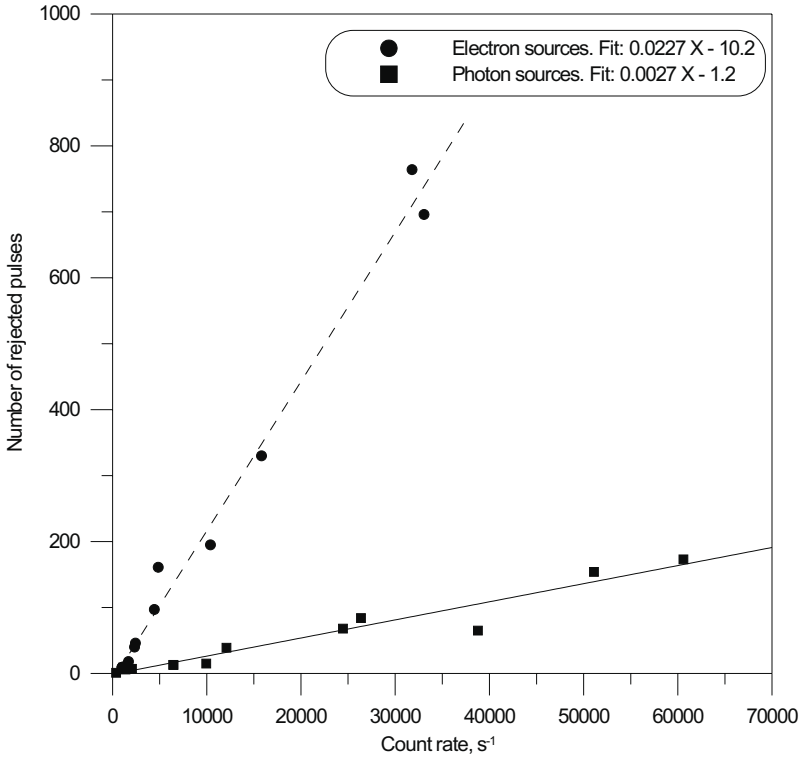

Figure 8. Number of rejected pulses as a function of count rate

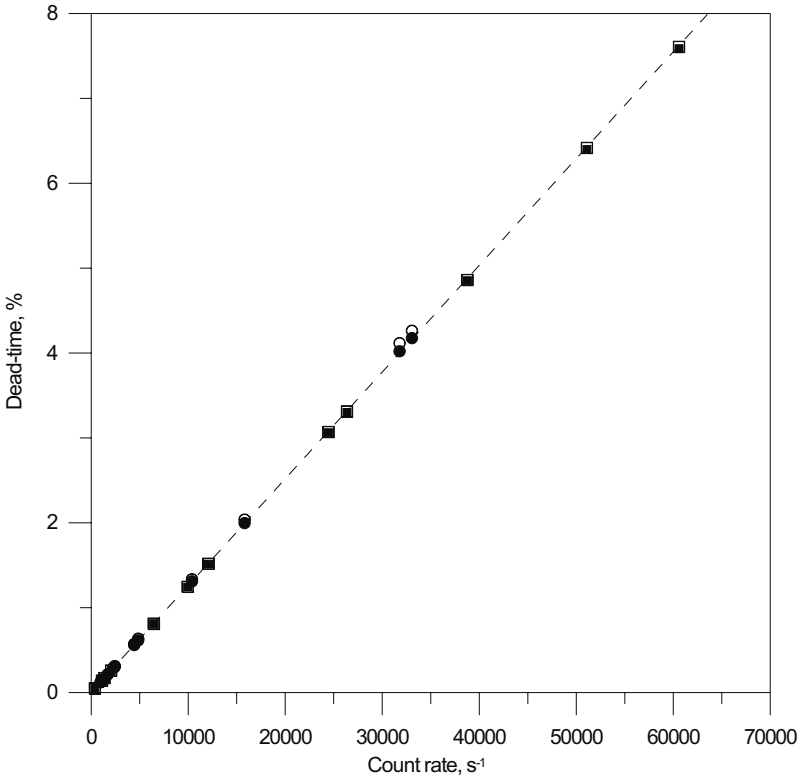

Figure 9. Percent dead-time as function of count rate.
Circle symbols: Electron sources. Square symbols: Photon sources.
Filled symbols: Dead-time calculated via equation 8 (i.e. optimized for electrons).
Open symbols: Dead-time calculated via equation 9 (i.e. optimized for photons).

choose an equation for dead-time correction depending on an analysis of the measured electron to photon ratio.

As for now the dead-time is calculated using the equation

$$T_{dead} = (N_{dt} + N_{event})\tau_s \tag{10}$$

5.4 Coincidence logic

When a pulse is approved by threshold detection system, the heights of the weighting functions from all three detectors are recorded at the time stamp belonging to the detectors respectively.

There is a user defined time window of 0.16 to 1.4 μs where triggers from different detectors are said to belong to the same event.

The height of the weighting function is called the *digital pulse height* (*dp*), and pulse heights belonging to the same event are bundled together in what is called a *triplet*, and stored in an array. The array of triplets are transferred to the host computer at regular intervals (e.g. after an acquisition time of one second) or when the buffer in which the array is stored is full.

The path of a pulse from a detector via preamplifier and digital signal processing to the collection of triplets is sketch in Figure 10.

When the array of triplets arrives at the host computer, each triplet is computed by itself, and finally energy absorption histograms are made and dose at 0.07 mm tissue calculated.

5.5 Calibration

Each digital pulse height in the triplet is converted to energy in keV by use of a first order polynomial. The two coefficients in each polynomial are described in chapter 11, where the calibration of the spectrometer is discussed.

At this stage it is also possible to store the digitized pulse heights or the calibrated pulse heights on hard-disc for later analysis.

5.6 Determination of particle type

An important task for the spectrometer is to identify whether the detected particle is an electron or a photon. The classification of particles based on the coincidence patterns shown in Table 4 (a similar table was shown on page 15). The 'noise threshold' is defined as the upper limit of the noise flank, where the registered counting rate due to noise is comparable to the counting rate due to nuclear events.

Table 4. Coincidence patterns. '•' indicates a registered energy absorption above the noise threshold.

Coincidence pattern	Detector 1	Detector 2	Detector 3	Classification
1	-	-	•	Photon
2	-	•	-	Photon
3	-	•	•	Not defined
4	•	-	-	Electron (low energy)
5	•	-	•	Not defined
6	•	•	-	Electron (medium energy)
7	•	•	•	Electron (high energy)

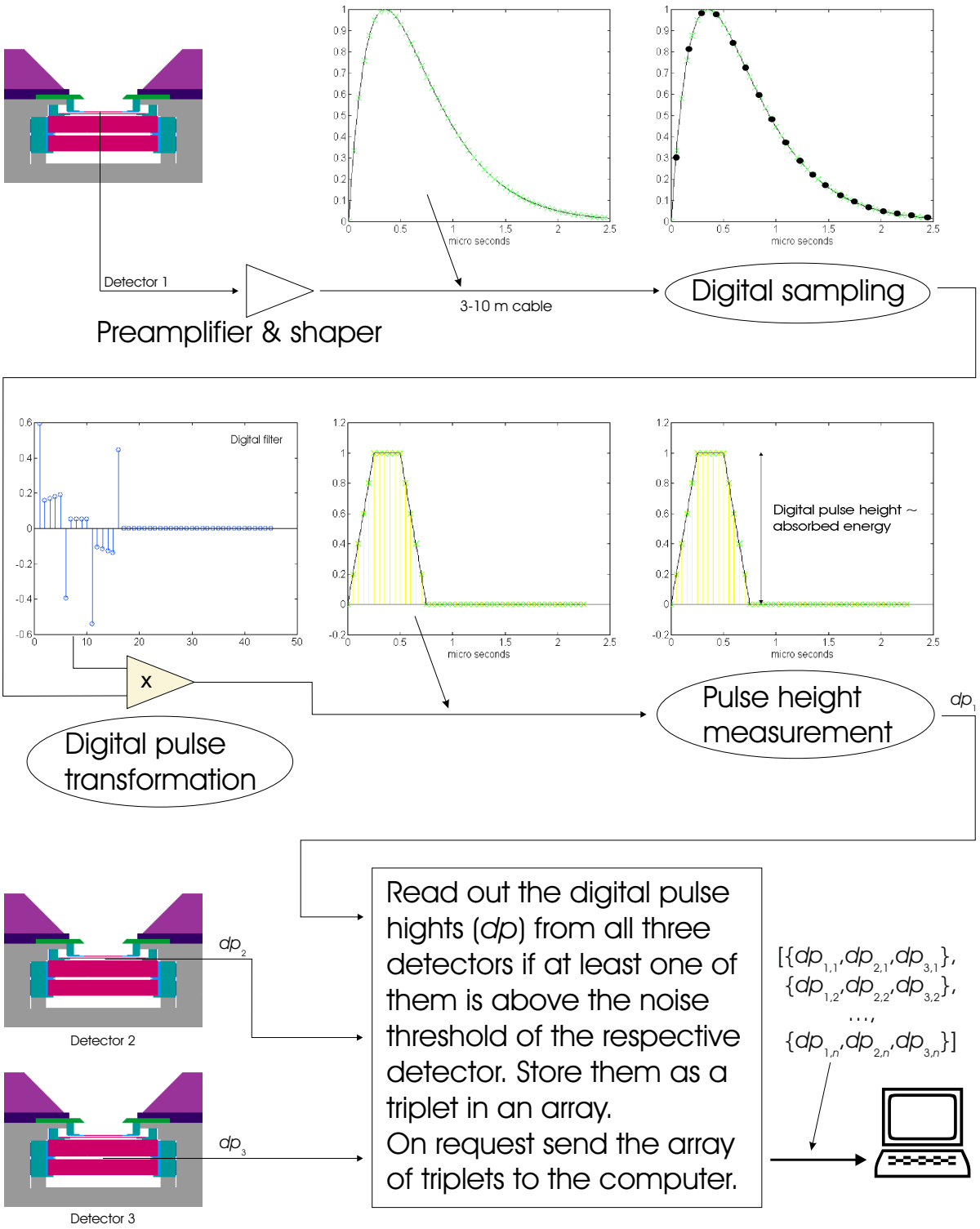

Figure 10. The pathway of the signal in the detector probe.
Top: The pulse from the detector is amplified and shaped by a preamplifier and a CR,RC filter, and then digitized by a analogue-to-digital converter.
Middle: In a programmable logic device, the digital values are transformed via a FIR filter to a weighting function with a flat top and straight slopes. The height of the weighting function is measured, and this value is called the digital pulse height (dp). The height of the weighting function is proportional to the energy absorbed in the detector.
Bottom: If the digital pulse height is above the noise threshold, it is recorded together with the digital pulse heights from the two other detectors. The three values are treated as a single object called a triplet. The triplets are stored in an array, which is later send to the host computer.

The classification scheme is sensible to noise. If for example detector 1 is misinterpreted, an electron event will not be classified as an electron, and a photon event not as a photon.

Especially the pulse height detection in detector 1 is problematic, since energy absorption from high energy electrons is close to or below the noise threshold.

Coincidence pattern 5 is later reclassified as photon events due to noise in detector 1 (see section 9.6).

5.7 Introduction of particle threshold

Two features are noted about the noise properties of the telescope arrangement

- An electron event will almost certainly be registered by at least one detector.
  Monte Carlo calculations show that an electron with energy up to 150 keV will deposit its entire energy in the front detector, i.e. well above the noise threshold.[3]
  In the energy range from about 150 to 400 keV the energy deposition in detector 1 is comparable to the noise level, but the energy registered in detector 2 is well above the noise threshold here.
  Finally for electrons above 400 keV the energy deposited in detector 1 and 2 is fairly low, but is above the noise threshold in detector 3.

- The noise in the three detectors is uncorrelated, and especially uncorrelated with the registration of a particle entering the spectrometer.

Based on the above considerations a so called *particle threshold* is introduced [22]: If a pulse height above the noise threshold is registered in one of the three detectors, the coincidence pattern will be decided on the basis of a new set of lower noise thresholds called particle thresholds, which enable registration of electron energy depositions located in the noise region of the two other detectors.

The particle thresholds for the front and the middle detector should be set so low that the vast majority of high energy electrons are registered, but not so low that the noise of the detector becomes predominant.

The particle threshold is also useful for detector 3. The noise threshold of 124 keV means that the total energy registered by the spectrometer in some cases will be more than 100 keV lower than the actual particle energy. Particularly electrons in the 200 to 400 keV range will be sensitive to this. By use of the particle threshold the fraction of electrons being registered at too low an energy can be reduced.

If the particle thresholds are set too low, photons are likely to be registered as electrons. The choice of particle thresholds is based on measurements of pure beta- and photon radiation fields and is discussed in chapter 12.

5.8 Determination of particle energy

When the pulse height in at least one detector is above the noise threshold, the energy of the registered particle was originally defined as the sum of the absorbed energy registered in the three detectors. This definition is used by [22], but leads to an overestimation of absorbed energy for low energy particles.

The assumption that the energy of a particle is the sum of the absorbed energy registered by three detectors, only works when no noise is present. Figure 11 illustrates the noise distribution in detector 3, approximated by a Gaussian curve with a FWHM of 130 keV centered around 0 keV. The noise threshold (124 keV) and the particle threshold (83 keV) is marked by vertical lines. Detector 2 is kept out for reasons of clarity in the following example.

Imagine that the spectrometer is irradiated with an electron source so low in energy, that the electrons only interacts with the front detector. When a particle is registered in detector 1, the pulse height from the two other detectors will be compared to the noise- and particle thresholds. In 6% of the events the noise in detector 3 will be above the particle threshold, and the particle will be classified as an coincidence pattern 5 event [+−+]. Since it is not classified as an electron it will not change the mean energy of the registered electrons.

[3] For a graphical display of the energy absorption in the Risø telescope spectrometer see J. Borg and J. Helt-Hansen [9].

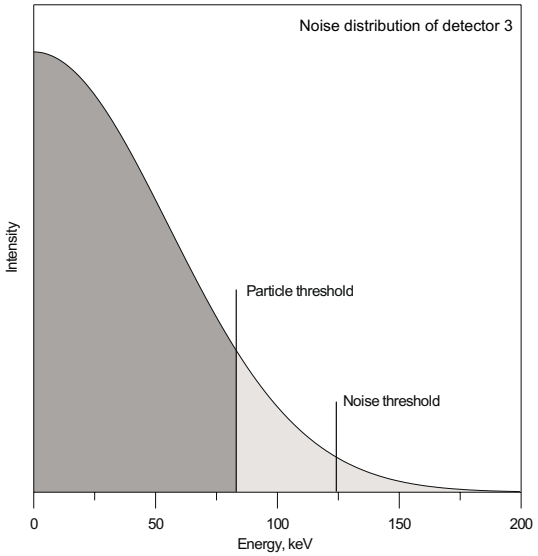

Figure 11. The noise distribution in detector 3, approximated by a gaussian curve with a FWHM of 130 keV.

In 50% of the cases the noise in detector 3 will be negative and not registered at all, but in 43% it will be between 0 keV and the noise threshold at 83 keV (the dark shaded area of Figure 11). If the energy of the particle registered in detector 1 is taken to be the sum of the registered energy in all of the three detectors, it will in average lead to an overestimation of 34 keV, i.e. the mean energy of the Gaussian curve between 0 and 83 keV.

The solution is only to sum the registered absorbed energy from the detectors, where the pulse height is above the particle threshold. This is also coherent with the definition of the particle threshold i.e. the energy level where the noise level becomes dominant even when coincidence between the detectors is taken into consideration. The correct method for determination of particle energy is used in this report.

Spectra of Pm-147, Tl-204 and Sr-90/Y-90 has been measured and the difference between the two algorithms for determination of particle energy leads to shift in the measured mean energy of 13%, 3% and 0.3% respectively.

The overestimation becomes less with increasing particle energy, because the electrons starts to reach detector 3.

Even the correct way of defining the particle energy leads to a slight overestimation. For a low energy particle only registered in detector 1, registration of noise in detector 2 above the particle threshold, will still give a coincidence pattern interpreted as an electron.

The noise in detector 2 is approximated by a Gaussian curve with a FWHM of 28 keV and the particle threshold for the detector is 26 keV.

The mean energy of the noise above the particle threshold in detector 2 is 30 keV, but this part of the noise is only coincident with detector 1 in 1% of the events, giving an overall surplus of less than 1 keV.

Similar will a medium energy electron - leading to registration in detector 1 and 2 - be coincident with noise above the particle threshold in detector 3 in 7% of the events. The mean energy of the registered noise is 107 keV leading to an average surplus of energy for medium energy particles of 7 keV.

5.9 Display of digitized spectra

A special problem arises due to the relatively large bin widths of the digitized pulse heights [22].

If a histogram of the absorbed energy is to be made for a detector, it is important that the ratio of counts per energy is equal to the original measurement. The terminology used is, that the calibration of the histogram is the same as the digital pulse heights.

Unless the distance between the digitized pulse heights are much smaller than the binwidth of the histogram, special precautions have to be taken to meet this requirement. For the Risø telescope spectrometer, the distance between the digitized pulse heights are 3-20 keV depending on the detector, and this is considerably more than for a conventional analogue system.

Figure 12a and 12b shows what happens if there is a mismatch between the calibration of the digitized pulse heights and the histogram. Because the bins in the histogram does not have the same weight, the depicted energy distribution splits up in what looks like two or more curves.

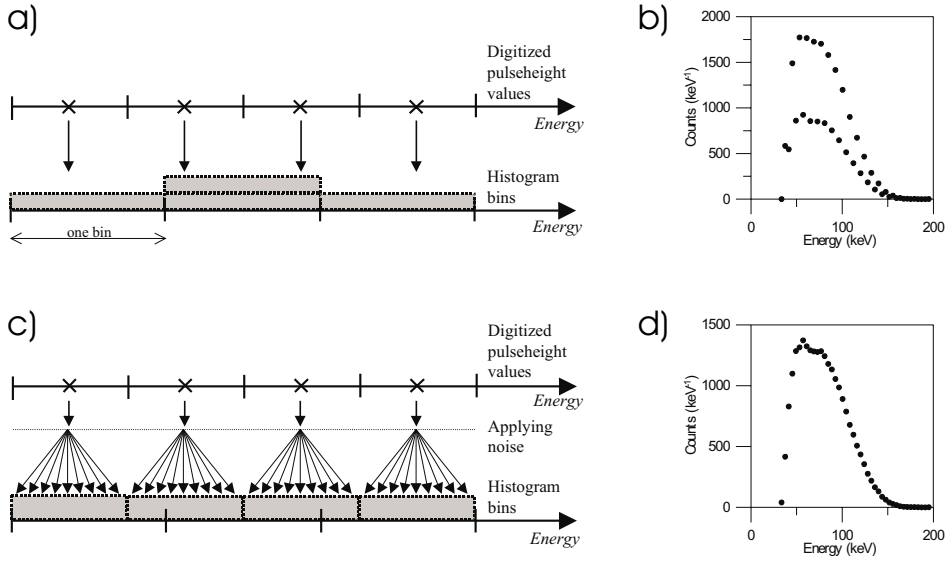

Figure 12. Display of digitized spectra. (a) All electrons with energies in the interval between two vertical markers will be assigned the digital pulse height energy shown with a cross. If the calibration of the digital pulse height values does not match the calibration of the histogram, the depicted energy distribution will split into several curves, since the bin of the histogram will have different weights. (b) Energy distribution in detector 1 for a Pm-147 point source placed 10 from the detector surface. The digital pulse height values have a calibration of 2.6 keV/channel and the histogram 4.0 keV/channel. (c) If white noise is added to the digitized energy value, the histogram will reflect the same ratio of counts per energy as the digital pulse height values, thus avoiding the split-up artifact. The white noise shall have an amplitude equal to the width of one channel. (d) Same data as in (b). White noise with a peak-to-peak amplitude of 2.6 keV has been added to each count. [22]

There are two ways to eliminate the split-up artifact. Either the binwidth of the histogram can be made a whole multiple of the distance between the digitized pulse heights, or noise can be added to the digital pulse heights.

If white noise with a peak-to-peak amplitude equal to the distance between the digitized pulse heights is added to each count, the histogram will reflect the

same number of counts per energy as the digitized pulse heights, and the split-up artifact will disappear. This is shown in Figure 12c and 12d.

Summation of digitized spectra

Calculation of the energy distribution of electrons involves the summation of the digitized energy from all of the three detectors.

The depicted energy distribution will not show the split-up artifact if the calibration of the digitized pulse heights is the same for all tree detectors and equal to the calibration of the histogram. This is not obtainable for the Risø telescope spectrometer since each detector has a different hardware-determined amplification, which cannot easily be changed.

To avoid the split-up artifact noise is added to each of the digitized detector outputs as described above. The noise is added by the software and a smooth depiction of the energy distribution is achieved independent of the binwidth of the histogram displaying the distribution.

By adding noise to the digitized pulse heights, the resolution of the instrument is lowered by an amount roughly equal to the total amplitude of the noise added. In the case of the Risø telescope spectrometer this is a minor component of the total noise.

The method of applying white noise is used for all histograms except for the ones showing an energy distribution in a single detector. In this case the method of matching the calibration of the histogram to the digitized pulse heights is used.

5.10 Calculation of skin dose at 0.07 mm tissue

The scope of the instrument is not only to act at a spectrometer but also as a dose-meter.

Conversion coefficients from electron fluence to dose-equivalent at 0.07 mm tissue, $H'(0.07)$, is given in ICRU report 56 [35]. The coefficients are based on Monte Carlo calculations using six different code systems. The results were collected in the framework of EURADOS Working Group 4 'Numerical Dosimetry', and presented in a report by B. Grosswendt and J.-L. Chartier [19].

Table 5 shows the conversion coefficients from electron planar fluence to dose-equivalent at 0.07 mm in a ICRU tissue slab based on values from [19]. The conversion coefficients are also shown in Figure 13.

One way to calculate an estimate of $H_{\mathrm{p}}(0.07)$ from the measured energy distribution of electrons, is to fold the measured spectrum with the ICRU conversion factors for normal incidence. As a first attempt this is what is done in the spectrometer.

Each bin in the unnormalized spectrum (i.e. measured counts per bin) is multiplied by the ICRU conversion factor for normal incidence, using a linear interpolation to the midpoint energy of the bin. Since the area of the front detector is 0.5 cm^2, the result is multiplied by a factor of two as an estimate for the fluence per cm^2. The dose contribution from each bin is summed to get $H_{\mathrm{p}}(0.07)$. An estimate for the dose rate, $\dot{H}_p(0.07)$, is obtained by dividing $H_{\mathrm{p}}(0.07)$ by the acquisition time.

An additional correction factor can be used to correct for an observed energy dependence of the dose response of the spectrometer when the ICRU conversion factors are used [22].

Table 5. Values of absorbed dose/planar fluence [nGy cm^2] at 0.07 mm depth in a slab of ICRU tissue, irradiated by mono-energetic electrons at various angles of incidence. Based on [19]. Uncertainties over 100% are not displayed.

Energy	Angle						
[keV]	0°	15°	30°	45°	60°	75°	89°
70	0.211 ± 16%	0.178 ± 16%	0.112 ± 29%	0.051 ± 30%	0.018 ± 80%	0.004	0.000
80	1.056 ± 5%	0.988 ± 6%	0.786 ± 9%	0.519 ± 16%	0.278 ± 42%	0.116	0.057
90	1.527 ± 5%	1.464 ± 9%	1.251 ± 11%	0.962 ± 18%	0.614 ± 40%	0.325	0.115
100	1.661 ± 3%	1.613 ± 5%	1.457 ± 7%	1.195 ± 10%	0.790 ± 21%	0.390 ± 82%	0.172
200	0.834 ± 5%	0.903 ± 4%	1.078 ± 4%	1.264 ± 6%	1.252 ± 7%	0.950 ± 13%	0.401
400	0.455 ± 4%	0.489 ± 3%	0.600 ± 3%	0.856 ± 4%	1.226 ± 9%	1.163 ± 9%	0.401
600	0.366 ± 4%	0.390 ± 2%	0.475 ± 4%	0.668 ± 9%	1.106 ± 10%	1.345 ± 16%	0.401 ± 73%
700	0.344 ± 4%	0.366 ± 3%	0.441 ± 5%	0.617 ± 8%	1.044 ± 11%	1.441 ± 17%	0.458 ± 61%
800	0.329 ± 4%	0.349 ± 2%	0.418 ± 2%	0.580 ± 6%	0.980 ± 9%	1.491 ± 23%	0.458 ± 55%
1000	0.312 ± 4%	0.328 ± 2%	0.391 ± 4%	0.542 ± 4%	0.916 ± 10%	1.576 ± 16%	0.516 ± 42%
1500	0.287 ± 3%	0.305 ± 8%	0.357 ± 2%	0.484 ± 4%	0.804 ± 7%	1.743 ± 13%	0.630 ± 25%
2000	0.279 ± 2%	0.295 ± 3%	0.343 ± 5%	0.458 ± 3%	0.746 ± 9%	1.781 ± 14%	0.859 ± 10%
3000	0.276 ± 2%	0.287 ± 3%	0.330 ± 3%	0.434 ± 2%	0.698 ± 7%	1.719 ± 11%	1.146 ± 7%
4000	0.272 ± 1%	0.283 ± 6%	0.326 ± 4%	0.429 ± 2%	0.688 ± 5%	1.692 ± 9%	1.432 ± 3%

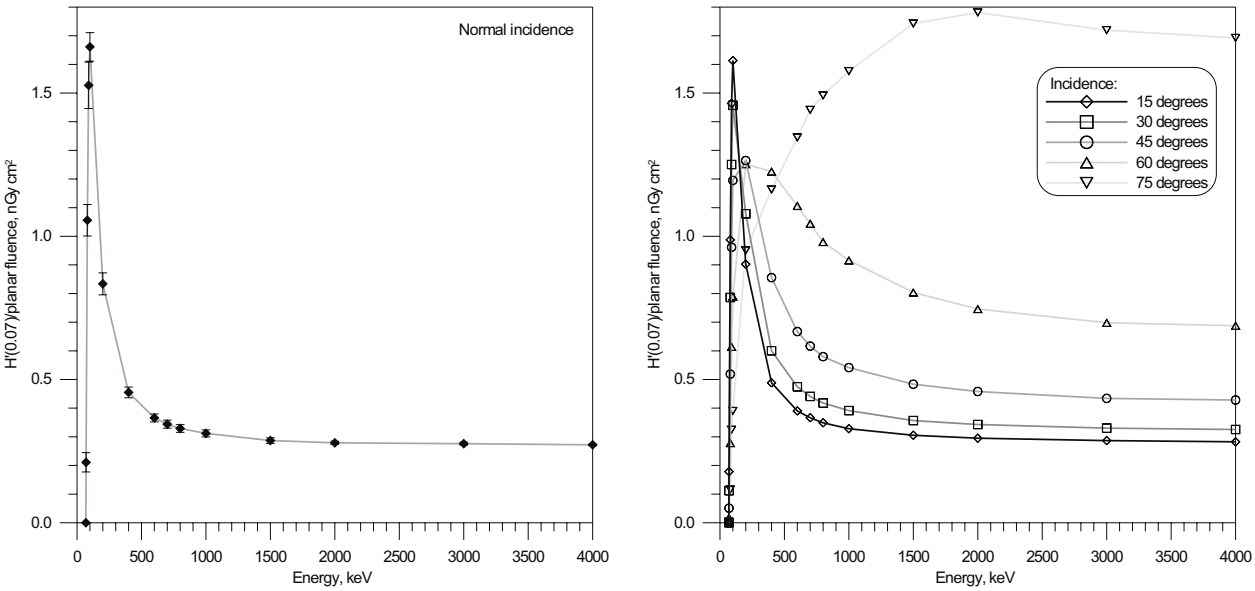

Figure 13. Conversion coefficients from planar fluence to dose-equivalent at 0.07 mm depth in a slab of ICRU tissue, irradiated with monoenergetic electrons at various angles, based on [35][19]. Left: Normal incidence. Right: Incidence angles from 15 to 75 degrees.

6 Monte Carlo Analysis

The Monte Carlo method takes its name through the use of probability distributions and random numbers, thus leading the thoughts to the famous casino in Monaco. The structure of a Monte Carlo calculations is similar to that of a spot test (e.g. a opinion poll) where a representative sample is drawn from the possible outcomes. Just like an opinion poll, the Monte Carlo technique has the ability to give an incorrect answer, if one is not careful how the method is applied. This chapter gives an overview how the EGS4/EGSnrc Monte Carlo programs, used for describing radiation transport, works, and focus on some of the parameters which are essential for the calculations. In the following *Monte Carlo* will only be used in the context of particle transport.

The essence of Monte Carlo calculations is described by D.W.O. Rogers and A.F. Bielajew: [53]

> In the context of radiation transport, Monte Carlo techniques are those which simulate the random trajectories of individual particles by using machine-generated (pseudo-)random numbers to sample from the probability distributions governing the physical processes involved. By simulating a large number of histories, information can be obtained about average values of macroscopic quantities such as energy deposition.

The Monte Carlo technique is in general applied when no exact analytical solution exist or if it is very time consuming to solve. Solving the transport equations for photon- and electron transport analytically can be very complex if not impossible, especially for non homogeneous media.

Section 1 of this chapter deals with algorithms used to simulate particle transport. Section 2 and 3 focus on a special feature of the electron transport called restricted stopping power and its influence on the calculations of the Risø telescope spectrometer. Section 4 is addressing the specific user code used for the calculations presented later in this report.

6.1 Particle transport

EGS4

EGS4 (Electron Gamma Shower version 4) [47][53] is a general purpose code providing subroutines used for Monte Carlo calculation of electron and photon transport. The user can describe quantities to calculate (e.g. dose), and the geometry of the problem, by writing subroutines in the transport code or by using a pre-written code like DOSRZ (described later) to facilitate this process.

EGS4 is a so called analogue model, which means that it tries to simulate the actual physical processes as closely as possible. As default EGS4 does not imply any variance reductions techniques.

Cross sections. PESG4

A fundamental part of a Monte Carlo calculation is the cross sections describing the interaction between particles and matter. In EGS4 these data are provided by a stand-alone data preparation program called PEGS4 (Preprocessor for EGS4). The user specifies the composition of the materials used and energy thresholds for creation of secondary particles.

In EGS4 terminology the lower energy threshold for secondary particle creation is AE for electrons (knock-on electrons/delta-rays) and AP for photons (bremsstrahlung).

PEGS4 produces a data set by piecewise linear fitting, which can be used by EGS4 directly.

Photon transport

A Monte Carlo calculation starts by setting up the phase-space for an initial photon i.e. its position, direction and energy. The parameters can all be fixed (a mono energetic point source pointing in one direction), but have in general some randomness build in (e.g. the direction can be sampled from a 4π sphere).

The phase-space parameters is placed on a 'last-in first-out' stack, and the photon is then transported to a point where a discrete event takes place. How far the photon is transported is sampled from a probability distribution which is governed by the appropriate cross sections. What kind of discrete event that takes place and what direction and energy the primary photon, and maybe secondary particles, will have, is likewise determined by a sample between the relevant cross sections. If secondary particles are created their phase-space parameters are stored on the stack, but always such that top particle on the stack has the lowest energy to prevent stack-overflow.

If the photon has left the geometry it is discarded. If the particle energy falls below a predefined threshold the transport is stopped, and the rest of the kinetic energy is absorbed in the material at this point.

When the stack is empty, a new primary photon may be started. The complete transport of one initial particle and subsequent secondary particles is called a *history*.

Figure 14 shows a simplified flow diagram for EGS4 photon transport.

The cross sections for photoelectric effect, free electron Compton scattering and pair-production are obtained from Hubbell (1969) [28] and the Rayleigh data from Hubbel and Øverbo (1979) [30]. See also [42].

Ignoring uncertainties arising from the fitting procedure, the uncertainty for the photon cross section regarding photo-electric effect is 3-5%. For Compton interactions 2-3% and less for low Z materials [57][29].

Electron transport

The question of CPU time is very important within the Monte Carlo technique. An electron slowing down from 500 to 250 keV in gold makes about 7000 elastic scatterings [4]. To simulate each interaction in an analytical fashion would take an unacceptable amount of time.[4] To overcome this problem condensed history formalism is introduced for electron transport. The transport of photons involves relatively few interactions and the technique is thus not needed.

The condensed history formalism speeds up the calculation by breaking up the electron track in parts and grouping the effect of the individual interactions together along each section.

Deflections due to elastic scattering are modeled by using a multiple scattering theory. EGS4 uses a revised Molière theory [46][5]. Molière theory requires at least 25 atoms to participate in a multiple scatter substep, thus limiting the minimum step size which can be taken [6][1]. This limitation can introduce artifacts when a particle is crossing the interface between geometrical regions. The step size restraint has been removed with the PRESTA II code (Parameter Reduced Electron Step Transport Algorithm) included in the EGSnrc version of EGS4. EGSnrc is a new version of EGS4 developed at the National Research Council

[4] There is no sign that this should change in the years to come, even with the present development in CPU speed.

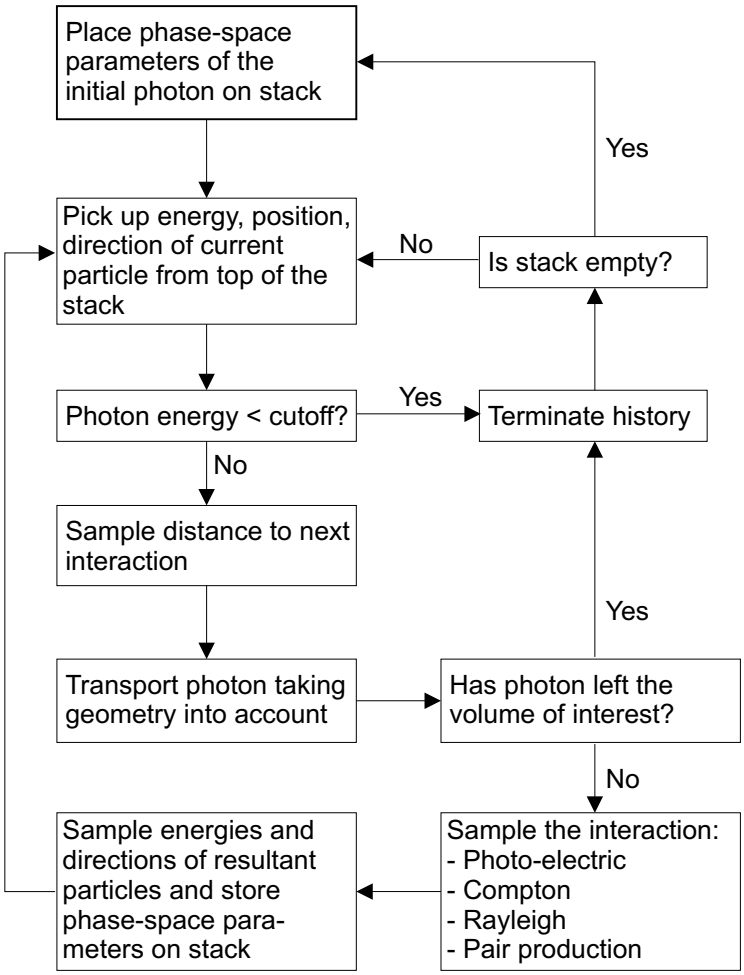

Figure 14. Simplified flow chart for photon transport in EGS4 [53]

of Canada [40][41][42][55], and is used for the calculation presented in this report. The new boundary crossing algorithm models uses single scattering when a particle approaches a boundary between two regions [37].

For large multiple scattering substeps there will be a discrepancy between the length of the strait line taken in a substep, and the length of the curled path the electron actually takes. There will also be a lateral displacement between the end-point of the strait line and the actual end-point of the electron. Path-length correction and lateral displacement correlation is taken care of by the PRESTA I [7] in EGS4 and has been improved substantially in PRESTA II, by introducing a new electron transport algorithm [38].

An advantage obtained by the use of PRESTA II and EGSnrc is, that the user do not have to worry about choosing an appropriate maximum step-size, which in the previous versions of EGS could be a delicate task.

6.2 Stopping power

Cross sections for knock-on electron collisions are based on the Møller cross section given in ICRU Report 37 [33], radiative cross sections (production of bremsstrahlung) on standard Bethe-Heitler cross sections. Density effects can be included to make a better match between ICRU 37 and the collision cross sections and integrated radiative cross sections [14]. See also [42].

For the inelastic-scattering cross sections ICRU estimates an uncertainty of 1-2% for low Z materials and 5-10% for high Z materials. For the radiative cross section the estimated uncertainty is about 5% below 2 MeV and 2-5% above [33].

Restricted stopping power

The realization of the cross sections for electron interaction is more complicated than for photons, due to the way EGS4/EGSnrc models the production of secondary particles.

EGS4/EGSnrc are a so-called *class II* models [3] in which the effects of production of secondary particles are split into two groups depending on whether the energy of the secondary particle is below or above the production threshold values AE (knock-on electrons/delta-rays) and AP (bremsstrahlung), i.e. a grouping in continuous and discrete events.

Both AE and AP is given in units of total secondary particle energy, i.e. AE includes the rest-mass of the electron (511 keV).

If a secondary particle is produced, this explicit changes the energy and the direction of the primary electron at the place where the creation takes place. This is contrary to a class I model, where the energy loss to secondary particles are incorporated in a energy straggling distribution used in the multiple scattering step.

The energy loss of the primary electron during the substep is calculated using a continuous-slowing-down model taking into account the energy which would have been lost to secondary particles with energies below AE and AP. The stopping power used is called the *restricted stopping power* since it is restricted to the creation of secondary particles below AE and AP. Lowering AE or AP gives a lower value of the restricted stopping power.

In the case where AP is higher than and AE is more than half of the initial electron energy[5] the restricted stopping power becomes equal to the unrestricted stopping power used in the continuous slowing down approximation (CSDA).

In the CSDA model no secondary particles are created, and all energy lost by the primary electron is thus absorbed directly on its path. In a model including production of delta rays the energy loss will be spread out on bigger area along the path of the primary electron.

Ignoring other restraints which may be imposed, the length of a multiple scatter step is picked from a probability distribution which is dependent on AE and AP.

After the electron has been transported the distance of a multiple scattering step, the deflection angle the electron would have experienced, if the production of all secondary particles below AE and AP had been calculated, is sampled from a probability distribution using a multiple scattering theory. The primary electron is then given this new direction.

The electron transport scheme (shown in Figure 15) is similar to that of photons except for the extra multiple scatter loop.

6.3 Effects of changing the thresholds for secondary particle production

The mean energy loss per distance by a primary electron is independent of the threshold values AE and AP, since the energy losses due creation of secondary particles are exactly counterbalanced by the reduction in the continuous energy loss. On the other hand the energy fluence spectrum can change by altering AE

[5] Knock-on electrons has by convention a maximum of half the initial energy since the primary and secondary particle is indistinguishable.

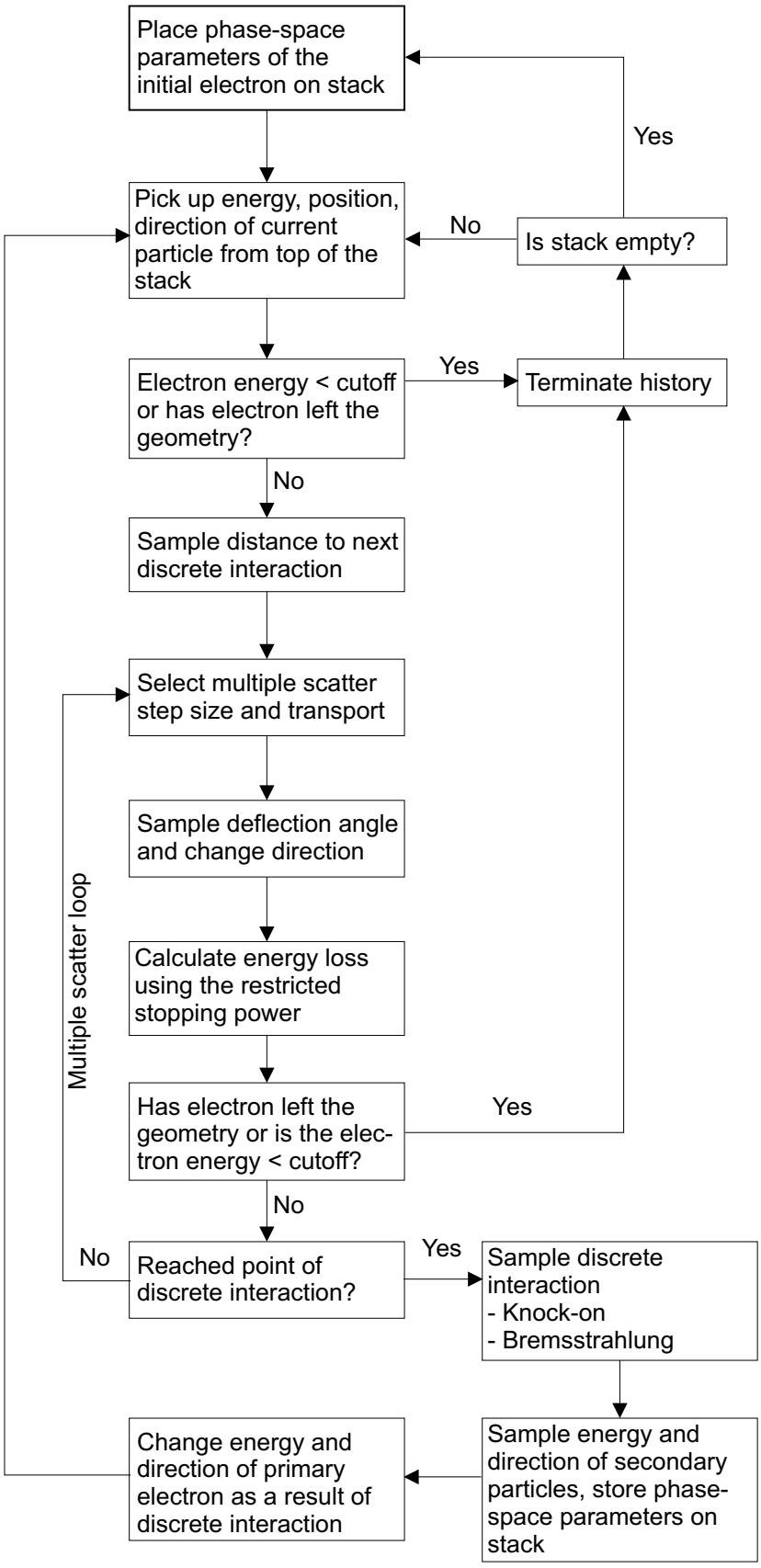

Figure 15. Simplified flow chart for electron transport in EGS4 [53]

and AP, since energy straggling will be reduced for high values of AE and AP [53]. Very low threshold values (e.g. AE=512 keV i.e. 1 keV kinetic and AP=1 keV) should be chosen if a precise calculation of the energy straggling is important for the application studied, but if the main component of the Monte Carlo calculation is electron transport this will slow down the calculation considerably.

Spectrometer calculations

For the spectrometer calculations shown in this report AE=521 keV (10 keV kinetic) and AP=1 keV.

Single electrons passing through thin regions are especially sensitive to the lack of energy straggling when the thresholds for secondary particle production is raised [47], and it is therefore worthwhile to illustrate the differences in calculated energy absorption in detector 1 for different thresholds for secondary particle production.

Figure 16 shows the calculated energy absorption of a 1.25 MeV pencil beam of electrons hitting at normal incidence a 52 μm thick slab with the same composition as detector 1, using CSDA, AE=521 keV and AE=512 keV respectively. AP=1 keV for the last two calculations. 100 000 histories has been calculated in each case. The CSDA stopping power for silicon has its lowest value at 1.25 MeV.

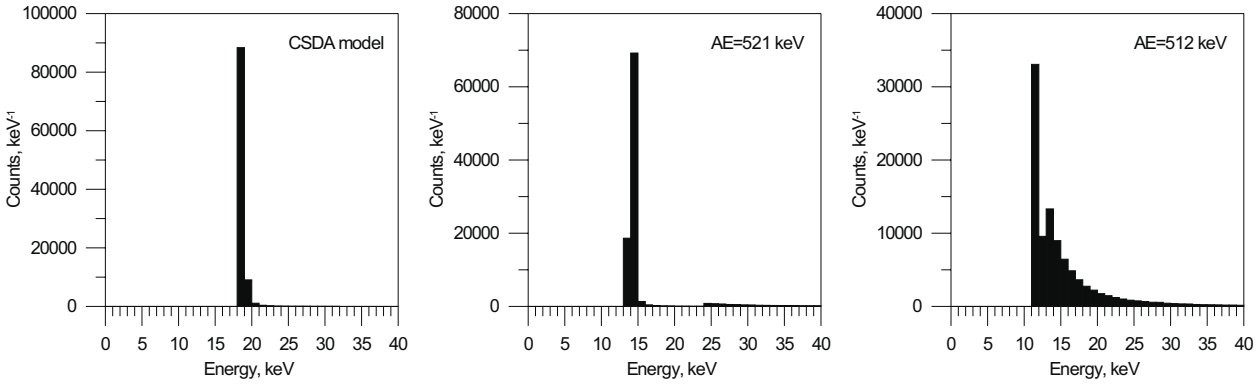

Figure 16. Calculated energy absorption in a slab similar to detector 1 hit at normal incidence by a pencil beam of 1.25 MeV electrons.
Left: CSDA model. Middle: AE=521 keV (10 keV kinetic). Right: AE=512 keV (1 keV kinetic).

Table 6 shows the mass stopping power and the calculated energy loss for a primary 1250 keV electron penetrating detector 1 at normal incidence.

Table 6. Mass stopping power and energy loss for primary electrons in detector 1 for 1250 keV electrons at normal incidence

Material	Thickness [μm]	CSDA [MeV cm^2/g]†	AE=521 keV [MeV cm^2/g]‡	AE=512 keV [MeV cm^2/g]‡
Germanium	0.06	1.291	0.923	0.753
Silicon	51.89	1.529	1.151	0.959
Energy loss		18.5 keV	13.9 keV	11.6 keV

† From ICRU report 37 [33]

‡ Restricted mass stopping power from PEGS4

In the CSDA model all electrons are expected to loose 18.5 keV passing though the slab. It is seen in Figure 16 that nearly all electrons looses this amount of energy.

For AE=521 keV the energy loss for a primary electron going straight through the slab without producing secondary particles is 13.9 keV. In the middle histogram one can see that the main peak is shifted down to this value. At 24 keV and above a small peak is observed. This is a token of the production of delta rays with at least 10 keV. The mean absorbed energy per electron is 16.9 keV.

For AE=512 keV energy straggling becomes more evident. The energy loss for primary electrons going trough the slab without discrete interactions is 11.6 keV. Again a gab can be seen between the main peak and the events where secondary particles are produced. This time the gab is 1 keV wide. The calculated mean absorbed energy is 16.8 keV per primary electron.

That the mean absorbed energy per electron in the latter cases is about 2 keV less than that for the CSDA model is thought to be caused by delta rays and bremsstrahlung leaving the slab.

The angle distribution of the electrons leaving the slab has been calculated, and does not change significantly in the three models.

Simulation of noise thresholds

In the analysis of the Monte Carlo simulations of the spectrometer the noise thresholds will be taken into account. As described above can the choice of production threshold for secondary particles influence on this analysis, by changing the absorbed energy distribution in the two thin front detectors.

If for example a noise threshold of 18 keV is assumed for detector 1 in the calculations above, all incident electrons will be registered in the CSDA model, 10% will be registered in the AE=521 keV case and 20% when AE=512 keV.

This is only true if noise is not taken into consideration. If the noise of detector 1 is approximated with a Gaussian curve with a FWHM of 34 keV, and the above spectra are folded with this curve, the differences between the calculations are minimized.

Figure 17 shows the calculated energy absorption in detector 1 for the AE=512 and AE=521 keV calculation folded with the approximated noise distribution. The two calculations differs less than 2%.

Determination of incident angle

The absorbed energy at 0.07 mm tissue is dependent on the incident angle of the electron, and it could therefore be advantageous if is was possible to obtain information about the incident angle distribution of electrons registered by the spectrometer.

As a first order approximation the incident angle, θ, could be calculated by the equation $\cos(\theta) = \frac{l \cdot S(E)}{\Delta E}$ where l is the thickness of the front detector, $S(E)$ the stopping power and ΔE the energy of the electron loss registered in the front detector.

Figure 16 and 17 shows that such a determination of the incident angle is impossible, since ΔE is described by a broad distribution due to energy straggling and noise.

6.4 DOSRZnrc

DOSRZnrc is a user program (interface) for EGSnrc, designed for calculation of absorbed dose in cylindrical r-z geometries. The usercode is distributed together with the EGSnrc software.

The user specifies a geometry etc. by arguments in a input file, which is read by DOSRZnrc. The geometry is described by regions (voxels) set up in a matrix style

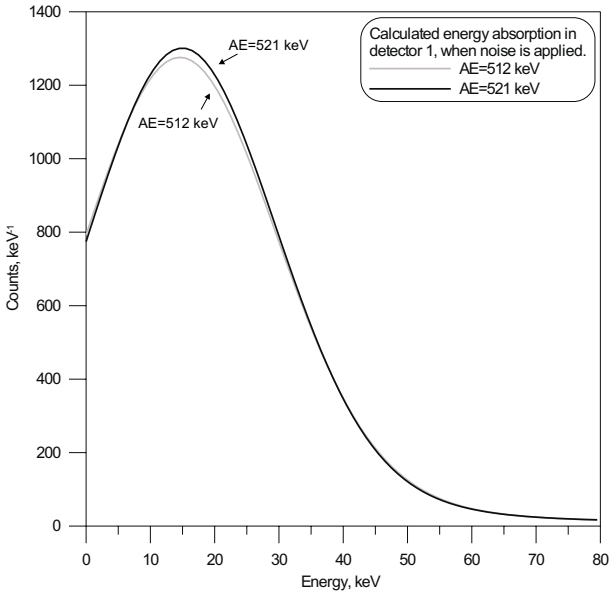

Figure 17. Calculated energy absorption in a slab similar to detector 1 hit at normal incidence by a pencil beam of 1.25 MeV electrons. The calculated spectrum is folded with a gauss curve with a FWHM of 34 keV to simulate the noise contribution.

(see appendix C for details). The particle source can be chosen from a collection of predefined geometries. The initial particles can either be mono energetic or be described by a user defined energy spectrum. Photons, electrons and positrons can be modeled.

As default DOSRZnrc calculates the absorbed energy distribution for one set of regions. Dose - calculated as energy absorbed in a region divided by the mass of the region - can be displayed for one coherent disc or a 'square' torus.

Since the determination of a coincidence pattern requires information about the energy deposition of individual electrons in the three detector elements, DOSRZnrc has been modified to accomplish this task. DOSRZnrc has also been modified so the user code can identify a number of particle parameters as a particle is crossing a given surface. The modified code is called 'DOSRZnrc-rts' and the new input options and the code modifications are further described in appendix B.

Computing time

The description of the geometry influences on the CPU time used to complete a computation. If the electron is in a region of the geometry, where it has little or no chance of reaching the region of interest, its history might as well be terminated. In the calculations shown later in this report the particle history is terminated if it reaches the area behind the source (except for the Cl-36 calculations) or the area beside target, as sketched in Figure 18.

To include electrons scattered in air above the target the radius of the modeled geometry is extended outside the radius of the target.

Even though boundary crossing between two regions is done in single-scatter mode, boundary crossing is only a small part of the total particle transport. EGS4/EGSnrc is therefore not so sensitive to the number of regions in a given geometry [52]. EGS4/EGSnrc is likewise not very sensitive to the number of regions where the dose is registered [36].

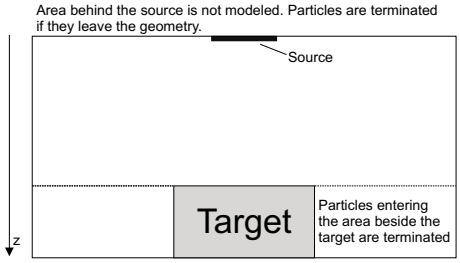

Figure 18. Areas where the particle history is terminated, target being the detector assembly or tissue plate.

7 Monte Carlo configuration

The Monte Carlo calculations presented in this report were all done at the Ionizing Radiation Standards, National Research Council of Canada. The code used is DOSRZnrc-rts which uses EGSnrc as Monte Carlo engine.

Two types of geometries has been modeled:

Telescope spectrometer Calculation of coincidence patterns and absorbed energy in the detector with various source sizes and distances between the source and detector. These calculations are among other things used to analyze the effectiveness of the detector.

Tissue disc A central task for the spectrometer is to calculate skin dose at 0.07 mm tissue depth based on the measured energy spectrum. The tissue disc geometry is used to provide information about the skin dose for different source geometries. By source geometry is meant the particle energy, the radius of the source and the distance between the source and target.

This chapter deals with the setup of the two types of geometries. Examples of the exact geometries are given in appendix C. Chapter 9 gives a discussion of the data obtained with the Monte Carlo calculations.

Since Monte Carlo calculations simulates a physical situation, words used to describe a real experimental setup - like 'irradiation' etc. - are often used to describe a calculation, even though everything takes place inside the CPU of the computer.

7.1 Geometries used in the Monte Carlo calculations

Description of materials

The cross sections data file for DOSRZnrc-rts is produced with PEGS4. The threshold for secondary particle production is 521 keV (10 keV kinetic) for electrons (AE) and 1 keV for photons (AP).

The upper energy bound for the data provided is 4.0 MeV kinetic energy (UE=4.522 MeV, UP=4.0 MeV), since the spectrometer is not designed to measure higher energies. Limiting the energy interval covered by PEGS4 as mush as possible can give better fits, though the improvement is thought to be very small in this case. Data for Rayleigh scattering is included. The Saltzer and Berger density corrections are used. Appendix A gives further details on the input parameters used for PEGS4 including composition of materials.

Selected input options

Calculations of the telescope spectrometer is done with maximum of 90 000 000 histories. The maximum number of registered counts in the detector is 200 000 when the source is placed on top of the Perspex shield and 100 000 for larger distances between source and detector. 200 000 counts are registered in the photon calculations.

The tissue plate geometry uses the same number of histories as used for the similar source geometry in the detector setup.

Particle parameters can be stored when particles are crossing the surface of the front detector in the spectrometer calculations, and when crossing the tissue surface with a distance less than 0.564 cm to the central axis in the tissue disc calculations.

Compton scattering is modeled using an impulse approximation i.e. the binding effects and Doppler broadening is taken into account contrary to the pure Klein-Nishina formalism which treats the electrons as free. Rayleigh scattering is modeled. X-ray fluorescence is modeled using helium for all regions, since the materials used in the spectrometer (except the Pt-Ir diaphragm) have relatively low Z values. PRESTA II and the exact boundary crossing algorithm is used.

Appendix B.2 gives an example of an DOSRZnrc-rts input file.

7.2 Source geometry

DOSRZnrc provides a list of predefined source geometries. The direction of the initial particle can e.g. be parallel, lie within a cone or a 4π sphere.

When a parallel beam is used, the top of the geometry is irradiated at a user defined angle. The maximum radius of the beam is equal to the radius of the geometry.

The cone option is not used in this work, since the statistical weight of the particles becomes non-uniform and not equal to one, incompatible with the calculation of coincidence patterns etc.

The most used option in this work is the 4π sphere simulating a diffuse source. The source can be placed as a disc or a torus around the the central axis. Except for the calculation of the Cl-36 source, the source is all ways placed at the very top of the geometry as sketched in Figure 18 on page 42. The height of the source is 0.01 cm. A point source is simulated by a disc with radius 0.01 cm.

When the source is placed at the top of the geometry essentially half of the histories are immediately terminated, since they are leaving the geometry. These histories does not take up much CPU time, because they are very short lived.

Electron sources

Each spectrometer and tissue disc geometry is irradiated with mono-energetic electrons covering 22 energies in the range from 50 to 3500 keV.[6]

The energy spectrum for the Cl-36 source is calculated using a program made by Len van der Zwan, NRCC, based on work by W.G. Cross *et al* [13]. Cl-36 is 2^{nd} forbidden, and the calculated spectrum is shown in Figure 19.

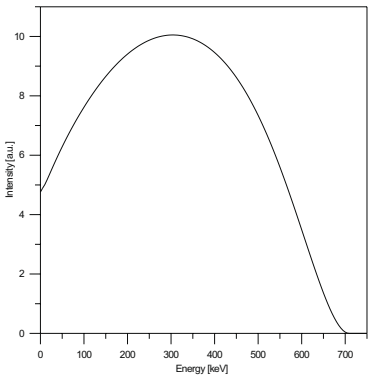

Figure 19. Unnormalized calculated spectrum for Cl-36

[6] The initial energies are: 50, 60, 70, 80, 90, 100, 125, 150, 200, 250, 300, 400, 500, 600, 800, 1000, 1200, 1500, 2000, 2500, 3000 and 3500 keV.

Photon sources

The spectrometer has likewise been simulated with photons in the energy interval from 50 to 3500 keV, and with the sources listed in Table 7.

Table 7. Energy and intensity per disintegration of photon sources used in this work

Source	Energy [keV]	Intensity
Co-60	1173	0.999
	1332	1.000
Cs-137	661.7	1.000
Bi-207	569.7	0.978
	1064	0.749
	1770	0.0685

It is not possible to do a calculation with both electrons and photons as initial particles, and it is also not possible to extract any time information from the calculations.

7.3 Description of detector geometry

Figure 20 depicts the geometry of the telescope spectrometer used in the Monte Carlo calculations. The geometry is based on information from the detector manufacturer Q-par Angus Ltd. [17].

After the Monte Carlo calculations were accomplished the detector house was disassembled and three inconsistencies was discovered.

- The radius of detector 2 was 5.6 mm instead of 7.0 mm. (The detector was originally ordered with a radius of 5.6 mm). The larger radius is not believed to have a significant effect, since it is placed in the 'shadow' of the ceramics holding detector 1.
- The position of detector 3a and 3b is about 2 mm further to the back. This will ad an extra energy loss in air in the order of 1 keV.
- The diaphragm is turned so the minimum inner radius is at the top. This may influence on the fraction of particles which are scattered from the diaphragm into the active volume of the detector, and on the number of particles reaching the active part of the detector at a high angle.

The detector geometry is very complicated and is composed of about 1300 regions. The geometry is first sketched in spreadsheet, and then by a custom build program transformed into the format of the DOSRZnrc-rts inputfile. At the same time the active volume of the four detector elements are localized.

Due to a change of the number of elements in the height of detector 3a, the localization of the active part of detector 3b failed, i.e. the energy deposition in detector 3b has not been scored (detector 3a and 3b can be seen in Figure 20).

All electron calculations with an initial energy of 2000 keV or above has been recalculated with a correct description of the active volume of detector 3b and likewise for all photon calculations. Calculations of electrons with an initial energy below 2000 keV will show a reduced number of 'coincidence pattern 1' events (i.e. registration of bremsstrahlung in detector 3), by roughly a factor of two.

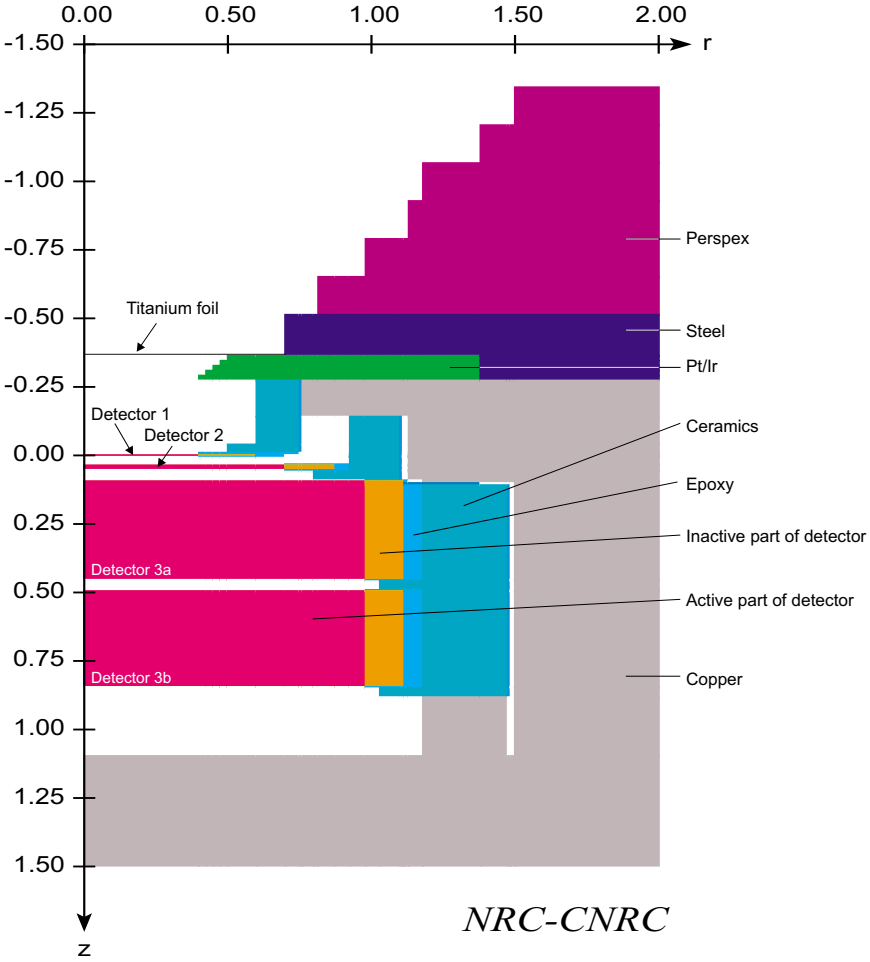

Figure 20. Geometry of the Risø Telescope Spectrometer [17] used in the Monte Carlo calculations. All lengths in cm. Graphics: IRS/NRCC

Step-like versus conical modeling of the diaphragm and the Perspex shield

DOSRZnrc can not model conical surfaces, and the inner surface of the Pt/Ir diaphragm and the Perspex shield is instead described by step-like shape as depicted in Figure 20.

One potential problem of this approach arise from the observation, that the back scatter coefficient for electrons is rising with incident angle. There is roughly a factor of two difference in the back scatter coefficient between a diffuse beam and a beam with normal incidence to a surface [56].

In the step-like model the surface of the diaphragm or the Perspex shield will be normal to the direction of a parallel beam of electrons along the central axis. In the conical description the surfaces will be 45° to the beam, and the electrons therefore have a greater probability of being back-scattered into the active part of the detector. See figure 21.

To analyze the difference between the two descriptions, the top part of the detector down to the surface of first detector, is modeled with a Monte Carlo code called BEAM, which is designed to facilitate the modeling of electron accelerators [54]. Through a graphical user interface geometries can be setup by use of e.g. cones and plates. A variety of source geometries are available as well. BEAM uses EGS4 as Monte Carlo engine.

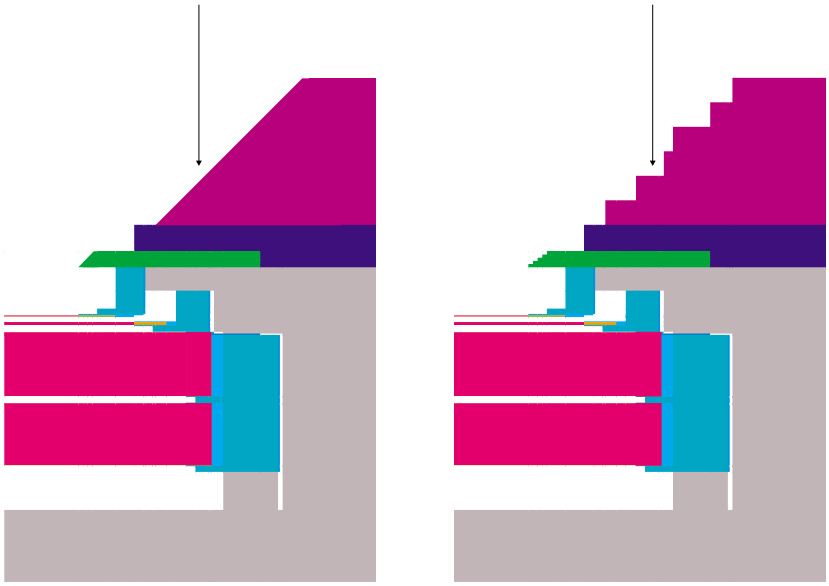

NRC-CNRC

Figure 21. Shape of the Pt-Ir diaphragm and the Perspex shield.
Left: Conical surface. Right: Step-like surface. Graphics: IRS/NRCC

With the BEAM code a latch bit can be assigned to each individual history, and this bit can be changed if the particle interacts with specified regions of the geometry. In this case the latch bit is changed if the primary electron interacts with the Perspex shield or the Pt/Ir diaphragm. A special program (BEAMDP) is used to analyze the calculations taking the latch bit into account.

The calculations uses an maximum fractional energy loss per electron step of 0.01 (ESTEPE), maximum electron step size of 1.0 cm (SMAX), electron transport cutoff is 521 keV total energy (ECUT) and photon transport cutoff is 10 keV (PCUT). The detector is irradiated by a parallel beam of electrons with radius 1.645 cm i.e. the maximum inner radius of the hole in the Perspex shield. The beam is either parallel to or at a 30 degree angle to the central axis. Each calculation consists of 5 000 000 histories.

Table 8 lists the planar fluence at the front of the active part of detector 1 normalized per history, together with the fraction of electrons which have been in touch with the Pt-Ir diaphragm or the Perspex shield. The fraction of interacting electrons increases with energy from almost nothing at 50 keV to about 8% at 3500 keV.

The differences between the step-like and the conical model is shown in Table 9. It is seen that the fraction of electrons interfering with the diaphragm or the shield differs a lot in the two models, but it should be kept in mind, that it is only a small part of the particles which interacts at all. The total fluence at the front of detector 1 does not differ significantly in the two models except for very low energies. The 7% difference at 50 keV is most likely due to the different geometry rather than the different backscatter probabilities from the surfaces.

The differences between the two models cannot justify the extra time necessary for a modelling of the conical surfaces.

Table 8. Electron fluence at the front face of detector 1.

Energy [keV]	Fluence per history [cm^{-1}]	Fraction of scattered electrons	Fluence per history [cm^{-1}]	Fraction of scattered electrons
	Conical model		Step-like model	
	Normal incidence			
50	0.060 ± 0.02%	0.005 ± 3.5%	0.064 ± 0.01%	0.009 ± 2.6%
100	0.100 ± 0.02%	0.027 ± 1.2%	0.098 ± 0.01%	0.006 ± 2.6%
300	0.116 ± 0.04%	0.029 ± 1.1%	0.119 ± 0.03%	0.020 ± 1.3%
500	0.118 ± 0.05%	0.029 ± 1.1%	0.121 ± 0.03%	0.023 ± 1.2%
1000	0.120 ± 0.06%	0.035 ± 1.0%	0.119 ± 0.05%	0.016 ± 1.4%
3500	0.125 ± 0.14%	0.066 ± 0.7%	0.125 ± 0.14%	0.057 ± 0.8%
	30 degrees incidence			
50	0.048 ± 0.03%	0.006 ± 3.8%	0.051 ± 0.02%	0.010 ± 2.8%
100	0.078 ± 0.03%	0.041 ± 1.1%	0.076 ± 0.02%	0.012 ± 2.1%
300	0.093 ± 0.10%	0.063 ± 0.8%	0.090 ± 0.10%	0.039 ± 1.0%
500	0.094 ± 0.10%	0.070 ± 0.8%	0.092 ± 0.10%	0.055 ± 0.9%
1000	0.096 ± 0.11%	0.077 ± 0.7%	0.092 ± 0.12%	0.058 ± 0.9%
3500	0.096 ± 0.17%	0.086 ± 0.7%	0.094 ± 0.17%	0.075 ± 0.8%

Table 9. Scattered electrons and total fluence ratio between the step-like and conical model.

Energy [keV]	Ratio of scattered electrons $\frac{\text{step-like model}}{\text{conical model}}$	Ratio of total fluence $\frac{\text{step-like model}}{\text{conical model}}$
	Normal incidence	
50	1.70 ± 4.4%	1.07 ± 0.03%
100	0.22 ± 2.9%	0.99 ± 0.02%
300	0.70 ± 1.7%	1.02 ± 0.05%
500	0.78 ± 1.6%	1.03 ± 0.05%
1000	0.46 ± 1.7%	0.99 ± 0.08%
3500	0.87 ± 1.0%	1.00 ± 0.20%
	30 degrees incidence	
50	1.72 ± 4.7%	1.06 ± 0.03%
100	0.28 ± 2.4%	0.98 ± 0.03%
300	0.62 ± 1.3%	0.97 ± 0.14%
500	0.78 ± 1.2%	0.97 ± 0.15%
1000	0.76 ± 1.1%	0.96 ± 0.16%
3500	0.88 ± 1.0%	0.97 ± 0.24%

7.4 Description of tissue disc geometry

ICRU report 56 gives a list of conversion factors from incident fluence to absorbed dose at 0.07 depth in a slab of ICRU tissue irradiated by mono-energetic electrons at various angles of incidence [35].

These values are based on Monte Carlo calculations of a 30 cm × 30 cm square box of ICRU 4-element tissue 15 cm in height, consistent with that recommended by the ICRU for use in the procedure for calibrating radiation protection dosemeters. The front of the slab is irradiated with a parallel beam of monoenergetic electrons on the whole top surface [19].

The tissue disc used in this work is a cylinder made by 4-component ICRU tissue, 15 cm in radius and height.

Dose is scored in a 0.007 mm high region located from 0.06965 mm to 0.07035 mm depth similar to the approach of Hirayama [23].

The dose scoring region is in this work limited to a disc of 1 cm^2 around the central axis. Figure 22 shows an outline of the tissue disc geometry and the location of the dose scoring region.

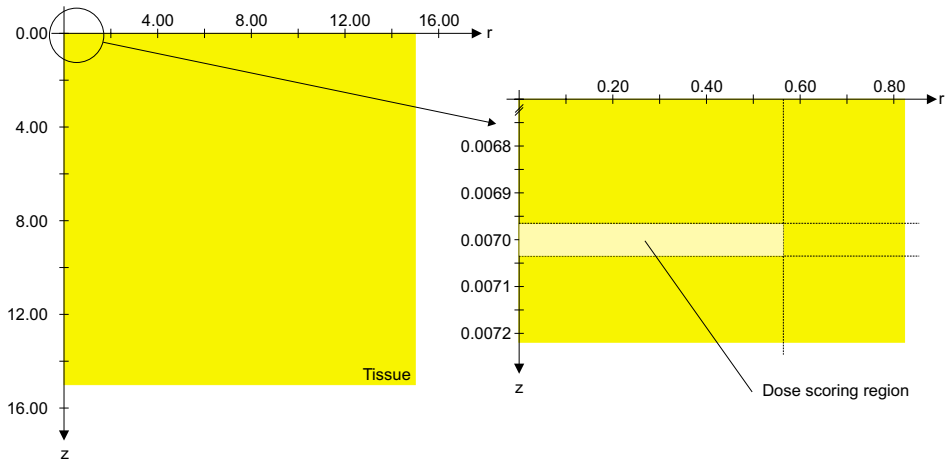

Figure 22. Geometry of the tissue disc. All lengths in cm.

7.5 CPU time

The Monte Carlo calculations has been carried out on 200 MHz Pentium-Pro machines. The CPU time used per calculation has been between 3 and 40 hours, in average about 20 hours. No variance techniques has been used to reduce computing time.

In total 2 Gb of binary data was produced covering the registration of more than 50 million individual particles.

8 Validation of Monte Carlo calculations

Since the output of a Monte Carlo calculation is a statistical quantity, it can be hard to determine whether a result is true to reality or not. To establish credibility about the Monte Carlo calculation, a control calculation should be made. The output of the control calculation should be a quantity which is measurable with a high degree of accuracy, and quantities such as particle energy, materials and the size of the regions where the dose is calculated should not differ too much from the calculations one wish to support - in this case the calculation of the spectrometer and the tissue disc.

8.1 Comparison between calculation and measurement of dose at 0.07 mm tissue

The original plan was to validate the Monte Carlo calculations by simulating a Cl-36 source in front of an extrapolation chamber, calculating the absorbed dose in the collector volume, and to compare this simulation with measurements made with the extrapolation chamber. The extrapolation chamber measuring method is the basic method for determination of dose rates in beta radiation fields with a high degree of accuracy, and would thus be ideal for validation of the Monte Carlo calculations.

A Cl-36 source was made for this purpose by evaporation of solutions with approximately 3.7 MBq in 10 mm diameter, 1 mm deep depressions in a PMMA holder using a 1 mg/cm^2 mylar cover. The dry matter was 28 mg (approximately 36 mg/cm^2), which meant that self-absorption in the source had to be taken into account in the Monte Carlo calculations.

By visual inspection of the source it was found that the surface of the dry matter was so uneven, that a reliable Monte Carlo calculation was thought to be unattainable.

A new Cl-36 source with one tenth of the activity - and likewise one tenth of the dry matter - was made. This source is not suitable for extrapolation chamber measurements due to the low activity. Instead the comparison is made by use of thin LiF thermoluminescence detectors (TLD) with responses to beta radiation exposures traceable to the extrapolation chamber at Risø. The thermoluminescence detectors are 7 mm in diameter and consists of a thin layer of LiF grains with a thickness density of 1-2 mg/cm^2 fixed on a Kapton base. The thermoluminescence detectors were manufactured by Corad, Montpellier, France.

In addition to the 1 mg/cm^2 mylar cover the thermoluminescence detectors are covered by 6 mg/cm^2 tissue equivalent, to obtain dose at approximate 7 mg/cm^2 tissue. Three thermoluminescence detectors are irradiated in each measurement.

Monte Carlo simulation of the 0.37 MBq source placed 10 cm above the tissue disc has been made to calculate the dose at 0.07 mm tissue. The dose scoring region is restricted to a disc with a diameter equal to the thermoluminescence detectors. The dry matter is not included in the simulation, which will introduce an error of a few percent. The geometry used in the Monte Carlo calculation is shown in Figure 23. The energy thresholds for production of secondary particles are AE=512 keV (1 keV kinetic) for electrons and AP=1 keV for photons.

Table 10 shows the calculated and measured dose rates at 0.07 mm tissue.

An uncertainty of 15% is acceptable considering the uncertainties linked to the comparison. Especially the activity of the Cl-36 source is subject to an enlarged uncertainty since it has not been confirmed by other measurements.

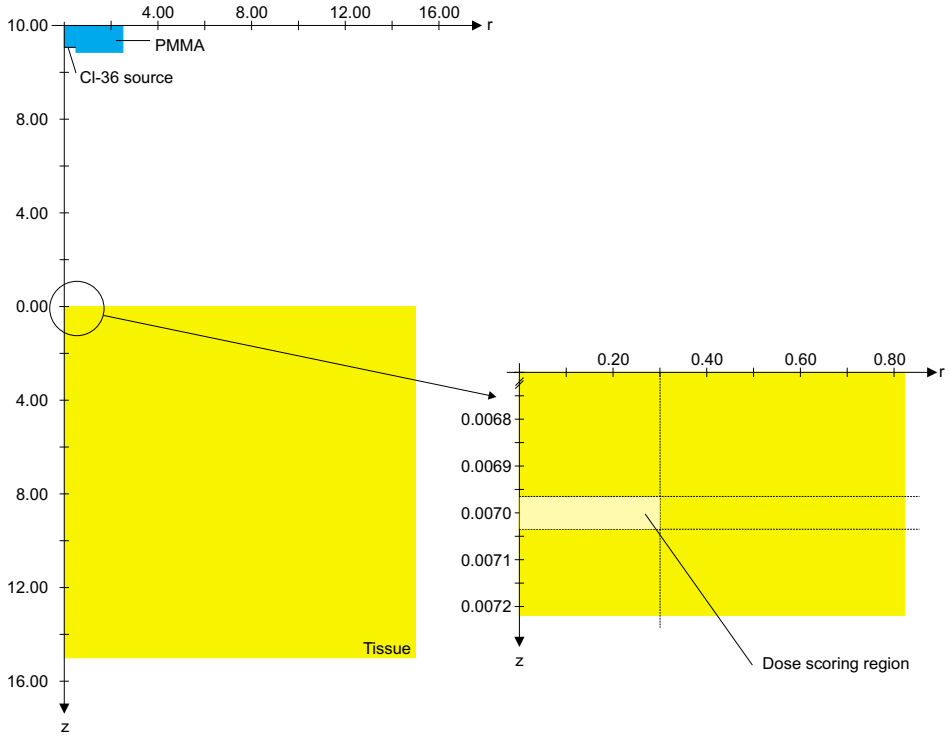

Figure 23. Geometry used to calculate the dose at 0.07 mm tissue, when a Cl-36 source is placed 10.0 cm above the tissue surface. The Cl-36 holder is made of PMMA. All lengths in cm.

Table 10. Comparison between calculated and measured dose rate at 0.07 mm tissue, from Cl-36 sources placed 10 cm from the tissue surface.

TLD material	Measured dose rate, $\dot{H}_p(0.07)$ [mGy/h]	Calculated dose rate, $\dot{H}_p(0.07)$ [mGy/h]	Ratio $\frac{\text{Calculated}}{\text{Measured}}$
$CaSO_4$:Dy	$0.888 \pm 1.2\%$	$0.765 \pm 1.8\%$	0.86 ± 0.02
LiF	$0.913 \pm 1.1\%$	$0.765 \pm 1.8\%$	0.84 ± 0.02

8.2 Calculation of ICRU conversion coefficients

The ICRU conversion coefficients from electron fluence to dose at 0.07 mm tissue depth are based on several Monte Carlo calculations, carried out by some of the leading experts in the field [19]. It is therefore nearby to do a calculation which as a result is expected to have the same conversion factors as listed in the ICRU report 56.

The top of the tissue disc geometry described in chapter 7.4 and also shown in Figure 23 is irradiated with mono-energetic electrons at normal incidence, and the dose is calculated at 0.07 mm depth for 1 cm^2. The beam radius is 2.6 cm and 1 100 000 histories are calculated corresponding to a planar fluence of 52 390 cm^{-2}.

Table 11 lists the ICRU and the calculated conversion factors from electron planar fluence at normal incidence to dose at 0.07 mm tissue. It is seen that except for the 70 keV calculation, the agreement between the two values are within the uncertainty. The description of the geometry used to calculate skin dose is therefore believed to be done correctly.

Table 11. Dose at 0.07 mm tissue per planar fluence for a normal incident electron beam. Comparison between ICRU values and EGSnrc/DOSRZnrc calculations

Energy [keV]	Calculated value [nGy/cm^2]	ICRU value [35][19] [nGy/cm^2]	Ratio $\frac{\text{Calculated}}{\text{ICRU}}$
70	$0.113 \pm 5.1\%$	$0.211 \pm 16\%$	$0.536 \pm 17\%$
80	$1.027 \pm 1.8\%$	$1.056 \pm 5.2\%$	$0.973 \pm 5.5\%$
90	$1.474 \pm 1.2\%$	$1.527 \pm 5.3\%$	$0.965 \pm 5.4\%$
100	$1.615 \pm 1.0\%$	$1.661 \pm 3.0\%$	$0.972 \pm 3.2\%$
200	$0.868 \pm 1.3\%$	$0.834 \pm 4.6\%$	$1.041 \pm 4.8\%$
300	$0.574 \pm 1.6\%$	$0.644 \pm 3.3\%^\dagger$	$0.891 \pm 3.7\%$
400	$0.466 \pm 0.7\%$	$0.455 \pm 4.1\%$	$1.025 \pm 4.2\%$
600	$0.380 \pm 1.1\%$	$0.366 \pm 3.8\%$	$1.037 \pm 4.0\%$
700	$0.357 \pm 1.1\%$	$0.344 \pm 4.1\%$	$1.037 \pm 4.2\%$
800	$0.330 \pm 0.9\%$	$0.329 \pm 4.1\%$	$1.004 \pm 4.2\%$
1000	$0.321 \pm 0.9\%$	$0.312 \pm 3.9\%$	$1.029 \pm 4.0\%$
1500	$0.298 \pm 1.2\%$	$0.287 \pm 3.4\%$	$1.038 \pm 3.6\%$
2000	$0.287 \pm 1.8\%$	$0.279 \pm 2.0\%$	$1.028 \pm 2.7\%$
3000	$0.274 \pm 1.6\%$	$0.276 \pm 1.8\%$	$0.993 \pm 2.4\%$

† Interpolated value

As an illustration the value for 300 keV is calculated as well, though it is not mentioned in the ICRU report 56. It is seen that if a linear interpolation is used to compute an ICRU value for 300 keV a fairly large error is made, and this should be avoided. One calculation for 300 keV electrons is mentioned in [19] and the calculated value is close to the value shown in table 11.

9 Results of Monte Carlo calculations

This chapter deals with the analysis of the data obtained by the Monte Carlo calculations. The chapter is structured like this:

Classification of particles entering the spectrometer The ability of the spectrometer to discriminate between electrons and photons in the ideal case of no noise is examined. A suggestion for an improved spectrometer design is presented.

Spectrometer efficiency for measuring electrons The performance of the spectrometer to identify the correct energy of registered electrons, and the capacity of measuring planar fluence of electrons is investigated.

Monte Carlo calculations including noise The spectrometer has an inherent noise level due to detector noise and electronic noise from the signal processing chain (preamplifiers etc.). This and the following sections deals with the calculated performance of the spectrometer when noise is taken into consideration. The consequences of using particle thresholds are discussed, and the spectrometer's ability to discriminate between electrons and photons and to register the correct electron energy distribution is investigated and compared with measurements.

Rejection of photons The spectrometer's ability to identify and reject photons when irradiated with a photon beam is studied, and a theoretical estimate of the photon rejection factor is established.

All results presented in this chapter are based on Monte Carlo calculations.

9.1 Classification of particles entering the spectrometer

This section describes the spectrometer's ability to classify electrons correctly and to make a correct registration of the energy distribution when the spectrometer is irradiated with an electron beam. To give a picture of the best results obtainable with the given geometry of the spectrometer, the detector noise is not included in the Monte Carlo calculations. By splitting up the calculations into two groups with and without noise, effects inherent to the detector design and to the noise becomes separated, clarifying the ways to solve the problems.

Registration of electron events of an electron point source in the vicinity of the detector surface

An electron point source irradiating in all directions is placed 1.34 cm from the surface of detector 1, i.e. in level with the front of the PMMA shield. This corresponds to a measurement of a hot particle as close as one can get with the PMMA shield mounted.

The spectrometer is irradiated with mono-energetic electrons covering 22 energies in the range from 50 keV to 3500 keV.

Figure 24 shows the fraction of each of the 7 coincidence patters as function of the mean energy registered by the spectrometer.

The uncertainty of the measured mean energy is not shown. The response function of the spectrometer is not normal distributed, in fact it is very asymmetric due to the *low energy tail*, and using the standard deviation makes no sense. The

low energy tail is the part of a detector response function which lies below the main peak, and is caused by incomplete energy absorption due to back scattering, escape of bremsstrahlung etc. The FWHM of the main peak is less than 5 keV in all cases.

The uncertainty (1sd) in the calculated fraction is less than 1%, i.e. less than the size of the symbols.

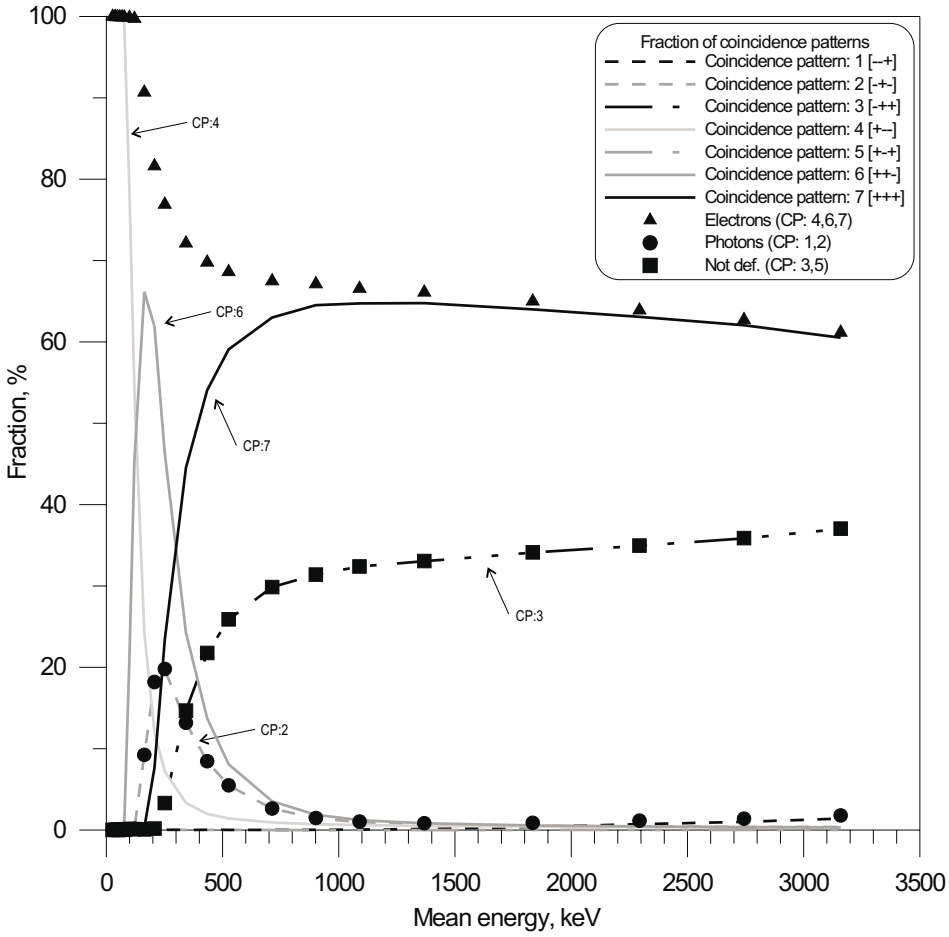

Figure 24. Calculated fractions of coincidence patterns. Electron point source at 1.34 cm distance from the surface of detector 1.

The fractions of the coincidence patterns describing electrons are shown by solid lines. For very low energies only coincidence pattern 4 [+−−] (i.e. only detector 1) is present. At about 100 keV the fraction of coincidence pattern 4 quickly drops, and coincidence pattern 6 [++−] starts to build up, as electrons are now reaching detector 2. Finally at about 250 keV detector 3 is reached and coincidence pattern 7 [+++] start to raise as coincidence pattern 6 goes down.

The sum of the coincidence patterns corresponding to electrons is shown with triangles. It is seen that for energies over 400 keV less than 70% of the registered counts are interpreted as electrons.

At 150 keV a peak of coincidence pattern 2 [−+−] is observed, and these counts are interpreted as photons. At higher energies coincidence pattern 3 [−++] is accounting for one third of the registered counts.

The reason for the very poor detection of electrons is explained by the way detector 1 is mounted. Outside the active area with a radius of 0.4 mm is a 1 mm strip where the silicon disc is covered by a thin epoxy layer (see for example Figure

2 on page 12). There is no bias applied to this part of the detector and it is thus inactive. The epoxy layer has an estimated thickness of 0.13 mm allowing electrons with energies of at least 150 keV to pass through this part of the detector.

With the point source placed 1.34 cm from the detector, the active part of the detector surface makes up 68% of the solid angle that covers the detector and the epoxy strip, in good agreement with the fraction of counts registered as electrons for high energies.

If the source is changed to a narrow pencil beam along the central axis the fraction of counts registered as electrons is nearly 100% since only a limited part reach the outer part of the detector. This is shown in Figure 25.

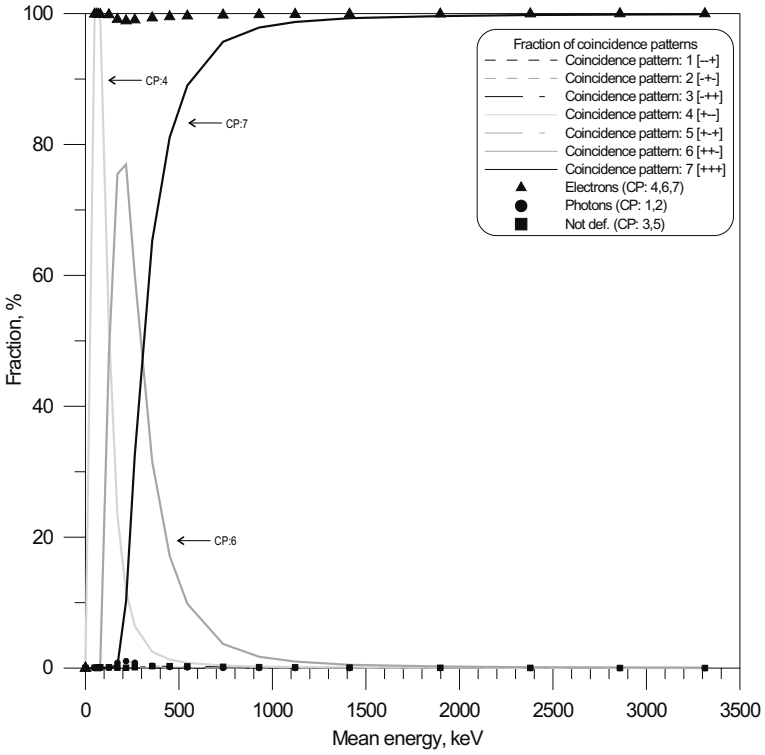

Figure 25. Calculated fractions of coincidence patters. Narrow electron beam normal to the surface of detector 1 originating 1.34 cm from the detector.

Registration of electron events of electron sources further away from the detector surface

Figure 26 shows the fraction of registered particles classified as electrons for different source geometries. Filled symbols are point sources and open symbols are broad sources i.e. with a radius of 5 cm.

When the point source is moved to a distance of 10 cm from the detector surface more than 85% of the counts are classified correctly as electrons. This behaviour is retained at distances of 20 cm and 30 cm, and also when the point source is replaced with a surface source of radius 5 cm - except when the broad source is placed 10 cm from the detector surface, where a minimum of 75% of the measured events are classified correctly.

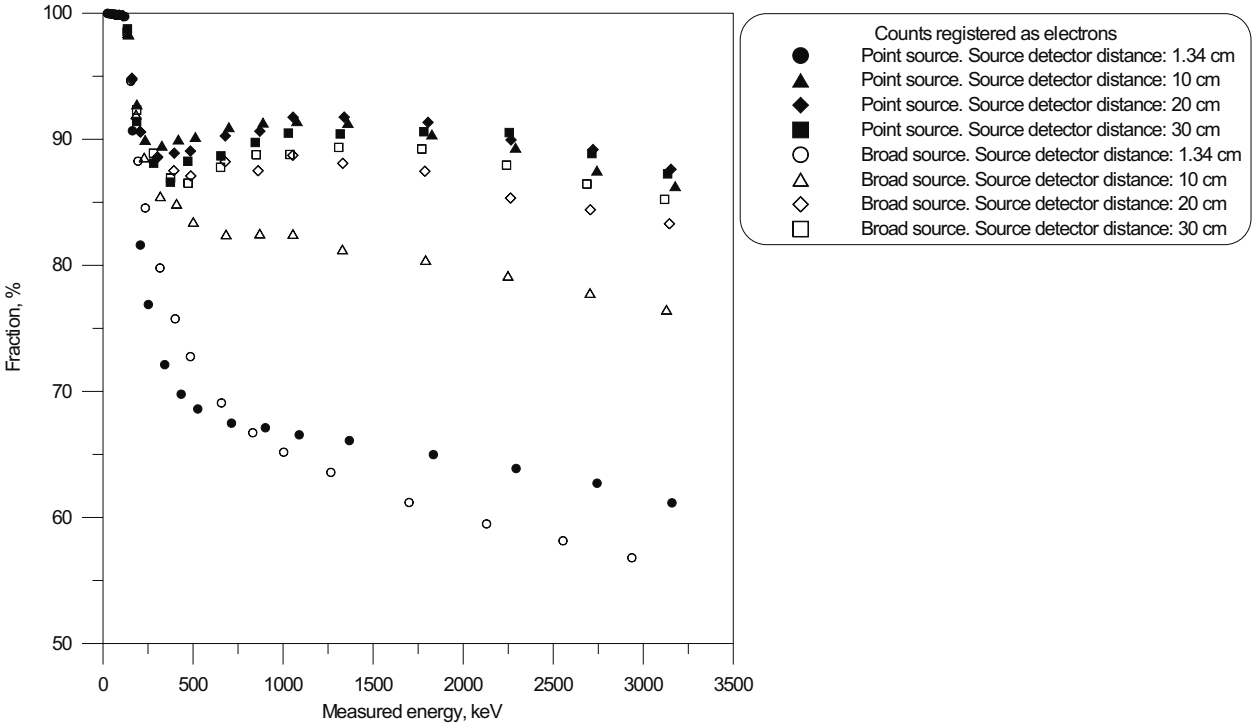

Figure 26. Calculated fraction of registered particles classified as electrons. The spectrometer is irradiated a point source or a broad source with radius 5 cm, at different distances between the source and detector 1.

Suggestion for an improved detector design

It is obvious that the thin mounting of the front detector is hampering a correct classification of the incoming electrons, especially for oblique incidence.

There are several ways to overcome the problem. The most obvious is to forget about coincidence pattern 2 and 3 ([−+−] & [−++]), and treat them as undefined events. The draw back from this approach is the unnecessary dead-time caused by these events.

A more suitable solution is to make the epoxy layer thicker or by other means assuring, that no electrons can bypass the front detector. The fraction of correctly classified events in pure electron field should then approach 100%, when noise is not taken into consideration.

Another procedure is to re-classify coincidence pattern 2 and 3 as electrons, instead of being interpreted as photons and 'not defined events'. As shown later (Figure 37) such a re-classification would only result in a 3% lower rejection factor for low energy photons, and less for higher energies, and it could therefore be natural to use this method to obtain a better efficiency for measuring electrons.

The re-classification method has two major drawbacks. The assumed area of the front detector will no longer be well defined, and the electrons bypassing the active part of detector 1 losses in the order of a 100 keV before they enter detector 2. There will therefore be a significant excess of electrons registered at lower energies, where the conversion factor from measured energy to $H_p(0.07)$ has its largest weight. It is therefore not advisable to re-classify coincidence pattern 2 and 3.[7]

[7] It would in principle be possible - by software - to add extra energy to coincidence pattern 2 and 3 events, to compensate for the energy loss through the non active part of detector 1. This method would make the calculation of skin dose more obscure, and a screening of the non active part seems to be the best solution.

9.2 Efficiency for measuring electrons

The spectrometer is used to measure energy distributions in electron radiation fields. This section examines the spectrometer's ability to identify the correct electron energy and the ability to register the correct planar fluence of electrons.

Ability to identify the correct energy An electron can be registered at too low an energy due to

- Back-scattering from the detectors
- Scattering out from the side of the active part of the detectors
- Escape of bremsstrahlung
- Energy absorption in material above and between the detectors

These interactions will result in a 'low energy tail' in the spectrometer response function. If the low energy tail is significant there will be a surplus of electrons registered with low energy and a shortfall of electrons registered with high energy.

As an illustration Figure 27 shows a Monte Carlo calculation of the spectrometer irradiated with a broad parallel electron beam at normal incidence until 350 000 counts has been registered. The source has a homogeneous intensity in the range from 1 to 3500 keV. The energy distribution of the electrons entering detector 1 is calculated at the same time.

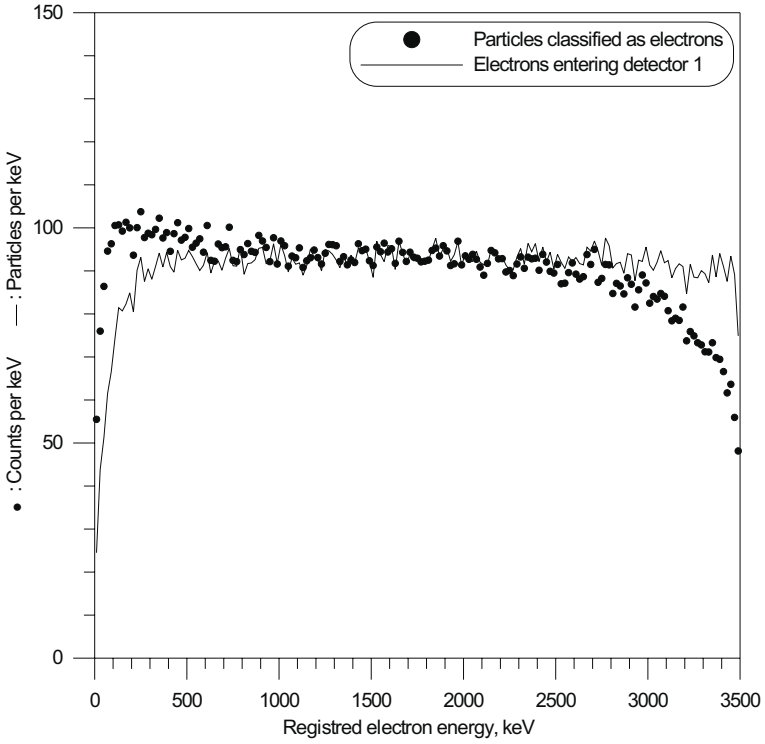

Figure 27. Dots: Calculated electron energy spectrum registered by the spectrometer from a source with homogeneous intensity from 1 to 3500 keV (coincidence patterns: 4,6,7). Line: Calculated energy distribution of electrons entering the active part of detector 1.

It is seen that the energy distribution of electrons entering detector 1 (black line) is fairly flat except for low energies where the electrons are either absorbed in the air or in the titanium foil or scattered away from the detector. It is also seen that even for high energies the number of electrons entering

detector 1 is about 8% less than the expected 100 counts per keV. This is believed to be caused by small angle scattering in air and in the thin titanium foil in interplay with the Pt/Ir diaphragm.

Looking at the calculated energy spectrum of electrons measured by the spectrometer (dots), one can see a surplus of about 10% of electrons registered with energy less than 500 keV and a shortfall of electrons registered with energies above 2.5 MeV. The number of electrons registered and the number of particles entering detector 1 is the same.

The interpretation of the figure is not that only the response function for electrons with high energy has a low energy tail, but rather that some of high energy electrons registered at a lower energy are compensating for the low energy tail occurrence there.

Figure 28 shows the calculated ratio between the mean energy registered by the spectrometer and the mean electron energy at the same position but with the spectrometer removed. The ratio is plotted as a function of the latter mean energy. It is seen that in general the measured mean energy is about 10-15% less than the real mean energy.

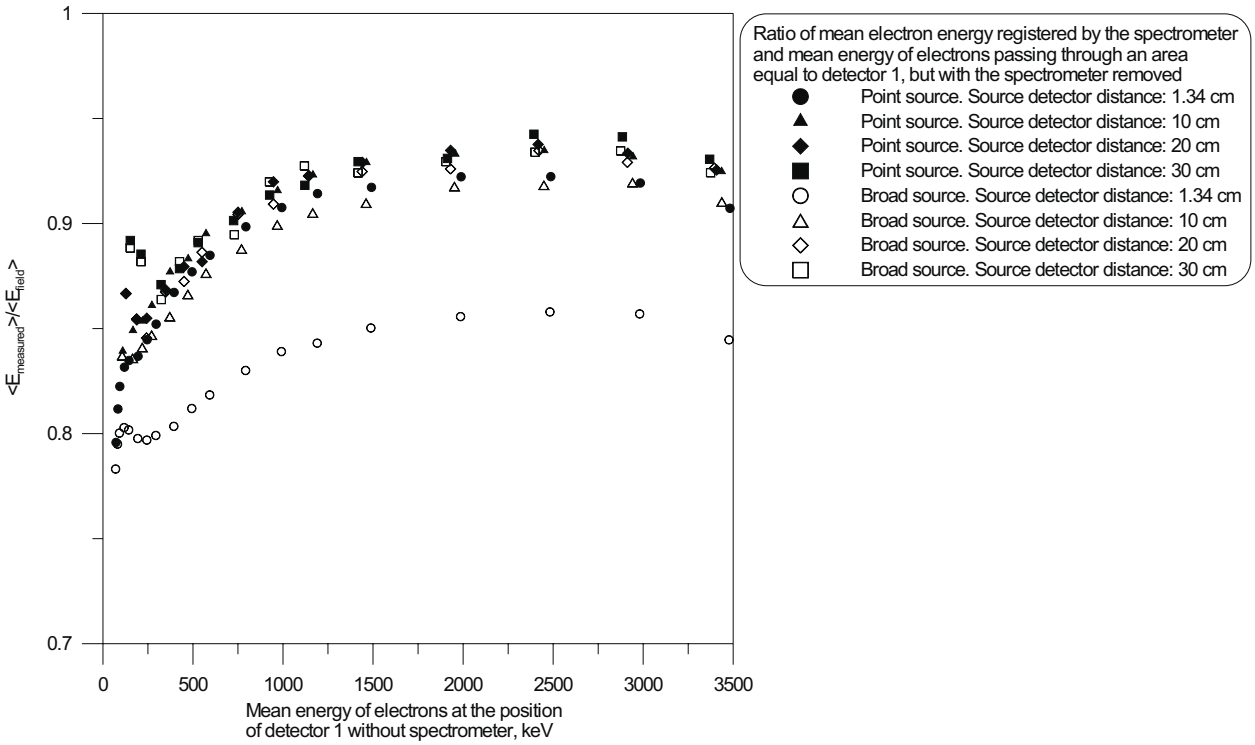

Figure 28. Calculated ratio between the mean energy registered by the spectrometer (coincidence pattern: 4,6,7) and the mean electron energy at the same position but with the spectrometer removed.

It is important to point out, that a correct measured spectrum cannot be obtained by simply scaling the energy axis with 10%, since the low energy tail in the response functions of the spectrometer, is described by a fairly broad distribution. Instead the original spectrum can be reconstructed by unfolding the measured spectrum with spectrometer response functions, which in principle can be obtained from Monte Carlo calculations.

Ability to register the correct planar fluence of electrons The planar fluence of electrons registered by the spectromter deviates from the planar fluence at the same position when the spectrometer is removed. Some particles

are absorbed by the titanium foil or blocked by diaphragm, and some are scattered into or away from the active part of the detector by parts of the spectrometer. Knowing the efficiency for measuring planar fluence can be an important issue, if e.g. the measured energy distribution is used to calculate skin dose using the ICRU conversion factors which is dependent on the electron planar fluence.

Figure 29 shows the ratio between the number of electrons registered by the spectrometer and the number of electrons passing through an area of the size of detector 1 placed at same position but with the spectrometer removed. The ratio is plotted as a function of the mean energy of the latter calculation. The uncertainty (1sd) is comparable with the height of the symbols.

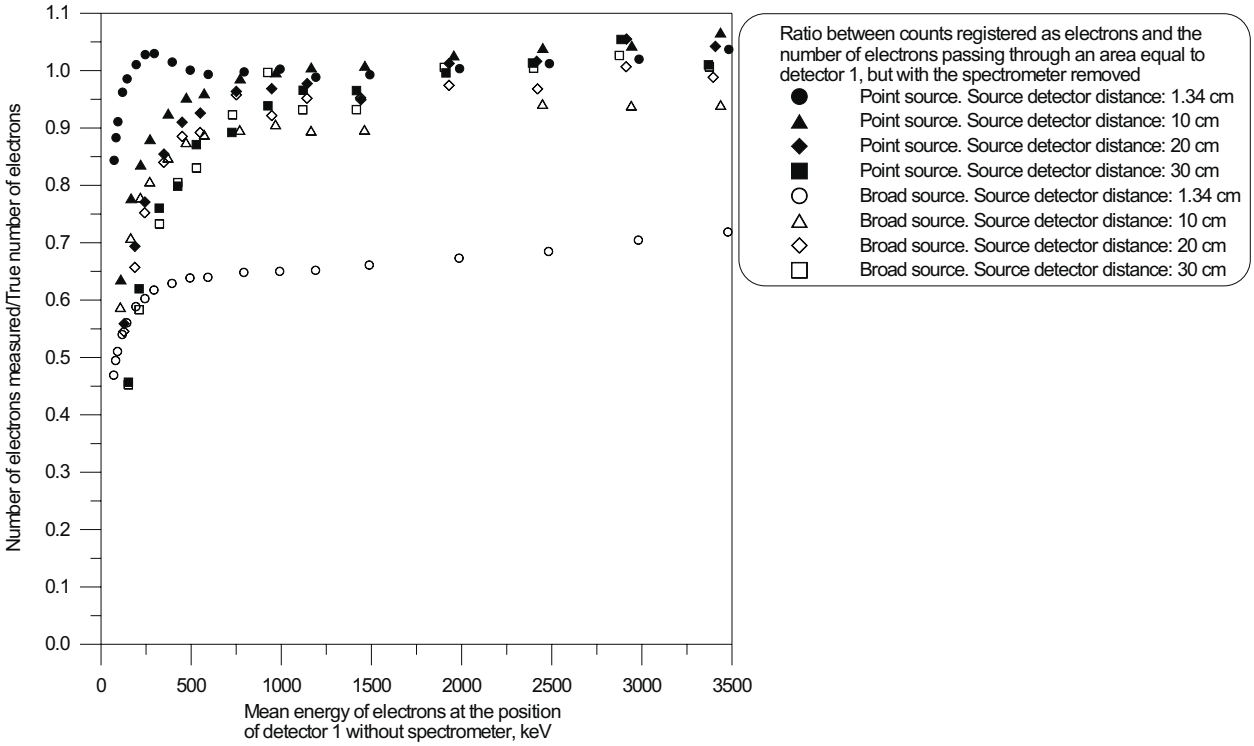

Figure 29. Calculated ratio between the number of electrons registered by the spectrometer (coincidence pattern: 4,6,7) and the number of electrons passing through the same area but with the spectrometer removed.

The efficiency for measuring the electron planar fluence is in general between 90 and 105% for high energies, and dropping rapidly as the measured mean energy is going towards lower energies (below approximately 500 keV). The efficiency for different sources are within 20% from each other, when the distance between the source and the front detector is 10 cm or more.

The correct spectrum can in principle be obtained by multiplying the number of counts in each bin with the inverse efficiency for measuring electron planar fluence corresponding to that bin, but it implies that a correct unfolding of the energy spectrum is done, before the efficiency is calculated.

9.3 Simulation of noise

It is essential to include the influence of noise in the Monte Carlo calculation, if the performance of the spectrometer is to be understood.

As an example of the huge influence noise has on the results, it can be mentioned, that if a particle threshold of 6 keV is used in detector 1, all high energy electrons penetrating the detector will be registered in the no-noise situation, but when noise is taken into account only 34% of the electrons will be registered as electrons.

The EGSnrc/DOSRZnrc Monte Carlo calculations does not include noise. Instead the noise is simulated in the subsequent data analysis by sampling from Gaussian distributions with a full-width-half-maximum value equal to the measured noise of the three detectors. The noise is sampled for each detector for each registered count. It is not enough just to fold the absorbed energy distributions with Gaussian distributions, since information about the coincidence patterns can not be obtained from the spectra alone.

The noise is approximated by Gaussian probability distributions with density

$$P(x) = \frac{1}{\sigma\sqrt{2\pi}} \exp\left(\frac{-x^2}{2\sigma^2}\right) \tag{11}$$

where σ^2 is the variance.

The noise contribution is sampled using the following algorithm which as output has to numbers (x_1 and x_2) which are distributed according to equation 11 [39].

Let $random(1)$ and $random(2)$ be two random numbers between 0 and 1. Calculate

$$r = \sigma\sqrt{-2 \cdot \ln(1 - random(1))} \tag{12}$$

$$\varphi = 2\pi \cdot random(2) \tag{13}$$

$$x_1 = r \cdot \cos(\varphi) \tag{14}$$

$$x_2 = r \cdot \sin(\varphi) \tag{15}$$

If the random number generator explicit exclude zero, '$1 - random(1)$' can be replaced by '$random(1)$' in equation 12.

The noise contribution from a detector is characterized by the full-width-half-maximum value (FWHM) of the response to a single energy, and not by the variance. The Gaussian distribution is easily scaled to the correct width by setting $\sigma = \mathrm{FWHM}/\sqrt{8 \cdot \ln(2)}$ in the above equations.

The FWHM for the three detectors is set to 34/28/130 keV, measured by photopeaks (detector 1 and 2), by pulsar resolution widths and by comparison of measured Compton edges with Monte Carlo calculations folded with Gaussian distributions (detector 3).[8]

The noise is added to each count, but the calculated energy registered by a detector is not allowed to become negative.

In the following the Gaussian distributions will be denoted the detector's noise distributions, keeping in mind that they are only approximations to the real noise.

9.4 Monte Carlo calculations including noise

Some of the basic properties in the Monte Carlo calculations including noise and also seen in the measurements, can be surprisingly well described by a simple picture of the noise distributions in two extreme situations:

[8]The FWHM given here are measured at the time when most of the data presented in this report were collected. The measurements used to make the energy calibration (Figure 44 and 45) were measured on a previous occasion where the noise levels were less.

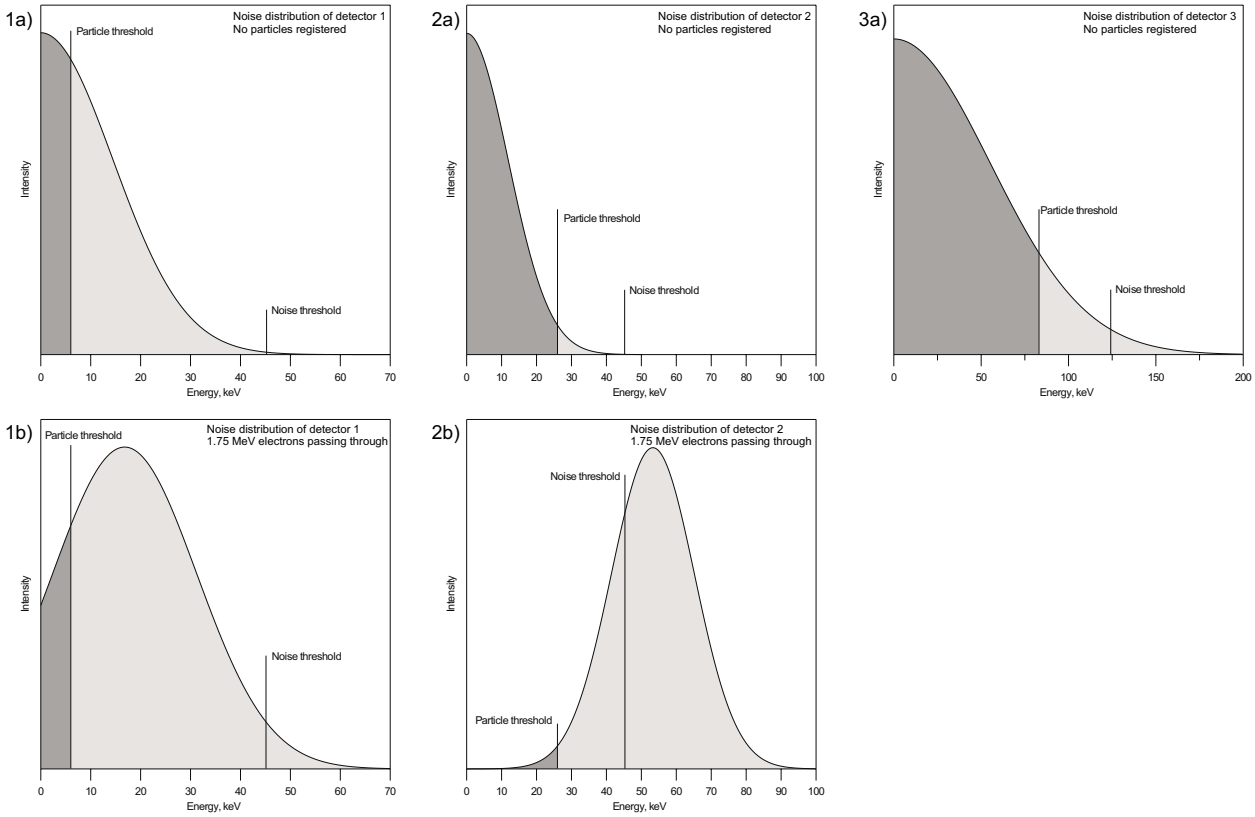

Figure 30. Approximations of noise distributions in the three detectors. Gaussian distributions are used as approximations for the real noise distributions. FWHM is 34 keV (detector 1), 28 keV (detector 2) and 130 keV (detector 3). Only the part above 0 keV is depicted.
Upper row: No particles registered.
Lower row: 1.75 MeV electrons passing through the front detectors. The average energy loss is 17 keV (detector 1) and 53 keV (detector 2).

- when no particles are registered by the detectors
- when high energy electrons are passing though detector 1 and 2, giving rise to a well defined minimum mean energy of absorption: 17 keV for detector 1 and 53 keV for detector 2.

If no particles are registered the noise distribution is centered around 0 keV, but in the case where high energy electrons are passing through the distributions are centered around 17 keV (detector 1) and 53 keV (detector 2).

The noise distributions are shown in Figure 30. The noise thresholds (45/45/124 keV) and particle thresholds (6/26/83 keV) are marked with vertical lines.

The presence of noise causes an interchange of some of the coincidence patterns and to explain the magnitude of this interchange, it is useful to calculate the fraction of the noise distributions below, between and above the noise- and particle thresholds. These values are calculated by numerical integration of equation 11 and shown in Table 12. Note that the fraction below the particle threshold also includes the distribution below 0 keV.

An example of what readily can be seen from Figure 30 and Table 12 is that the concept of particle thresholds is necessary if high energy electrons are to be detected as electrons. From Figure 1b it is seen that 97% of the high energy electrons passing through detector 1 is detected below the noise threshold, and thus not registered as electrons. If particle thresholds are used this fraction is lowered to 23%.

Table 12. Fraction of the noise distributions below, between and above the noise- and particle thresholds

		Percentage of the noise distribution...		
Fig.	Description	below particle threshold	between particle- and noise threshold	above noise threshold
1a)	Detector 1, no particles	66	34	0
1b)	Detector 1, with 1.75 MeV electrons	23	74	3
2a)	Detector 2, no particles	99	1	0
2b)	Detector 2, with 1.75 Mev electrons	1	23	76
3a)	Detector 3, no particles	93	5	1

9.5 Use of particle thresholds

Figure 31 shows the calculated fraction of coincidence patterns with and without the use of particle threshold, for an electron point source placed 10 cm in front of detector 1, as function of the mean electron energy measured by the spectrometer. To the left both noise- and particle thresholds are 45/45/124 keV (i.e. the particle threshold is not effective). To the right the particle thresholds are lowered to 6/26/83 keV. Gaussian noise with FWHM 34/28/130 keV is added to each count.

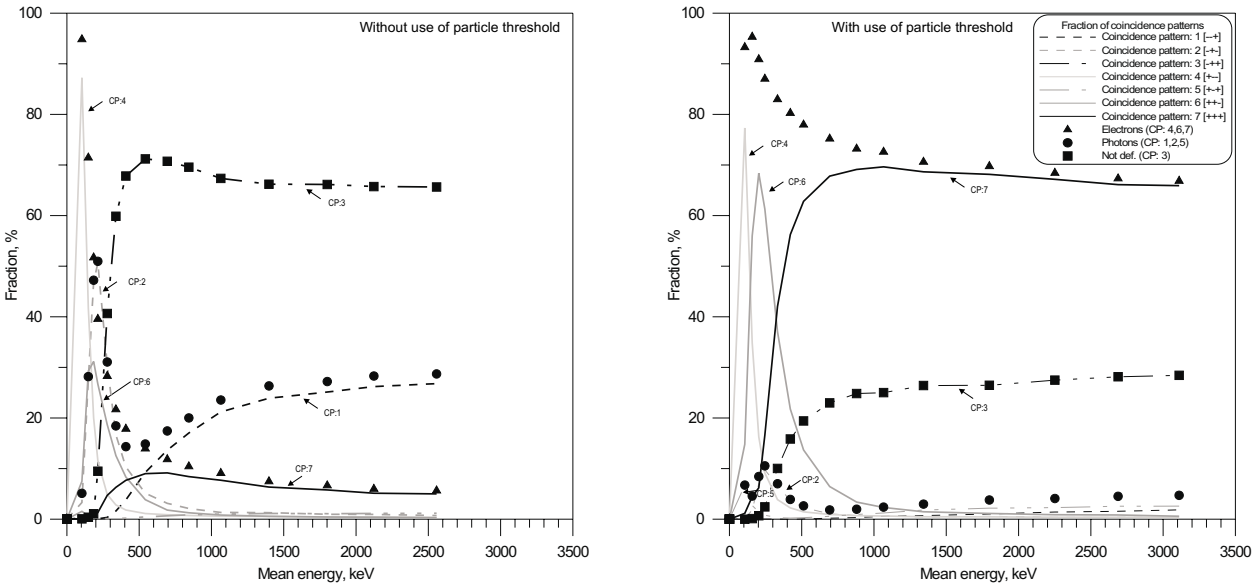

Figure 31. Calculated fraction of the registered coincidence patterns for an electron point source at 10 cm distance. Gaussian noise added to each count.
Left: Without use of particle threshold. Right: With use of particle threshold.

In the original setup without the use of particle thresholds, the response of the spectrometer is dominated by non-electron coincidence patterns, and for energies above 400 keV less than 20% of the registered events are classified as electrons.

By the use of particle thresholds the fraction of registered electron events is raised to 67% or more, which is comparable to the no-noise situation.

It is also seen that the calculated measured mean energy generally shifts to a lower energy when the particle threshold is not invoked. This is because high energy electrons deposits a relatively small amount energy in detector 1 and therefore have a greater possibility for not being registered as electrons.

It is clear that the concept of particle thresholds is a necessary and powerful tool in the situation where the noise levels are high, as is the case for the Risø spectrometer.

The fraction of events registered as electrons for three electron sources for different settings of the particle thresholds are presented in Table 17 on page 82. Table 13 compares these fractions with the calculated values (Figure 31). The calculated values are obtained by folding the calculated fractions with the measured spectrum.

Table 13. Fraction of events registered as electrons without and with the use of particle threshold. Noise threshold settings: 45/45/124 keV.

	Fraction of electron events			
Particle threshold:	45/45/124 keV†		6/26/83 keV	
Source	Measured	Calculated	Measured	Calculated
Pm-147	90%	(92±1)%	98%	(94±1)%
Tl-204	29%	(61±2)%	85%	(87±2)%
Sr-90/Y-90	12%	(45±2)%	75%	(78±2)%

† I.e. the particle threshold is not effective.

There is good agreement between the calculated and measured fraction of counts registered as electrons in the case when particle thresholds are used. This is contrary to the case where only the noise thresholds are used. A factor of 2 and 4 in difference is obtained for Tl-204 and Sr-90/Y-90 respectively, and an explanation for this disagreement has not been found.

9.6 Reclassification of coincidence patterns

For Compton scattered photons coincidence pattern 1 [−−+] is the most dominant, but due to the noise in the front detector 34% of these events is registered as coincidence pattern 5 [+−+]. This value is verified experimentally for Co-60 and Cs-137 covered by a 4 mm PMMA filter. In both cases 63% of the events are classified at coincidence pattern 1 and 32% as coincidence pattern 5.

The mean energy surplus for the coincidence pattern 5 events is theoretically 16 keV, (i.e. the mean energy of the noise distribution above the particle threshold in detector 1) which is insignificant for Compton electrons registered in detector 3. It is therefore advantageous to reclassify coincidence pattern 5 as photons.

In the following coincidence pattern 5 will be regarded as a photon event instead of a 'not defined event', whenever noise is present.

9.7 Ability to identify electrons

Figure 32 shows the calculated fraction of the registered coincidence patterns for an electron point source at 10 cm distance. The figure represents the typical behaviour when noise is taken into consideration in the Monte Carlo calculation. For comparison the equivalent calculation without noise is shown to the right.

It is seen that the noise has a significant effect on the classification of electrons, since the fraction of electrons for most energies is lowered by 20 percentage points.

For high electron energies a greater share of the electrons passing through detector 1, are registered below the particle threshold, and coincidence pattern 3 [−++] makes up a considerable part of the registered events.

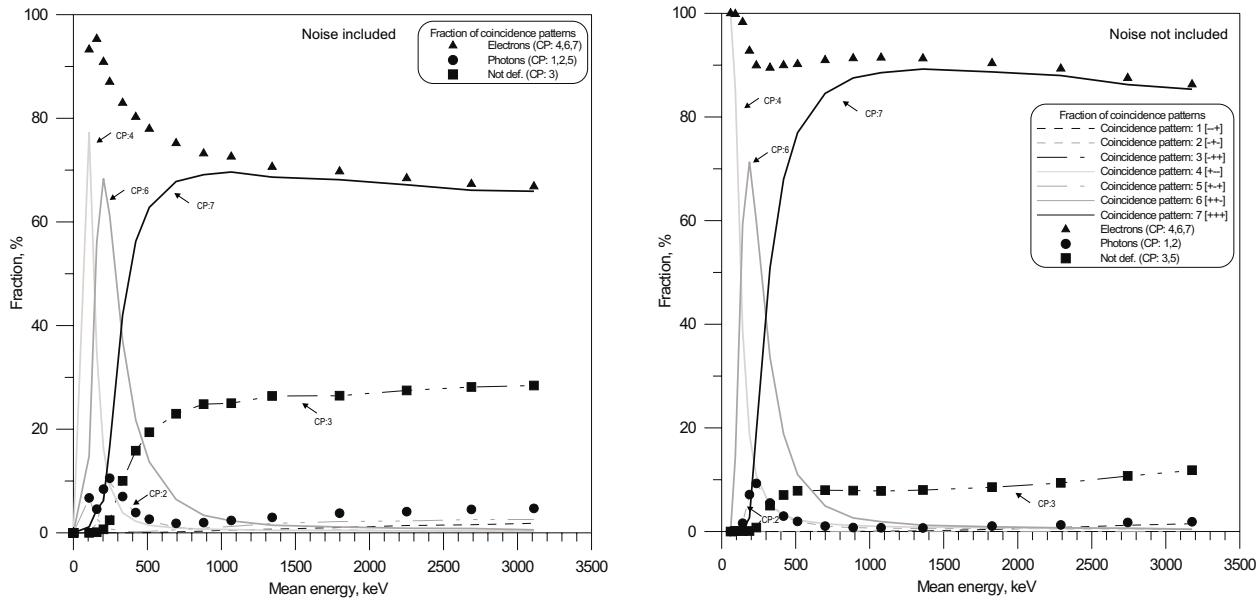

Figure 32. Calculated fraction of the registered coincidence patterns for an electron point source at 10 cm distance.
Left: Gaussian distributed noise added to each count. Right: No noise added.
Noise threshold: 45/45/124 keV. Particle threshold: 6/26/83 keV.

Interchange of coincidence pattern 3 and 7

The change in coincidence pattern 3 [–++] and 7 [+++] seen in Figure 32 can be explained by simple considerations about the noise distribution.

From Table 12 (1b) it is found that 23% of the events originally registered as coincidence pattern 7 will be registered as pattern 3 due to noise, and from (1a) that 34% will 'change' from coincidence pattern 3 to 7.

A calculation of the expected fraction of coincidence pattern 7 when noise is present, f'_{CP7}, is now straight forward

$$f'_{\mathrm{CP7}} = f_{\mathrm{CP7}} - p(\mathrm{CP7}\rightarrow 3) f_{\mathrm{CP7}} + p(\mathrm{CP3}\rightarrow 7) f_{\mathrm{CP3}} \tag{16}$$

where
f_{CP7}: fraction of coincidence pattern 7, when noise is not included.
$p(\mathrm{CP7}\rightarrow 3)$: probability that a coincidence pattern 7 event is registered as coincidence pattern 3. (Noise included).
f_{CP3}: fraction of coincidence pattern 3, when noise is not included.
$p(\mathrm{CP3}\rightarrow 7)$: probability that a coincidence pattern 3 event is registered as coincidence pattern 7. (Noise included).

The fractions of coincidence pattern 3 and 7 at about 1800 keV measured mean energy, are used as an example: $f_{\mathrm{CP7}} = 0.89$, $p(\mathrm{CP7}\rightarrow 3) = 0.23$, $f_{\mathrm{CP3}} = 0.09$, $p(\mathrm{CP3}\rightarrow 7) = 0.34$ which gives $f'_{\mathrm{CP7}} = 0.72$ in good agreement with the simulated value of 0.68. This shows that mechanism behind the change in the distribution of coincidence patterns due to noise is understood.

It is instructive to do a similar calculation for the case where a broad source is placed right in front of the spectrometer. The calculated coincidence pattern fractions are shown in Figure 33.

The coincidence pattern 3 is now pronounced because a large fraction of the electrons bypass the active volume of detector 1.

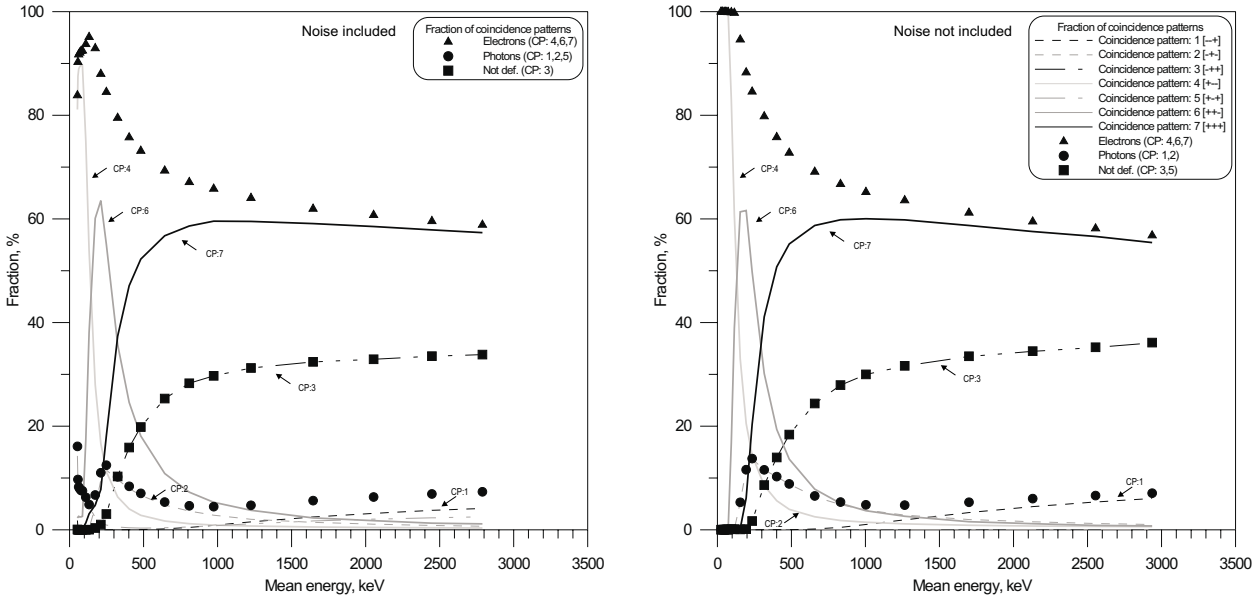

Figure 33. Calculated fraction of the registered coincidence patterns for a broad electron source at surface of the spectrometer.
Left: Gaussian noise added to each count. Right: No noise added.
Noise threshold: 45/45/124 keV. Particle threshold: 6/26/83 keV.

The fractions of coincidence pattern 3 and 7 at about 1600 keV calculated mean energy are $f_{\mathrm{CP3}} = 0.34$ and $f_{\mathrm{CP7}} = 0.59$.

A calculation using equation 16 gives $f'_{\mathrm{CP7}} = 0.57$ close to the simulated value of 0.59. That f'_{CP7} is similar to f_{CP7} means that the flow from coincidence pattern 7 to 3 is counterbalanced by the flow from 3 to 7.

It is notable that the change in the coincidence pattern 7 fraction due to noise is dependent on amount of electrons bypassing detector 1, and thus by the geometry of the source. This is especially evident in the analysis of the ability of measuring planar electron fluence as described later.

If the rim of detector 1 had been properly shielded the fraction of coincidence pattern 7 for high energy electrons would be 77% only due to noise in detector 1. It is therefore of great importance to reduce the noise in the front detector.

It can be seen from Figure 32 that the appearance of coincidence pattern 2 [-+-] is not affected by the noise. Coincidence pattern 2 originates from electrons bypassing the active volume of detector 1, and it can be shown that the fraction remains more or less constant because the flow from coincidence pattern 2 [-+-] to 4 [++-] is counter balanced by a flow in the opposite direction.

9.8 Influence of noise on the registration of electron energy

To the left in Figure 34 the calculated ratio between the mean energy measured by the spectrometer and the calculated real mean energy is shown, when noise is taken into consideration. To the right is the same setup but without the simulation of noise.

It is seen that the two graphs have completely different slops at low energy. In the calculation including noise the ratio approaches one, but this should be regarded as a coincidence caused by the noise. If other noise levels had been present the ratio would have approached another value.

The apparent compensation for the energy loss in titanium foil etc. has two

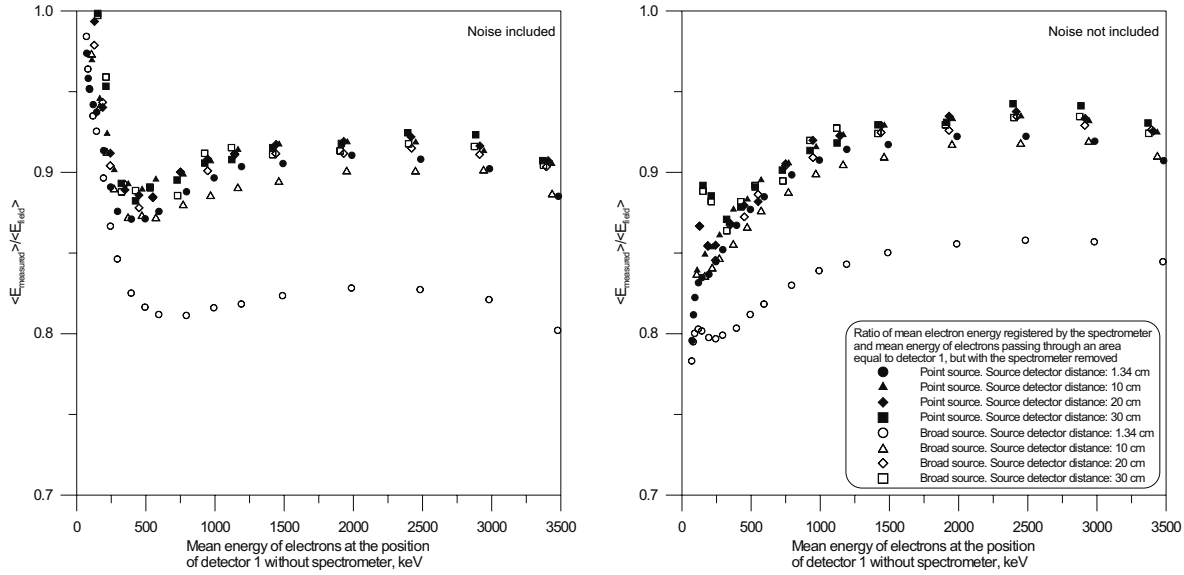

Figure 34. Calculated ratio between the mean energy registered by the spectrometer and the mean electron energy at the same position but with the spectrometer removed. The uncertainty is estimated to less than 5% for low energy and less than 2% for high energy electrons. Particle threshold: 6/23/80 keV. Noise threshold: 44/40/119 keV.

explanations.

- For low energy electrons the noise distributions in detector 1 and 2 will have a part of the low energy side below the noise threshold, and the mean energy is therefore slightly higher than the center value of the distribution.
- For low energy electrons registered in detector 1 and 2, the noise level in detector 3 is above the particle threshold in 8% of the cases, causing an average increase of the registered mean energy of 8 keV.

Figure 34 also shows that the calculated ratio between measured and real mean energy, drops a few percent for high energy electrons when noise is present. This is caused by coincidence pattern 3 events [−++] (electrons bypassing detector 1) turning into coincidence pattern 7 [+++] due to noise in detector 1. These events are approximately 150 keV less in energy.

9.9 Influence of noise on the registration of planar fluence

The fact that about 17% of the high energy electrons are classified as coincidence pattern 3 [−++] is also reflected in the ability to register the correct planar fluence. Figure 35 shows the calculated ratio of the planar fluence registered by the spectrometer and the calculated real planar fluence, for different electron sources. The broad source is 5 cm in radius.

The loss in efficiency for measuring planar electron fluence due to noise is in general 10-20% for all electron energies, excluded the sources very close to the spectrometer, where the change is less.

The drop is mainly caused by events, where the energy deposition in detector 1 is registered below the particle threshold due to noise, as discussed above (section 9.7).

The drop in efficiency for measuring planar fluence is smallest when the fraction of coincidence pattern 2 and 3 ([−+−] & [−++]) is high (generally for broad sources

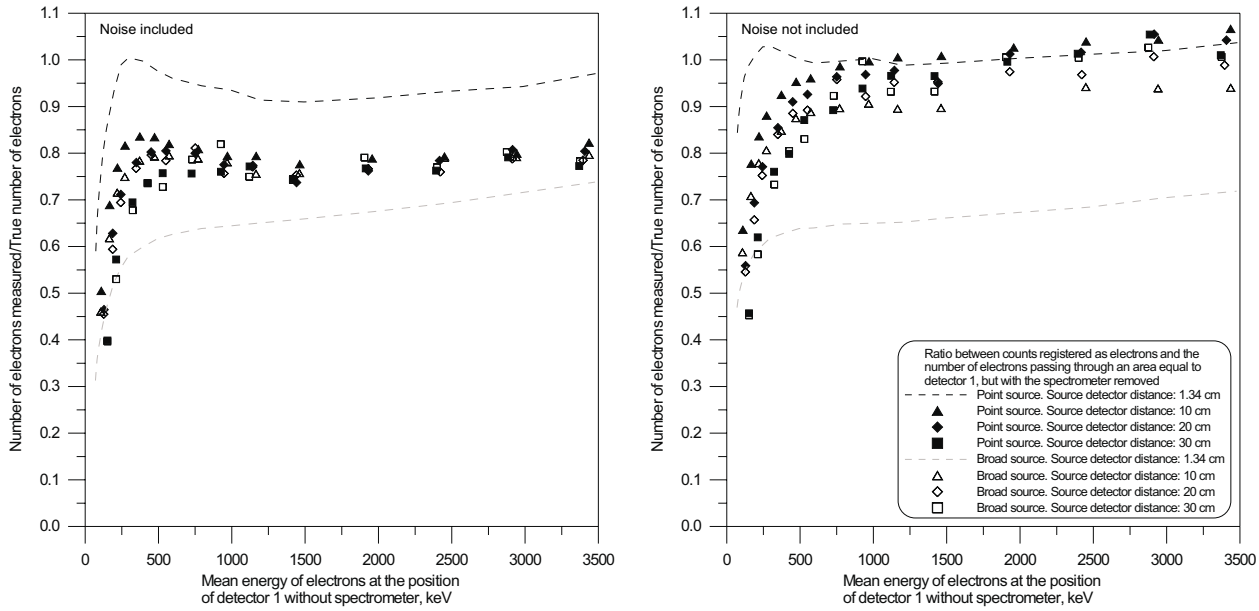

Figure 35. Calculated ratio between counts registered as electrons and the number of electrons passing through an area of 0.5 cm^2 placed at the position of detector 1, but with the spectrometer removed. The uncertainty is less than the symbols. Particle threshold: 6/23/80 keV. Noise threshold: 44/40/119 keV. (The data point for the broad source at 10 cm was corrupted, and thus not included).
Left: Gaussian noise added to each count. Right: No noise added.

and sources at close distance). As mentioned earlier this is because the flow from coincidence pattern 6 [++−] and 7 [+++] to 2 [−+−] and 3 [−++] is counteracted by a flow in the opposite direction.

This explains why the fraction of electrons is more or less unaffected by the detector noise for the sources placed close to the detector, and why the spread between broad and point sources is collapsing for high electron energies when noise is applied.

In the no-noise situation the efficiency for registering planar fluence is more than one for some of the sources. This is caused by back-scatter from the sides of the diaphragm and that the rim of the diaphragm is transparent to high energy electrons.

9.10 Rejection of photons

As will be shown in the section about the energy calibration of detector 3 (section 11.3 on page 77) the Monte Carlo calculation of the photon response is not a true simulation of the measurements made with the spectrometer at lower energies. The uncertainty is therefore greater than otherwise indicated.

Just as the spectrometer should be able to identify electrons, the spectrometer should also be able to identify and reject photons. Figure 36 shows the response to a broad beam of photons hitting the spectrometer at normal incidence with energies in the interval from 50 to 3500 keV. Note the broken and different scaled y-axis.

It is seen that about 97% registered events are classified correctly, in this idealized case where noise does not influence. It is also seen that the theoretically maximal rejection factor for photons (i.e. the fraction of counts not classified as electrons) is about 99% for all energies.

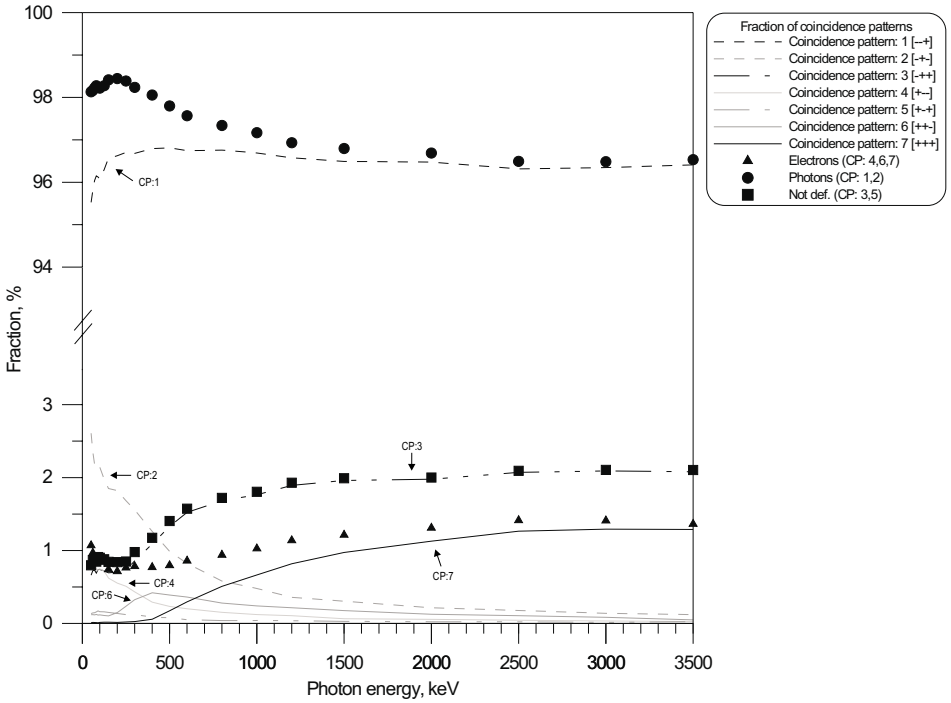

Figure 36. Calculated fraction of coincidence patters. Broad photon source with parallel photon beam normal to detector 1 at distance 1.34 cm. The uncertainty is less than the height of the symbols. Note the broken and different scaled y-axis. Coincidence patterns: Electrons: 4,6,7; Photons: 1,2.

Figure 37 shows the same source geometry, but includes the simulation of noise.

The distribution of the coincidence patterns can not readily be explained by simple considerations about the noise distributions, since the center of the Gaussian distributions can not easily be deduced - and in the case of Compton scattered electrons, is not well defined at all.

What is important for the performance of the dose meter, is that the fraction of events classified as electrons is as low as possible, since these events will add to the calculated dose, based on the measured electron spectra.

If only the noise thresholds are used (Figure 37 right) the fraction of registered electrons is less than 1% for photon energies above 300 keV. Below the registration of photo-absorption in detector 1 is apparent.

When particle thresholds are used it is apparent that a re-classification of coincidence pattern 5 [+−+] is necessary, since it, as expected, is expressed by a 30% fraction (Figure 37 left).

In both cases there is an energy dependence of coincidence pattern 3 [−++], but it is notable that coincidence pattern 7 [+++] is present with a similar energy dependence when particle thresholds are used.

Coincidence pattern 6 [+−−], which was totally missing in the no-particle threshold calculation, is also present. If the noise of detector 1 is reduced, the fraction of registered electron events in a pure photon field, would be reduced.

That the events classified as electrons in photon fields above 300 keV accounts for at least 2% is a serious drawback for the spectrometer, when measuring electron doses in a mixed photon/electron field. The mean energy of electrons set in motion in detector 3 by Compton scattered 1 MeV photons is of the order of 400 keV. If for example the photon field is an order of magnitude stronger than the electron field in terms of count rate, the Compton scattered electrons will make up about 20% of the measured electrons, in most cases causing a measurable distortion of the dose calculation. The influence of photons registered as electrons is further

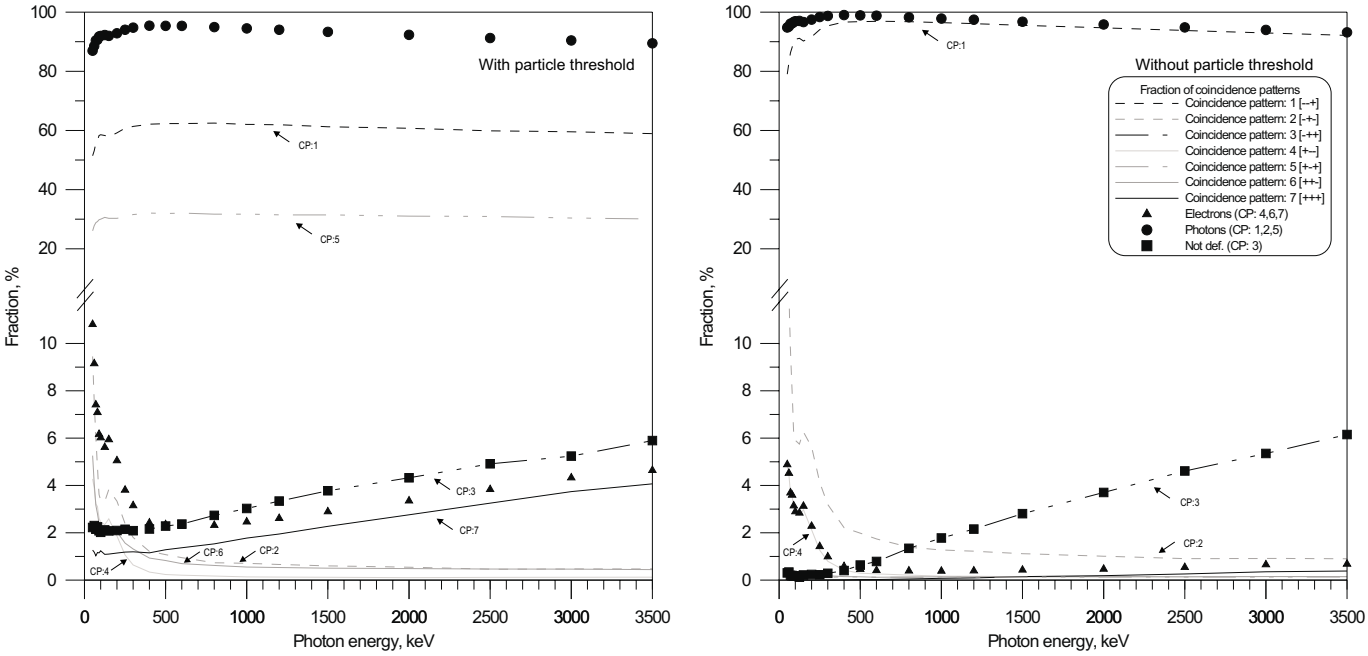

Figure 37. Calculated fraction of coincidence patters when noise is included. Broad photon source with parallel photon beam normal to detector 1 at distance 1.34 cm. The uncertainty is less than the height of the symbols. Note the broken and different scaled y-axis. Particle threshold: 6/23/80 keV. Noise threshold: 44/40/119 keV. FWHM of the noise distributions: 34/28/130 keV. Coincidence patterns: Electrons: 4,6,7; Photons: 1,2,5.
Left: With the use of particle threshold. Right: Without the use of particle threshold.

discussed in section 12.8.

9.11 Summary

Monte Carlo calculations of the performance of spectrometer when irradiated with electrons and photons have been performed. The calculations suggest that the spectrometer design needs to be improved by a better shielding of the rim of detector 1.

To obtain comparable results between calculations and measurements a simulation of the detector noise has to be included, and this is done by sampling from Gaussian distributions with suitable widths.

Especially the noise level of the front detector is a problem, since it reduces the fraction of correctly classified electrons significantly.

The use of particle thresholds is shown to be a necessary and powerful tool to reduce the destructive influence of noise. The spectrometer is unfit to measure electron radiation fields if the concept of particle thresholds is not used. A drawback of the method is an enhanced fraction of events classified as electrons when the spectrometer is working in a pure photon radiation field.

The influence of noise on the behaviour of the spectrometer is generally well understood, and can in many cases be explained by simple considerations with Gaussian distributions.

10 Conversion factors from electron measurement to $H_{\mathrm{p}}(0.07)$

The main objective of the Risø telescope spectrometer is to determine skin dose - i.e. $H_{\mathrm{p}}(0.07)$ - based on the electron energy distribution measured by the spectrometer.

The original idea was to use ICRU conversion factors from electron fluence (at normal incidence) to $H'(0.07)$, but as shown later, this leads to unsatisfactory results especially for low energy electrons.

Instead, Monte Carlo calculations are used to establish a new set of conversion factors which are dependent of the specific spectrometer design.

An attempt is made to calculate the dose directly from the measured spectrum i.e. without unfolding and correction for planar fluence efficiency. This approach is justified by the observation, that the unfolding procedure is very time consuming, and that the unfolding procedure and planar fluence correction in themselves may introduce uncertainties to the dose calculation. This could for instance happen if the response functions used in the unfolding procedure are dependent on the source geometry.

If the measured energy distribution is needed for identification of beta emitting isotopes, it should be noted that leaving out the unfolding procedure and the planar fluence correction will not alter the position of the maximal energy registered, but will most likely change the position of the most probable energy, i.e. the peak of the β-spectrum, to a lower energy.

10.1 Outline for Monte Carlo calculation

The spectrometer specific conversion factor is calculated by merging two Monte Carlo calculations.

For a given source geometry the number of counts classified as electrons per history and the registered mean energy are calculated.

For a similar geometry, but with the spectrometer replaced by a tissue disc, the dose per history is calculated. The dose calculation is restricted to a 1 cm^2 disc around the central axis in 0.07 mm depth, in accordance with the ICRP recommendations for calculation of dose equivalent.

The spectrometer specific conversion factor, η_{det}, is given as the inverse ratio between the two calculations as a function of the mean electron energy registered by the spectrometer.

$$\eta_{\mathrm{det}}(E) = \left. \frac{\text{Calculated dose at 0.07 mm tissue}|_{1\ \mathrm{cm}^2}\ /N_t}{\text{Number of registered electrons}\ /N_s} \right|_{<E_{e^-}>} \tag{17}$$

where
N_t: Histories in tissue disc calculation
N_s: Histories in spectrometer calculation
$< E_{e^-} >$: Mean electron energy registered by the spectrometer

A similar calculation is done but with the number of registered electrons replaced by the planar fluence at the tissue surface right above the 1 cm^2 disc and with the registered mean electron energy replaced by the mean energy of the electrons as they cross the tissue surface.

$$\eta_{\mathrm{tissue}}(E) = \left. \frac{\text{Calculated dose at 0.07 mm tissue}|_{1\ \mathrm{cm}^2}}{\text{Planar electron fluence}} \right|_{<E_{e^-\ tissue}>} \tag{18}$$

where
$< E_{e^- \, tissue} >$: Mean electron energy at tissue surface

This simulates a 'perfect' detector measuring the energy and planar fluence of the electrons without disturbance from the detector geometry, and the conversion factors should be close to the ICRU conversion factors folded by the angle distribution at the tissue surface. The results from this calculation will be discussed first.

This report only focus on the dose at 0.07 mm tissue, but the analysis could in principle be extended to cover strongly penetrating beta radiation, by calculating dose at 3 mm or 10 mm tissue.

10.2 Planar fluence at tissue surface conversion factors

There are two important differences in the setup between this work and the calculations used to determine the ICRU conversion factors (Table 5 on page 33)

- In this work the dose scoring region is limited to a disc of 1 cm^2 at the central axis.
- The incident beam can in most cases not be described as parallel and normal to the tissue surface, and the radiation field is not homogeneous over the target disc of 1 cm^2. This also explains why it is decided to use the notation of $H_p(0.07)$ instead of $H'(0.07)$.

It is therefore expected that there will be deviations between the ICRU conversion factors from planar fluence to $H'(0.07)$, and the calculations presented here from planar fluence over the 1 cm^2 disc to $H_p(0.07)$.

Figure 38 and 39 shows the calculated conversion factor from planar fluence over the 1 cm^2 disc to $H_p(0.07)$ (equation 18), for different source geometries. As a guideline the ICRU conversion factor for normal incidence is plotted as well. The calculated conversion coefficients are also listed in appendix D.

It is seen that the calculated conversion factor, η_{tissue}, has a slightly higher value than the ICRU conversion factor for high energy electrons at normal incidence. Because the calculated electron radiation field in general has an angle to the tissue surface, the electrons will travel a greater distance in the dose scoring region at 0.07 mm depth (roughly as one over cosine to the angle), thus giving a greater dose in this region per electron. This is particularly clear for the broad source at close distance to the tissue surface. At the same time the calculated conversion factor gets smaller for very low energy electrons, since a smaller part of these electrons are reaching the dose scoring region. A nice illustration can be found in [23].

Figure 40 shows the normalized electron angle distribution of electrons at the tissue surface, for a point source at different distances from the surface, obtained by Monte Carlo calculations. Backscattered electrons leaving the tissue are not included. For electrons entering the tissue with energies below 1 MeV, it is clear that an assumption of normal incidence can not be preserved. For this reason alone the attempt to calculate personal dose equivalent with the use of the ICRU conversion factors for normal incidence is believed to be inaccurate.

Figure 41 shows the normalized electron angle distribution of electrons at the tissue surface, for a broad source 5 cm in diameter at different distances from the surface. The differences compared to the point source in Figure 40 are notable and apparent at all distances. Recalling the ICRU conversion coefficients which have an angle dependence (Table 5 and Figure 13 on page 33), a dependence on the source geometry for a given energy distribution at the tissue surface is expected.

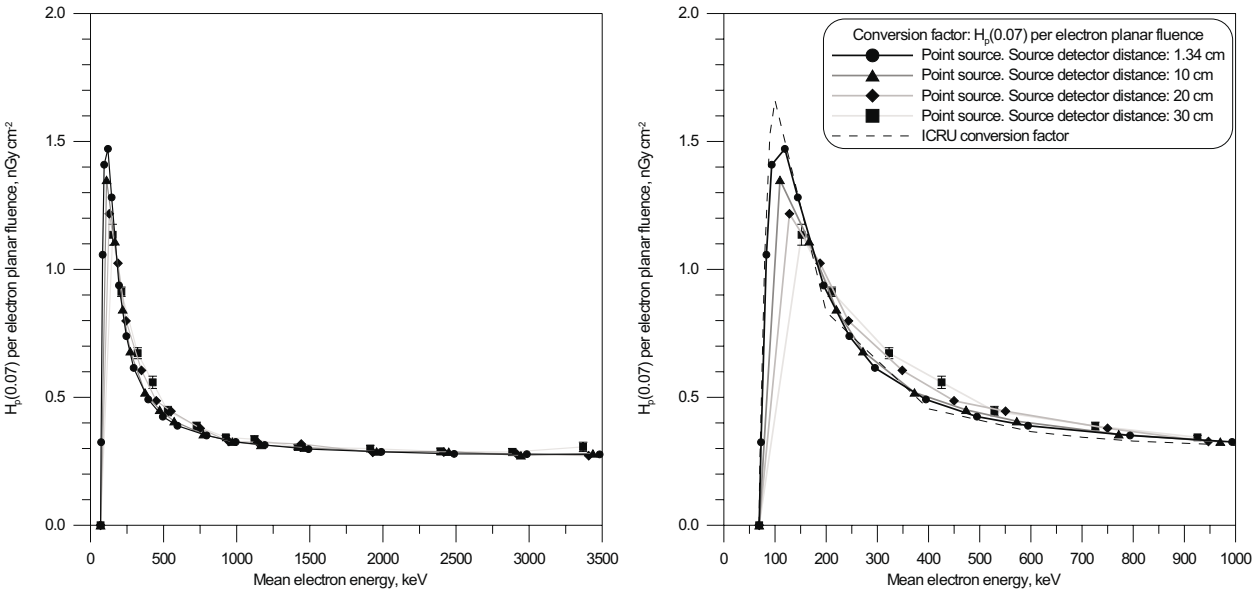

Figure 38. Calculated conversion factor, η_{tissue}, from electron planar fluence over a 1 cm^2 disc at the central axis to $H_p(0.07)$ as a function of the mean energy of the electrons at tissue surface within the 1 cm^2 disc (equation 18). The electron source is a point source placed at various distances from the tissue surface. The Figure to the right is identical to the one to the left, except for a change in the energy scale.

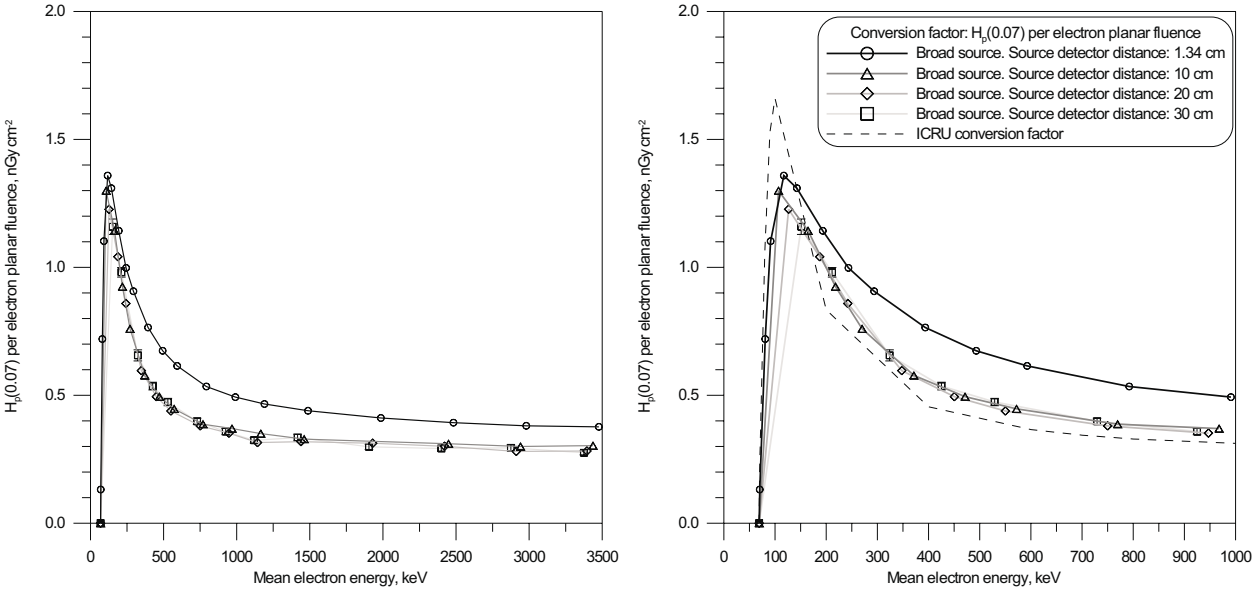

Figure 39. Calculated conversion factor, η_{tissue}, from electron planar fluence over a 1 cm^2 disc at the central axis to $H_p(0.07)$ as a function of the mean energy of the electrons at tissue surface within the 1 cm^2 disc (equation 18). The electron source is 5 cm in diameter and placed at various distances from the tissue surface. The Figure to the right is identical to the one to the left, except for a change in the energy scale.

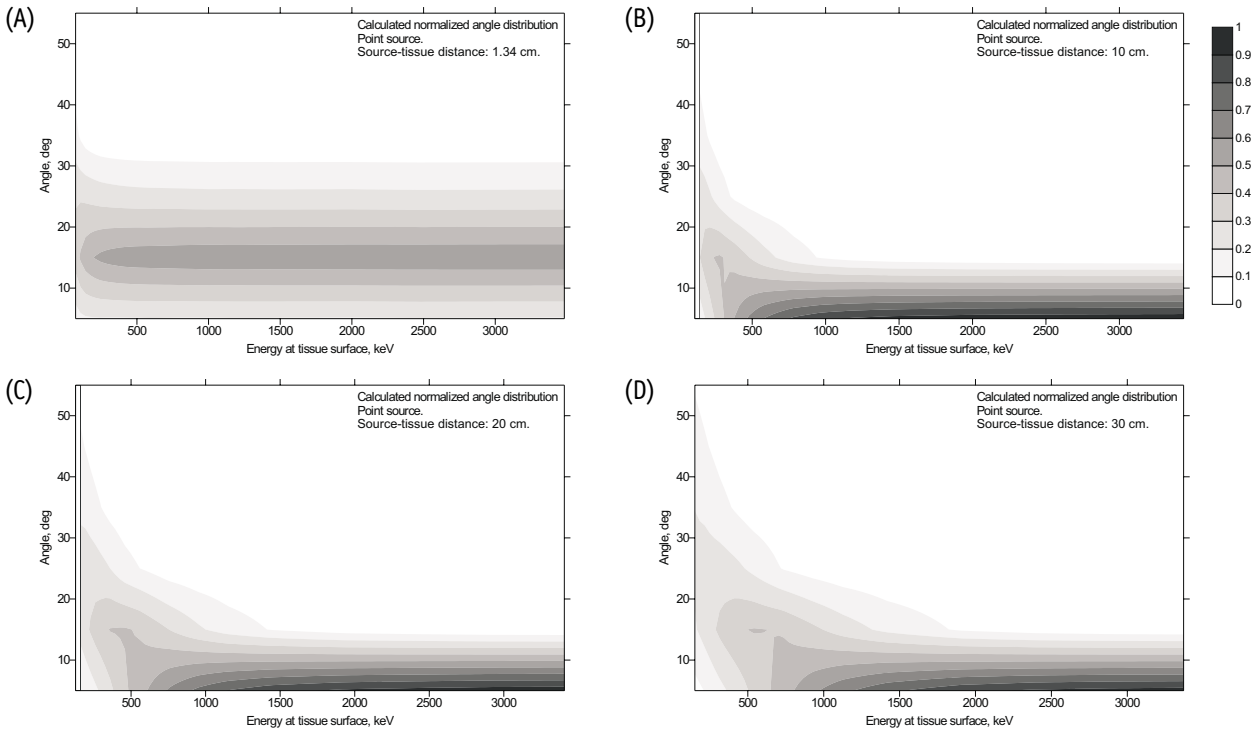

Figure 40. Calculated normalized angle distribution of electrons entering a tissue surface, for a point source placed at different distances from the surface: A) 1.34 cm. B) 10 cm. C) 20 cm. D) 30 cm.

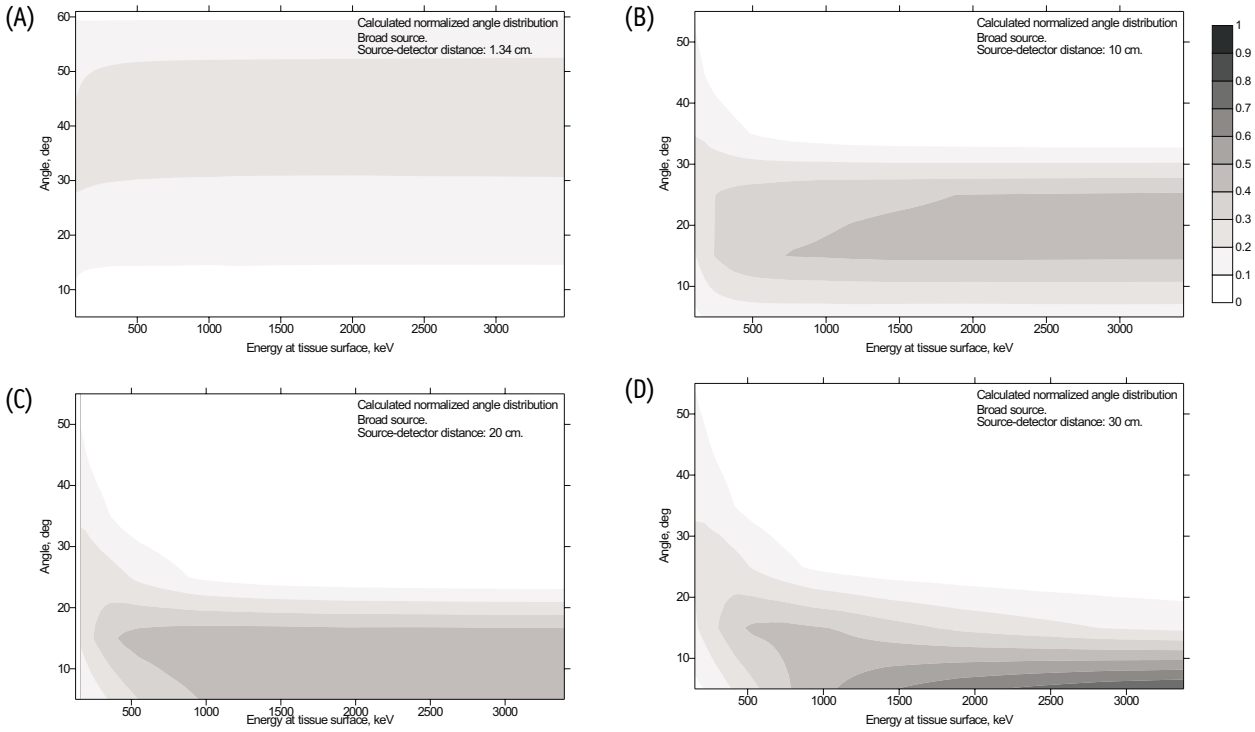

Figure 41. Calculated normalized angle distribution of electrons entering a tissue surface, for a source 5 cm in diameter placed at different distances from the surface: A) 1.34 cm. B) 10 cm. C) 20 cm. D) 30 cm.

Inadequate Monte Carlo calculations at low electron energy

The point of measurements in Figure 38 and 39 are connected by straight lines matching the linear interpolation used by the algorithm, used in the spectrometer to calculate skin dose.

Figure 38 and 39 points out an important shortcoming of the Monte Carlo calculations for low energy. It is obvious that there is a rapid change in the conversion factor in the energy range form 70 to 200 keV. At the same time it is clear that the mesh of calculation points are too coarse in this region - particularly for sources placed 10 cm or more away from the tissue surface. One would expect all the conversion coefficients to rise with a slope comparable to the ICRU coefficients but this is only obtained by the calculations with 1.34 cm distance between source and tissue.

As shown below the lack of calculation points is also present in the spectrometer dependent conversion factors, and is somewhat an obstacle for a correct dose calculation. Additional Monte Carlo calculations in the low energy region have not been performed, since the spectrometer soon will be replaced. An exception is the case where a point source is placed 10 cm in front of the spectrometer, since measurements are available for this type of source geometry. Four simulations with an initial electron energy of 130, 135, 140 and 145 keV are calculated to make and a comparison between measured and calculated dose rates possible.

10.3 Spectrometer specific conversion factors

Figure 42 and 43 shows the spectrometer specific conversion factor, η_{det}, for a number of different source geometries. The calculated conversion factors are also listed in appendix D.

Two times the ICRU conversion factor is shown as well. If the ICRU conversion factor is used to calculate $H_{\mathrm{p}}(0.07)$ from the measured number of electrons, is has to be multiplied by two, since the area of detector 1 is 0.5 cm^2.

Except when a point source is placed at the surface of the spectrometer, it can be seen from the figures that the use of the ICRU conversion factors for normal incidence is expected to lead to an underestimation of $H_{\mathrm{p}}(0.07)$.

Dependence in the conversion factors on the distance between source and spectrometer

Even when leaving out the extreme case when the source placed on the surface of the spectrometer (open and filled circles), it is seen from Figure 42 and 43 that for energies below 500 keV, there is a marked spread in the conversion values for different source distances. At 200 keV there is roughly a 30% difference in the conversion factor between the sources placed at 10 and 30 cm. The difference between the point and broad source at the same distance is 10% or less.

Depending on the desired accuracy of the spectrometer, information of the distance to the source need to be fed to the spectrometer before a dose calculation is performed. It has not been possible to verify this experimentally. Certainly a separate set of conversion factors are needed for measurement of large contaminated surfaces measured at close distance.

It is evident from the figures that rapid change in the conversion factor at low energies is not well modelled with the current set of calculations. It is thus expected that extra calculations are needed to optimize the dose calculations performed by the spectrometer when irradiated with low to medium energy beta radiation.

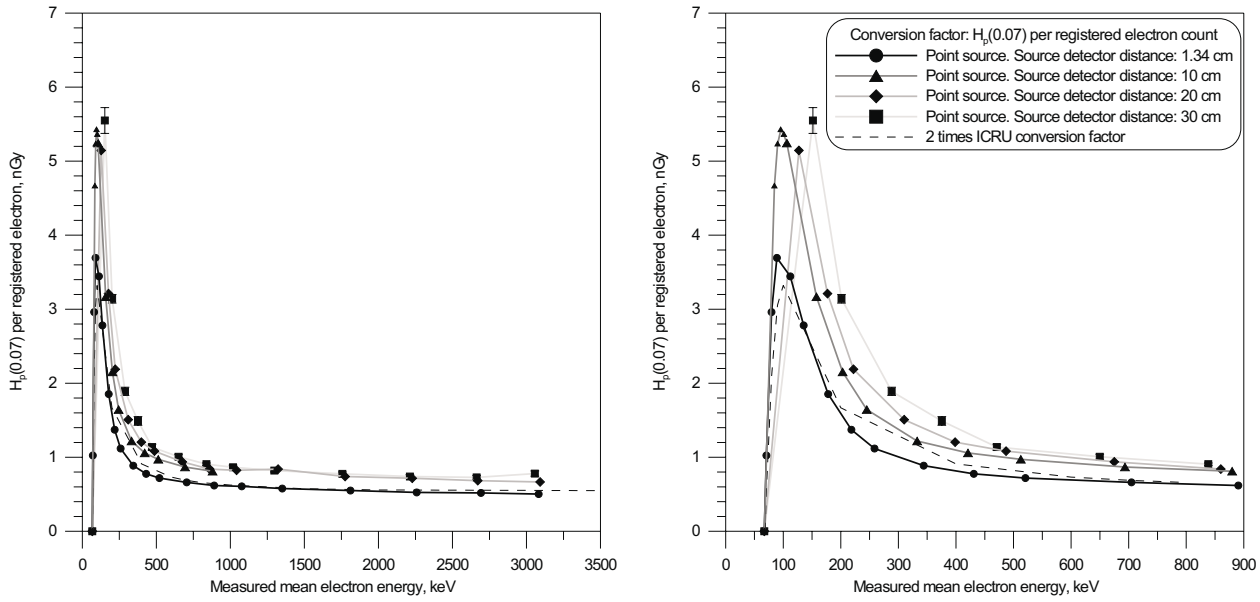

Figure 42. Calculated conversion factor, η_{det}, from measured electron counts by the spectrometer to $H_p(0.07)$ as a function of the measured mean energy (equation 17). The electron source is a point source placed at various distances from surface of detector 1. The figure to the right is identical to the one to the left, except for a change in the energy scale. By a dotted line two times the ICRU conversion factor ($H'(0.07)$) is shown. The conversion factor for 10 cm distance between source and spetrometer has four extra data points shown by small triangles.

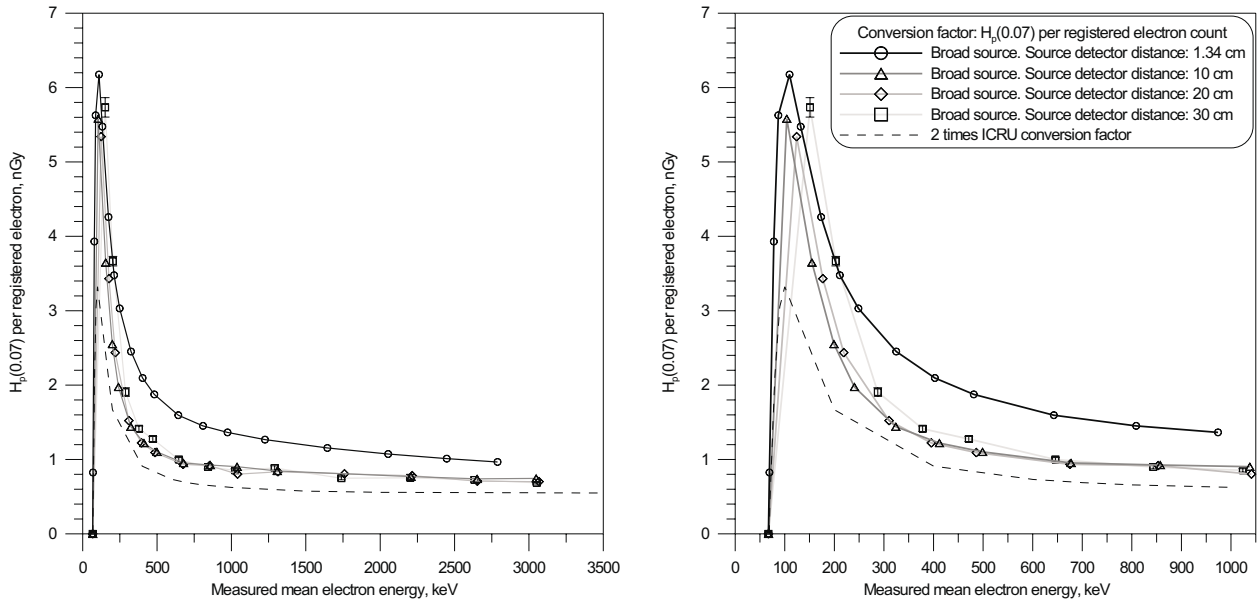

Figure 43. Calculated conversion factor, η_{det}, from measured electron counts by the spectrometer to $H_p(0.07)$ as a function of the measured mean energy (equation 17). The electron source is 5 cm in diameter and placed at various distances from the surface of detector 1. The figure to the right is identical to the one to the left, except for a change in the energy scale. By a dotted line two times the ICRU conversion factor ($H'(0.07)$) is shown.

11 Energy calibration of the spectrometer

In this chapter is 'channel number' frequently used instead of 'digital pulse height'.

11.1 Energy calibration of detector 1

Photon-absorption peaks from low energy gamma-rays are convenient to use for energy calibration of the detectors, since they have a symmetric shape around a well defined midpoint energy.[9] Table 14 shows the photon sources used for the energy calibration of detector 1 and 2.

Table 14. Photon sources used for energy calibration of detector 1 and 2.

Source	Photo-line [31] [keV]
Am-241	59.5
Co-57	122.1

The activity of the Co-57 source is so low, that it only can be used for detector 2, which has a larger volume and better noise characteristics than detector 1.

Detector 1 has only been calibrated using the photo-absorption peak from Am-241 (59.5 keV). A comparison between measured and Monte Carlo calculated endpoint energy of C-14, was not useful, since detector 1 is transparent to the high energy electrons of C-14.

Figure 44 shows the measurement of the 59.5 keV photo-absorption peak from Am-241. The peak is asymmetric due to noise cutoff at channel 16. The center of the peak is estimated to channel 21. The ratio between channel number and energy (keV) for detector 1 is set to 2.83.

It is indeed unsatisfactory to use only one point for an energy calibration, but no other means has been found. The energy calibration of detector 1 is therefore subject to an enlarged uncertainty.

11.2 Energy calibration of detector 2

Detector 2 is energy calibrated using photo-absorption peaks from Am-241 (59.5 keV) and Co-57 (122.1 keV), seen in Figure 45. An attempt to use the photo-absorption peak from from Eu-152 (40 keV) was unsuccessful, since the peak lies on the limit of the noise level of detector 2.

The photo-absorption peaks are located at channel number 16 (Am-241) and 33 (Co-57).

By linear interpolation the equation between channel number (i.e. digital pulse height, dp) and absorbed energy (keV) in detector 2 is found to be

$$E(dp) = 3.68[\text{keV/ch}]dp + 0.58[\text{keV}]$$

[9] If the detector is not totally depleted, an extra tail on the low energy side can occur, due to incomplete charge collection.

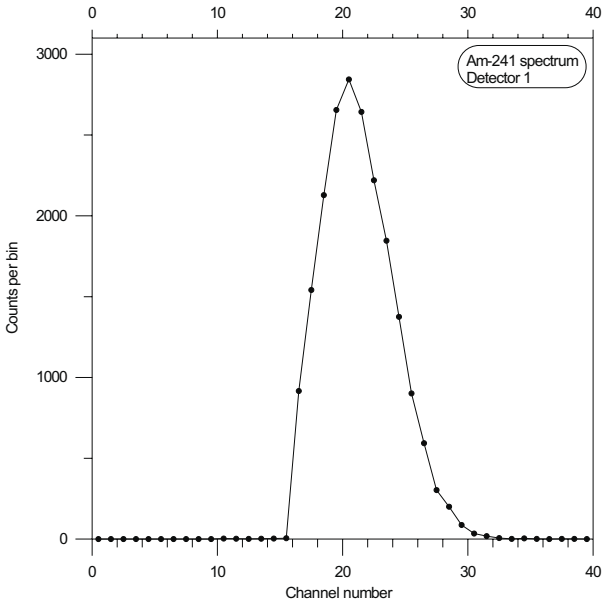

Figure 44. Energy calibration of detector 1. Photo-absorption of 59.5 keV photons from Am-241. Background spectrum is subtracted.

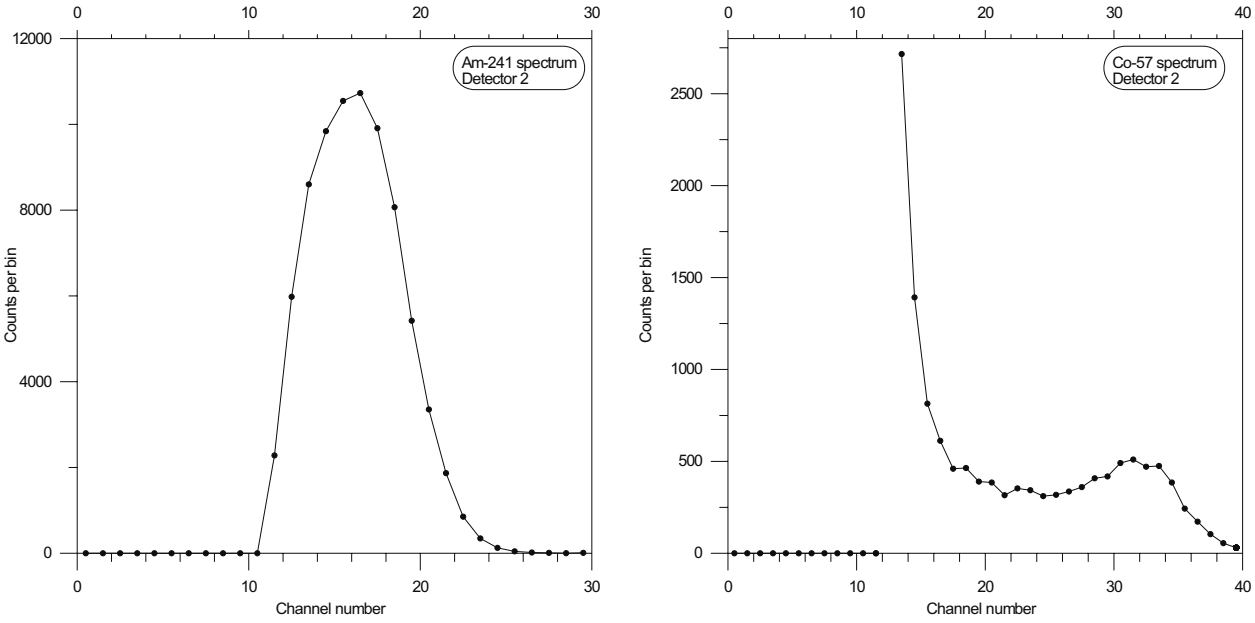

Figure 45. Energy calibration of detector 2. Left: Photo-absorption of 59.5 keV photons from Am-241. Right: Photo-absorption of 122.1 keV photons from Co-57. Background spectra are subtracted from both spectra.

11.3 Energy calibration of detector 3

Due to the high noise level of detector 3, photo-absorption peaks cannot be used to energy calibrate this detector. Instead Compton edges from photon sources listed in Table 15 are used.

Scattering of photons on electrons is called Compton scattering. The case of unpolarized radiation scattered on free electrons at rest, is described by the Klein-Nishina cross section, and the energy transfer to an electron integrated over all angles is given by [18]

Table 15. Photon sources used for energy calibration of detector 3.

Source	Photo-line [31] [keV]	Intensity [per disintegration]	Compton edge [keV]
Co-60	1173	0.999	963.2
	1332	1.000	1117.6
Cs-137	661.6	0.946	477.4
Bi-207	569.7	0.978	393.3
	1064	0.749	857.7
	1442	0.002	-
	1770	0.069	1547.0

$$\frac{_e\sigma}{dT} = \frac{\pi r_0^2}{m_0c^2}\frac{1}{\alpha^2}\left(2 + \left(\frac{T}{h\nu_0 - T}\right)^2\left(\frac{1}{\alpha^2} + \frac{h\nu_0 - T}{h\nu_0} - \frac{2}{\alpha}\frac{(h\nu_0 - T)}{T}\right)\right) \quad (19)$$

for $T \leq h\nu_0\frac{2\alpha}{1+2\alpha}$, otherwise zero.

where
r_0: The classical electron radius, $r_0 = e^2/m_0c^2 = 2.818$ fm
α: $h\nu_0/m_0c^2$
T: Kinetic energy of the electron
$h\nu_0$: Photon energy
m_0c^2: Electron rest mass

The energy where the cross section goes to zero, called the Compton edge, is only dependent on the photon energy, and is therefore suited for calibration purposes.

Doppler-broadening

The electrons can generally not be considered as free and stationary, and Doppler-broadening therefore influences the sharpness of the Compton edge. It can be shown that the Doppler-broadening goes approximately like $\sqrt{b/T}$, where b is the binding energy of the electron [18]. The Doppler-broadening has thus only a significant effect when the binding energy of the electron is of the order of the energy transferred to the electron in the Compton scattering process.

The binding energy of the K-shell electrons in silicon is about 1.8 keV, and the Doppler-broadening does not influence the sharpness of the Compton edge measured with silicon detectors. This has also been confirmed by Monte Carlo calculations.

Broadening by noise

When measuring a photo line with the thick third silicon detector, the Compton edge will not appear sharp due to the detector noise. The precise position of the Compton edge can therefore be hard to determine.

If the top of the Compton edge can be identified in the measurement, a possible way to find the position of the edge, is outlined in the following procedure based on a method proposed by U. Ankerhold and J. Böhm, PTB. A sketch is shown in Figure 46.

The Compton edge described by equation 19, is folded by Gaussian distributions with a FWHM equal to the detector noise. The position on the y-axis where the

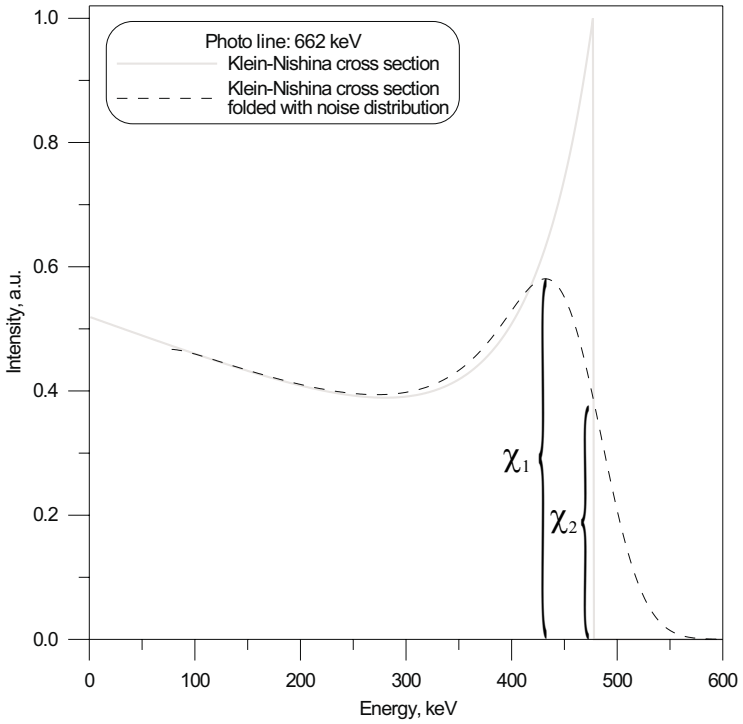

Figure 46. Calibration using Compton edge. A possible measured spectrum is marked by the dotted line. The position of the Compton edge is found as the point on the slope where the height is a certain fraction (χ_2/χ_1) of the total height of the measured Compton edge.

folded spectrum crosses the unfolded spectrum is determined, and expressed as a fraction of the total height of the Compton edge (χ_2/χ_1 in the figure). The fraction can be used as a guideline in a measured spectrum. The fraction χ_2/χ_1 depends on the FWHM of the noise distribution and the energy of the photo line or lines, but is typically in the range of 0.6 to 0.8.

The above procedure is not useful for calibration of detector 3, since the top of the Compton edge can not be unambiguous identified in the measurements, even though Monte Carlo calculations of photon beams incident on the detector assembly shows that a top should be detectable (Figure 47).

That the top is not present in the measurements, and that the measured spectra has a surplus of low energy electrons compared to the calculated spectra, is believed to be caused by scattered radiation from the rest of the detector probe which is not modeled in the Monte Carlo calculations. Measurements at PTB with a similar detector assembly, which is not encapsulated in a chassis, are in line with calculated spectra.

Instead the calibration of detector 3 is solely based on the position of the slopes of the Compton edges. The response of the detector assembly when irradiated with a broad beam of photons at normal incidence is calculated by Monte Carlo calculations for the sources listed in Table 15. The calculated response is folded with a Gaussian distribution with FWHM=130 keV to simulate the noise in detector 3. The measured spectrum is then scaled to get the best fit between the measured and calculated spectra. The measured spectrum is scaled under the assumption that the energy is directly proportional to the channel number, i.e. there is no offset.

Figure 47 shows the calculated response, the calculated response folded with the Gaussian distribution and the scaled measured spectra.

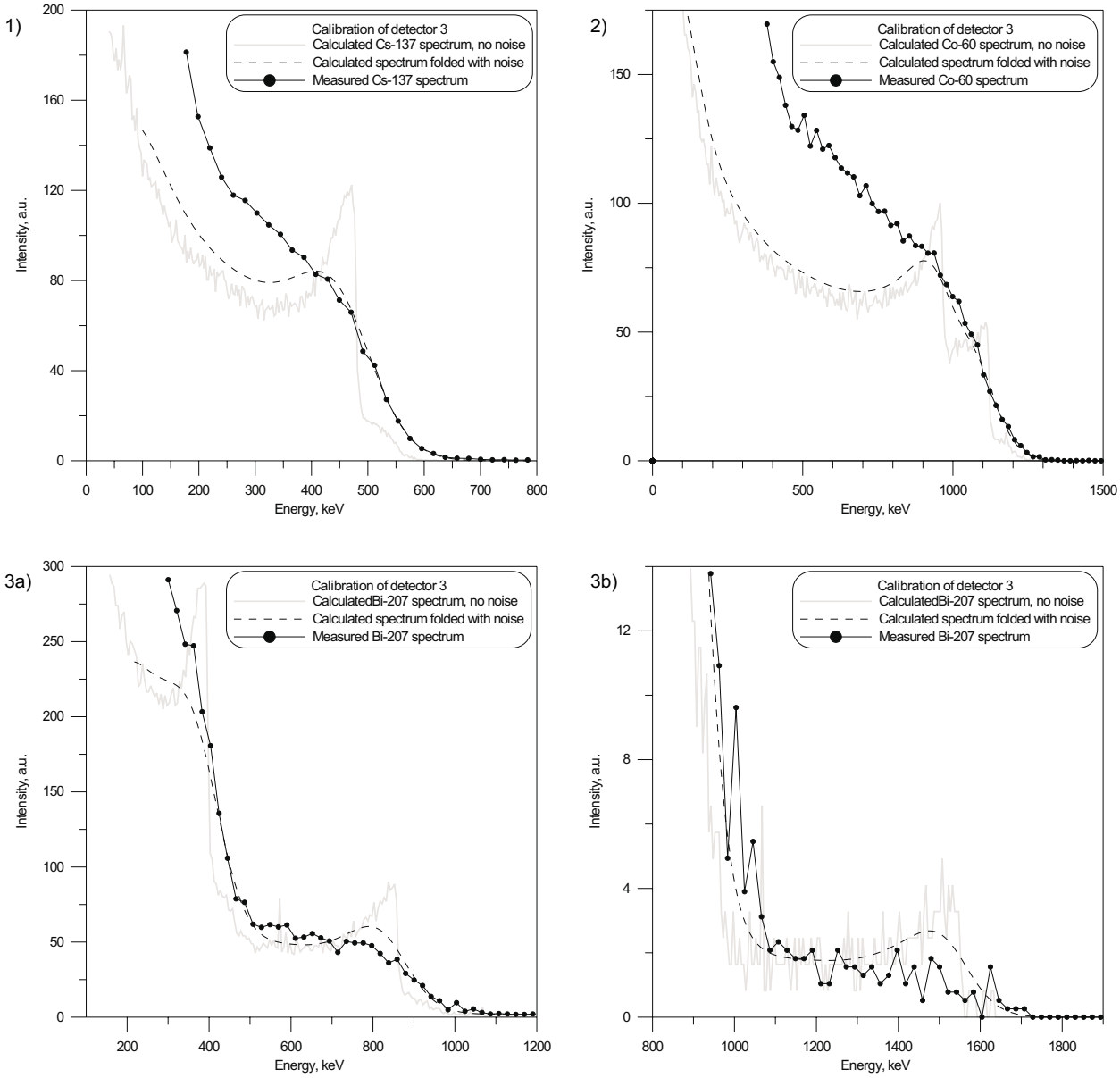

Figure 47. Energy calibration of detector 3. Gray line: Monte Carlo calculations of broad photon beams at normal incidence to the detector assembly. Note that the rest of the detector probe is not included in the calculations. Dotted line: The Monte Carlo calculation folded with a Gaussian distribution with FWHM=130 keV, simulating the noise contribution. Solid line: Measured energy spectrum scaled to fit the Monte Carlo calculation.
1) Cs-137 spectrum. 2) Co-60 spectrum. 3a) Bi-207 spectrum. 3b) Bi-207 spectrum zoomed in on the Compton edge at 1547 keV. Characteristics of the spectra are described in Table 15.

The ratio between channel number and energy (keV) is determined to 20.9 (Cs-137), 20.6 (Co-60) and 20.7 (Bi-207). The good agreement for the three Compton edges of the calculated and scaled Bi-207 spectrum is notable, since they cover a large span of energies (393-1547 keV).

The ratio between channel number and energy (keV) for detector 3 is taken as the average of the above mentioned values i.e. 20.73.

To summarize are the coefficients describing the relationships between digital pulse height and absorbed energy listed in Table 16.

Table 16. Coefficients of the first order polynomials used to describe the relationship between digital pulse heights and absorbed energy in the detectors

	1^{st} order coefficient	zero order coefficient
Detector 1	2.83	0.00
Detector 2	3.68	0.58
Detector 3	20.73	0.00

12 Measurements

This chapter examines some of the measurements done with the spectrometer. As mentioned earlier the measurements are limited in number, due to the enhanced noise levels. This means that questions like the dependence of the dose calculation on the source geometry has not been investigated, and that it has not been possible to do extra measurements to follow up on the data presented here.

12.1 Coincidence efficiency and photon rejection capability

The efficiency of the spectrometer for counting electrons and photons are investigated by measurements in pure beta and photon radiation fields. Ideally, a measurement in a pure electron radiation field should only lead to registration of coincidence pattern 4, 6 and 7 ([+−−], [++−] & [+++]), and for a measurement in a pure photon radiation field these patterns should not appear.

Table 17 indicates the percentage of counts registered as electrons (coincidence pattern 4, 6 and 7) and as photons (coincidence pattern 1, 2 and 5 ([−−+], [−+−] & [+−+]).

The first line in the table indicates that if particle thresholds are not used, the efficiency for counting electrons is clearly unacceptable. When irradiated by Sr-90/Y-90 only 12% of the counts are classified as electrons.

Table 17. Influence of particle thresholds on beta/photon indication. Noise threshold settings: 45/45/124 keV. Electrons defined as coincidence pattern 4,6 and 7. Photons defined as coincidence pattern 1,2 and 5.

Particle thresholds, Detector 1/2/3	Electrons (%)/Photons (%)			
	Pure beta radiation fields			Pure photon radiation field
Energy (keV)	Pm-147	Tl-204	Sr-90/Y-90	Co-60
45/45/124	91/9	30/38	12/29	1/97
17/34/124	98/2	67/16	45/11	2/96
17/17/124	98/2	67/16	46/7	2/93
9/26/83	99/1	82/8	68/5	3/95
9/19/83	99/1	82/8	69/4	3/93
9/8/83	99/1	82/8	69/3	9/70
6/26/83	99/1	87/6	75/4	3/95
6/19/83	99/1	87/6	76/3	4/95
3/26/83	99/1	90/5	80/3	4/95
3/19/83	99/1	90/5	82/2	5/93
3/8/83	99/1	90/4	82/2	15/70

By introducing the particle thresholds the efficiency is improved considerably, although a 100% efficiency is never reached. This is due to electrons bypassing the front detector and to interchange between coincidence patterns caused by noise. These phenomena were discussed in the chapter about Monte Carlo calculations of the spectrometer.

As the particle thresholds are lowered the share of counts registered as electrons in a pure photon radiation field is rising, which can be explained by increasing involvement by the noise.

As a compromise a particle threshold of 6/26/83 keV was chosen. With these settings the spectrometer will have an efficiency for counting electrons in a beta radiation field of at least 75% depending on the electron energy. The price paid for using particle thresholds is an increased registration of counts as electrons in a pure photon radiation field. With the chosen particle thresholds up to 3% of the counts measured from photon radiation fields are registered as electrons.

12.2 Measurement of electron spectra from pure beta emitters

C-14 source

The C-14 source is made of a circular PMMA disc 5 cm in diameter, 1 mm thick, with C-14 nuclei uniformly distributed throughout the PMMA. The source is mounted on a 11 mm thick PMMA disc. A measurement is done with the source placed 50 mm from the surface of detector 1.

Monte Carlo calculations of the energy spectrum from the C-14 source in 50 mm distance have been performed using EGS4 [8]. The calculated spectrum is folded with a Gaussian distribution with a FWHM of 14 keV, to simulate the noise of the front detector at the time the measurement of the C-14 source was done. The effect of the folding is in this case very small, and is basically just smoothing the calculated spectrum.

Figure 48 shows the calculated and measured beta energy spectra of the C-14 source in 50 mm distance from the source. The calculated spectrum is scaled to obtain parallel tails.

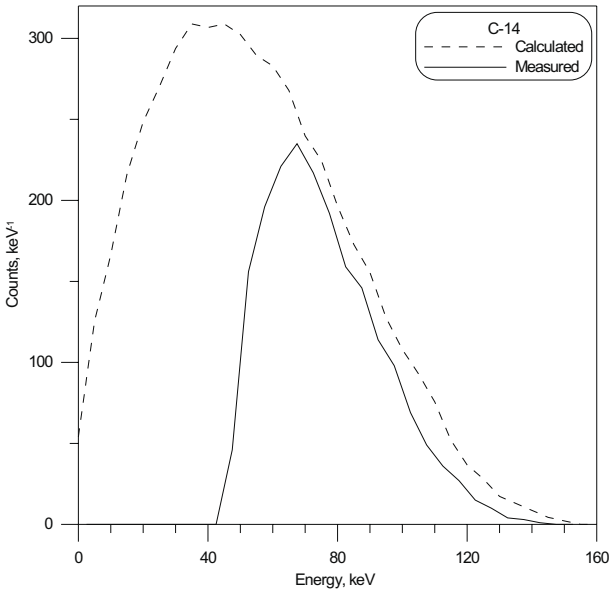

Figure 48. Calculated and measured beta energy spectra of a C-14 source in 50 mm distance from the source. The calculated spectrum [8] is scaled to obtain parallel tails. Background spectrum is subtracted.

From the Monte Carlo calculation the measurable endpoint energy is found to be 155 keV.

In the energy domain around 150 keV is the efficiency 93% (section 9.8, Figure 34), i.e. that the expected measured endpoint energy of the C-14 source is 144 keV, in good agreement with the measured value.

PTB/Buchler secondary standard sources. Pm-147, Tl-204, Sr-90/Y-90

Results from measurement of beta spectra from the PTB/Buchler secondary standard sources measured at a distance 10 cm from the sources without use of beam-flattening filter are shown in Figure 49.

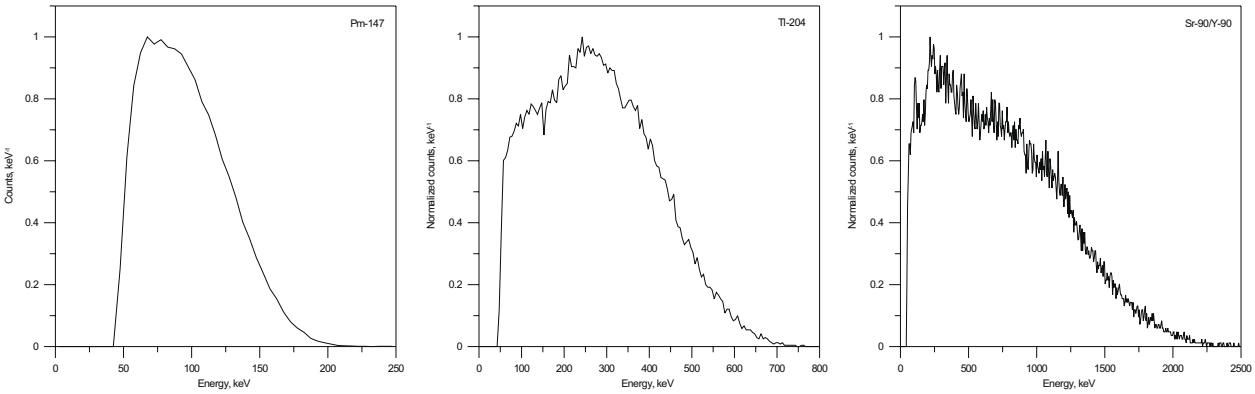

Figure 49. Beta energy spectra obtained for three PTB/Buchler secondary standard sources, measured at a distance of 10 cm from the sources without use of beam-flattening filter.
Left: Pm-147. Middle: Tl-204. Right: Sr-90/Y-90.

A dip can be seen at about 130 keV in the Sr-90/Y-90 energy spectrum. This is caused by the different noise thresholds for the three detectors.

PTB/Buchler secondary standard sources. Comparison with measurements made by PTB

Energy spectra of the Pm-147 and Tl-204 PTB/Buchler secondary standard sources has been measured with use of beam-flattening filter at PTB using a two element telescope spectrometer with silicon detectors of thickness 300 and 5000 μm, respectively.

Figure 50 shows a comparison between the PTB measurement and a similar measurement made with the Risø spectrometer. Both spectra are normalized to the maximum number of counts per bin.

There is agreement between the measurements made at PTB and at Risø, though the peak of the beta spectrum generally is measured at a lower energy with the Risø spectrometer compared to the PTB measurement.

An attempt to unfold the spectra has not been made, since the response functions of the PTB spectrometer is not known.

12.3 Measurement of electron and photon spectra in mixed beta/photon radiation fields

Bi-207 source

Bi-207 is a conversion electron source with electron energies shown in Table 18, and photon lines at 570, 1064 and 1770 keV (Compton edge energies: 393, 860 and 1547 keV).

The Bi-207 source is about 5 mm in diameter placed as a droplet between two 2.2 mg/cm^2 polyester foils.

Bi-207 is a prime example of how the coincidence/anti-coincidence principle works. Figure 51 shows energy spectra measured at 10 cm distance from the source.

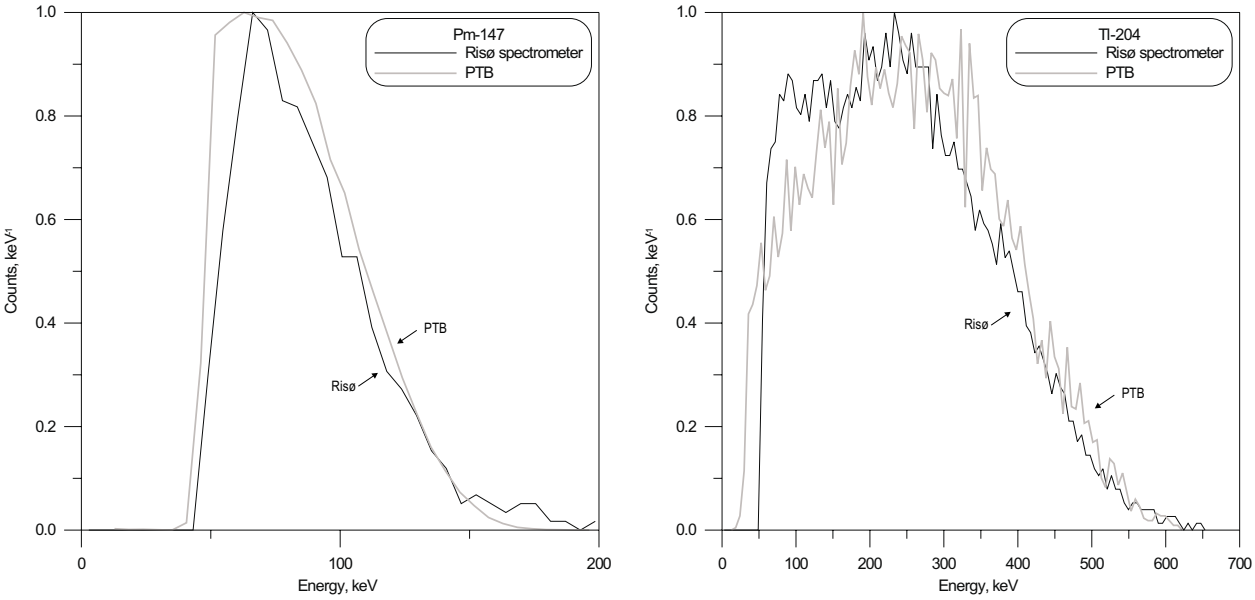

Figure 50. Comparison of beta energy spectra obtained for PTB/Buchler secondary standard sources, measured with use of beam-flattening filter at a distance of 20 cm from the Pm-147 source and 30 cm from the Tl-204 source.
Left: Pm-147. Right: Tl-204.

Table 18. Main conversion electrons lines for Bi-207. [31]

Line	Intensity [per disintegration]	Energy [keV]	Weighted average energy [keV]
$K\gamma_2$	$1.56 \cdot 10^{-2}$	481.7	491
$L_1\gamma_2$	$2.29 \cdot 10^{-3}$	553.8	
$K\gamma_4$	$7.26 \cdot 10^{-2}$	975.6	987
$L_1\gamma_4$	$1.42 \cdot 10^{-2}$	1048	

The upper row shows the energy distribution in the three detectors and the lower row how electron and photon spectra are obtained from these distributions using coincidence and anti-coincidence considerations.

It should be noted that the conversion electron lines are only resolved when the coincidence patterns for electrons are used. The position of the conversion electron peaks is in agreement with the weighted average energy listed in Table 18.

In the photon spectrum the Compton edges at 393 keV and 860 keV can easily be seen. The edges are also dominant in the energy spectrum from detector 3, but the presence of electrons are also evident.

Cs-137 source

Cs-137 has a beta-decay to Ba-137 (5.4%) with a maximum energy of 1.176 MeV and a beta-decay to Ba-137m (94.6%) with a maximum energy of 0.514 MeV. Ba-137m decays to Ba-137 and emits a gamma line at 662 keV (Compton edge: 477 keV), and conversion electrons with energies from 624 to 661 keV (weighted mean energy: 630 keV).

Figure 52 shows a Cs-137 spectrum measured at 100 mm distance from the source.

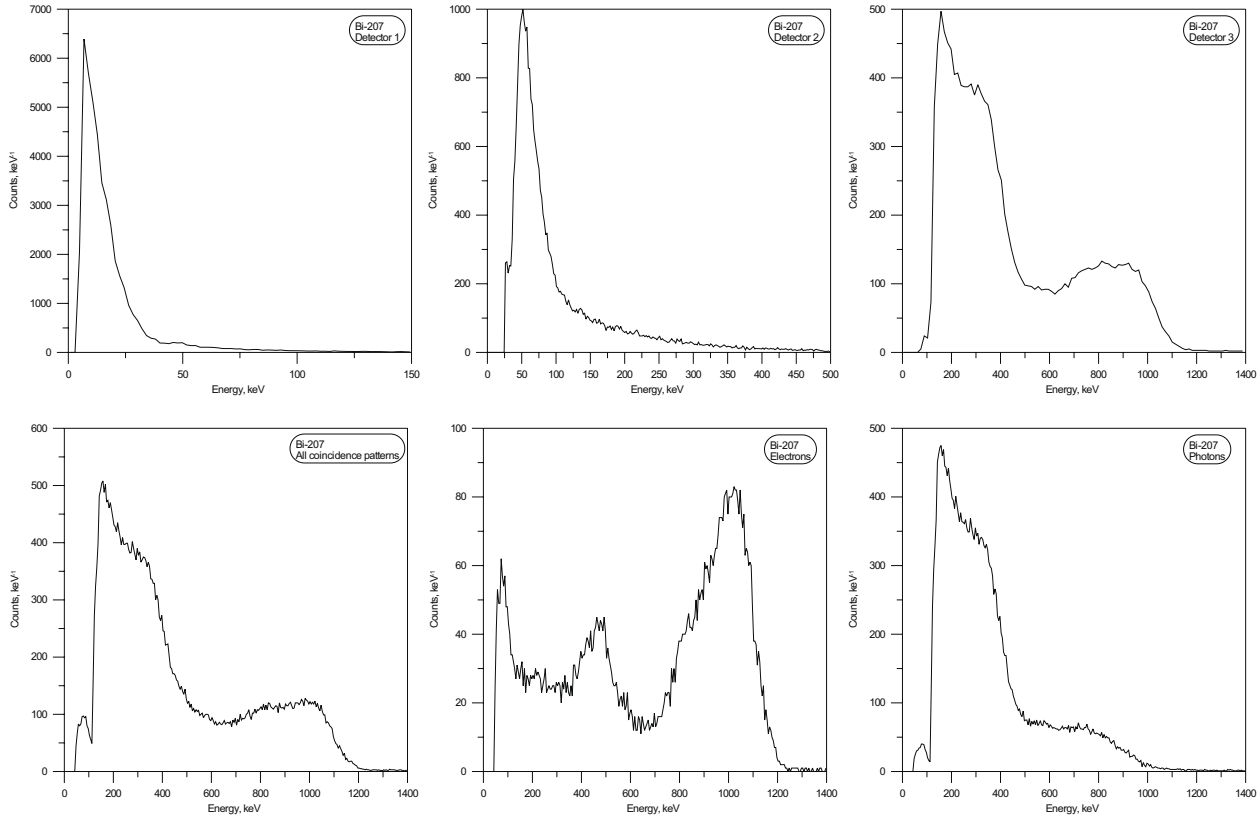

Figure 51. Energy spectra obtained from a Bi-207 source measured at 10 cm distance from the source.
Upper row: Energy spectra from detector 1, 2 and 3.
Lower row: Energy spectra obtained using coincidence/anti-coincidence considerations. Left: All coincidence patterns accepted. Middle: Coincidence pattern 4, 6 and 7 (electrons). Right: Coincidence pattern 1, 2 and 5 (photons).

Again the electron and photon spectra are clearly separated. The beta spectrum with a endpoint energy of 514 keV can be seen together with the conversion lines at 630 keV.

The different lower cutoff energy for the electron and photon spectra is explained by the fact that photons are mainly registered in detector 3 with a high noise level, while low energy electrons are registered in detector 1 and 2 with lower noise levels.

When the source is covered by 4 mm PMMA no electrons reaches the spectrometer, while the photon spectrum remains.

Co-60 source

Co-60 has two photo lines at 1173 keV and 1332 keV (Compton edge: 963 keV and 1118 keV). The two photon emissions follow a beta decay (99.9%) with a maximum energy of 319 keV.

Figure 53 shows Co-60 electron and photon spectra measured at 100 mm distance from the source.

The beta energy spectrum is resolved together with Compton edge around 1 MeV.

In the spectrum where the source is shielded by PMMA, it is notable that a residual electron spectrum is present. This spectrum is caused by photons registered in detector 3, but where the noise is above the particle threshold in detector 1 and 2, leading to a registration as an electron. The effect can also be seen in

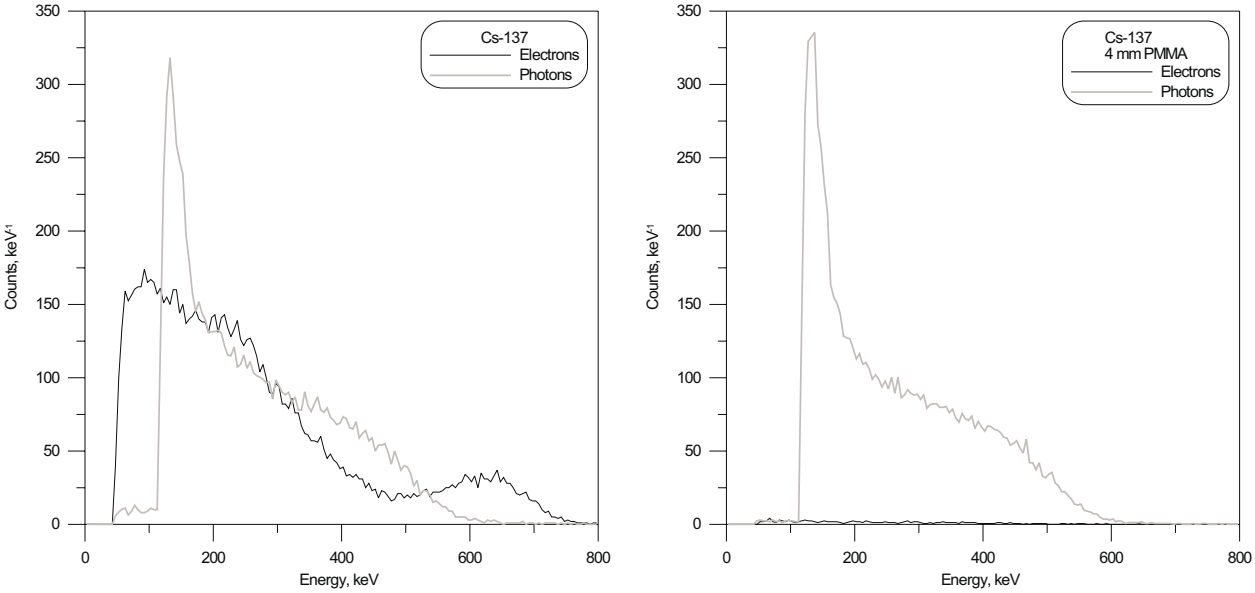

Figure 52. Left: Beta and photon energy spectra of a 10 mm diameter, 3.7 MBq Cs-137 source covered by a 1 mg/cm^2 mylar foil measured at 100 mm distance from the spectrometer.
Right: Same source but shielded by 4 mm PMMA.

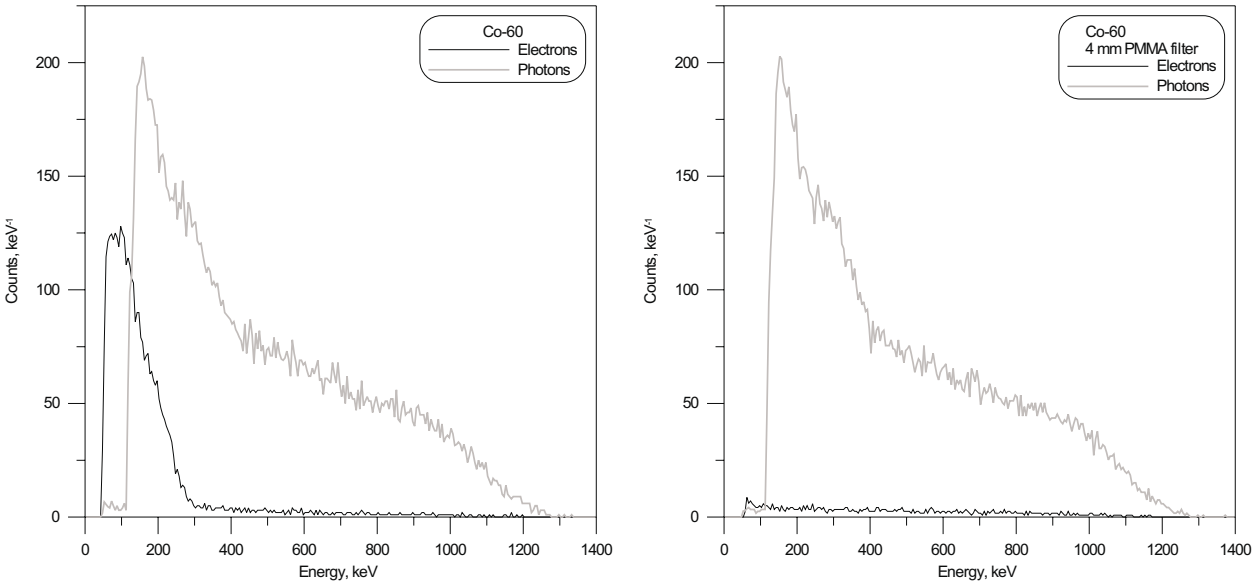

Figure 53. Left: Beta and photon energy spectra of a 10 mm diameter, 3.7 MBq Co-60 source covered by a 1 mg/cm^2 mylar foil measured at 100 mm distance from the spectrometer.
Right: Same source but shielded by 4 mm PMMA.

the electron energy spectrum when the source is uncovered, where the spectrum extends well above the beta endpoint energy.

12.4 Measurement of beta dose rates

The beta dose rate is calculated by folding the unnormalized measured electron spectrum by a suitable conversion factor divided by the total acquisition time

minus the dead-time.

The algorithm for calculation of skin dose works as follows:

Let $\overrightarrow{H}_{\overrightarrow{E_c}}$ be an array describing the conversion factor from measured electron counts (or electron fluence if the ICRU factor is used) to dose at 0.07 mm tissue for a discrete number of energies, $\overrightarrow{E_c}$.

Let H(E) be a function which for a given energy E by linear interpolation in $\overrightarrow{H}_{\overrightarrow{E_c}}$ finds a conversion factor value.

Let $\overrightarrow{N}(E)$ be the measured energy spectrum, where N is the number of counts for a given bin, and E is the midpoint energy of the bin. Assume there are n bins in the spectrum. The dose at 0.07 mm tissue is calculated by

$$H_{\mathrm{p}}(0.07) = \sum_{i=1}^{n} N(E_i) \cdot \mathrm{H}(E_i) \tag{20}$$

If the ICRU factor is used, the result should be multiplied by two since the area of detector 1 is 0.5 mm^2.

12.5 Calculation of $\dot{H}_p(0.07)$ using ICRU conversion coefficients

The spectrum from three PTB/Buchler secondary standard sources (Pm-147, Tl-204 and Sr-90/Y-90) is measured at a distance of 10 cm from the source without beam-flattening filter.

Table 19 shows a comparison between calculated beta dose rates using the conversion factor from electron fluence at normal incidence to $H'(0.07)$ described in ICRU report 56 (Table 5 on page 33) and dose rates measured with an extrapolation chamber. The uncertainty in the calculated dose is estimated to ±7%, mainly based on the uncertainty in the ICRU conversion factors.

Table 19. Results from beta dose rate measurement obtained by the Risø telescope spectrometer, using the ICRU conversion factor from electron fluence at normal incidence to $H'(0.07)$[35]. Beta radiation fields from the PTB/Buchler standard sources without beam-flattening filter at a distance of 10 cm. Noise threshold settings: 45/45/124 keV. Particle threshold settings: 6/26/83 keV. Electrons defined as coincidence pattern 4,6 and 7.

Source parameters		Electron measurement results				
Irradiation field	$\dot{H}_p(0.07)$ [mSv/h]	Count rate [c/s]	Fraction [%]	Avg. energy [keV]	$\dot{H}_p(0.07)$ [mSv/h]	Ratio†
Pm-147	14.5	996	99	96	6.5	0.45
Tl-204	7.9	1301	87	279	5.8	0.74
Sr-90/Y-90	95.6	30 372	75	742	74.7	0.78

† Calculated/true electron dose rate.

It is seen that there is a general under-response in the dose rate calculated by the spectrometer, in the case of Pm-147 by more than a factor of two.

That only a fraction of counts are registered as electrons (column 4 in the table) from exposure in a pure beta radiation field leads to underestimation of the dose rate. In a pure beta radiation field 100% of the registered counts are caused by electrons and a correction can easily be calculated. If this is done the calculated dose rate becomes 6.6 mSv/h (Tl-204) and 93.4 mSv/h (Sr-90/Y-90), and the ratio between calculated and true electron dose rate is 0.83 (Tl-204) and 0.98 (Sr-90/Y-90).

The fact that the electron radiation field is not normal to the tissue surface when the source is at 10 cm distance, may also contribute to the underestimation of the dose rate (Figure 38-40 on page 72-73).

12.6 Calculation of $\dot{H}_p(0.07)$ using spectrometer specific conversion coefficients

One way to optimize the dose calculation performed by the spectrometer would be to introduce a energy-correlated correction factor, as outlined in [22]. A more direct method is to use Monte Carlo calculations to obtain a conversion factor based on what the spectrometer actually measures, i.e. electron counts with a given energy, as presented in the previous chapter. The immediate advantage is, that the spectrometer efficiency, both regarding the measurement of electron planar fluence and electron energy, and the influence of detector noise, is directly incorporated in the conversion factor.

Table 20 shows a comparison between the true dose rate from the three PTB/-Buchler standard sources described above, and calculated dose using the spectrometer specific conversion factor for a point source 10 cm from the spectrometer. The calculated conversion factor is shown in Figure 42 on page 75 and in Table 27 on page 118. The stated uncertainties are estimates based on the uncertainty of the calculated conversion factor and of the calibration of the detectors (discussed below).

Table 20. Results from beta dose rate measurement obtained by the Risø telescope spectrometer, using the calculated conversion factor from electron counts measured by the spectrometer to $H_p(0.07)$ for a point source placed 10 cm from the surface of detector 1 (Figure 42 on page 75 and Table 27 on page 118). Beta radiation fields from the PTB/Buchler standard sources without beam-flattening filter at a distance of 10 cm. Noise threshold settings: 45/45/124 keV. Particle threshold settings: 6/26/83 keV. Electrons defined as coincidence pattern 4,6 and 7.

Source parameters		Electron measurement results	
Irradiation field	$\dot{H}_p(0.07)$ [mSv/h]	$\dot{H}_p(0.07)$ [mSv/h]	Ratio†
Pm-147	14.5	10.5±10%	0.72
Tl-204	7.9	7.6± 5%	0.97
Sr-90/Y-90	95.6	81.5± 7%	0.85

† Calculated/true electron dose rate.

There are marked improvements for the Pm-147 and Tl-204 sources and reasonable improvement for the Sr-90/Y-90 source. For low energy electrons the dose rate calculation is within 30% of the true dose rate, and the accuracy is better for higher energies. The uncertainty level is acceptable for routine survey purposes.

Keeping the high noise level of the detector assembly in mind, the results shown in Table 20 are indeed satisfactory. Not only does the results indicate that the spectrometer is capable of measuring beta dose rates in pure electron radiation fields with an acceptable precision, it also shows that the behaviour of the spectrometer is well understood, and that Monte Carlo calculations is a powerful tool in this regard.

With the obtained accuracy of the calculated skin dose it is also clear, that an unfolding of the measured energy distribution is unnecessary.

12.7 Dependence of skin dose calculation on the energy calibration of the detectors

Chapter 11 dealt with the energy calibration of the three detectors. Due to the high noise levels of the detectors only a few sources were usable for the determination of the coefficients in the first order polynomials describing the relationship between digital pulse height and absorbed energy in the detector elements.

To investigate whether an accurate calibration is decisive for the accuracy of the skin dose calculation, Table 21 shows the relative change in the calculated value of $\dot{H}_p(0.07)$, then the first order coefficient of the calibration polynomial is changed ±5% or ±10% (with reference to the values in Table 16 on page 81).

Table 21. Relative change in the calculated value of $\dot{H}_p(0.07)$ when the first order coefficient of the calibration polynomial is changed ±5% or ±10%. Noise threshold settings: 45/45/124 keV. Particle threshold settings: 6/26/83 keV. Electrons defined as coincidence pattern 4,6 and 7.

Change in 1st order coefficient			Relative change in calculated $\dot{H}_p(0.07)$		
Detector 1	Detector 2	Detector 3	Pm-147	Tl-204	Sr-90/Y-90
−5%			−6%	−4%	−7%
+5%			+5%	0%	0%
−10%			−12%	−5%	−7%
+10%			+9%	0%	0%
	−5%		0%	+2%	+2%
	+5%		−1%	−2%	−2%
	−10%		0%	+5%	+3%
	+10%		−1%	−4%	−3%
		−5%	0%	+1%	+4%
		+5%	0%	0%	−3%
		−10%	0%	+2%	+7%
		+10%	0%	−1%	−5%

It is seen that the calculation of $\dot{H}_p(0.07)$ is especially dependent on a correct calibration of detector 1. This is also the calibration with the biggest uncertainty since only one measurement is used to establish the calibration equation.

This illustrates again that it is very important that the thin front detector has a low noise level, partly to ensure a low interchange rate of coincidence patterns, partly to enable a precise energy calibration and thus an accurate determination of $\dot{H}_p(0.07)$.

The uncertainty in the first order coefficient for the calibration polynomial of detector 1 and 2 is estimated to be between 5 and 10%, and less than 5% for detector 3.

12.8 Calculation of $\dot{H}_p(0.07)$ in mixed beta/photon radiation fields

The capability of the spectrometer to calculate $\dot{H}_p(0.07)$ in mixed electron/photon radiation fields was tested by measurements in beta/photon beams from Co-60 and Cs-137 sources and also from Pm-147, Tl-204 and Sr-90/Y-90 (PTB/Buchler) placed in the radiation field from a $3.7 \cdot 10^{-7}$ Bq (1 mCi) Co-60 calibration source. The spectrometer specific conversion factor was used to calculate $\dot{H}_p(0.07)$.

In all measurements the beta source was placed at a distance of 10 cm from the spectrometer. The Co-60 and Cs-137 sources were prepared by evaporation of

solutions with approximately 3.7 MBq in 10 mm diameter, 1 mm deep depressions in a PMMA holder and using a 1 mg/cm^2 mylar cover. The dose rates from these sources were determined by use of thin LiF thermoluminescence detectors. Separation of beta and photon dose rates was made by use of a 4 mm PMMA filter. The results are shown in Table 22.

Table 22. Results from measurement in beta/photon and pure photon radiation fields. Noise threshold settings: 45/45/124 keV. Particle threshold settings: 6/26/83 keV. Electrons defined as coincidence pattern 4,6 and 7. Photons defined as coincidence pattern 1,2 and 5.

Irradiation field	Source parameters $\dot{H}_p(0.07)$		Count rate	Measurement results Fraction		Avg. energy	$\dot{H}_p(0.07)$	Ratio†
	Electrons [mSv/h]	Photons [mSv/h]	Total [c/s]	Elec. [%]	Phot. [%]	Electrons [keV]	Electrons [mSv/h]	
Co-60	3.5	0.095	1397	29	55	209	3.1	0.88
Cs-137	7.1	0.034	1341	50	46	253	5.6	0.78
Pm-147 + γ(Co-60)‡	14.5	2.39	16 445	8	91	204	13.2	0.91
Tl-204 + γ(Co-60)	7.9	2.39	16 129	9	90	320	10.7	1.36
Sr-90/Y-90 + γ(Co-60)	95.6	2.39	42 740	49	38	737	84.0	0.88
Co-60 + PMMA♯	0.0	0.095	1191	3	95	431	0.2	
Cs-137 + PMMA♯	0.0	0.034	1191	2	99	200	0.1	
γ(Co-60)	0.0	2.39	15 658	3	96	405	2.8	

‡ γ(Co-60): Photon radiation field from Co-60 calibration source † Calculated/true electron dose rate.
♯ PMMA: Electrons shielded by a 4 mm PMMA filter.

The last three rows in Table 22 shows that in a pure photon radiation field about 3% of the counts will be registered as electrons due to noise mainly in detector 1. This was also foreseen by Monte Carlo calculations (Figure 37 on page 69). The photons registered as electrons will be called 'false electrons'.

False electrons obviously affects the accuracy of the calculated beta dose rate, in the case of Tl-204 by 40%.

If the measured dose rate of 2.8 mSv/h due to false electrons is subtracted from the calculated dose for the PTB/Buchler standard sources, the dose rates becomes 10.4 mSv/h (Pm-147), 7.9 mSv/h (Tl-204) and 81.2 mSv/h (Sr-90/Y-90) in agreement with the values measured in a pure beta radiation field (Table 20).

Improved algorithm with reduced electron-contamination for calculation of $\dot{H}_p(0.07)$

The vast majority of false electrons is known to originate from photon events in detector 3 wrongly classified as electrons due to noise. The energy distribution of the false electrons is therefore similar to the energy distribution belonging to photons, but with 3% of the intensity.

A correction for the dose caused by the false electrons can be made, by calculating the skin dose based on the photon energy distribution, taking 3% of this value and subtract it from the skin dose calculated from the electron energy distribution. This is thus a dynamic correction, which is only dependent on the registered photons and not on the measured electron spectrum.

Table 23 shows the calculated skin dose at 0.07 mm tissue, for pure photon radiation fields, pure electron radiation fields and mixed photon/electron radiation fields, using the correction for false electrons.

The method is quite successful. The dose rate calculation of Pm-147, Tl-204 and Sr-90/Y-90 is independent to a few percent, whether or not proton radiation field from the Co-60 calibration source is present.

Table 23. Results from measurement in beta/photon radiation fields. Dose at 0.07 mm tissue is calculated using an improved algorithm correcting for false electrons. Noise threshold settings: 45/45/124 keV. Particle threshold settings: 6/26/83 keV. Electrons defined as coincidence pattern 4,6 and 7. Photons defined as coincidence pattern 1,2 and 5.

Irradiation field	Source parameters $\dot{H}_p(0.07)$ Electrons [mSv/h]	$\dot{H}_p(0.07)$ Photons [mSv/h]	Count rate Total [c/s]	Measurement results Fraction Elec. [%]	Fraction Phot. [%]	$\dot{H}_p(0.07)$ Electrons [mSv/h]	Ratio†
Co-60	3.5	0.095	1397	29	55	3.1	0.87
Co-60 + PMMA♯	0.0	0.095	1191	3	95	0.0	
Cs-137	7.1	0.034	1341	50	46	5.4	0.76
Cs-137 + PMMA	0.0	0.034	611	2	97	−0.1	
Pm-147	14.5	0.00	996	99	1	10.5	0.72
Pm-147 + γ(Co-60)‡	14.5	2.39	16 445	8	91	10.4	0.72
Tl-204	7.9	0.00	1301	87	6	7.6	0.97
Tl-204 + γ(Co-60)	7.9	2.39	16 129	9	90	7.9	1.00
Sr-90/Y-90	95.6	0.00	30 372	75	6	81.6	0.85
Sr-90/Y-90 + γ(Co-60)	95.6	2.39	42 740	49	38	81.4	0.85
γ(Co-60)	0.0	2.39	15 658	3	96	0.1	

♯ PMMA: Electrons shielded by a 4 mm PMMA filter. † Calculated/true electron dose rate.

‡ γ(Co-60): Photon radiation field from Co-60 calibration source.

The calculated dose for the Co-60 and Cs-137 source is unchanged compared to Table 22, because the photon count rate is low.

The false electrons caused by the photon radiation field from the Co-60 calibration source is reduced by a factor of 20.

That the calculated dose is insensible to photon radiation, makes the spectrometer suitable for routine survey purposes. Some work still has to be done, to improve the efficiency for low energy electrons.

12.9 Future perspectives

Throughout this report focus has been set on one question: what would the skin dose be, if a piece of tissue was placed at the point in space, where the spectrometer is located? Monte Carlo calculations, used to calculate a correspondence between what the spectrometer measures and skin dose, has proven to be a strong, successful and not least a flexible tool, and there is no reason why the Monte Carlo technique should be limited to the question above.

A future track could be to exploit the possibilities of uncoupling the location of dose calculation and the location of measurement, e.g. by asking the question: if the spectrometer measures the radiation field above a contaminated surface (lets say in a distance of a couple of centimeters), what would the skin dose be, if a piece of tissue came in touch with the surface? The point where the dose is calculated is thus moved a couple of centimeters in front the location where the measurement takes place.

Another question similar to this could be: if the spectrometer measures the radiation field above a contaminated tissue surface, what is the skin dose? In this case the point where the dose is calculated is moved to the other side of the source, from where the measurement takes place. There will probably be complications such as diffusion of radioactive material into the skin, which could render such a

measurement, but this just to illustrate, that a dose measurement not necessarily needs to take place where the detector is located.

There must of course be a correlation between the skin dose and the events registered by the spectrometer. The spectrometer needs for example to be fairly close to the contaminated surface, to register 70 keV electrons contributing to $H_{\mathrm{p}}(0.07)$, in the above mentioned example. But Monte Carlo calculations can be used to investigate if there is such a correlation, and one of the great advantages of the technique is, that it can be done even before the detection system is built.

Monte Carlo calculations have in this report been used to calculate electron dose rates at 0.07 mm tissue, but could as well have been used to calculate conversion coefficients for dose rates at other depths which are important for deterministic effects.

12.10 Summary

The coincidence/anti-coincidence principle works satisfactory, when the concept of particle thresholds is used, and the spectrometer can resolve both electron and photon spectra in mixed electron/photon radiation fields.

With noise thresholds of 45/45/124 keV and particle thresholds of 6/26/83 keV is the efficiency for counting electrons in a pure beta radiation field is between 75% and 99% depending on the electron energy. In a pure photon radiation field 3% of the counts are registered as electrons.

Energy distributions from a number of pure beta emitters (C-14, Pm-147, Tl-204, Sr-90/Y-90) and mixed beta/photon emitters (Bi-207, Cs-137, Co-60) has been measured. Key features like beta endpoint energies, conversion electron peaks and Compton edges can be identified in agreement with the physical properties of the radio-isotopes.

Calculation of $\dot{H}_p(0.07)$ has been performed for pure beta emitters (Pm-147, Tl-204, Sr-90/Y-90) using the ICRU conversion coefficients [35]. The ratio between calculated and true dose rate was 0.45 (Pm-147), 0.74 (Tl-204) and 0.78 (Sr-90/Y-90).

By using spectrometer specific conversion coefficients based on Monte Carlo calculations, the accuracy of the dose calculation is improved. The ratio between calculated and true dose rate is in this case 0.72 (Pm-147), 0.97 (Tl-204) and 0.85 (Sr-90/Y-90). Taking the high noise level of the spectrometer into consideration these results are indeed satisfactory.

Photons wrongly classified as electrons may contribute significantly to the calculated electron dose when the spectrometer is used in a mixed beta/photon radiation field. A correction factor based on the measured photon spectrum is used to make the calculated dose rate to a few percent independent of the presence of a photon radiation field.

13 Conclusion

Equipment

A portable telescope spectrometer with three silicon surface barrier detectors has been developed. The spectrometer is characterized by digital signal processing beginning at an early stage in the signal chain, ensuring a light and portable instrument. 255 channels are available for each of the three detectors. The spectrometer is controlled by a laptop computer, which also handles all subsequent data analysis, including calculation of electron dose rate at 0.07 mm tissue, $\dot{H}_p(0.07)$.

By use of coincidence/anti-coincidence considerations counts are classified as originating from electrons or photons.

Due to the large spacing between the digitized pulse heights, histograms of energy distributions based on more than one detector (e.g. electrons) are likely to split up in what looks like several curves. This artifact is prevented by adding white noise to the digitized pulse heights.

Poor intrinsic properties of the silicon surface barrier detectors, malfunctioning ohmic contacts and heat conduction paste seeping into the detector assembly, have resulted in enhanced noise levels. Noise thresholds of 45/45/124 keV makes the spectrometer unfit for use, because the absorbed energy in the front and the middle detector often will be below the noise threshold. The efficiency for registering electrons is less than 20% for electron energies above 400 keV.

To compensate for the loss of electrons, a second set of lower energy thresholds, named particle thresholds, are introduced, allowing a search for lost electrons into the noise area. With particle thresholds of 6/26/83 keV the efficiency for counting electrons in a pure beta radiation field is raised to at least 75% depending on the electron energy.

Monte Carlo calculations

Monte Carlo calculations of particle transport through the spectrometer have been performed to explain basic properties of the performance of the instrument.

Monte Carlo calculations show that even if the spectrometer was noise-free, more than 10% of the electrons entering the spectrometer would bypass the front detector in a 1 mm wide rim around the active area, and thus not be classified as electrons. An improved detector design will include a better shielding of the area around the front detector.

It is essential to include the detector noise in the simulation of the spectrometer and this is done by sampling from Gaussian distributions. There are in general good agreement between measurements and Monte Carlo calculations including noise.

The calculated ratio between measured and real mean electron energy is about 0.9 for electron energies above 250 keV, and approaching 1 for lower energies. That the ratio is rising for low electron energies is a phenomenon caused by detector noise.

The calculated ratio between measured and real electron planar fluence is in general about 0.75. For electron energies below 300 keV the ratio is falling rapidly due to absorption in material above the front detector.

The enhanced noise level of the front detector is identified to be the most important problem, for the performance of the spectrometer.

The noise originating from the front detector is:

- Rendering a reliable energy calibration of the detector. This is especially important because an accurate calculation of $H_{\mathrm{p}}(0.07)$ depends on a precise energy calibration of the front detector.

- Causing coincidence patterns originally interpreted as electrons to be classified as non-electrons.
- Causing photon events in the third detector to be interpreted as 'not defined' events, because noise is registered in the first detector. This problem is solved by reclassifying the event, where detector 1 and 3 are in anti-coincidence with detector 2, as a photon.
- Causing coincidence patterns originally interpreted as photons to be classified as electrons. In a pure photon radiation field 3% of the counts will be registered as electrons and this leads to an overestimation of the electron dose, when the spectrometer measures in a mixed electron/photon radiation field.

Monte Carlo calculations predict some dose dependence on the diameter of the source and on the distance between source to detector, but this is caused by differences in the electron angle distribution at tissue surface, and not by the design of the spectrometer.

Measurements

Energy distributions from a number of radioactive sources have been measured. The spectrometer can resolve both electron and photon spectra, and key features like beta endpoint energies, conversion electron peaks and Compton edges can be identified in agreement with the physical properties of the radio-isotopes.

Calculation of $\dot{H}_p(0.07)$ has been performed for pure beta emitters (Pm-147, Tl-204, Sr-90/Y-90) using the ICRU conversion coefficients from electron fluence at normal incidence to $H'(0.07)$ [35]. The ratio between calculated and true dose rate was 0.45 (Pm-147), 0.74 (Tl-204) and 0.78 (Sr-90/Y-90).

Monte Carlo calculations have been used to establish new conversion coefficients from measured electron counts to $\dot{H}_p(0.07)$. The conversion coefficients incorporate the influence of detector noise and the efficiency for measuring electron fluence and electron energy.

Using spectrometer specific conversion coefficients the ratio between calculated and true dose rate is 0.72 (Pm-147), 0.97 (Tl-204) and 0.85 (Sr-90/Y-90). The accuracy is notable, taking the high noise level of the spectrometer into consideration.

In mixed electron/photon fields a correction is needed to compensate for photons wrongly classified as electrons, but when the correction is used the calculated dose is to a few percent independent of the presence of a photon radiation field.

It is concluded that the spectrometer is suitable for routine survey purposes, though some work still has to be done, to improve the accuracy of the dose rate measurements for low energy electrons.

Acknowledgements

I would like to thank some of the people who have helped me during my Ph.D. project:

Poul Christensen, Risø. It has been a great privilege to have Poul as supervisor, both professionally and as a good friend. It characterizes everything Poul does that he is very responsible, thorough and knowledgeable, and at the same time open for new ideas and ways to do things. I have enjoyed our partnership very much and I will always benefit from the great knowledge Poul have shared with me.

Leif Sarholt, University of Copenhagen. I cannot think of a single administrative problem during my time as Ph.d. student, big or small, that Leif has not solved with an outstanding professionalism and readiness to help. I have valued the sincere interest Leif has had in the things I have been working at.

Anders Damkjær, Risø. If things have needed structure or clarification Anders has been the one I have turned to for advise, and I have never returned empty-handed from his office. Thanks for many fruitful discussions.

Henning E. Larsen, Risø. Much of of the credit for the success of this project belongs to Henning. He is the one who have designed and build all the electronics in the spectrometer. The early digital signal processing is a very complicated construction, and it has been a pleasure to know, that Henning was in charge for this part of the project.

I will always remember Henning for this quotation: If you don't have problems with noise, you're not pushing your instrument hard enough.

Dave Rogers and his crew, Ionizing Radiation Standards, National Research Council of Canada. It is needless to say, that this project could not have been carried out successfully, without the tremendous support I have received from IRS. Not only have all my Monte Carlo calculations been carried out on computers at IRS, but I also have had the privilege to have Dave as my supervisor during my stay in Ottawa. Many good advises and suggestions have saved me from many pitfalls during my introduction to the Monte Carlo method.

Thank you all for the wonderful time I had in Ottawa. I hope, we will meet again some day - and I will bring the doughnuts all right.

Our colleagues in the EU project: **Jürgen Böhm, Peter Ambrosi, Ulrike Ankerhold** and **Klaus Helmstädter**, Physikalisch-Technische Bundesanstalt (PTB). **Monty W. Charles** and **Philip Dareley**, School of Physics & Astronomy, University of Bermingham.

The development of the telescope spectrometer has been part of an EU project, and I would like to thank our partners for rewarding discussions during our meetings. I would especially like to thank the PTB group for many good and indispensable comments and for sharing with us there experiences with a similar telescope detector.

Jette Borg. Jette made some of the preliminary research for the design of the spectrometer, and during the last three years I have referred to this work many times. I would also like to thank Jette for taking good care of me in Ottawa. Thanks for all the fun we have had, and for always being such a wonderful colleague.

Table of variables and expressions

The table below lists some of the important variables and expressions/terms used in this report. Variables are printed in *italic*, expressions in `typewriter` and arguments used in EGS4/EGSnrc/DOSRZnrc in sans serif.

Variable/expression	Description
`//`	Noise thresholds are specified by the notation e.g. 45/45/124 keV, meaning the threshold for detector 1, 2 and 3 respectively. The notation is also used to specify FWHM values, leakage currents etc. for the detectors.
`[+++]`	Label to ease the interpretation of coincidence patterns, showing which detectors enters into a pattern. E.g. Coincidence pattern 6 has the label [++−] i.e. detector 1 and 2 is included but not detector 3.
α	Angle.
η_{det}	Spectrometer specific conversion factor from registered electron counts to dose at 0.07 mm tissue restricted to a 1 cm^2 disc [nGy/count].
η_{tissue}	Conversion factor from planar fluence at tissue surface to dose at 0.07 mm tissue restricted to a 1 cm^2 disc [nGy/electron].
σ^2	Variance.
τ_s	Shaping time. The length of the weighting function, 1.25μs.
A	The first order coefficient used in the first order polynomial used to convert from digital pulse height to absorbed energy in a given detector.
`ADC`	Analogue-to-digital converter.
AE	Lower energy threshold for production of knock-on electrons in units of total secondary particle energy, i.e. AE includes the rest-mass of the electron (511 keV).
AP	Lower energy threshold for production of bremsstrahlung in units of total secondary particle energy.
B	The zero order coefficient used in the first order polynomial used to convert from digital pulse height to absorbed energy in a given detector.
`CSDA`	Continuous-slowing-down-approximation.
`CP`	Abbreviation of 'coincidence pattern'.
`Coincidence pattern`	The detectors where a pulse height above the noise/particle threshold has been recorded interpreted in a binary fashion. See e.g. table 2 on page 15.

continued on next page

Variable/expression	Description
d	Depth in tissue [mm].
`Detector`	The depleted part of the silicon wafer.
`Detector 1`	The front detector.
`Detector 2`	The middle detector.
`Detector 3`	The back detector consisting of detector 3a and 3b.
`Detector 3a`	The upper detector of detector 3.
`Detector 3b`	The lower detector of detector 3.
`Detector assembly`	The three detectors and the copper housing holding the detectors.
`Digital pulse height`	The height of the weighting function illustrated in figure 10 on page 27.
`DOSRZ(nrc)`	User code for EGS4/EGSnrc designed for calculation of absorbed dose in cylindrical r-z geometries.
dp	Digital pulse height value. Range: $0 \ldots 255$ digital units.
E	Energy.
`Energy`	If not stated explicitly, 'energy' means the kinetic energy of a particle.
ECUT	Lower energy threshold for transport of electrons.
E_g	Band gab energy (solid state).
`EGS4/EGSnrc`	Electron Gamma Shower version 4, is a general purpose code providing subroutines used for Monte Carlo calculation of electron and photon transport.
`False electrons`	Notation used about the counts wrongly classified as electrons, when the spectrometer is irradiated by a pure photon radiation field.
`FIR filter`	Finite Impulse Response filter.
`FWHM`	Full-width-half-maximum.
`geometry`	The description of a setup (coordinates) used in a Monte Carlo calculation.
$H'(0.07)$	Directional dose equivalent at 0.07 mm tissue depth.
$H_{\mathrm{p}}(0.07)$	Personal dose equivalent at 0.07 mm tissue depth.
`history`	The complete transport of one initial particle and secondary particles created along its path, in a Monte Carlo calculation.
`IRS`	Ionizing Radiation Standards. National Research Council of Canada, Ottawa, Canada.
`Low energy tail`	The part of a detector response function which lies below the main peak. The low energy tail is caused by incomplete energy absorption due to back scattering, escape of bremsstrahlung etc.
m	Used as index.
n	Used as index.

continued on next page

Variable/expression	Description
NRC / NRCC	National Research Council of Canada, Ottawa, Canada.
Noise threshold	The upper limit of the noise flank, where the registered count rate due to noise is comparable to the count rate due to nuclear events.
Particle threshold	Lower energy limit used for registration of the coincidence patterns.
PCUT	Lower energy threshold for transport of photons.
PTB	Physikalisch Technische Bundesanstalt, Braunschweig, Germany.
r	Radius.
sd	Abbreviation of 'standard deviation'.
Shaping time	The length of the weighting function, 1.25μs.
Spectrometer	Risø telescope spectrometer.
Triplet	The digital pulse heights from the three detectors treated as a single object.
Weighting function	The analogue pulse from the detector is first sampled using an analogue-to-digital converter, and the digitized values are then manipulated to form a 'digital pulse' with a predefined shape. This digital pulse is called a weighting function (see figure 6 on page 23).
z	z direction in DOSRZ geometry, going from top to bottom.
Z	Number of protons in a nuclei.

A PEGS4 - Data preparation for EGSnrc

Table 24 gives the composition of the materials used in the EGSnrc Monte Carlo calculations. Except for MACOR the composition of the materials is from the PEGS4 distribution (i.e. ICRU report 37 [33]). MACOR is form [9].

Table 24. Composition of materials used in the EGSnrc Monte Carlo calculations.

Material ID	Density [g/cm^3]	Composition fraction by weight
Air-STP	$1.124 \cdot 10^{-3}$	C (0.000124), N (0.755267), O (0.231781), Ar (0.012827)
Au	19.3	Au (1.0)
C	2.00	C (1.0)
Cu	8.933	Cu (1.0)
Epoxy [a]	1.20	H (0.055491), C (0.755751), O (0.188758)
Ge (Ge-A)	5.36	Ge (1.0)
Macor [b]	2.52	B (0.021739), O (0.453026), F (0.04), Mg (0.10252), Al (0.08468), Si (0.21502), K (0.083015)
Mylar [c]	1.38	H (0.41959), C (0.625017), O (0.333025)
PMMA [d]	1.19	H (0.0806376), C (0.600558), O (0.319988)
Pt-Ir	21.56	Pt (0.1), Ir (0.9)
Si (Si-A)	2.33	Si (1.0)
Steel [e]	8.06	C (0.001), Si (0.007), Cr (0.18), Mn (0.01), Fe (0.712), Ni (0.09)
Teflon [f]	2.25	C (0.240183), F (0.759818)
Ti	4.54	Ti (1.0)
Tissue	1.0	H (0.101), C (0.111), N (0.026), O (0.762)

[a] Polycarbonate, makrolon, lexan.

[b] Machineable glass ceramics:
46% Si_2, 16% Al_2O_3, 17% MgO, 10% K_2O, 7% B_2O_3, 4% F.

[c] Polyethyleneterephthalate.

[d] Plexiglas.

[e] Stainless steel type 302.

[f] Polytetrafluorethylene.

IAPRIM (normalization of bremsstrahlung cross sections), IRYL (Rayleigh scattering data) and EPSTFL (ICRU report 37 density correction applied) has been turned on for all materials except for Pt-Ir where EPSTFL=0. GASP=1 (Gas pressure = 1 atm.) for AIR.

The lower threshold for secondary particle production was set to AE=521 keV (10 keV kinetic) for electrons and AP=1 keV for photons. The upper energy bound for the cross section data was set to 4.0 MeV kinetic energy for both electrons and photons (UE=4.522 MeV, UP=4.0 MeV).

Two variants of silicon (Si & Si-A) and germanium (Ge & Ge-A) has been

defined. They both have the same composition, but enables the program which transform the geometry from a spreadsheet to DOSRZnrc-rts input commands, to distinguish between active parts of the detectors (Si-A and Ge-A) and inactive parts (Si and Ge).

B Modifications to DOSRZnrc

As default DOSRZnrc can only specify the absorbed energy distribution for one set of regions. Dose - i.e. energy absorbed in a region divided by the mass of the region - can be calculated for one coherent disc or a 'square' torus.

To make the DOSRZnrc useful for the calculations of the telescope spectrometer, two new functions has been added to the code:

- Three sets of regions can be defined as detector 1, 2 and 3 respectively. For each history where energy has been absorbed in at least one of the detector volumes, the absorbed energy energy in the three detector volumes can be written to a file. It is therefore possible to identify the coincidence pattern in a later analysis. It is also possible to write the history number (i.e. the number of the initial particle) to the file at the same time.
- Then a particle is crossing the $z = 0.0$ plane in the geometry, within a specified distance (r) from the central axis, the particle type, kinetic energy, distance and angle to the central axis and history number can be written to a file. Which way the particle is crossing the plane can be determined by the angle, and multiple crossing can be revealed by the history number.

The modified code is called 'DOSRZnrc-rts' and the new input options are listed in Table 25. A printout of the source code changes is available below.

Crossing the $z = 0.0$ surface

The way the DOSRZnrc-rts code detects if a particle is crossing the $z = 0.0$ surface is by checking whether the sign of the z variable in the particles position parameters will change in the next step. The particle parameters are thus not read at the $z = 0.0$ surface, but at the place where the last step before the crossing starts.

A test was performed by calculating 100 keV and 2000 keV electrons going though 10 cm air before hitting a tissue surface at $z = 0.0$ cm. 509 and 1054 electrons were registered in the 100 keV and 2000 keV case respectively. The mean value of the electron z variable at the beginning of the crossing step was -0.0077 cm and -0.028 cm. The values read out by the DORSZnrc-rts program is thus very close to the actual values at the $z = 0.0$ surface.

B.1 Source code changes

Table 25 describes the new options available in DOSRZnrc-rts. The changes made in the source code of DOSRZnrc is listed below. The source code is written i Mortran, a modified version of Fortran, which is compiled into Fortran. The changes was made to the version 26 (SID 1.9 26 Feb 1999) of the DOSRZnrc code. The line numbers mentioned should only be used as a guideline; a search on the appropriate text string should be used instead.

The SWAP routines listed are used to swap the byte order of numbers written to a file, since UNIX and Windows uses the opposite byte order.

Table 25. New options in the DOSRZnrc-rts inputfile

Option	Description
In the 'Monte Carlo inputs' section:	
MAX COUNTS	Number of counts registered by the detector. The calculation is terminated if MAX COUNTS or NUMBER OF HISTORIES has been reached - whatever happens first.
COUNT RADIUS [cm]	Particle information can be written to a file using the IFULL option then the particle crosses $z = 0.0$ and its distance to the center axis is equal or less than COUNT RADIUS. The registration of coincidence patterns is not affected by this parameter.
IFULL= triplets	A binary output file (`*.calib`) will be made. Each time energy is absorbed in at least one detector a 3-tuple will be written containing the absorbed energy in detector 1, detector 2 and detector 3.
IFULL= cross0	A binary output file (`*.cross`) will be made. Each time a particle crosses $z = 0.0$ with $r <$ COUNT RADIUS a 5-tuple will be written. The 5-tuple contains the history number, the particle type, the distance to the central axis, the particle kinetic energy and the angle to the central axis.
IFULL= trip+cross0	Two binary output files (`*.cross` and `*.htrip`) will be made. The later file contains 4-tuples with the history number and the absorbed energy in detector 1, detector 2 and detector 3, and is written each time radiant energy is absorbed in at least one detector.
In the 'pulse height distribution input' section: If IFULL= triplets or IFULL= trip+cross0	
REGION OF DETECTOR 1	Comma separated string of region numbers for detector 1.
REGION OF DETECTOR 2	Comma separated string of region numbers for detector 2.
REGION OF DETECTOR 3	Comma separated string of region numbers for detector 3.

```
"FILE: egsnrc.macros
(in definition of $MXALINP line 2538)
REPLACE {$MXALINP} WITH {7};     "To make max IFULL=7"

"FILE: dosrznrc.environment
(Add text at about line 36)
    if (-e $inputfile.calib)    \rm $inputfile.calib
    ln -s $inputfile.calib      fort.47 # Triplet binary listing file
    if (-e $inputfile.cross)    \rm $inputfile.cross
    ln -s $inputfile.cross      fort.48 # Cross Z=0 binary listing file
    if (-e $inputfile.htrip)    \rm $inputfile.htrip
    ln -s $inputfile.htrip      fort.49 # hstry,triblet binary listing file

"FILE: dosrznrc.mortran
(in definition of $MXMED line 1085)
REPLACE {$MXMED} WITH {17}         "MAX # OF MEDIA"

(in comman/score/ section line 1589)
(in E-section)
EDET(4),EDETSR(4),
MXCOUNT,
COUNTR,
(last in statement before })
REAL*8 EDET;
REAL*4 EDETSR;
INTEGER*4 TEMPINT,TEMPINT2;
INTEGER*4 SWAPI,SWAPII;
INTEGER SWAPDUMMY1,SWAPDUMMY2,SWAPYES;
REAL*4 SWAPA;
EQUIVALENCE(SWAPA,SWAPI);

(in "data declarations" line 1843)
REPLACE {$NVALUE} WITH {550}  "max number of values per input"

(in "temporary variables for parallel post-processing" line 1872.
 Would proberly be better in commin/sore)
INTEGER ITMPVAR1, ITMPVAR2, ITMPVAR3, ITMPVAR4, LOFREC5,LOFREC6,LOFREC7;

(just above "DO IBATCH=1,$STAT[" line 2245)
IF(IFULL.EQ.5) [
OPEN(UNIT=47,file='fort.47',FORM='UNFORMATTED',ACCESS='DIRECT',RECL=12);
]
IF(IFULL.EQ.6) [
OPEN(UNIT=48,file='fort.48',FORM='UNFORMATTED',ACCESS='DIRECT',RECL=20);
]
IF(IFULL.EQ.7) [
OPEN(UNIT=48,file='fort.48',FORM='UNFORMATTED',ACCESS='DIRECT',RECL=20);
OPEN(UNIT=49,file='fort.49',FORM='UNFORMATTED',ACCESS='DIRECT',RECL=16);
]
LOFREC5=0;
LOFREC6=0;
LOFREC7=0;

(just below "PHENER = 0.0;" line 2354)
           /EDET(2),EDET(3),EDET(4)/=0.0;  "ZERO TO KEEP TRACK OF ENERGY"
                                           "DEPOSITED IN TRIPLET REGIONS"

(below "call shower", after "ifull.eq.2" statement. line 2378)
    IF(((IFULL.EQ.5).OR.(IFULL.EQ.7)).AND.((EDET(2)+EDET(3)+EDET(4)).GT.0.0))[
                LOFREC5=LOFREC5+1;
                EDETSR(2)=EDET(2)*1000.0;
                EDETSR(3)=EDET(3)*1000.0;
                EDETSR(4)=EDET(4)*1000.0;
                "WRITE(*,'(I12,3F10.2)')IFULL,EDETSR(2),EDETSR(3),EDETSR(4);"
                "Swap bytes to make single reals readable for Windows (LabView)"
                "Byteswap: 4->1, 3->2, 2->3, 1->4"
                SWAPA=EDETSR(2);
                SWAPII=0;
                SWAPDUMMY1=SWAPI;
                SWAPDUMMY2=SWAPII;
                CALL MVBITS(SWAPDUMMY1, 24, 8, SWAPDUMMY2, 0);
                CALL MVBITS(SWAPDUMMY1, 16, 8, SWAPDUMMY2, 8);
                CALL MVBITS(SWAPDUMMY1, 8, 8, SWAPDUMMY2, 16);
                CALL MVBITS(SWAPDUMMY1, 0,8,SWAPDUMMY2, 24);
                SWAPI=SWAPDUMMY2;
                EDETSR(2)=SWAPA;
                SWAPA=EDETSR(3);
                SWAPII=0;
                SWAPDUMMY1=SWAPI;
                SWAPDUMMY2=SWAPII;
                CALL MVBITS(SWAPDUMMY1, 24, 8, SWAPDUMMY2, 0);
                CALL MVBITS(SWAPDUMMY1, 16, 8, SWAPDUMMY2, 8);
                CALL MVBITS(SWAPDUMMY1, 8, 8, SWAPDUMMY2, 16);
                CALL MVBITS(SWAPDUMMY1, 0,8,SWAPDUMMY2, 24);
                SWAPI=SWAPDUMMY2;
```

```
                EDETSR(3)=SWAPA;
                SWAPA=EDETSR(4);
                SWAPII=0;
                SWAPDUMMY1=SWAPI;
                SWAPDUMMY2=SWAPII;
                CALL MVBITS(SWAPDUMMY1, 24, 8, SWAPDUMMY2, 0);
                CALL MVBITS(SWAPDUMMY1, 16, 8, SWAPDUMMY2, 8);
                CALL MVBITS(SWAPDUMMY1, 8, 8, SWAPDUMMY2, 16);
                CALL MVBITS(SWAPDUMMY1, 0,8,SWAPDUMMY2, 24);
                SWAPI=SWAPDUMMY2;
                EDETSR(4)=SWAPA;
                "End of byteswap. Now write to (binary) file"
                IF (IFULL.EQ.7)[
                "do also write ihstry"
                  LOFREC7=LOFREC7+1;
                  SWAPI=IHSTRY;
                  SWAPII=0;
                  SWAPDUMMY1=SWAPI;
                  SWAPDUMMY2=SWAPII;
                  CALL MVBITS(SWAPDUMMY1, 24, 8, SWAPDUMMY2, 0);
                  CALL MVBITS(SWAPDUMMY1, 16, 8, SWAPDUMMY2, 8);
                  CALL MVBITS(SWAPDUMMY1, 8, 8, SWAPDUMMY2, 16);
                  CALL MVBITS(SWAPDUMMY1, 0,8,SWAPDUMMY2, 24);
                  SWAPI=SWAPDUMMY2;
                  TEMPINT=SWAPI;
                  WRITE(49,REC=LOFREC7)TEMPINT,EDETSR(2),EDETSR(3),EDETSR(4);
                  IF (LOFREC7.GE.MXCOUNT)[
                    close(48);close(49);
                    WRITE(*,'(A1)')' ';
                    WRITE(*,'(A8,I12)')'IHSTRY: ',IHSTRY;
                    GO TO :END-SIM:;
                  ] "Reached max counts"
                ]
                ELSE
                [
                  WRITE(47,REC=LOFREC5)EDETSR(2),EDETSR(3),EDETSR(4);
                ]
            ] "end of IFULL=5 or 7 and write triplet blok"

(just above ":END-SIM:;" line 2527)
IF(IFULL.EQ.5) [close(47);]
IF(IFULL.EQ.6) [close(48);]
IF(IFULL.EQ.7) [close(48);close(49);]

(one statement below "END OF IFULL=1" line 3138)
IF(((IFULL.EQ.5).OR.(IFULL.EQ.7)).AND.(IPHR(IRL).NE.0))[
    "WE ARE IN THE TRIPLET SENSITIVE REGION AND WE MUST SCORE THE ENERGY "
    "DEPOSITED. USE THE WEIGHT LATER RIGHT AWAY"
    EDET(IPHR(IRL))=EDET(IPHR(IRL))+WT(NP)*EDEP;
] "end IFULL=5 or 7 and IPHR<>0 block"
IF((IFULL.GE.6).AND.(SIGN(1,Z(NP)).NE.(SIGN(1,(Z(NP)+USTEP*W(NP))))))[
    "WE ARE CROSSING THE Z=0 BOUNDARY "
    EDETSR(4)=SQRT(X(NP)*X(NP)+Y(NP)*Y(NP));    "radius"
    IF (EDETSR(4).LE.COUNTR)[                   "r<=COUNTR"
      EDETSR(2)=E(NP)-RM;                       "particle kin. energy"
      EDETSR(3)=ACOS(W(NP))*57.29577951;        "angle to the z-axis in deg."
        "a bit of a mess, but saves declaration of variables"
      SWAPI=IHSTRY;
      SWAPII=0;
      SWAPDUMMY1=SWAPI;
      SWAPDUMMY2=SWAPII;
      CALL MVBITS(SWAPDUMMY1, 24, 8, SWAPDUMMY2, 0);
      CALL MVBITS(SWAPDUMMY1, 16, 8, SWAPDUMMY2, 8);
      CALL MVBITS(SWAPDUMMY1, 8, 8, SWAPDUMMY2, 16);
      CALL MVBITS(SWAPDUMMY1, 0,8,SWAPDUMMY2, 24);
      SWAPI=SWAPDUMMY2;
      TEMPINT=SWAPI;
      TEMPINT2=IQ(NP);
      SWAPI=TEMPINT2;
      SWAPII=0;
      SWAPDUMMY1=SWAPI;
      SWAPDUMMY2=SWAPII;
      CALL MVBITS(SWAPDUMMY1, 24, 8, SWAPDUMMY2, 0);
      CALL MVBITS(SWAPDUMMY1, 16, 8, SWAPDUMMY2, 8);
      CALL MVBITS(SWAPDUMMY1, 8, 8, SWAPDUMMY2, 16);
      CALL MVBITS(SWAPDUMMY1, 0,8,SWAPDUMMY2, 24);
      SWAPI=SWAPDUMMY2;
      TEMPINT2=SWAPI;
      SWAPA=EDETSR(2);
      SWAPII=0;
      SWAPDUMMY1=SWAPI;
      SWAPDUMMY2=SWAPII;
      CALL MVBITS(SWAPDUMMY1, 24, 8, SWAPDUMMY2, 0);
      CALL MVBITS(SWAPDUMMY1, 16, 8, SWAPDUMMY2, 8);
      CALL MVBITS(SWAPDUMMY1, 8, 8, SWAPDUMMY2, 16);
      CALL MVBITS(SWAPDUMMY1, 0,8,SWAPDUMMY2, 24);
```

```
      SWAPI=SWAPDUMMY2;
      EDETSR(2)=SWAPA;
      SWAPA=EDETSR(3);
      SWAPII=0;
      SWAPDUMMY1=SWAPI;
      SWAPDUMMY2=SWAPII;
      CALL MVBITS(SWAPDUMMY1, 24, 8, SWAPDUMMY2, 0);
      CALL MVBITS(SWAPDUMMY1, 16, 8, SWAPDUMMY2, 8);
      CALL MVBITS(SWAPDUMMY1, 8, 8, SWAPDUMMY2, 16);
      CALL MVBITS(SWAPDUMMY1, 0,8,SWAPDUMMY2, 24);
      SWAPI=SWAPDUMMY2;
      EDETSR(3)=SWAPA;
      SWAPA=EDETSR(4);
      SWAPII=0;
      SWAPDUMMY1=SWAPI;
      SWAPDUMMY2=SWAPII;
      CALL MVBITS(SWAPDUMMY1, 24, 8, SWAPDUMMY2, 0);
      CALL MVBITS(SWAPDUMMY1, 16, 8, SWAPDUMMY2, 8);
      CALL MVBITS(SWAPDUMMY1, 8, 8, SWAPDUMMY2, 16);
      CALL MVBITS(SWAPDUMMY1, 0,8,SWAPDUMMY2, 24);
      SWAPI=SWAPDUMMY2;
      EDETSR(4)=SWAPA;
      LOFREC6=LOFREC6+1;
      WRITE(48,REC=LOFREC6)TEMPINT,TEMPINT2,EDETSR(2),EDETSR(3),EDETSR(4);
    ]  "end of r<=COUNTR blok"
] "end of IFULL>=6 i.e. crossing Z=0 block"

(just above "Variables used to point to the inputs" line 3633)
INTEGER REG_D1,REG_D2,REG_D3,MAXCOUNT;  "triplet region input, max counts"
REAL COUNTR;                            "count radius in cm"

(in "M-C Input" line 3659)
        NUM_MXCOUNT,       "Max counts and count radius"
        NUM_COUNTR,
        NUM_REG_D1,        "Triplets regions"
        NUM_REG_D2,
        NUM_REG_D3,

(in the IFULL input section - "VALUES_SOUGHT(IVAL)='IFULL';" line 3902)
IVAL=IVAL+1;
NUM_MXCOUNT=IVAL;
VALUES_SOUGHT(IVAL)='MAX COUNTS';
NVALUE(IVAL)=1;
TYPE(IVAL)=1;
VALUE_MIN(IVAL)=0;
VALUE_MAX(IVAL)=999999999;
DEFAULT(IVAL)=200000;

IVAL=IVAL+1;
NUM_COUNTR=IVAL;
VALUES_SOUGHT(IVAL)='COUNT RADIUS';
NVALUE(IVAL)=1;
TYPE(IVAL)=1;
VALUE_MIN(IVAL)=0.001;
VALUE_MAX(IVAL)=999999999;
DEFAULT(IVAL)=999999;

IVAL=IVAL+1;
NUM_IFULL=IVAL;
VALUES_SOUGHT(IVAL)='IFULL';
NVALUE(IVAL)=1;
TYPE(IVAL)=3;
ALLOWED_INPUTS(IVAL,0)='DOSE AND STOPPERS';
ALLOWED_INPUTS(IVAL,1)='ENTRANCE REGIONS';
ALLOWED_INPUTS(IVAL,2)='PULSE HEIGHT DISTRIBUTION';
ALLOWED_INPUTS(IVAL,3)='SCATTER FRACTION';
ALLOWED_INPUTS(IVAL,4)='OFMET Fricke';  "To score quantities of interest"
                                        "for the OFMET Fricke experiments"
                                        "e.g. brems loss, backscatter loss etc"
ALLOWED_INPUTS(IVAL,5)='TRIPLETS';
ALLOWED_INPUTS(IVAL,6)='CROSS0';
ALLOWED_INPUTS(IVAL,7)='TRIP+CROSS0';

(in "* CARD MC1 *" line 3957)
MXCOUNT=VALUE(NUM_MXCOUNT,1);
COUNTR=VALUE(NUM_COUNTR,1);

(above "IF (ERROR_FLAG=1)" line 3970)
OUTPUT NCASE,IXXIN,JXXIN,TIMMAX,MXCOUNT,COUNTR,IFULL,STATLM,IKERMA;
    ( / ' # OF HISTORIES:',T60,I12/
    ' 1ST INITIAL RANDOM NUMBER SEED:',T60,I12/
    ' 2ND INITIAL RANDOM NUMBER SEED:',T60,I12/
    ' MAXIMUM CPU TIME ALLOWED:'      ,T60,F10.2,'HRS'/
    ' MAXIMUM COUNTS (ONLY RTS):',T60,I12/
    ' RADIUS USED IN CROSSING-FILE:',T60,F10.2/
    ' SCORING OPTION IFULL (0,1,2,3):'  ,T60,I12/
```

```
    ' STATISTICAL ACCURACY DESIRED:'  ,T60,F10.4,'%'/
    ' KERMA WILL(1) or WILL NOT(0) be scored:',T60,I2);

(in PULSE HEIGHT DISTRIBUTION INPUT below "end of IFULL=2 block" line 4057.
 just above "SOURCE CONFIGURATION INPUT")
IF ((IFULL.EQ.5).OR.(IFULL.EQ.7)) [
     OUTPUT;(/' INPUTS FOR TRIPLETS SCORING REGIONS (DETECTOR 1,2,3)'/);
     "INITIALIZE FLAGS TO NO PULSE HEIGHT DISTRIBUTION IN EACH REGION"

     DO J=1,NREG [IPHR(J)=0;]
     IVAL=IVAL+1;
     NUM_REG_D1=IVAL;
     VALUES_SOUGHT(IVAL)='REGION OF DETECTOR 1';
     TYPE(IVAL)=0;
     VALUE_MIN(IVAL)=1;
     VALUE_MAX(IVAL)=NREG;

     IVAL=IVAL+1;
     NUM_REG_D2=IVAL;
     VALUES_SOUGHT(IVAL)='REGION OF DETECTOR 2';
     TYPE(IVAL)=0;
     VALUE_MIN(IVAL)=1;
     VALUE_MAX(IVAL)=NREG;

     IVAL=IVAL+1;
     NUM_REG_D3=IVAL;
     VALUES_SOUGHT(IVAL)='REGION OF DETECTOR 3';
     TYPE(IVAL)=0;
     VALUE_MIN(IVAL)=1;
     VALUE_MAX(IVAL)=NREG;

     DELIMETER='PULSE HEIGHT DISTRIBUTION INPUT';
     $GET_INPUTS(NUM_REG_D1,NUM_REG_D3);

     OUTPUT;(/' *** SPECIAL INPUT CARD FOR WRITING TRIPLETS ***'/);
     DO J=1,NVALUE(NUM_REG_D1) [
        REG_D1=VALUE(NUM_REG_D1,J);
        IPHR(REG_D1)=2;
        OUTPUT REG_D1,MED(REG_D1); (/T10,' REGION(D1)',I4,' HAS MEDIUM',I3);
     ]
     $SKIP-LINE;
     DO J=1, NVALUE(NUM_REG_D2) [
        REG_D2=VALUE(NUM_REG_D2,J);
        IPHR(REG_D2)=3;
        OUTPUT REG_D2,MED(REG_D2); (/T10,' REGION(D2)',I4,' HAS MEDIUM',I3);
     ]
     $SKIP-LINE;
     DO J=1, NVALUE(NUM_REG_D3) [
        REG_D3=VALUE(NUM_REG_D3,J);
        IPHR(REG_D3)=4;
        OUTPUT REG_D3,MED(REG_D3); (/T10,' REGION(D3)',I4,' HAS MEDIUM',I3);
     ]
     $SKIP-LINE;

] "end of IFULL=5 or 7 block"
```

B.2 Example of an input file for DOSRZnrc-rts

This example of an input file for DOSRZnrc-rts is describing a 2.0 MeV electron point source 10 cm from the surface of detector 1.

```
TITLE= Risoe Telescope Spectrometer. Energy=2000keV

# This DOSRZnrc inputfile describes the geometry of the RTS unit, including the
# PMMA shield. Source: point source. Distance: 10 cm. Particle: Electron.
# Energy: 2000 keV


########################################

 :start I/O control:

 IWATCH= off                           #off,interactions,steps,deposited,graph

 STORE INITIAL RANDOM NUMBERS= no      #no,last,all

 IRESTART= first                       #first,restart,make,analyze,start-RNS
                                       #parallel

 OUTPUT OPTIONS= material summary      #short, dose summary, material summary,
                                       #material and dose summary, long;

 STORE DATA ARRAYS= yes                #no,yes

 ELECTRON TRANSPORT= normal            #normal, no interactions;

 DOSE ZBOUND MIN= 1
 DOSE ZBOUND MAX= 60
 DOSE RBOUND MIN= 0
 DOSE RBOUND MAX= 40

 :stop I/O control:

########################################

 :start Monte Carlo inputs:

 NUMBER OF HISTORIES= 90000000

 MAX COUNTS= 200000

 COUNT RADIUS= 2.0

 INITIAL RANDOM NO. SEEDS= 1,  3

 MAX CPU HOURS ALLOWED=    90.000

# IFULL= pulse height distribution
# IFULL= triplets
 IFULL= trip+cross0                    #entrance region,
                                       #pulse height distribution,
                                       #dose and stoppers,scatter fraction;

 STATISTICAL ACCURACY SOUGHT=  0.0000

 SCORE KERMA= no                       #yes,no

 :stop Monte Carlo inputs:

########################################

:start geometrical inputs:

# Geometry discriping the RTS unit

METHOD OF INPUT= individual

Z OF FRONT FACE=  -1.34450000

DEPTH BOUNDARIES=  -1.34350000,  -1.21890000,  -1.01130000,  -0.92890000,
                   -0.80430000,  -0.63310000,  -0.51350000,  -0.36350000,
                   -0.36330000,  -0.34530000,  -0.32730000,  -0.30930000,
                   -0.29130000,  -0.27330000,  -0.14130000,  -0.04000000,
                   -0.01000000,   0.00000000,   0.00000250,   0.00000550,
                    0.00519500,   0.00519800,   0.00520000,   0.00820000,
                    0.03220000,   0.03720000,   0.03720300,   0.03720600,
                    0.05289500,   0.05289800,   0.05290000,   0.05890000,
                    0.09090000,   0.09490000,   0.09490300,   0.09490600,
                    0.10090000,   0.10840000,   0.45389400,   0.45389700,
                    0.45390000,   0.45890000,   0.49090000,   0.49590000,
```

```
                  0.49590200,   0.49590500,   0.84509400,   0.84509700,
                  0.84510000,   0.85010000,   0.88210000,   0.99670000,
                  1.49670000

RADII=   0.00100000,   0.40000000,   0.42500000,   0.45000000,
         0.47500000,   0.50000000,   0.60000000,   0.70000000,
         0.75000000,   0.76000000,   0.80000000,   0.81500000,
         0.87500000,   0.92500000,   0.98000000,   1.03000000,
         1.10000000,   1.11000000,   1.11500000,   1.13000000,
         1.18000000,   1.38000000,   1.47500000,   1.48500000,
         1.50000000,   2.00000000

MEDIA= AIR-STP,
       TI,
       GE,
       AU,
       SI,
       CU,
       PT-IR,
       MACOR,
       EPOXY,
       MYLAR,
       TEFLON,
       STEEL,
       PMMA,
       GE-A,
       SI-A

DESCRIPTION BY= regions

MEDNUM=          2,    4,   14,   15,   14,    4,    4,   14,   15,   14,
                 4,    4,   14,   15,   14,    4,    4,   14,   15,   14,
                 4,    6,    2,    4,   14,   15,   14,    4,    4,   14,
                15,   14,    4,    4,   14,   15,   14,    4,    4,   14,
                15,   14,    4,    6,    2,    7,    9,    4,    3,    5,
                 3,    4,    9,    4,   14,   15,   14,    4,    4,   14,
                15,   14,    4,    4,   14,   15,   14,    4,    6,    2,
                 7,    9,    4,    3,    5,    3,    4,    9,    4,   14,
                15,   14,    4,    4,   14,   15,   14,    4,    4,   14,
                15,   14,    4,    6,    2,    7,    9,    4,    3,    5,
                 3,    4,    9,    4,   14,   15,   14,    4,    4,   14,
                15,   14,    4,    4,   14,   15,   14,    4,    6,    2,
                 7,    9,    4,    3,    5,    3,    4,    9,    4,   14,
                15,   14,    4,    4,   14,   15,   14,    4,    4,   14,
                15,   14,    4,    6,    2,    7,    8,    9,    4,    3,
                 5,    3,    4,    9,    4,   14,   15,   14,    4,    4,
                14,   15,   14,    4,    4,   14,   15,   14,    4,    6,
                 2,    7,    8,    9,    4,   14,   15,   14,    4,    4,
                14,   15,   14,    4,    4,   14,   15,   14,    4,    6,
                12,    2,    7,    8,    9,    9,    4,    3,    5,    3,
                 4,    9,    4,   14,   15,   14,    4,    4,   14,   15,
                14,    4,    6,   12,    2,    7,   10,    9,    4,    3,
                 5,    3,    4,    9,    4,   14,   15,   14,    4,    4,
                14,   15,   14,    4,    6,   12,    2,    7,    6,    9,
                 4,    3,    5,    3,    4,    9,    4,   14,   15,   14,
                 4,    4,   14,   15,   14,    4,    6,   12,    2,    7,
                 6,    9,    4,    3,    5,    3,    4,    9,    8,    4,
                14,   15,   14,    4,    4,   14,   15,   14,    4,    6,
                13,   12,    2,    7,    6,    9,    4,    3,    5,    3,
                 4,    9,    8,    4,   14,   15,   14,    4,    4,   14,
                15,   14,    4,    6,   13,   12,    2,    7,    6,    9,
                 8,    4,   14,   15,   14,    4,    4,   14,   15,   14,
                 4,    6,   13,   12,    2,    7,    6,    8,    4,   14,
                15,   14,    4,    4,   14,   15,   14,    4,    6,   13,
                12,    2,    7,    6,    8,    9,    4,    3,    5,    3,
                 4,    9,    9,    4,    3,    5,    3,    4,    9,    6,
                13,   12,    2,    7,    6,    8,    9,    4,    3,    5,
                 3,    4,    9,    8,    9,    4,    3,    5,    3,    4,
                 9,    8,    6,   13,   12,    2,    7,    6,   10,    9,
                 4,    3,    5,    3,    4,    9,    8,    9,    4,    3,
                 5,    3,    4,    9,    8,    6,   13,   12,    2,    7,
                 6,    9,    4,    3,    5,    3,    4,    9,    8,    9,
                 4,    3,    5,    3,    4,    9,    8,    6,   13,   12,
                 2,    7,    6,    9,   11,    9,    8,    9,    8,    6,
                13,   12,    2,    7,    6,   11,    9,    8,    9,    8,
                 6,   13,   12,    2,    7,    6,   11,    8,    6,   13,
                12,    6,    8,    6,   13,   12,    6,   10,    6,   13,
                12,    6,    6,   13,   12,    6

START REGION=   10,   20,   21,   22,   23,   24,   28,   29,   30,   31,
                32,   36,   37,   38,   41,   42,   46,   47,   48,   49,
                50,   53,   63,   73,   74,   75,   76,   77,   81,   82,
                83,   84,   85,   89,   90,   91,   94,   95,   99,  100,
               101,  102,  103,  106,  116,  121,  125,  126,  127,  128,
               129,  130,  131,  134,  135,  136,  137,  138,  142,  143,
               144,  147,  148,  152,  153,  154,  155,  156,  159,  169,
```

```
                 173,  178,  179,  180,  181,  182,  183,  184,  187,  188,
                 189,  190,  191,  195,  196,  197,  200,  201,  205,  206,
                 207,  208,  209,  212,  222,  225,  231,  232,  233,  234,
                 235,  236,  237,  240,  241,  242,  243,  244,  248,  249,
                 250,  253,  254,  258,  259,  260,  261,  262,  265,  275,
                 277,  284,  285,  286,  287,  288,  289,  290,  293,  294,
                 295,  296,  297,  301,  302,  303,  306,  307,  311,  312,
                 313,  314,  315,  318,  328,  329,  336,  337,  338,  339,
                 340,  341,  342,  343,  346,  347,  348,  349,  350,  354,
                 355,  356,  359,  360,  364,  365,  366,  367,  368,  371,
                 381,  382,  387,  390,  399,  400,  401,  402,  403,  407,
                 408,  409,  412,  413,  417,  418,  419,  420,  421,  424,
                 433,  434,  435,  440,  443,  451,  452,  453,  454,  455,
                 456,  457,  460,  461,  462,  465,  466,  470,  471,  472,
                 473,  474,  477,  486,  487,  488,  493,  504,  505,  506,
                 507,  508,  509,  510,  513,  514,  515,  518,  519,  523,
                 524,  525,  526,  527,  530,  539,  540,  541,  546,  557,
                 558,  559,  560,  561,  562,  563,  566,  567,  568,  571,
                 572,  576,  577,  578,  579,  580,  583,  592,  593,  594,
                 599,  610,  611,  612,  613,  614,  615,  616,  617,  619,
                 620,  621,  624,  625,  629,  630,  631,  632,  633,  636,
                 644,  645,  646,  647,  652,  663,  664,  665,  666,  667,
                 668,  669,  670,  672,  673,  674,  677,  678,  682,  683,
                 684,  685,  686,  689,  697,  698,  699,  700,  705,  716,
                 723,  725,  726,  727,  730,  731,  735,  736,  737,  738,
                 739,  742,  750,  751,  752,  753,  758,  759,  778,  779,
                 780,  783,  784,  788,  789,  790,  791,  792,  795,  802,
                 804,  805,  806,  811,  812,  830,  831,  832,  833,  836,
                 837,  838,  840,  841,  842,  843,  844,  845,  846,  848,
                 855,  857,  858,  859,  864,  865,  883,  884,  885,  886,
                 889,  890,  891,  892,  893,  894,  895,  896,  897,  898,
                 899,  900,  901,  907,  910,  911,  912,  917,  918,  936,
                 937,  938,  939,  942,  943,  944,  945,  946,  947,  948,
                 949,  950,  951,  952,  953,  954,  960,  963,  964,  965,
                 970,  989,  990,  991,  992,  995,  996,  997,  998,  999,
                1000, 1001, 1002, 1003, 1004, 1005, 1006, 1007, 1013, 1016,
                1017, 1018, 1023, 1042, 1046, 1047, 1051, 1052, 1059, 1060,
                1066, 1069, 1070, 1071, 1076, 1099, 1100, 1104, 1105, 1112,
                1113, 1118, 1122, 1123, 1124, 1129, 1152, 1153, 1166, 1170,
                1175, 1182, 1206, 1219, 1223, 1228, 1235, 1259, 1272, 1276,
                1281, 1288, 1325, 1328, 1334, 1341

STOP REGION=      10,   20,   21,   22,   23,   24,   28,   29,   30,   31,
                  32,   36,   37,   40,   41,   42,   46,   47,   48,   49,
                  50,   54,   63,   73,   74,   75,   76,   77,   81,   82,
                  83,   84,   85,   89,   90,   93,   94,   95,   99,  100,
                 101,  102,  103,  107,  116,  121,  125,  126,  127,  128,
                 129,  130,  131,  134,  135,  136,  137,  138,  142,  143,
                 146,  147,  148,  152,  153,  154,  155,  156,  160,  169,
                 174,  178,  179,  180,  181,  182,  183,  184,  187,  188,
                 189,  190,  191,  195,  196,  199,  200,  201,  205,  206,
                 207,  208,  209,  213,  222,  227,  231,  232,  233,  234,
                 235,  236,  237,  240,  241,  242,  243,  244,  248,  249,
                 252,  253,  254,  258,  259,  260,  261,  262,  266,  275,
                 280,  284,  285,  286,  287,  288,  289,  290,  293,  294,
                 295,  296,  297,  301,  302,  305,  306,  307,  311,  312,
                 313,  314,  315,  319,  328,  333,  336,  337,  338,  339,
                 340,  341,  342,  343,  346,  347,  348,  349,  350,  354,
                 355,  358,  359,  360,  364,  365,  366,  367,  368,  372,
                 381,  386,  389,  396,  399,  400,  401,  402,  403,  407,
                 408,  411,  412,  413,  417,  418,  419,  420,  421,  425,
                 433,  434,  439,  442,  443,  451,  452,  453,  454,  455,
                 456,  457,  460,  461,  464,  465,  466,  470,  471,  472,
                 473,  474,  478,  486,  487,  492,  495,  504,  505,  506,
                 507,  508,  509,  510,  513,  514,  517,  518,  519,  523,
                 524,  525,  526,  527,  531,  539,  540,  545,  546,  557,
                 558,  559,  560,  561,  562,  563,  566,  567,  570,  571,
                 572,  576,  577,  578,  579,  580,  584,  592,  593,  598,
                 599,  610,  611,  612,  613,  614,  615,  616,  617,  619,
                 620,  623,  624,  625,  629,  630,  631,  632,  633,  637,
                 644,  645,  646,  651,  652,  663,  664,  665,  666,  667,
                 668,  669,  670,  672,  673,  676,  677,  678,  682,  683,
                 684,  685,  686,  690,  697,  698,  699,  704,  705,  722,
                 723,  725,  726,  729,  730,  731,  735,  736,  737,  738,
                 739,  743,  750,  751,  752,  757,  758,  776,  778,  779,
                 782,  783,  784,  788,  789,  790,  791,  792,  796,  803,
                 804,  805,  810,  811,  829,  830,  831,  832,  835,  836,
                 837,  838,  840,  841,  842,  843,  844,  845,  846,  849,
                 856,  857,  858,  863,  864,  882,  883,  884,  885,  888,
                 889,  890,  891,  892,  893,  894,  895,  896,  897,  898,
                 899,  900,  902,  909,  910,  911,  916,  917,  935,  936,
                 937,  938,  941,  942,  943,  944,  945,  946,  947,  948,
                 949,  950,  951,  952,  953,  955,  962,  963,  964,  969,
                 970,  989,  990,  991,  994,  995,  996,  997,  998,  999,
                1000, 1001, 1002, 1003, 1004, 1005, 1006, 1008, 1015, 1016,
                1017, 1022, 1023, 1045, 1046, 1050, 1051, 1058, 1059, 1061,
```

```
             1068, 1069, 1070, 1075, 1094, 1099, 1103, 1104, 1111, 1112,
             1114, 1121, 1122, 1123, 1128, 1151, 1152, 1165, 1167, 1174,
             1181, 1204, 1218, 1220, 1227, 1234, 1257, 1271, 1273, 1280,
             1287, 1310, 1326, 1333, 1340, 1379

:stop geometrical inputs:

########################################

# Only if IFULL= pulse height distribution or triplets

:start pulse height distribution input:

REGION OF DETECTOR 1=   21,   22,   23,   74,   75,   76

REGION OF DETECTOR 2=   29,   30,   31,   82,   83,   84,  135,  136,
                       137,  188,  189,  190,  241,  242,  243,  294,
                       295,  296,  347,  348,  349,  400,  401,  402

REGION OF DETECTOR 3=   37,   38,   39,   40,   41,   47,   48,   49,
                        90,   91,   92,   93,   94,  100,  101,  102,
                       143,  144,  145,  146,  147,  153,  154,  155,
                       196,  197,  198,  199,  200,  206,  207,  208,
                       249,  250,  251,  252,  253,  259,  260,  261,
                       302,  303,  304,  305,  306,  312,  313,  314,
                       355,  356,  357,  358,  359,  365,  366,  367,
                       408,  409,  410,  411,  412,  418,  419,  420,
                       461,  462,  463,  464,  465,  471,  472,  473,
                       514,  515,  516,  517,  518,  524,  525,  526,
                       567,  568,  569,  570,  571,  577,  578,  579,
                       620,  621,  622,  623,  624,  630,  631,  632,
                       673,  674,  675,  676,  677,  683,  684,  685,
                       726,  727,  728,  729,  730,  736,  737,  738,
                       779,  780,  781,  782,  783,  789,  790,  791

SLOTE= 0.01

DELTAE= 0.005

:stop pulse height distribution input:

########################################

 :start source inputs:

 INCIDENT PARTICLE= electron             #electron,photon,positron,(all);

 SOURCE NUMBER= 3                      #0,1,2,3,4,10,11,12,13,14,20,21;

#---------------------------------------

 SOURCE OPTIONS=  0.0, 0.001, -1.3445,  -1.3435

#---------------------------------------

 INCIDENT ENERGY= monoenergetic             #monoenergetic,spectrum;

 INCIDENT KINETIC ENERGY(MEV)= 2.000

# SPEC FILENAME= /usr/people/jhhansen/egs4/spec/Bi207.spec

# SPEC IOUTSP= include                  # none,include

 :stop source inputs:

########################################

 :start transport control:

 ESTEPE= 0.0000

 SMAX=  0.0000

 ELECTRON CUTOFF(MeV)=  0.521           #ECUT

 PHOTON CUTOFF(MeV)=  0.0100            #PCUT

 RAYLEIGH SCATTERING= on                #on,off; Special PEGS4 data needed if on

 COMPTON SCATTERING= impuls approximation
                                        #Klein-Nishina,Impuls Approximation

#---------------------------------------

 ELECTRON RANGE REJECTION= off          #off,on;
```

```
 ESAVEIN= 0.0                          #Only used if range rejection is on but
                       # must always be input.

#--------------------------------------

 X-RAY FLUORESCENCE= on;               #on,off
  FLUOR IZ=           2
  FLUOR START REGION= 2
  FLUOR STOP REGION=  1379

#--------------------------------------

PE ANGULAR DISTRIBUTION=on             #on,off

#--------------------------------------

 REDUCE CALLS TO HOWFAR= no            #no,yes;

 RUSSIAN ROULETTE DEPTH= 0.0000

 RUSSIAN ROULETTE FRACTION= 0.0000

 EXPONENTIAL TRANSFORM C= 0.0000

 PHOTON FORCING= off                    #on,off;

 START FORCING= 1

 STOP FORCING AFTER= 1

#--------------------------------------

 NESTEP= 0

 NSMAX= 0

 :stop transport control:

########################################

 :start plot control:

 PLOTTING= off                          #on,off;

# LINE PRINTER OUTPUT= On               #on,off; if PLOTTING= on

# EXTERNAL PLOTTER OUTPUT= Off           #on,off; if PLOTTING= on

# EXTERNAL PLOT TYPE= Histogram         #histogram,point,both;
                                       # if EXTERNAL PLOTTER OUTPUT= on

# PLOT RADIAL REGION IX= 0              # if PLOTTING= on
# PLOT PLANAR REGION IZ= 1, 2           # if PLOTTING= on

 :stop plot control:

########################################

 :start transport physics:

 ESTEPE= 0.25

 XIMAX= 0

 ELECTRON-STEP ALGORITHM= PRESTA-II

 BOUNDARY CROSSING ALGORITHM= exact

 SKIN DEPTH FOR BCA= 0.0

 :stop transport physics:

########################################
```

C Geometry data used for DOSRZnrc-rts

Examples of geometries used in the Monte Carlo calculations presented in this report is outlined in the following figures. Since DOSRZnrc is used for cylindrical geometries, only two coordinates (r & z) are needed to describe a geometry.

The geometries are originally first described in a spreadsheet, and then by a custom build program transformed into a format which can be inserted in the DOSRZnrc-rts inputfile. The figures below are transcripts of the spreadsheets modified so the materials are depicted in words instead of numbers.

Legend for spreadsheet figures

All lengths are given in cm. First column indicates the thickness of a given row. Second column indicates the position of the row. The value just beside the row is the position the lowest part of the voxel, and the value just above is the position of the top part of the voxel. The top row indicates the outer radius of the regions.

Example: The air volume within the source holder made of PMMA in Figure 54 has a thickness of 0.215 cm and is positioned between -10.000 cm and -9.785 cm. Its outer radius is 0.5 cm.

Materials are described in Table 24 on page 100.

Thiskness	Position	Radius →				
	-10.910000	0.35	0.50	2.50	15.00	30.00
0.910000	-10.000000	PMMA	PMMA	PMMA	Vacuum	Vacuum
0.215000	-9.785000	Air	Air	PMMA	Vacuum	Vacuum
9.785000	0.000000	Air	Air	Air	Air	Air
0.006965	0.006965	Tissue	Tissue	Tissue	Tissue	Vacuum
0.000070	0.007035	Tissue	Tissue	Tissue	Tissue	Vacuum
0.291465	0.298500	Tissue	Tissue	Tissue	Tissue	Vacuum
0.003000	0.301500	Tissue	Tissue	Tissue	Tissue	Vacuum
0.693500	0.995000	Tissue	Tissue	Tissue	Tissue	Vacuum
0.010000	1.005000	Tissue	Tissue	Tissue	Tissue	Vacuum
13.995000	15.000000	Tissue	Tissue	Tissue	Tissue	Vacuum

Figure 54. Tissue disc with Cl-36 source above it. Legend: See above.

Thickness	Position	Radius →		
	-10.000000	0.56419	15	650
10.000000	0.000000	Air	Air	Air
0.006965	0.006965	Tissue	Tissue	Vacuum
0.000070	0.007035	Tissue	Tissue	Vacuum
0.291465	0.298500	Tissue	Tissue	Vacuum
0.003000	0.301500	Tissue	Tissue	Vacuum
0.693500	0.995000	Tissue	Tissue	Vacuum
0.010000	1.005000	Tissue	Tissue	Vacuum
13.995000	15.000000	Tissue	Tissue	Vacuum

Figure 55. Tissue plate geometry with 10 cm air above it. Legend: See above.

Thickness	Position	Radius →																							
	-10.0000000	0.400	0.425	0.450	0.475	0.500	0.600	0.700	0.750	0.760	0.800	0.815	0.875	0.925	0.980	1.030	1.100	1.110	1.115	1.130	1.180	1.380	1.475	1.485	1.500	2.000	6.700
8.6565000	-1.3435000	Air	Air	Air	Air	Air	Air	Air	Air	Air	Air	Air	Air	Air	Air	Air	Air	Air	Air	Air	Air	Air	Air	Air	Air	Air	Air
0.1246000	-1.2189000	Air	Air	Air	Air	Air	Air	Air	Air	Air	Air	Air	Air	Air	Air	Air	Air	Air	Air	Air	Air	Air	Air	Air	Air	PMMA	Vacuum
0.2076000	-1.0113000	Air	Air	Air	Air	Air	Air	Air	Air	Air	Air	Air	Air	Air	Air	Air	Air	Air	Air	Air	Air	Air	PMMA	PMMA	PMMA	PMMA	Vacuum
0.0824000	-0.9289000	Air	Air	Air	Air	Air	Air	Air	Air	Air	Air	Air	Air	Air	Air	Air	Air	Air	Air	Air	Air	PMMA	PMMA	PMMA	PMMA	PMMA	Vacuum
0.1246000	-0.8043000	Air	Air	Air	Air	Air	Air	Air	Air	Air	Air	Air	Air	Air	Air	Air	Air	PMMA	PMMA	PMMA	PMMA	PMMA	PMMA	PMMA	PMMA	PMMA	Vacuum
0.1712000	-0.6331000	Air	Air	Air	Air	Air	Air	Air	Air	Air	Air	Air	Air	Air	PMMA	PMMA	PMMA	PMMA	PMMA	PMMA	PMMA	PMMA	PMMA	PMMA	PMMA	PMMA	Vacuum
0.1196000	-0.5135000	Air	Air	Air	Air	Air	Air	Air	Air	Air	Air	Air	PMMA	PMMA	PMMA	PMMA	PMMA	PMMA	PMMA	PMMA	PMMA	PMMA	PMMA	PMMA	PMMA	PMMA	Vacuum
0.1500000	-0.3635000	Air	Air	Air	Air	Air	Air	Steel	Steel	Steel	Steel	Steel	PMMA	Steel	Steel	Steel	Steel	Steel	Steel	Steel	Steel	Steel	Steel	Steel	Steel	Steel	Vacuum
0.0002000	-0.3633000	Ti	Ti	Ti	Ti	Ti	Ti	Ti	Ti	Ti	Ti	Ti	Steel	Steel	Steel	Ti	Ti	Ti	Ti	Ti	Ti	Ti	Steel	Steel	Steel	Steel	Vacuum
0.0180000	-0.3453000	Air	Air	Air	Air	Air	Pt-Ir	Pt-Ir	Pt-Ir	Pt-Ir	Pt-Ir	Pt-Ir	Pt-Ir	Pt-Ir	Pt-Ir	Pt-Ir	Pt-Ir	Pt-Ir	Pt-Ir	Pt-Ir	Pt-Ir	Pt-Ir	Pt-Ir	Steel	Steel	Steel	Steel	Vacuum
0.0180000	-0.3273000	Air	Air	Air	Air	Pt-Ir	Pt-Ir	Pt-Ir	Pt-Ir	Pt-Ir	Pt-Ir	Pt-Ir	Pt-Ir	Pt-Ir	Pt-Ir	Pt-Ir	Pt-Ir	Pt-Ir	Pt-Ir	Pt-Ir	Pt-Ir	Pt-Ir	Pt-Ir	Steel	Steel	Steel	Steel	Vacuum
0.0180000	-0.3093000	Air	Air	Air	Pt-Ir	Pt-Ir	Pt-Ir	Pt-Ir	Pt-Ir	Pt-Ir	Pt-Ir	Pt-Ir	Pt-Ir	Pt-Ir	Pt-Ir	Pt-Ir	Pt-Ir	Pt-Ir	Pt-Ir	Pt-Ir	Pt-Ir	Pt-Ir	Pt-Ir	Steel	Steel	Steel	Steel	Vacuum
0.0180000	-0.2913000	Air	Air	Pt-Ir	Pt-Ir	Pt-Ir	Pt-Ir	Pt-Ir	Pt-Ir	Pt-Ir	Pt-Ir	Pt-Ir	Pt-Ir	Pt-Ir	Pt-Ir	Pt-Ir	Pt-Ir	Pt-Ir	Pt-Ir	Pt-Ir	Pt-Ir	Pt-Ir	Pt-Ir	Steel	Steel	Steel	Steel	Vacuum
0.0180000	-0.2733000	Air	Pt-Ir	Pt-Ir	Pt-Ir	Pt-Ir	Pt-Ir	Pt-Ir	Pt-Ir	Pt-Ir	Pt-Ir	Pt-Ir	Pt-Ir	Pt-Ir	Pt-Ir	Pt-Ir	Pt-Ir	Pt-Ir	Pt-Ir	Pt-Ir	Pt-Ir	Pt-Ir	Pt-Ir	Steel	Steel	Steel	Steel	Vacuum
0.1320000	-0.1413000	Air	Air	Air	Air	Air	Macor	Macor	Mylar	Cu	Cu	Cu	Cu	Cu	Cu	Cu	Cu	Cu	Cu	Cu	Cu	Cu	Cu	Cu	Cu	Cu	Vacuum
0.1013000	-0.0400000	Air	Air	Air	Air	Air	Air	Macor	Macor	Mylar	Air	Air	Air	Air	Macor	Macor	Macor	Mylar	Air	Air	Cu	Cu	Cu	Cu	Cu	Cu	Vacuum
0.0300000	-0.0100000	Air	Air	Air	Air	Air	Macor	Macor	Macor	Mylar	Air	Air	Air	Air	Macor	Macor	Macor	Mylar	Air	Air	Cu	Cu	Cu	Cu	Cu	Cu	Vacuum
0.0100000	0.0000000	Air	Epoxy	Epoxy	Epoxy	Epoxy	Epoxy	Epoxy	Epoxy	Air	Air	Air	Air	Air	Macor	Macor	Macor	Mylar	Air	Air	Cu	Cu	Cu	Cu	Cu	Cu	Vacuum
0.0000025	0.0000025	Au	Au	Au	Au	Au	Au	Au	Au	Air	Air	Air	Air	Air	Macor	Macor	Macor	Mylar	Air	Air	Cu	Cu	Cu	Cu	Cu	Cu	Vacuum
0.0000030	0.0000055	Ge-A	Ge	Ge	Ge	Ge	Ge	Epoxy	Air	Air	Air	Air	Air	Air	Macor	Macor	Macor	Mylar	Air	Air	Cu	Cu	Cu	Cu	Cu	Cu	Vacuum
0.0051890	0.0051945	Si-A	Si	Si	Si	Si	Si	Epoxy	Air	Air	Air	Air	Air	Air	Macor	Macor	Macor	Mylar	Air	Air	Cu	Cu	Cu	Cu	Cu	Cu	Vacuum
0.0000030	0.0051975	Ge-A	Ge	Ge	Ge	Ge	Ge	Epoxy	Air	Air	Air	Air	Air	Air	Macor	Macor	Macor	Mylar	Air	Air	Cu	Cu	Cu	Cu	Cu	Cu	Vacuum
0.0000025	0.0052000	Au	Au	Au	Au	Au	Au	Epoxy	Air	Air	Air	Air	Air	Air	Macor	Macor	Macor	Mylar	Air	Air	Cu	Cu	Cu	Cu	Cu	Cu	Vacuum
0.0030000	0.0082000	Air	Epoxy	Epoxy	Epoxy	Epoxy	Epoxy	Epoxy	Air	Air	Air	Air	Air	Air	Macor	Macor	Macor	Mylar	Air	Air	Cu	Cu	Cu	Cu	Cu	Cu	Vacuum
0.0240000	0.0322000	Air	Air	Air	Air	Air	Air	Air	Air	Air	Air	Air	Air	Air	Macor	Macor	Macor	Mylar	Air	Air	Cu	Cu	Cu	Cu	Cu	Cu	Vacuum
0.0050000	0.0372000	Air	Air	Air	Air	Air	Air	Air	Epoxy	Epoxy	Epoxy	Epoxy	Epoxy	Epoxy	Macor	Macor	Macor	Mylar	Air	Air	Cu	Cu	Cu	Cu	Cu	Cu	Vacuum
0.0000025	0.0372025	Au	Au	Au	Au	Au	Au	Au	Au	Au	Au	Au	Au	Epoxy	Macor	Macor	Macor	Mylar	Air	Air	Cu	Cu	Cu	Cu	Cu	Cu	Vacuum
0.0000030	0.0372055	Ge-A	Ge-A	Ge-A	Ge-A	Ge-A	Ge-A	Ge-A	Ge	Ge	Ge	Ge	Ge	Epoxy	Macor	Macor	Macor	Mylar	Air	Air	Cu	Cu	Cu	Cu	Cu	Cu	Vacuum
0.0156890	0.0528945	Si-A	Si-A	Si-A	Si-A	Si-A	Si-A	Si-A	Si	Si	Si	Si	Si	Epoxy	Macor	Macor	Macor	Mylar	Air	Air	Cu	Cu	Cu	Cu	Cu	Cu	Vacuum
0.0000030	0.0528975	Ge-A	Ge-A	Ge-A	Ge-A	Ge-A	Ge-A	Ge-A	Ge	Ge	Ge	Ge	Ge	Epoxy	Macor	Macor	Macor	Mylar	Air	Air	Cu	Cu	Cu	Cu	Cu	Cu	Vacuum
0.0000025	0.0529000	Au	Au	Au	Au	Au	Au	Au	Au	Au	Au	Au	Au	Epoxy	Macor	Macor	Macor	Mylar	Air	Air	Cu	Cu	Cu	Cu	Cu	Cu	Vacuum
0.0060000	0.0589000	Air	Air	Air	Air	Air	Air	Air	Epoxy	Epoxy	Epoxy	Epoxy	Epoxy	Epoxy	Macor	Macor	Macor	Mylar	Air	Air	Cu	Cu	Cu	Cu	Cu	Cu	Vacuum
0.0320000	0.0909000	Air	Air	Air	Air	Air	Air	Air	Air	Air	Air	Macor	Macor	Macor	Macor	Macor	Macor	Mylar	Air	Air	Cu	Cu	Cu	Cu	Cu	Cu	Vacuum
0.0040000	0.0949000	Air	Air	Air	Air	Air	Air	Air	Air	Air	Air	Air	Air	Air	Epoxy	Epoxy	Epoxy	Epoxy	Epoxy	Epoxy	Air	Cu	Cu	Cu	Cu	Cu	Vacuum
0.0000025	0.0949025	Au	Au	Au	Au	Au	Au	Au	Au	Au	Au	Au	Au	Au	Au	Au	Au	Au	Au	Epoxy	Air	Cu	Cu	Cu	Cu	Cu	Vacuum
0.0000030	0.0949055	Ge-A	Ge-A	Ge-A	Ge-A	Ge-A	Ge-A	Ge-A	Ge-A	Ge-A	Ge-A	Ge-A	Ge-A	Ge-A	Ge-A	Ge	Ge	Ge	Ge	Epoxy	Air	Cu	Cu	Cu	Cu	Cu	Vacuum
0.0059945	0.1009000	Si-A	Si-A	Si-A	Si-A	Si-A	Si-A	Si-A	Si-A	Si-A	Si-A	Si-A	Si-A	Si-A	Si-A	Si	Si	Si	Si	Epoxy	Air	Cu	Cu	Cu	Cu	Cu	Vacuum
0.0075000	0.1084000	Si-A	Si-A	Si-A	Si-A	Si-A	Si-A	Si-A	Si-A	Si-A	Si-A	Si-A	Si-A	Si-A	Si-A	Si	Si	Si	Si	Teflon	Teflon	Air	Air	Air	Air	Cu	Vacuum
0.3454940	0.4538940	Si-A	Si-A	Si-A	Si-A	Si-A	Si-A	Si-A	Si-A	Si-A	Si-A	Si-A	Si-A	Si-A	Si	Si	Si	Si	Si	Epoxy	Epoxy	Macor	Macor	Mylar	Air	Cu	Vacuum
0.0000030	0.4538970	Ge-A	Ge-A	Ge-A	Ge-A	Ge-A	Ge-A	Ge-A	Ge-A	Ge-A	Ge-A	Ge-A	Ge-A	Ge-A	Ge	Ge	Ge	Ge	Ge	Epoxy	Epoxy	Macor	Macor	Mylar	Air	Cu	Vacuum
0.0000025	0.4538995	Au	Au	Au	Au	Au	Au	Au	Au	Au	Au	Au	Au	Au	Au	Au	Au	Au	Au	Epoxy	Epoxy	Macor	Macor	Mylar	Air	Cu	Vacuum
0.0050000	0.4588995	Air	Air	Air	Air	Air	Air	Air	Air	Air	Air	Air	Air	Air	Air	Epoxy	Epoxy	Epoxy	Epoxy	Epoxy	Epoxy	Macor	Macor	Mylar	Air	Cu	Vacuum
0.0320000	0.4908995	Air	Air	Air	Air	Air	Air	Air	Air	Air	Air	Air	Air	Air	Air	Air	Macor	Macor	Macor	Macor	Macor	Macor	Macor	Mylar	Air	Cu	Vacuum
0.0050000	0.4958995	Air	Air	Air	Air	Air	Air	Air	Air	Air	Air	Air	Air	Air	Air	Epoxy	Epoxy	Epoxy	Epoxy	Epoxy	Epoxy	Macor	Macor	Mylar	Air	Cu	Vacuum
0.0000025	0.4959020	Au	Au	Au	Au	Au	Au	Au	Au	Au	Au	Au	Au	Au	Au	Au	Au	Au	Au	Epoxy	Epoxy	Macor	Macor	Mylar	Air	Cu	Vacuum
0.0000030	0.4959050	Ge-A	Ge-A	Ge-A	Ge-A	Ge-A	Ge-A	Ge-A	Ge-A	Ge-A	Ge-A	Ge-A	Ge-A	Ge-A	Ge	Ge	Ge	Ge	Ge	Epoxy	Epoxy	Macor	Macor	Mylar	Air	Cu	Vacuum
0.3491890	0.8450940	Si-A	Si-A	Si-A	Si-A	Si-A	Si-A	Si-A	Si-A	Si-A	Si-A	Si-A	Si-A	Si-A	Si	Si	Si	Si	Si	Epoxy	Epoxy	Macor	Macor	Mylar	Air	Cu	Vacuum
0.0000030	0.8450970	Ge-A	Ge-A	Ge-A	Ge-A	Ge-A	Ge-A	Ge-A	Ge-A	Ge-A	Ge-A	Ge-A	Ge-A	Ge-A	Ge	Ge	Ge	Ge	Ge	Epoxy	Epoxy	Macor	Macor	Mylar	Air	Cu	Vacuum
0.0000025	0.8450995	Au	Au	Au	Au	Au	Au	Au	Au	Au	Au	Au	Au	Au	Au	Au	Au	Au	Au	Epoxy	Epoxy	Macor	Macor	Mylar	Air	Cu	Vacuum
0.0050000	0.8500995	Air	Air	Air	Air	Air	Air	Air	Air	Air	Air	Air	Air	Air	Air	Epoxy	Epoxy	Epoxy	Epoxy	Epoxy	Epoxy	Macor	Macor	Mylar	Air	Cu	Vacuum
0.0320000	0.8820995	Air	Air	Air	Air	Air	Air	Air	Air	Air	Air	Air	Air	Air	Air	Air	Macor	Macor	Macor	Macor	Macor	Macor	Macor	Mylar	Air	Cu	Vacuum
0.1146000	0.9966995	Cu	Cu	Cu	Cu	Cu	Cu	Cu	Cu	Cu	Cu	Cu	Cu	Cu	Cu	Cu	Cu	Cu	Cu	Cu	Cu	Cu	Cu	Cu	Cu	Cu	Vacuum
0.5000000	1.4966995	Cu	Cu	Cu	Cu	Cu	Cu	Cu	Cu	Cu	Cu	Cu	Cu	Cu	Cu	Cu	Cu	Cu	Cu	Cu	Cu	Cu	Cu	Cu	Cu	Cu	Vacuum

Figure 56. Risø telescope detector with 10 cm air above it. Legend: See previous page.

D Tables of conversion factors

This appendix lists the calculated conversion factors from planar fluence over a 1 cm^2 tissue disc or measured electron counts by the spectrometer to $H_p(0.07)$.

Table 26. Calculated conversion factor, η_{tissue}, from electron planar fluence over a 1 cm^2 disc at the central axis to $H_p(0.07)$ as a function of the mean energy of the electrons at tissue surface within the 1 cm^2 disc (equation 18). The electron source is ether a point source or a broad source 5 cm in radius placed at various distances from the tissue surface. The data are also shown in Figure 38 and 39 on page 72.

Source type	Distance from source to tissue surface	Mean electron energy	Conversion factor	Uncertainty	Uncertainty
	[cm]	[keV]	[nGy cm^2]	[nGy cm^2]	%
Point	1.34	69.0	0.000	0.0E+0	0.0
		72.6	0.325	2.3E-3	0.7
		83.1	1.057	7.4E-3	0.7
		93.5	1.409	5.6E-3	0.4
		119.1	1.471	5.9E-3	0.4
		144.5	1.281	5.1E-3	0.4
		194.9	0.937	3.7E-3	0.4
		245.1	0.739	4.4E-3	0.6
		295.2	0.615	3.1E-3	0.5
		394.9	0.492	3.9E-3	0.8
		494.7	0.425	3.0E-3	0.7
		594.5	0.389	1.9E-3	0.5
		793.8	0.351	1.8E-3	0.5
		993.2	0.326	1.6E-3	0.5
		1191.5	0.314	1.9E-3	0.6
		1491.3	0.298	1.5E-3	0.5
		1988.9	0.287	1.7E-3	0.6
		2487.1	0.279	1.4E-3	0.5
		2984.4	0.278	1.9E-3	0.7
		3482.3	0.277	1.7E-3	0.6
Broad	1.34	69.0	0.000	0.0E+0	0.0
		70.1	0.132	1.8E-3	1.4
		80.8	0.720	4.3E-3	0.6
		91.4	1.102	5.5E-3	0.5
		117.2	1.359	2.7E-3	0.2
		142.7	1.309	3.9E-3	0.3
		193.3	1.143	4.6E-3	0.4
		243.5	0.998	4.0E-3	0.4
		293.6	0.907	3.6E-3	0.4
		393.5	0.765	3.1E-3	0.4
		493.2	0.674	2.7E-3	0.4
		592.7	0.615	3.1E-3	0.5
		792.1	0.534	2.1E-3	0.4
		991.0	0.493	2.5E-3	0.5

continued on next page

Source type	Distance from source to tissue surface [cm]	Mean electron energy [keV]	Conversion factor [nGy cm^2]	Uncertainty [nGy cm^2]	Uncertainty %
		1189.8	0.466	2.3E-3	0.5
		1487.9	0.440	2.6E-3	0.6
		1986.1	0.411	1.6E-3	0.4
		2482.4	0.393	2.0E-3	0.5
		2980.6	0.381	1.9E-3	0.5
		3477.0	0.377	1.9E-3	0.5
Point	10.0	69.0	0.000	0.0E+0	0.0
		109.6	1.350	1.5E-2	1.1
		166.6	1.110	1.1E-2	1.0
		219.9	0.844	8.4E-3	1.0
		271.9	0.680	8.2E-3	1.2
		372.5	0.519	5.7E-3	1.1
		473.3	0.451	4.5E-3	1.0
		572.5	0.407	6.9E-3	1.7
		771.7	0.356	3.9E-3	1.1
		970.1	0.327	4.6E-3	1.4
		1166.4	0.314	4.4E-3	1.4
		1463.4	0.303	3.9E-3	1.3
		1957.1	0.288	4.0E-3	1.4
		2450.7	0.287	3.7E-3	1.3
		2943.9	0.273	4.9E-3	1.8
		3436.1	0.281	2.2E-3	0.8
Broad	10.0	69.0	0.000	0.0E+0	0.0
		106.9	1.300	1.7E-2	1.3
		164.5	1.143	1.3E-2	1.1
		218.1	0.925	8.3E-3	0.9
		270.2	0.760	4.6E-3	0.6
		371.3	0.578	6.9E-3	1.2
		471.4	0.495	6.4E-3	1.3
		572.1	0.447	4.5E-3	1.0
		769.6	0.387	5.0E-3	1.3
		967.8	0.370	5.2E-3	1.4
		1165.2	0.350	8.1E-3	2.3
		1461.1	0.329	2.3E-3	0.7
		2448.8	0.311	4.0E-3	1.3
		2941.0	0.300	2.4E-3	0.8
		3437.1	0.303	3.3E-3	1.1
Point	20.0	69.0	0.000	0.0E+0	0.0
		128.1	1.217	3.4E-2	2.8
		188.0	1.024	1.6E-2	1.6
		243.4	0.799	2.2E-2	2.7
		348.7	0.605	1.3E-2	2.1
		449.8	0.486	1.2E-2	2.4
		550.5	0.446	9.4E-3	2.1
		749.9	0.379	1.3E-2	3.3
		947.0	0.327	7.2E-3	2.2

continued on next page

Source type	Distance from source to tissue surface [cm]	Mean electron energy [keV]	Conversion factor [nGy cm^2]	Uncertainty [nGy cm^2]	Uncertainty %
		1143.5	0.324	1.0E-2	3.2
		1441.6	0.318	1.1E-2	3.4
		1930.9	0.285	8.3E-3	2.9
		2416.7	0.286	5.4E-3	1.9
		2915.0	0.279	8.7E-3	3.1
		3408.1	0.272	4.3E-3	1.6
Broad	20.0	69.0	0.000	0.0E+0	0.0
		126.6	1.227	2.2E-2	1.8
		187.3	1.041	3.0E-2	2.9
		242.1	0.859	1.4E-2	1.6
		347.7	0.596	1.4E-2	2.3
		450.5	0.495	9.9E-3	2.0
		550.0	0.439	9.6E-3	2.2
		750.1	0.380	8.4E-3	2.2
		946.9	0.352	1.0E-2	2.9
		1142.4	0.315	8.8E-3	2.8
		1439.5	0.319	1.0E-2	3.2
		1930.4	0.313	5.6E-3	1.8
		2421.3	0.301	7.2E-3	2.4
		2912.3	0.281	7.9E-3	2.8
		3395.6	0.282	7.1E-3	2.5
Point	30.0	69.0	0.000	0.0E+0	0.0
		151.8	1.135	4.1E-2	3.6
		211.0	0.913	1.8E-2	2.0
		322.9	0.673	2.2E-2	3.2
		425.5	0.559	2.4E-2	4.3
		528.7	0.446	1.8E-2	4.1
		725.9	0.388	1.6E-2	4.0
		925.5	0.344	7.6E-3	2.2
		1120.9	0.336	1.4E-2	4.1
		1417.0	0.306	9.2E-3	3.0
		1913.3	0.300	1.3E-2	4.2
		2393.2	0.289	1.3E-2	4.4
		2884.4	0.286	1.4E-2	4.9
		3369.3	0.306	1.8E-2	6.0
Broad	30.0	69.0	0.000	0.0E+0	0.0
		151.2	1.159	3.0E-2	2.6
		211.4	0.981	1.9E-2	1.9
		323.9	0.656	2.2E-2	3.3
		425.3	0.536	1.5E-2	2.8
		529.1	0.474	1.4E-2	3.0
		729.4	0.398	1.2E-2	3.1
		924.7	0.358	1.2E-2	3.4
		1118.7	0.324	1.1E-2	3.3
		1416.5	0.335	1.3E-2	4.0
		1904.3	0.299	1.0E-2	3.4

continued on next page

Source type	Distance from source to tissue surface [cm]	Mean electron energy [keV]	Conversion factor [nGy cm^2]	Uncertainty [nGy cm^2]	Uncertainty %
		2399.3	0.292	9.9E-3	3.4
		2875.1	0.295	1.1E-2	3.7
		3374.4	0.275	8.0E-3	2.9

Table 27. Calculated conversion factor, η_{det}, from measured electron counts by the spectrometer to $H_p(0.07)$ as a function of the measured mean energy (equation 17). The electron source is ether a point source or a broad source 5 cm in radius placed at various distances from the surface of detector 1. The data are also shown in Figure 38 and 39 on page 75.

Source type	Distance from source to the surface of detector 1 [cm]	Mean electron energy [keV]	Conversion factor [nGy cm^2]	Uncertainty [nGy cm^2]	Uncertainty %
Point	1.34	67.0	0.000	0.0E+0	0.0
		70.7	1.024	5.0E-3	0.5
		79.6	2.961	1.6E-2	0.5
		89.0	3.693	1.1E-2	0.3
		112.2	3.444	1.1E-2	0.3
		135.4	2.781	9.6E-3	0.3
		178.0	1.853	6.8E-3	0.4
		218.4	1.372	7.9E-3	0.6
		258.5	1.118	5.5E-3	0.5
		343.9	0.886	7.0E-3	0.8
		431.0	0.776	5.3E-3	0.7
		520.6	0.719	3.5E-3	0.5
		704.9	0.661	3.1E-3	0.5
		890.5	0.618	2.9E-3	0.5
		1076.6	0.607	3.4E-3	0.6
		1350.3	0.577	2.6E-3	0.5
		1811.1	0.550	3.0E-3	0.5
		2258.6	0.525	2.4E-3	0.5
		2692.6	0.518	3.4E-3	0.6
		3082.4	0.502	2.8E-3	0.6
Broad	1.34	67.0	0.000	0.0E+0	0.0
		69.0	0.825	7.7E-3	0.9
		77.9	3.930	1.7E-2	0.4
		87.0	5.627	2.1E-2	0.4
		109.6	6.176	9.8E-3	0.2
		132.1	5.475	1.4E-2	0.2
		173.3	4.259	1.5E-2	0.4
		211.0	3.477	1.3E-2	0.4
		248.5	3.031	1.1E-2	0.4
		324.7	2.451	9.3E-3	0.4
		402.7	2.095	8.1E-3	0.4

continued on next page

Source type	Distance from source to the surface of detector 1 [cm]	Mean electron energy [keV]	Conversion factor [nGy cm^2]	Uncertainty [nGy cm^2]	Uncertainty %
		481.2	1.875	9.2E-3	0.5
		642.7	1.595	6.3E-3	0.4
		808.7	1.452	7.2E-3	0.5
		973.8	1.364	6.8E-3	0.5
		1225.4	1.267	7.6E-3	0.6
		1645.1	1.154	4.6E-3	0.4
		2053.9	1.073	5.4E-3	0.5
		2447.5	1.011	5.1E-3	0.5
		2788.9	0.966	5.0E-3	0.5
Point	10.0	67.0	0.000	0.0E+0	0.0
		84.6	4.659	7.9E-2	1.7
		90.2	5.226	6.8E-2	1.3
		95.5	5.420	5.4E-2	1.0
		101.2	5.356	7.0E-2	1.3
		106.3	5.245	4.6E-2	0.9
		157.6	3.168	2.8E-2	0.9
		203.2	2.152	2.0E-2	0.9
		245.1	1.644	1.8E-2	1.1
		332.5	1.219	1.2E-2	1.0
		420.9	1.058	9.3E-3	0.9
		512.7	0.972	1.4E-2	1.5
		693.6	0.868	7.8E-3	0.9
		879.8	0.811	9.0E-3	1.1
		1066.1	0.778	8.6E-3	1.1
		1342.4	0.767	7.7E-3	1.0
		1798.0	0.724	7.8E-3	1.1
		2251.3	0.710	7.0E-3	1.0
		2688.4	0.671	9.2E-3	1.4
		3110.6	0.670	4.1E-3	0.6
Broad	10.0	67.0	0.000	0.0E+0	0.0
		104.0	5.582	5.7E-2	1.0
		154.7	3.648	3.5E-2	1.0
		199.1	2.551	2.1E-2	0.8
		240.5	1.975	1.1E-2	0.6
		323.9	1.441	1.6E-2	1.1
		411.7	1.221	1.4E-2	1.2
		498.9	1.103	9.9E-3	0.9
		677.4	0.953	1.1E-2	1.1
		857.3	0.925	1.1E-2	1.2
		1037.9	0.903	1.8E-2	1.9
		1307.3	0.846	5.0E-3	0.6
		2206.6	0.770	8.4E-3	1.1
		2651.9	0.740	5.0E-3	0.7
		3048.3	0.745	6.9E-3	0.9
Point	20.0	67.0	0.000	0.0E+0	0.0
		127.3	5.144	1.2E-1	2.3

continued on next page

Source type	Distance from source to the surface of detector 1 [cm]	Mean electron energy [keV]	Conversion factor [nGy cm^2]	Uncertainty [nGy cm^2]	Uncertainty %
		176.8	3.211	4.7E-2	1.4
		222.0	2.189	5.5E-2	2.5
		310.0	1.508	2.9E-2	1.9
		398.5	1.204	2.5E-2	2.1
		487.1	1.083	2.0E-2	1.8
		675.0	0.939	2.6E-2	2.7
		860.1	0.839	1.5E-2	1.8
		1041.6	0.823	2.1E-2	2.5
		1322.3	0.840	2.2E-2	2.6
		1774.9	0.739	1.6E-2	2.2
		2228.2	0.716	1.0E-2	1.5
		2671.2	0.683	1.6E-2	2.4
		3092.0	0.666	8.2E-3	1.2
Broad	20.0	67.0	0.000	0.0E+0	0.0
		123.9	5.340	8.0E-2	1.5
		176.7	3.431	9.0E-2	2.6
		218.9	2.436	3.6E-2	1.5
		310.4	1.522	3.2E-2	2.1
		395.6	1.222	2.2E-2	1.8
		486.4	1.092	2.1E-2	1.9
		675.2	0.935	1.7E-2	1.9
		853.1	0.917	2.2E-2	2.4
		1041.3	0.803	1.8E-2	2.3
		1312.3	0.834	2.1E-2	2.5
		1759.9	0.808	1.1E-2	1.4
		2215.3	0.782	1.5E-2	1.9
		2653.3	0.708	1.6E-2	2.2
		3067.8	0.701	1.4E-2	2.0
Point	30.0	67.0	0.000	0.0E+0	0.0
		151.5	5.549	1.7E-1	3.1
		201.2	3.141	5.8E-2	1.8
		288.4	1.890	5.5E-2	2.9
		375.5	1.490	5.9E-2	4.0
		471.0	1.137	4.1E-2	3.6
		649.9	1.007	3.4E-2	3.4
		838.3	0.907	1.6E-2	1.8
		1017.7	0.865	2.8E-2	3.3
		1297.0	0.820	1.9E-2	2.3
		1756.2	0.776	2.5E-2	3.2
		2212.7	0.740	2.5E-2	3.3
		2663.2	0.728	2.7E-2	3.7
		3056.8	0.780	3.6E-2	4.6
Broad	30.0	67.0	0.000	0.0E+0	0.0
		150.8	5.734	1.3E-1	2.3
		202.8	3.666	6.3E-2	1.7
		287.6	1.906	5.8E-2	3.1

continued on next page

Source type	Distance from source to the surface of detector 1 [cm]	Mean electron energy [keV]	Conversion factor [nGy cm^2]	Uncertainty [nGy cm^2]	Uncertainty %
		378.0	1.413	3.6E-2	2.6
		471.2	1.275	3.4E-2	2.6
		645.9	0.999	2.6E-2	2.6
		843.1	0.898	2.5E-2	2.8
		1023.9	0.854	2.3E-2	2.7
		1290.3	0.886	2.8E-2	3.2
		1739.1	0.747	2.0E-2	2.7
		2201.9	0.753	2.0E-2	2.6
		2633.6	0.725	2.1E-2	2.9
		3051.8	0.686	1.5E-2	2.3

E Description of software

This appendix gives a description of the software developed for control of the Risø Telescope Spectrometer, data acquisition and data analysis. The outline followed is inspired by PTB guidelines for software documentation [50].

1. **Program Characteristics**
   (a) **Program identification**
      i. Program name
      Control- and data acquisition: `RTS control v24.exe`
      (Source code: `RTSv24.llb > Bias and temperature control and monitoring.vi`
      Subsequent call to `RTSv24.llb > Operate acquisition 2D.vi`).
      Data analysis: `RTS analysis v24.exe`
      (Source code: `RTSv24.llb > Data analysis.vi`).
      ii. Current version
      This documentation is based on v24, December 1998.
      iii. Program release
      The data acquisition program is only to be used with the Risø Telescope Spectrometer (RTS) model 1. No policy has yet been made for the distribution of the program or its source code.
   (b) **Keywords**
   Detector control, test of detector functionality, data acquisition, determination of electron and photon spectra, calculation of dose rate.
   (c) **Program abstract**
      i. Program task
      The control- and data acquisition program consist of two distinct program tasks:
      - Detector control. By servo-control to keep the bias of the tree detectors at a constant level independent of detector temperature and leakage currents. By servo-control to keep the temperature of the detector unit at predefined level. A separate task is to perform a test sequence which plots the relationship between bias and leakage current for each detector. The test provides a tool to check the quality of the detector assembly.
      - Data acquisition. To define noise levels, acquisition lengths etc. Record accepted pulse heights and convert these to absorbed energy. Discriminating between electrons and photons and displaying their respective spectra. Calculation of absorbed dose rate $\dot{H}_p(0.07)$ in tissue at depth 0.07 mm.

      The task of the data analysis program is similar to the acquisition program except that recording of pulse heights from the detector unit is disabled and data are instead read from a file. Extra analysis tools are available.
      ii. Program run
      Detector control and acquisition. The newest shaping filters in the `RTS\system` directory are automatically uploaded to the detector base unit and initialization files with servo-control parameters, conversion factors etc. are read. Detector bias can then be applied. When the desired bias is reached acquisition is allowed. The acquisition window is launched from the detector control window. Before an acquisition can take place the user must specify a filename (without extension) for data-logging. Different types of log- and data files

will be created with different extensions. If the recorded data is to be stored, the user must specify a format (digital pulse heights or pulse heights in units of keV). Calculation of absorbed dose rate $\dot{H}_p(0.07)$ is performed by folding the energy spectra for electrons with suitable conversion factors.
Data-analysis. The user must first specify a filename for the data file to analyze. If the data file exists in more than one format the user must choose one of these formats. The data analysis can then be performed in a similar way as in the acquisition program. An extensive analysis tool can be invoked. Statistical data and histograms can be printed or written to a file.

(d) **Device required**
Minimum: Pentium or similar, 133 MHz, 32 Mb RAM, 15 Mb free space on hard-drive, mouse. For data acquisition: GPIB card installed.
Recommended: Fast hard-drive, minimum 500 MHz, 128 Mb RAM.

(e) **Program size for executables**
Detector control and acquisition: 3.4 Mb
Data-analysis: 3.3 Mb
LabView runtime-engine: 3.2 Mb

(f) **Program requirements**

i. Operating system
Windows 9x, 2000, NT.

ii. Programming language
The programs are developed in the graphical programing environment 'G' using LabView™ 4.1, 5.0 and 5.1 from National Instruments. The current version is build under version 5.1. Executable files can run without LabView, but the LabView runtime-engine must be installed. The runtime-engine is free-ware and can for example be downloaded from the National Instruments web-site (www.ni.com).

iii. Other requirements
For data acquisition: GPIB software installed. This software is bundled with the LabView 5.1 distribution, but can also be downloaded from the National Instruments web-site.

(g) **Data organization**
The program make use of 6 initialization files and produces 9 types data- and log-files. These files are described in this paragraph. If an initialization file does not exist, a standard one will automatically be created. Files for storing acquisition data can be arbitrary placed.

i. File structure

The file structures of the programs are sketched in figure 57 and 58.

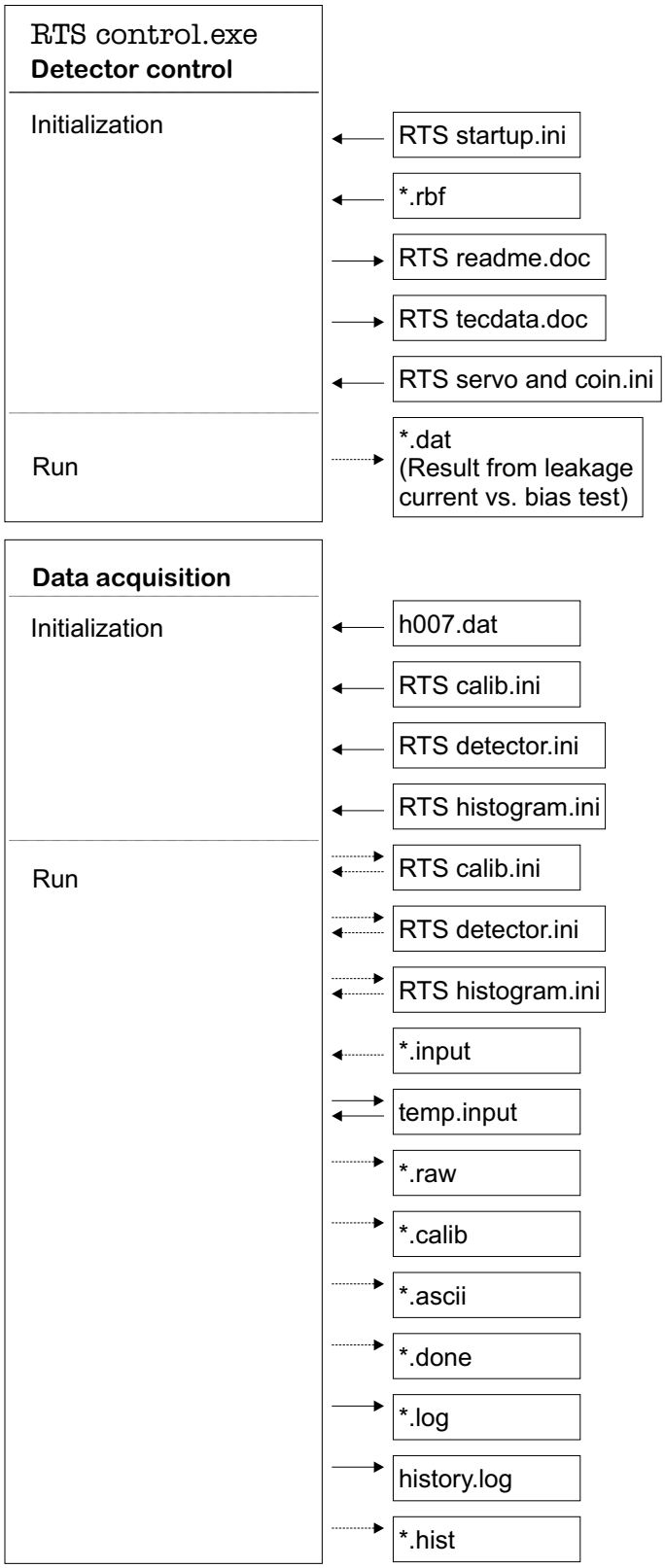

Figure 57. File structure of the detector control and acquisition program. Dotted lines indicates that the read or write of a files is determined by the user.

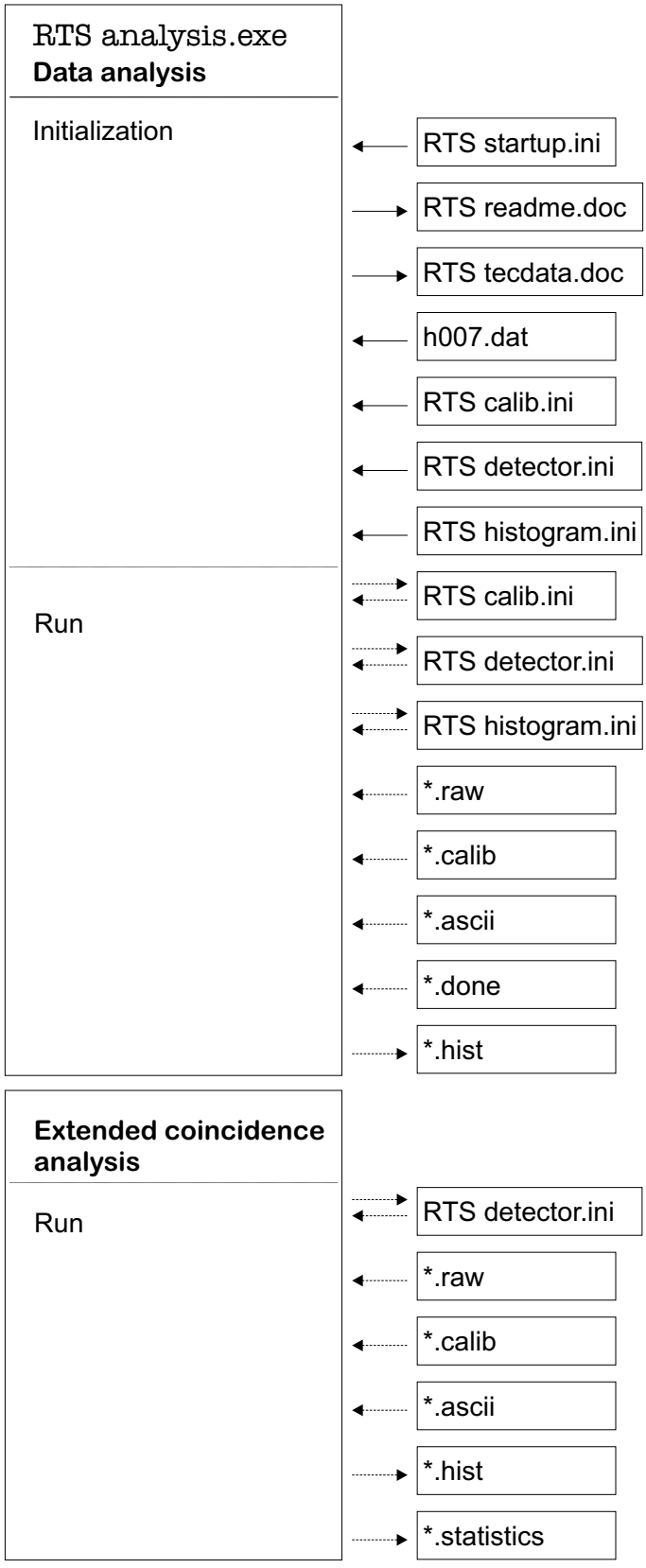

Figure 58. File structure of the data analysis program. Dotted lines indicates that the read or write of a files is determined by the user.

Table 28. Coincidence patterns. '•' indicates a registered energy absorption above the noise/particle threshold.

Coincidence pattern	Detector 1	Detector 2	Detector 3	Normal classification
1	-	-	•	Photon
2	-	•	-	Photon
3	-	•	•	Not defined
4	•	-	-	Electron (low energy)
5	•	-	•	Redefined as photon due to noise
6	•	•	-	Electron (medium energy)
7	•	•	•	Electron (high energy)

ii. File descriptions:

Initialization files

`RTS startup.ini` (Windows directory)

'Use_path=[Path]': Path to the directory the user prefers to place data files.

'RTS_file_path=[Path]': Path to the directory where initialization files are placed, in the following called 'RTS system directory'.

'GPIB_cable_length=[{1,8}, meters]': Length of the GPIB cable.

'Temperature=[0 . . . 30, degrees Celsius]': Prefered temperature of the detector assembly.

'Sound=[on/off]': Decides whether beebs should sound when the specified detector bias is reached or left.

'True_exit=[on/off]': Determines if the windows should close when the exit button is pressed. The 'off' position is only relevant for program development.

`RTS servo and coin.ini` (RTS system directory)

'd1_up_velocity, d1_down_velocity, d1_down_penalty, d2_velocity, d3_velocity=[Real]': Parameters used in the servo-control of the bias voltage. These values should not be changed.

'coinpattern_electrons=[List of comma separated unsigned bytes]': List of coincidence patters to be interpreted as electrons. See Table 28.

'coinpattern_photons=[List of comma separated unsigned bytes]': List of coincidence patters to be interpreted as photons.

'correctionfactor_a, correctionfactor_b=[Real]': Coefficients for an optional skin dose correction equation.

`RTScalib.ini` (RTS system directory)

The calibration of each detector is described by the equation $E_n(dp) = A_n \cdot dp + B_n$, where n is the detector number {1,2,3} and dp the digital pulse height measured in digital units $\{0 \ldots 255\}$.

'calib1a=[Real]': A_1, 'calib1b=[Real]': B_1
'calib2a=[Real]': A_2, 'calib2b=[Real]': B_2
'calib3a=[Real]': A_3, 'calib3b=[Real]': B_3

`RTSdetector.ini` (RTS system directory)

'delay1, delay2, delay3=[0 . . . 31]': Delay between the three detectors in units of 83.33 ns.

'threshold1, threshold2, threshold3=[0 . . . 255]': The noise threshold for the three detectors in units of digital pulshight.

'p-threshold1, p-threshold2, p-threshold3=[0 . . . 255]': The particle threshold for the three detectors in units of digital pulshight.

'scew=[0 . . . 15, ×83.33 ns]': Time window in which pulse hight registerations from the detectors are said to be coincident. There is an offset of 160 ns.

'streamtimeout=[Real, seconds]': The same as frame timeout described on page 135.

`RTShistogram.ini` (RTS system directory)

'elecmin, elecmax=[Signed integer, keV]': The minimum and maximum value of the histogram showing the energy distribution of electrons in the Data acquisition window. The maximum value displayed is however adjusted by software (but only to a lower value) to make a nice looking histogram.

'photmin, photmax=[Signed integer, keV]': As above but for the photon histogram.

'bins=[Unsigned integer]': Number of bins in the 'electron', 'photon' and 'total' histogram displayed in the Data acquisition window.

Other initialization files

`*.rbf`

Shaping filter (binary).

`h007.dat`

Comma separated ASCII file containing the ICRU conversion factors from electron planar fluence [cm^{-1}] to absorbed dose at 0.07 $\mathrm{mg/cm}^2$ tissue [nGy] [35]. The file structure is sketched below (*Angle* being the incident angle of the electron beam, *Energy* the electron energy in keV, *factor* the conversion factor, `<CR>` carriage return, `<LF>` line feed).

$$\begin{array}{cccc} 0, & Angle_1, & \ldots, & Angle_n \\ Energy_1, & factor_{1,1}, & \ldots, & factor_{1,n} \\ \vdots, & \vdots, & \ddots, & \vdots \\ Energy_m, & factor_{m,1}, & \ldots, & factor_{m,n} \end{array} \begin{array}{l} \texttt{<CR><LR>} \\ \texttt{<CR><LR>} \\ \texttt{<CR><LR>} \\ \texttt{<CR><LR>} \end{array}$$

Information files

`RTS read me.doc, RTS tecdata.doc` (RTS system directory)

ASCII text files with information about the software and the detector. Can also be seen by pressing the 'about' button.

Input files

`workfile.input` (optional). 'workfile' should be read as an arbitrary filename.

User defined batch file, which can control one or more data acquisitions. The following commands are available with allowed arguments

in brackets and square brackets. In the following '∞' is used in a very loose fashion, usually meaning the maximum value of a double precision real - keeping in mind that numerical round-off errors may influence on the programs functionality for very high values.

'acq' Starts the acquisition.

'beep' Makes a beep.

'comment=[Text string]' Comment.

'counts=[0 . . . 4.294.967.295]' Maximum number of counts in an acquisition. If zero this value is interpreted as 4.294.967.295.

'delay(0 . . . 3)=[1 . . . 31]' Time delay of the detector. First argument: the detector number. Second argument the delay in units of 83.33 ns.

'display=[on/off]' Toggles whether energy distributions should be calculated and displayed.

'framefilecalib=[on/off]' If [on]: Writes the acquired data in a calibrated fashion (i.e. pulse heights in keV) in a binary file named `workfile.calib`.

'framefileraw=[on/off]' If [on]: Writes the acquired data in a raw format (i.e. digital pulse heights) in a binary file named `workfile.raw`.

'frametimeout=[0.1 . . . ∞]' Maximum time in seconds of a sub-acquisition. An acquisition is usually split into shorter acquisitions and these are called sub-acquisitions.

'maxframesize=[0 . . . $\infty/3$]' '∞' being the computers free memory in bytes. Maximum number of triplets (3 bytes) transferred from the base unit to the computer per sub-acquisition.

'nextfile' Changes the name of the workfile. E.g. `workfile` to `workfile1` to `workfile2` etc.

'p-threshold(1 . . . 3)=[1 . . . 255]' Particle threshold. First argument: the detector number. Second argument the threshold value in digital pulse height.

'printgraph=[1,2,3,e,p,t,a]' Prints the energy distribution histograms on the default Windows printer. [1,2,3]: detector 1,2 and 3. [e,p,t]: electrons, photons, total. [a]: all.

'readout=[0 . . . ∞]' If zero or argument is left out: Writes to the ASCII file `workfile.log`. See file contents below. This operation can be repeated at regular time intervals specified by the argument in seconds.

'rem' Remarks.

'savegraph=[1,2,3,e,p,t,a]' Saves the energy distribution histograms to a ASCII file named `workfile.hist`. [1,2,3]: detector 1,2 and 3. [e,p,t]: electrons, photons, total. [a]: all.

'scew=[0 . . . 15, $\times$83.33 ns]' Time window in which pulse hight registerations from the detectors are said to be coincident. There is an offset of 160 ns.

'servo(%)=[0 . . . 95]' Percentage of the maximum allowed bias voltage applied to all three detectors by the servo-control.

'servo(1)=[0 . . . 6.65]' Bias voltage [V] applied to detector 1 by the servo-control.

'servo(2)=[0 . . . 44.65]' Bias voltage [V] applied to detector 2 by the servo-control.

'servo(3)=[0 . . . 332.5]' Bias voltage [V] applied to detector 3 by the servo-control.

'sound=[on/off]' Decides whether beebs should sound when the specified detector bias is reached or left.

'stop' Sets detector bias equal zero and stops the program.

'temperature=[0 . . . 30]' Prefered temperature of the detector assembly in degrees Celsius.

'threshold(1 . . . 3)=[1 . . . 255]' Noise threshold. First argument: the detector number. Second argument the threshold value in digital pulse height.

'time=[0 . . . ∞]' Maximum time in seconds of an acquisition. If zero this value is interpreted as infinity.

'voltage(1)=[0 . . . 50.0]' Voltage [V] applied to detector 1.

'voltage(2)=[0 . . . 100.0]' Voltage [V] applied to detector 2.

'voltage(3)=[0 . . . 800.0]' Voltage [V] applied to detector 3.

'wait=[0 . . . ∞]' Seconds to wait.

'waituntilready' Wait until the specified detector bias is reached.

`temp.input` (RTS system directory)

When the start acquisition button is pressed the settings made in the graphical user interface are compiled into a batch-file called `temp.input` using the operators described above. This input file is then read by the command interpreter.

Logfiles

`*.done`

A copy of the `temp.input` file describing the commands used for the acquisition. Acquisition time and number of counts registered is also written in this file. Information about time of execution is also written. An example of a `*.done` file is shown in Figure 74 on page 148.

`*.log`

File containing information about: Date [d:m:y], Time [h:m:s], Time [seconds since 12:00 am, January 1, 1904], Detector bias [V], Percent of maximum bias voltage [%], Temperature of detector assembly [°C], Leakage currents [μA], Last registered count rate [s^{-1}], Last registered dose rate [mSv/h], Frame timeout [s], Deadtime in last sub-acquisition [ms].

`history.log` (RTS system directory)

Every time an acquisition starts and ends the following data is written to the `history.log` file: Date [d:m:y], Time [h:m:s], Time [seconds since 12:00 am, January 1, 1904], Detector bias [V], Percent of maximum bias voltage [%], Leakage currents [μA], Temperature of detector assembly [°C]. The intention with this file is to have a long term logging of the state of the detector.

Output files

`*.hist`

Histograms (First column: x values; second column: y values).

`*.statistics`

ASCII file with information about the distribution of coincidence patters, registered counts, mean energy etc.

Recording files

`*.ascii`

ASCII file with absorbed energy in keV. (First column: detector 1; second column: detector 2; third column: detector 3).

`*.calib`

Binary file with absorbed energy in keV. The pulse height in keV from each detector is represented by single precision (4 bytes), and each count is grouped in a triplet i.e. the value from detector 1 followed by the value from detector 2 followed by the value from detector 3.

`*.raw`

Binary file with digital pulshights $\{0 \ldots 255\}$. Each detector is represented by an unsigned byte, and each count as a triplet.

(h) **Responsibilities**

The routine for transferring data between the base unit and the computer is written by Henning Larsen, Department for Optic and Fluid dynamics, the rest by Jakob Helt-Hansen, Department for Radiation Safety Research, both Risø National Laboratory. Neither the authors nor Risø take any responsibility for damage this program may cause (direct or indirect).

2. **Program function**

(a) **Function**

i. Brief description

The program acquire digital pulse heights from the three detectors and converts these values to absorbed energy in keV. In the case of the data analysis program digital pulse heights or calibrated values has to be obtained from a file. The coincidence pattern for each count is found and the energy distribution for electrons, photons, all counts and the three detectors is calculated. The energy distribution for electrons is folded by conversion factors to calculate the dose rate at 0.07 mm tissue. White noise is added to the energy values to facilitate the summation and display of digitized spectra [22].

ii. Units of measurements

All energy measurements are computed in keV. Histograms of energy distribution is shown as counts per keV. Absorbed dose is computed in nGy.

(b) **Task solutions**

i. Algorithm for identification of particles using particle thresholds.

Let NT_n be the noise threshold for detector n, $n \in \{1, 2, 3\}$, and PT_n be the particle threshold. Let E_n be the energy registered in detector n.

If $E_n \geq NT_n$ for any n, let the equation $E_n \geq PT_n$ determine the value of the coincidence pattern following the scheme in Table 28 on page 126.

ii. Algorithm for adding white noise to digital pulse heights.

Each detector is calibrated by the equation $E_n(dp) = A_n \cdot dp + B_n$, where n is the detector number {1,2,3} and dp the digital pulse height $\{0 \ldots 255\}$. Let $Random(1)$ be a computer generated random number between 0 and 1. For every count white noise is added to the detectors where energy has been registered using the equation:

$$E_{n,\text{noise}} = E_n(dp) + A_n(Random(1) - 0.5)$$

iii. Algorithm for calculation of $H_\text{p}(0.07)$.

Let $\overrightarrow{H}_{\overrightarrow{E_c}}$ be an array describing the conversion factor from measured electron counts (or electron fluence if the ICRU factors are used) to dose at 0.07 mm tissue for a discrete number of energies, $\overrightarrow{E_c}$.

Let H(E) be a function which for a given energy E by linear interpolation in $\overrightarrow{H}_{\overrightarrow{E_c}}$ finds a conversion factor value.

Let $\overrightarrow{N}(E)$ be the measured energy spectrum, where N is the number of counts for a given bin, and E is the midpoint energy of the bin. Assume there is n bins in the spectrum. (Note that the measured spectrum differs from the displayed spectrum since the latter is normalized per unit energy). The dose at 0.07 mm tissue is calculated by

$$H_\text{p}(0.07) = \sum_{i=1}^{n} N(E_i) \cdot \text{H}(E_i)$$

If the ICRU factors are used, the result should be multiplied by two since the area of detector 1 is 0.5 mm^2.

3. **Program structure**

The program structure is depicted in Figure 59 and 60.

4. **Program run**

This section describes the functionality of the different windows in the detector control & acquisition program and data analysis program. All options are identified by a name followed by a symbol showing how they interact.

☒: A tagbox
□: A field to enter text or numbers.
■: A button with two or more options.

Figures of screen prints are listed in section E.1 on page 143 ff.

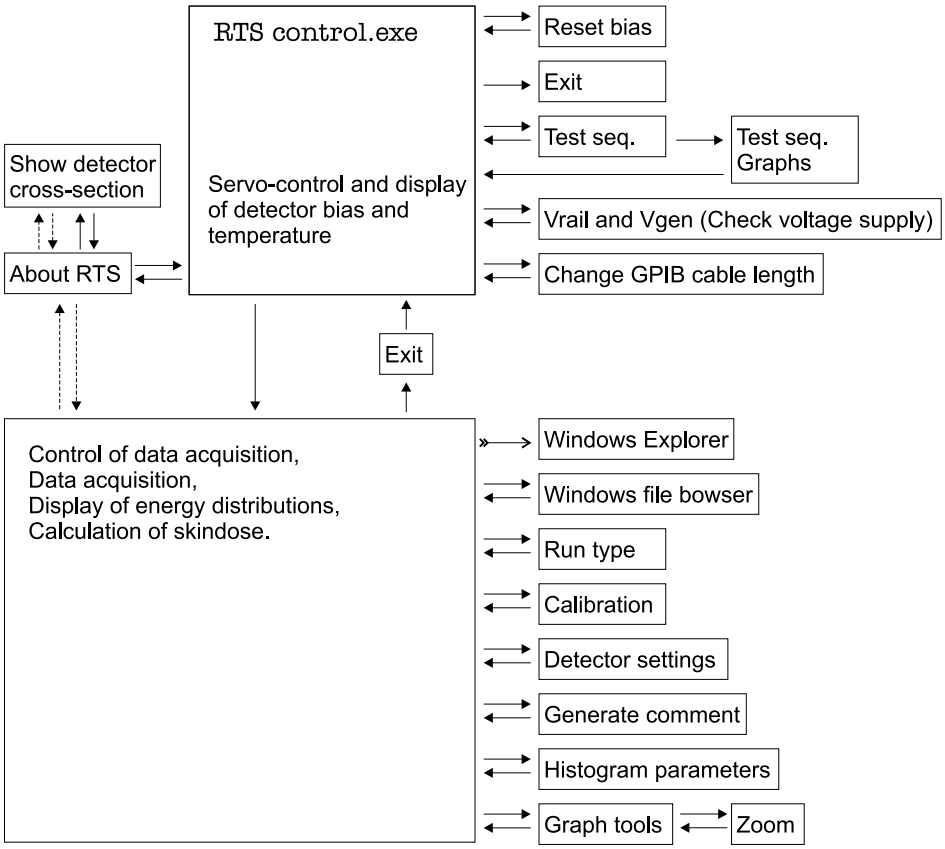

Figure 59. Program structure of the detector control and acquisition program.

Detector control (Main window).
Figure 61.

[Manual voltage setting] ☒.☐. Allows the user to set the voltage supply to the detectors manually. Note that this voltage is higher than the actual bias voltage due to leakage currents.

[Servo-controlled bias setting] ☒.☐. Allows the user to specify the bias voltage to the tree detectors. The voltage is specified as a percentage (usually 95%) of the maximum bias specified by the detector manufacture.

[Servo-controlled bias setting. Key in] ☒.☐. Allows the user to specify the bias voltage individually for each detector.

[Reset bias] ■. Shifts to Manual voltage setting and sets the voltage to zero.

[Reset] ■. Only visible when detector bias is applied. If a detector bias becomes higher than the maximum allowed bias, the detector is automatically shut down by hardware. To make the detector function again, a bias voltage of 0 V must be specified, and this can be done by pressing this button.

[Exit] ■. Stops the program.

[Temperature] ☐. Sets the temperature of the detector unit in degrees Celsius.

[Bandwidth] ☐. Sets the interval in which the temperature is allowed differ from the user specified value before the servo-control interacts.

[Test sequence] ■. Launches a subroutine to map the relationship between

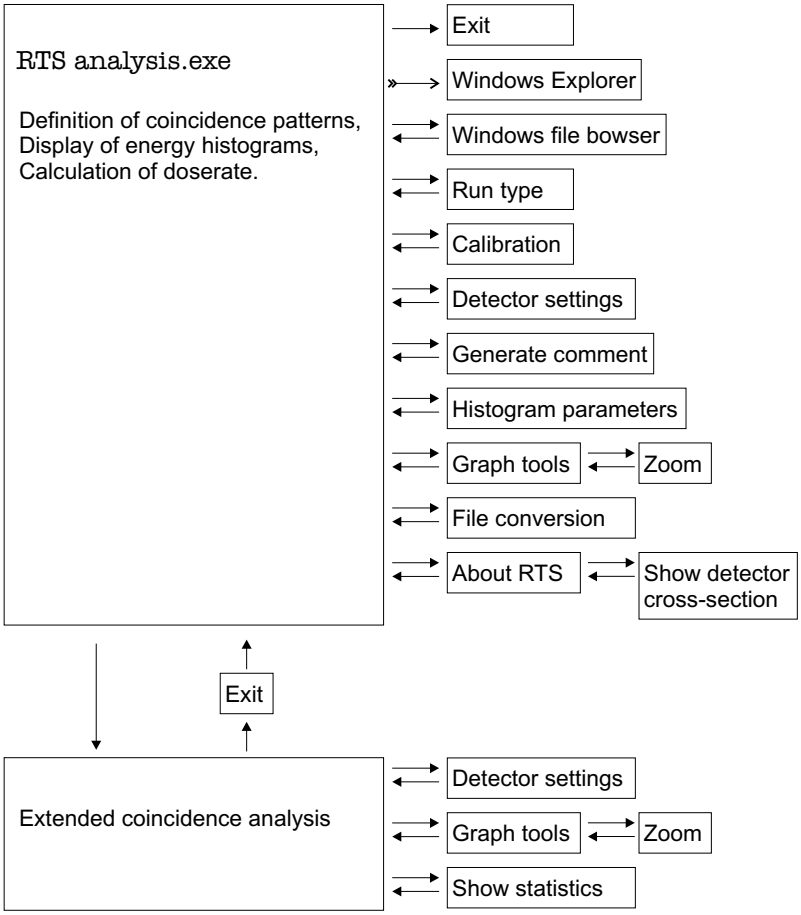

Figure 60. Program structure of the data analysis program.

bias voltage and leakage current.

[Sound on/off] ■. Toggles whether one 'beep' is heard when the specified bias is reached and two 'beebs' is heard if this state is left.

[Vgen/Vrail] ■. Displays the rail- and generator voltage.

[Change cable length] ■. Launches a window where the user is able to specify a new GPIB cable length. The program needs to know this length for timing proposes.

[Update period] □. How often the graphs in the 'Detector control window' are updated. Note that the time constants in the servo-control are not affected by this value.

[Launch acquisition] ■. Launches the Data acquisition window.

[About] ■. (Available in menubar). Launches a window with information about the Risø Telescope Spectrometer and the program.

Detector control > Test sequence.
Figure 62.

[Number of points to measure] □. The number of points between 0 and 95% of maximal detector bias for which the leakage current should be measured.

[Measure at temperature] □. The desired temperature of the detector unit in degrees Celsius.

[Abort test sequence if leakage current exceeds] ☒. Maximum allowed leakage current in μA.

[Cancel] ■. Returns to the 'detector control window' without performing the test.

[Start] ■. Begin the test sequence.

Detector control > Test sequence > Test sequence graphs (Show test result window).
Figure 63.

[Print data as graphs] ■. Prints the test result (i.e. leakage current versus bias voltage for each detector) to the default Windows printer.

[Write data to file] ■. Writes the data in an user specified ASCII file.

[Exit] ■. Returns to the 'Detector control window'.

Detector control > About (About window).
Figure 64.

[Show information about] ■. Toggles whether the information displayed is about the software or the detector unit.

[Show cross-section of the detector] ■. Launches a drawing of the detector which can be printed out.

Detector control > Data acquisition (Data acquisition window).
Figure 65.

[Run from inputfile] □. All buttons etc. in the data acquisition window, can be controlled by commands in a batch-file. If such a batch-file is used the 'Run from inputfile' should be tagged and the filename specified in the 'Inputfile' box below.

[Write .done file when recording] ☒. The `*.done` file is an ASCII file with all the commands used in the data acquisition plus information about acquisition time and number of registered counts. Some of this information is used by the data analysis program described later. If the user is performing a large number of test acquisitions it may be an advantage to un-tag this box.

[Press to save recorded counts raw/calibrated] ■. Pressing the 'raw' button will save the registered digital pulse heights in a binary file named `workfile.raw`. Pressing the 'calibrated' button will save the absorbed energy (in keV) registered in the three detectors in a binary file named `workfile.calib`. '`workfile`' being the filename specified in the 'workfile box'. Both buttons can be pressed at the same time.

[Workfile] □. The name of the data acquisition session. Data- and logfiles will have this name, but with different extensions. See also browse button below.

[Explorer] ■. Launches the Microsoft Windows Explorer.

[Next] ■. Changes the workfile name e.g. to `workfile1`, `workfile2` etc.

[Browse] ■. The only way to specify input- and/or workfiles is by using the standard Windows browser launched by pressing this button. This makes it impossible to specify an illegal filename.

[File operation] ■. Toggles whether it is allowed to overwrite an existing file.

[Write status every] □. Information about leakage currents, detector temperature etc. is written to a logfile (`*.log`) at the start and end of every acquisition. By specifying a time interval different than zero, this information will be written at regular intervals.

[Time] □. Maximum acquisition time in seconds. If zero this value will be interpreted as infinity.

[Counts] □. Maximum counts to register. If zero, this value will be interpreted as 4.294.967.295 i.e. the maximum value for an unsigned long.

[Wait] □. Seconds to wait for the acquisition to begin (after the 'start' button has been pressed).

[Clear] ■. Sets the 'Time', 'Count' and 'Wait' values to zero.

[Wait until ready] ☒. Holds the start of an acquisition to all detectors has reached the desired bias voltage.

[Comment] □. Text string to be written in log files.

[Generate] ■. Launches a window where the user can choose from a variety of predefined text pieces (e.g. different types of shielding) to ease the making of a comment. Figure 66.

[Clear] ■. Clears the comment.

[Runtime], [Calibration], [Detector settings] ■. Launches setup windows for data acquisition. See descriptions bellow.

[Max. framesize] □. A frame is amount of data (i.e. number of triplets) which is transferred from the base unit to the computer at a time. If the base unit receives more triplets from the detector than specified by the maximum framesize, the acquisition will temporarily stop and the data is send to the computer. The framesize is allocated in the memory of the computer. See also 'Frame timeout'.

[Frame timeout] □. An acquisition is usually split up into smaller sub-acquisitions of e.g. one second (frame timeout). This is done partly to reduce the memory allocated for the framesize partly to give a more smooth operation of the instrument.

[Flush] ■. It can sometimes be convenient to stop the analysis of triplets, e.g. if one is hung in a very large frame. This button will skip the analysis of the rest of the frame.

[Display detectors/particles] ■. Toggles the energy distributions shown in the histograms between 'detector 1, detector 2 and detector 3' and 'electrons, photons and total'.

[Display frames/sum up] ■. Toggles between whether the energy distributions shown in the histograms are replaced for every frame or if the frames are summed i.e. the distributions shown are the accumulated counts since the start of the acquisition.

[Show ... frame] ■. Since the analysis of the triplets is the most time consuming part of data acquisition (compared to the time used to write the data

to a file for later analysis), one can skip the analysis of all or some of the frames.

[Clear] ■. Clears the histograms.

[Histogram] ■. Launches a window where the user can specify the number of bins and energy range for the electron and photon histograms. The energy range for the 'total'-histogram is taken as the maximum of the energy intervals specified. Figure 70.

[Graph tools] ■. Launches a window showing absorbed energy distribution histograms. See description below.

[Start] ■. Starts the acquisition.

[Exit] ■. Returns to the 'Detector control window'.

[ ] ■. Under each histogram is a palette of tools to manipulate the histograms. This is a standard LabView tool. The scaling of the x- and y-axis is disabled in the 'data acquisition window', since the scaling is done by software to ensure a nice looking histogram.

Detector control > Data acquisition > Run type.
Figure 67.

[Data source] ■. For acquisition this button should be placed at 'detector'. The detector unit has and internal pulse generator which can be used for testing purposes by switching to 'test data'.

[Test source] ■. For acquisition this button should be placed at 'internal'. The detector probe has inputs for external pulse generators which can be used for testing purposes by switching to 'external'.

[Detector control feed] ■. In the 'on-line' position information about noise thresholds, acquisition length etc. is passed to the detector unit in the beginning of each sub-acquisition enabling the user to change e.g. noise thresholds while a acquisition takes place. Passing this information takes time and the user can make a faster acquisition by changing to 'at acq. start', where the information is send only once. This may be an advantage if one have a low count rate.

Detector control > Data acquisition > Calibration.
Figure 68.

[Detector {1,2,3},{A,B}] □. Each detector is calibrated using a first order polynomial, $E_n(dp) = A_n \cdot dp + B_n$, where n is the detector number {1,2,3} and dp the digital pulse height $\{0 \ldots 255\}$.

[Save] ■. Saves the specified values to an initialization file (`RTScalib.ini`).

[Load] ■. Loads the values last saved in the initialization file (`RTScalib.ini`).

[Digital units] ■. Sets $A_n = 1.0$ and $B_n = 0.0$ for all n, where n is the detector number {1,2,3}.

[Ok] ■. Returns to the 'data acquisition window'.

Detector control > Data acquisition > Detector setting
Figure 69.

[Noise threshold] □. Noise threshold for the three detectors. The value is inscribed in digital pulse heights, and shown in keV.

[Particle threshold] □. Particle threshold for the tree detectors.

[Detector delays] □. It is important that the pulses from a particle depositing energy in all three detectors are aligned in time. By changing the delay one can displace the pulses relative to each other. The displacement time is inscribed in units of 83.33 ns.

[Scew] □. Time window in which pulse height registrations from the detectors are said to be coincident. In units of 83.33 ns. There is an offset of 160 ns.

[Save] ■. Saves the specified values to an initialization file (`RTSdetector.ini`).

[Load] ■. Loads the last saved values from the initialization file (`RTSdetector.ini`).

[Ok] ■. Returns to the 'data acquisition window'.

Detector control > Data acquisition > Graph tools
Figure 71.

[Electrons, photons, etc.] ☒. By tagging these boxes one can decide which graphs to be printed if the [Print] button is pressed, or to be saved to an ASCII file (`*.hist`) if the [Save] button is pressed.

[Particle, photons, all, clear] ■. Put tags in the boxes described above.

[Print this page] ■. Prints the screen on the default Windows printer.

[Ok] ■. Returns to the 'data acquisition window'.

[Zoom] ■. Launches a window with the selected histogram, where it is possible to manipulate different features. Figure 72.

Detector analysis (Main window).
Figure 73.

[Source file] □. The name of the file to analyze.

[Browse] ■. Launches Windows browser to locate the source file.

[Explorer] ■. Launches Windows Explorer.

[Select a filename . . .] ■. To select the data type used for the analysis (if more than one is present).

[Read . . . counts] ■. Specify how many counts to read before ending the analysis.

[If not finished] ■. If the 'stop' button is pressed before an analysis has ended, the 'make display' button will ether restart the analysis or start from the point it was stopped.

[Detector settings] ■. See similar button described above (page 137).

[Calibration] ■. See similar button described above (page 136).

[Comment] □. Text string to be placed on printouts.

[Clear] ■. Clears the comment box.

[Load .done file] ■. Only visible when a `workfile.done` file is present. Loads comments and acquisition time from the `workfile.done` file.

[Show .done file] ■. Only visible when a `workfile.done` file is present. Launches a window showing the content of the `workfile.done` file. Figure 74.

[File Conversion] ■. Only visible when a source file has been selected. Launches a window where the user is able to convert between the `*.ascii`, `*.raw` and `*.calib` file formats. See description below.

[Random noise filter] ■. Only visible when a source file has been selected. Enable white noise filter to eliminate artifacts in the energy distribution histograms due to the large spacing between the digital pulse heights.

[Extended coincidence analysis] ■. Launches a window with extended analysis tools. See description below.

[Display] ■. Toggles the energy distributions shown in the histograms between 'detector 1, detector 2 and detector 3' and 'electrons, photons and total'.

[Coincidence patterns] □. Each coincidence pattern has a number described in Table 28 on page 126. In these boxes the user can specify which patterns should be assigned to electrons and photons respectively.

[Use $H'(0.07)$ conversion coefficients] ■. In the case where the ICRU values [35] is used for converting electron fluence into dose at 0.07 mm tissue, this button is used to choose the incident angle.

[Graph tools] ■. Launches a window showing energy distribution histograms. See above (page 137).

[Histogram parameters] ■. Launches a window for setting up parameters for the energy distribution histograms. See description below.

[Make display] ■. Starts the analysis.

[Exit] ■. Stops the program.

[Stop] ■. Only visible during an analysis. Stops the analysis. See also the 'If not finished' button above.

Detector analysis > File conversion.
Figure 75.

[Workfile] ■. Name of the file to convert.

[Source file] ■. Name of the file to create.

[Browse] ■. Windows browser to select workfile and source file.

[Convert (workfile)] ■. To select a format if more than one is present.

[to (source file)] ■. To select one or two formats for the converted file.

[Include] ☒. Include only the specified coincidence patterns in the converted file.

[Detector settings] ■. See similar button described above (page 137).

[Calibration] ■. See similar button described above (page 136).

[Number of counts to include] ■. Limit the converted file to this size.

[Make sourcefile] ■. Start the conversion.

[Automatic] ■. Convert all the files in the directory the workfile is placed.

[Exit] ■. Returns to the data analysis window.

Detector analysis > Histogram parameters.
Figure 70.

[From sourcefile] ■. Find minimum and maximum energy values in the histograms by searching the sourcefile.

[From calibration] ■. Let $E_n(dp) = A_n \cdot dp + B_n$, where n is the detector number {1,2,3} and dp the digital pulse height, be the calibration for each detector. Define the minimum of the energy interval in the histogram as:
Electrons, photons and total: $\min(B_1, B_2, B_3)$. Detector n: B_n.
Define the maximum energy interval in the histogram as:
Electrons, photons and total: $\sum_{n=1}^{3} A_n \cdot 255 + B_n$. Detector n: $A_n \cdot 255 + B_n$.

[Cancel] ■. Returns to data analysis window without any changes to the histograms.

[Ok] ■. Returns to data analysis window.

[No. of bins] □. Number of bins in the specified histograms.

[Minimum/maximum] □. Minimum and maximum energy values for the specified histograms.

Detector analysis > Extended coincidence analysis.
Figure 76.

[Coincidence patterns to use] ☒. Each coincidence pattern has a number described in Table 28 on page 126. In these boxes the user can specify which patterns to use.

[Electrons, photons, all, clear] ■. Presets the boxes described above.

[Detectors to sum] ☒. If a triplet satisfies the coincidence patterns selected, then sum the energy registered in these detectors.

[Histogram] □. Number of bins and energy interval to use in the energy distribution histogram.

[Adopt values from] ■. Adopt values for number of bins and energy interval already set in the data analysis window.

[Read ... counts] ■. Number of counts to use in the analysis.

[If not finished] ■. If the 'stop' button is pressed before an analysis has ended, the 'make display' button will ether restart the analysis or start from the point it was stopped.

[Random noise filter] ■. Enable white noise filter to eliminate artifacts in the energy distribution histogram due to the large spacing of the digital pulse heights.

[Detector settings] ■. See similar button described above (page 137).

[Focus] ■. By pressing this button two red lines will pop up in the histogram

window. With these lines the user can select an energy interval to use for the next analysis. Pressing the focus button will always place the two lines in the middle of the histogram.

[Incl. all] ■. Include the whole energy interval in the analysis.

[Zoom/print] ■. Similar to the graph toll function described above (page 137).

[Histogram to file] ■. Saves the histogram in an ASCII file named `workfile[ID].graph` where `[ID]` is the numbers shown under 'Coincidence patterns to use'. The ID is a binary interpretation of the coincidence patterns and the detectors chosen.

[Statistics] ■. Launches a window with information about the distribution of counts in the detectors and among the coincidence patterns. Figure 77.

[Make display] ■. Starts the analysis.

[Exit] ■. Returns to the main data analysis window.

[Stop] ■. Only visible when a analysis is running. Stops the analysis.

5. **Program testing**
   This is a prototype program. It has been used for the Risø Telescope Spectrometer for a period of one and a half year, but has not been through a rigid program testing as such.

6. **Program installation**
   See program requirements in section 1d. The executables and initialization files can be copied directly i.e. an installation program is not necessary. (Make sure the initialization files are not marked as read-only if the files are copied from a CD-Rom, and check the `RTS startup.ini` in the `Windows` directory.

7. **Error messages and erroneous behaviour**
   (a) `Error in 'RTS location.ini.`

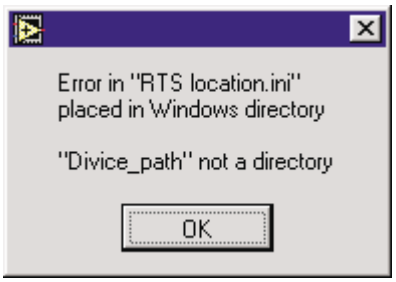

   The `RTS startup.ini` has properly not been found in the `Windows` directory. A default one has been created and the paths specified in the file are not the right ones. Edit the `RTS startup.ini` file.

(b) `Rail voltage failed.`

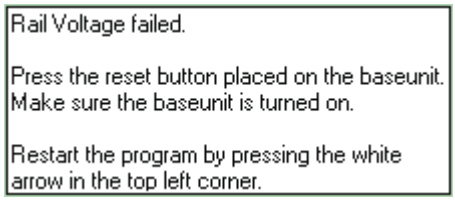

The voltage supply to the base unit failed. Turn on the base unit or the transformer if such is used.

(c) `Error 0 occurred at Send in GPIB.`

Install the GPIB card and software.

(d) `Communication error.`

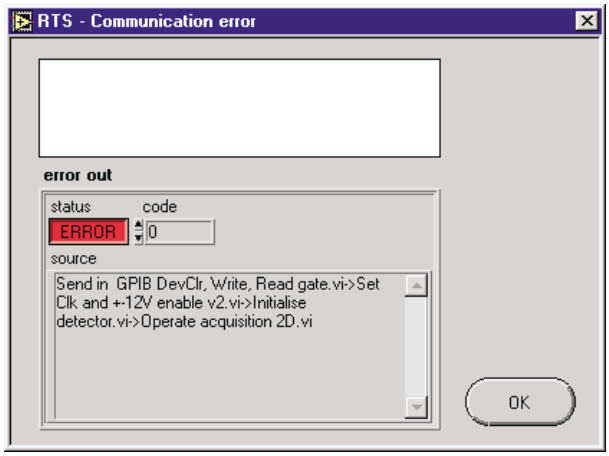

Install the GPIB card and software.

(e) `Error 1 occurred at Write File.`

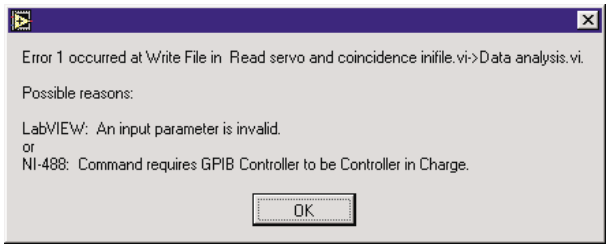

The initialization files in the `Windows` and the RTS system directory are properly copied from a CD-ROM. Make sure the files are not marked as 'Read Only'.

(f) `Error 8 occurred at Open File.`

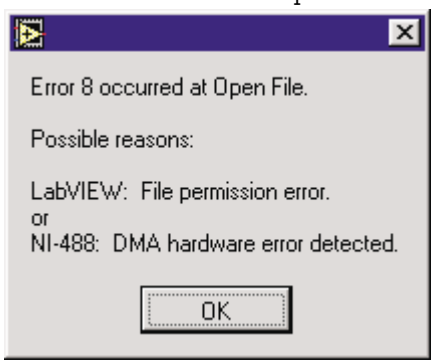

Make sure the initialization files in the `Windows` and RTS system directory are not marked as 'Read Only'. This error message will also appear in the data analysis program, if a read only file is accessed.

(g) `Servo-control does not work.`
`Calibration coefficients etc. are all zero.`
Coefficients for the servo-control, conversion from digital pulse height numbers to energy etc. are loaded from a text file and converted to numbers. If Windows is set to interpret ',' as decimal separator the conversion from text to numbers fails. In the Windows Control panel chose International settings and change the decimal separator from ',' to '.'.

(h) `Servo-control works sporadic.`
This is not an error. The bias voltage increases with decreasing leakage current, and the leakage current decreases with decreasing temperature. When the detector assembly is cooling the extra velocity in the bias voltage can cause the bias voltage to increase faster than expected by the servo-control, and thus exceed the maximum bias voltage allowed. To eliminate this problem the voltage settings are set on hold, if the measured temperature drops more than 0.1°C over a period of one second. A small square near the 'Servo-controlled bias settings' tagbox changes from green to yellow when the voltage settings are set on hold.

E.1 Screen prints

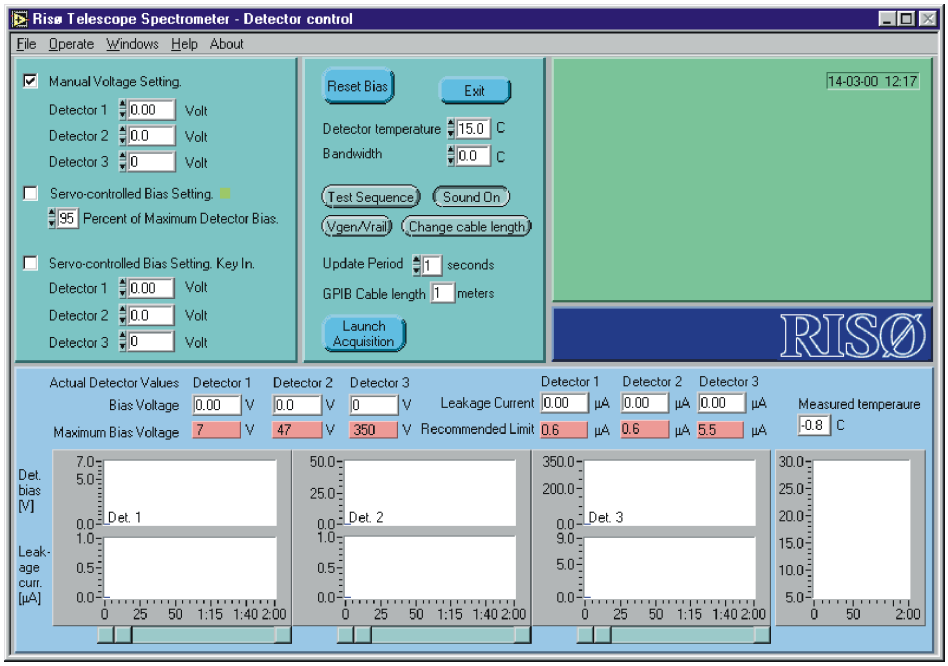

Figure 61. Detector control (Main window)

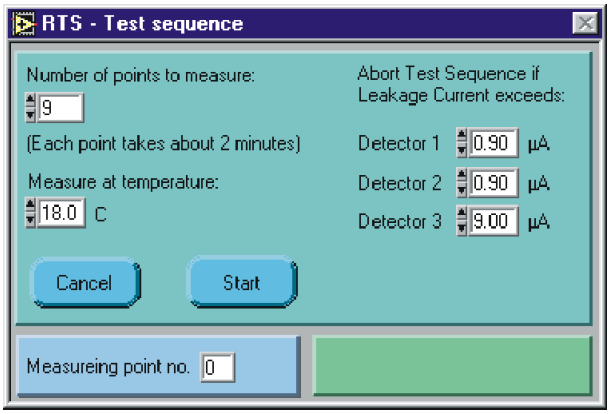

Figure 62. Detector control > Test sequence

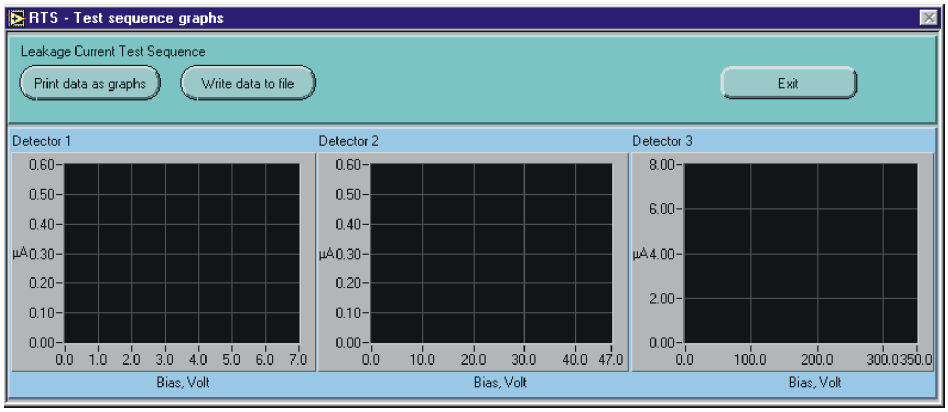

Figure 63. Detector control > Test sequence > Test sequence graphs (Show test result window)

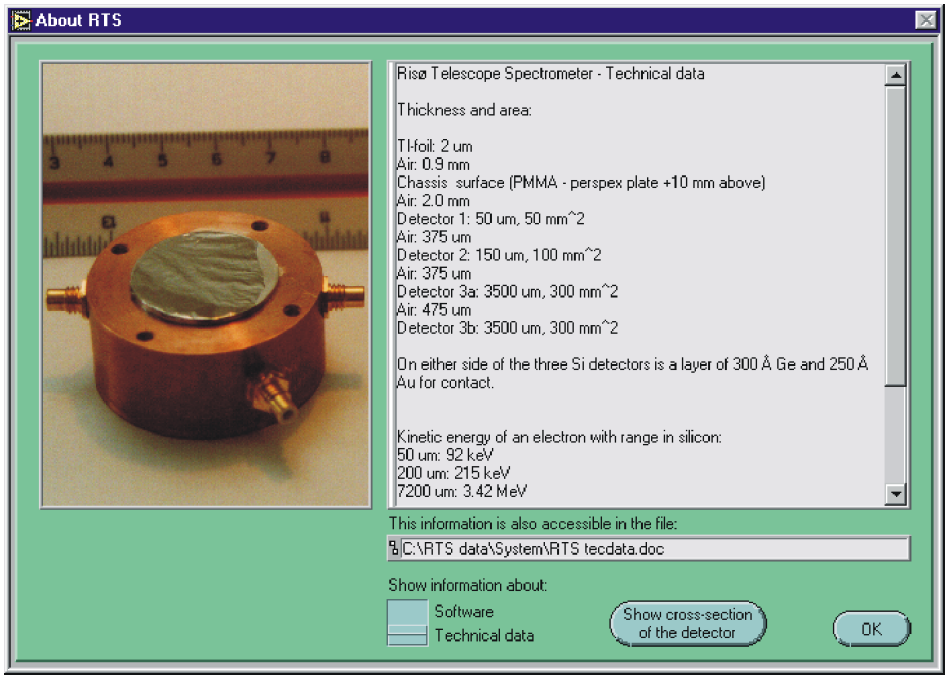

Figure 64. Detector control/Data analysis > About (About window)

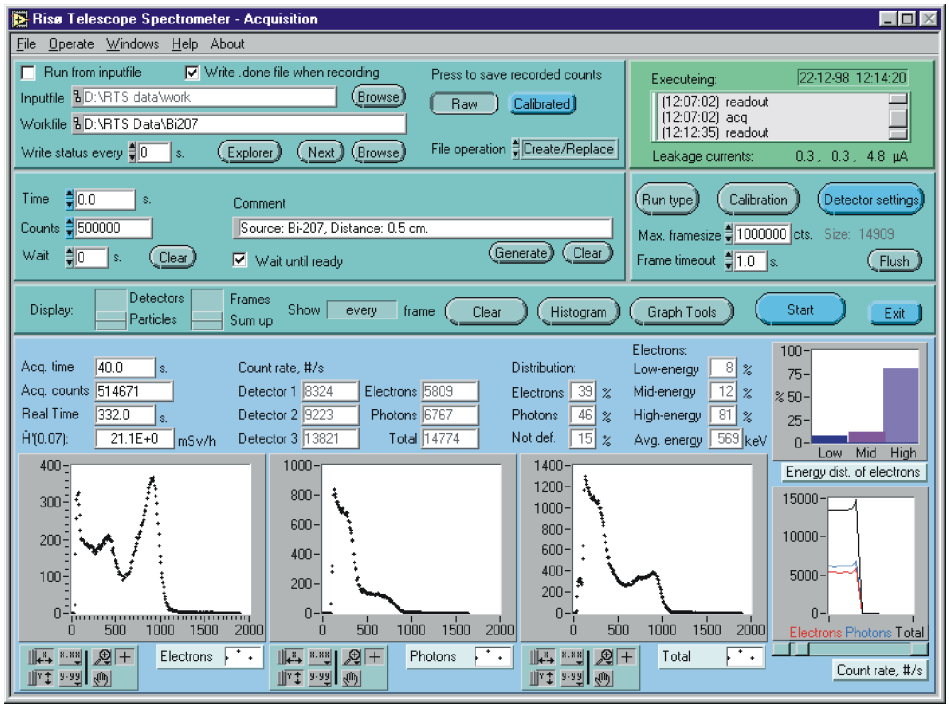

Figure 65. Detector control > Data acquisition (Data acquisition window)

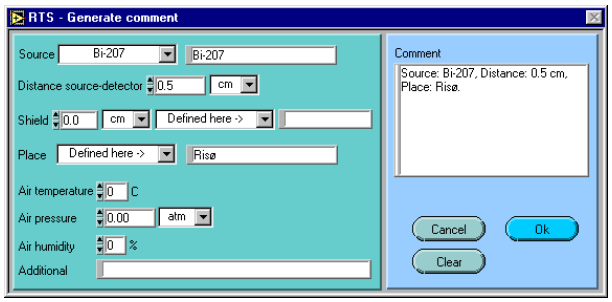

Figure 66. Detector control > Data acquisition (Data acquisition window > Generate comment)

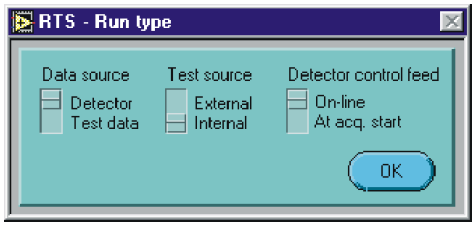

Figure 67. Detector control > Data acquisition > Run type

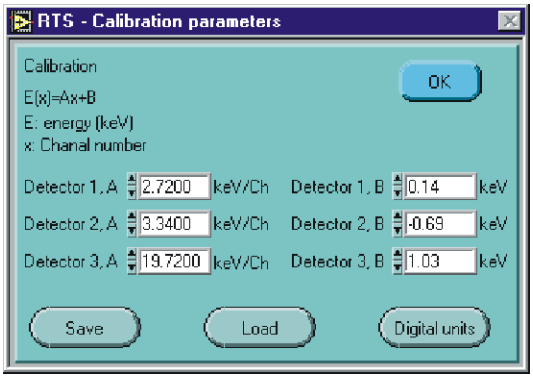

Figure 68. Detector control > Data acquisition > Calibration

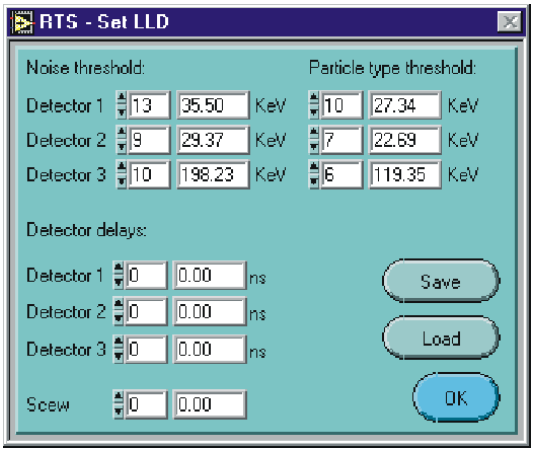

Figure 69. Detector control > Data acquisition > Detector setting

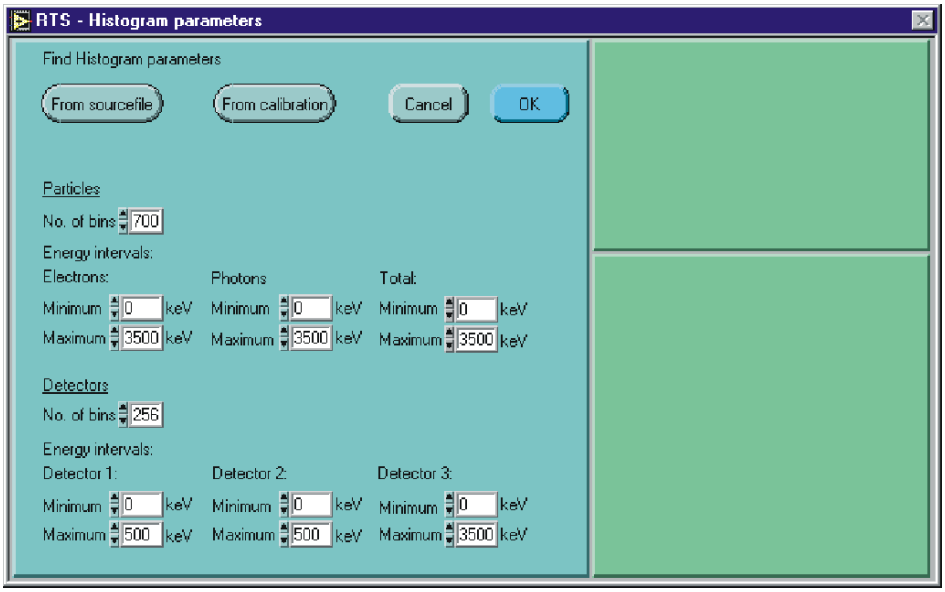

Figure 70. Detector control/Detector analysis > Histogram parameters

Figure 71. Detector control > Data acquisition > Graph tools

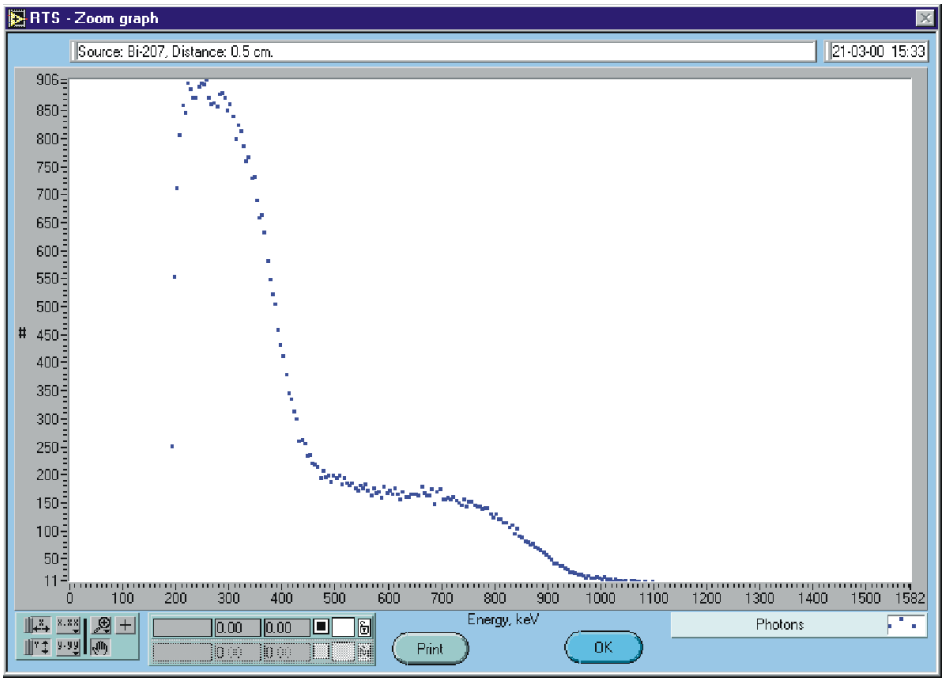

Figure 72. Detector control > Data acquisition > Graph tools > Zoom graph

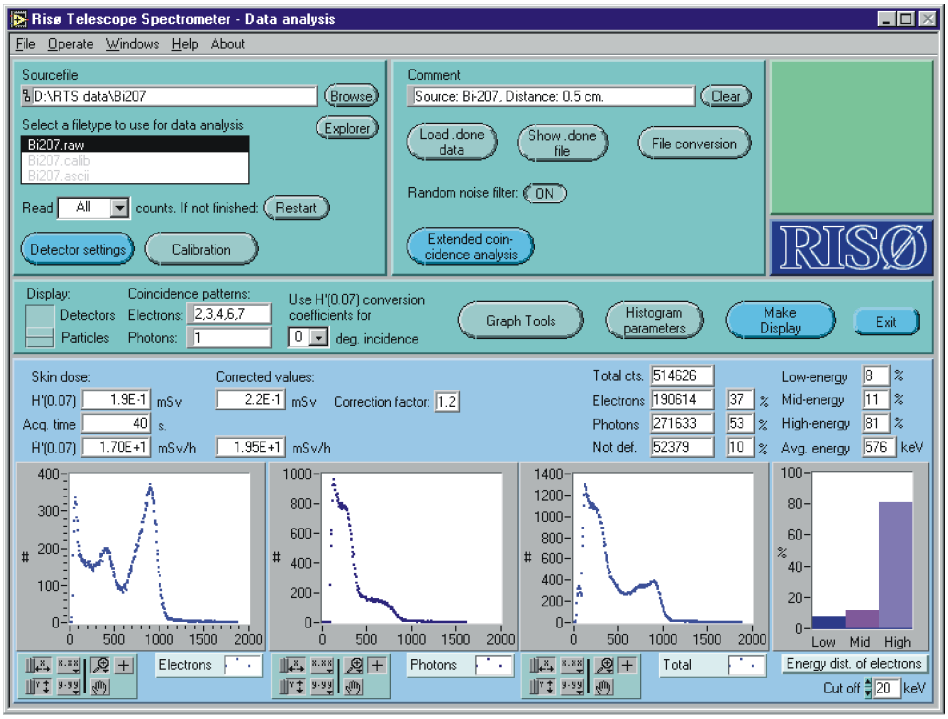

Figure 73. Detector analysis (Main window)

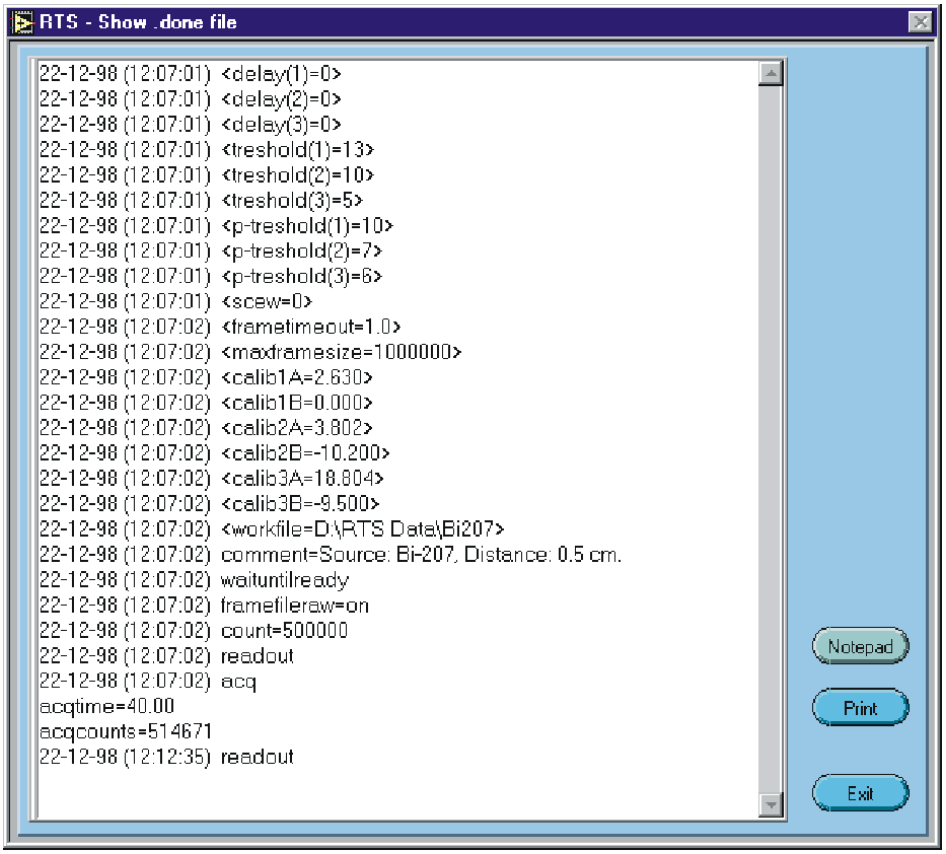

Figure 74. Detector analysis > Show .done file

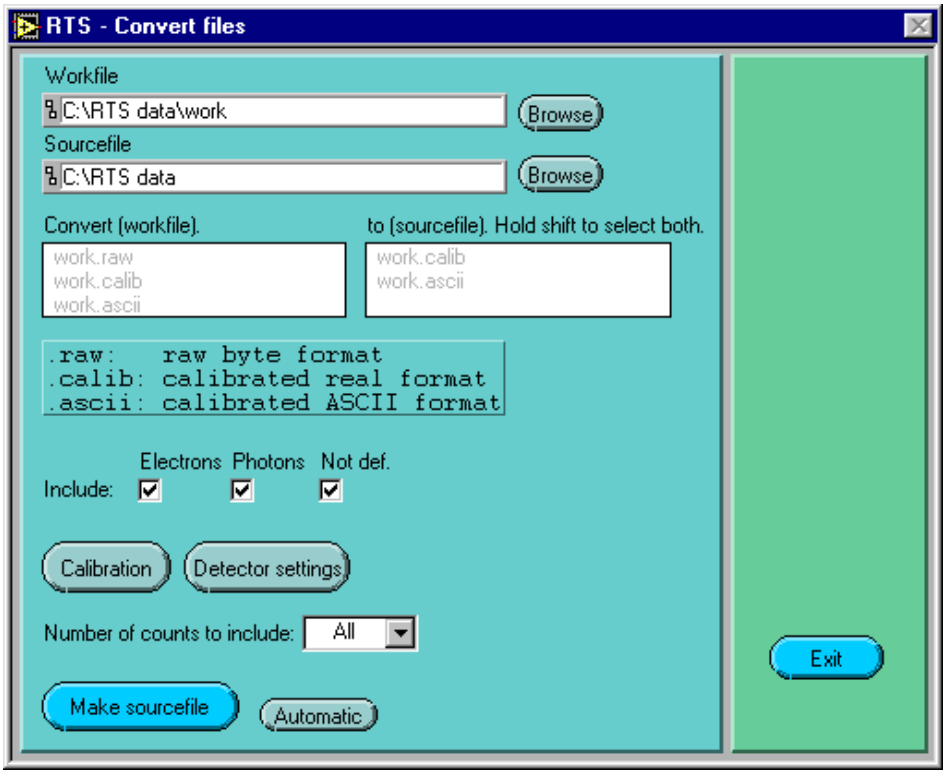

Figure 75. Detector analysis > File conversion

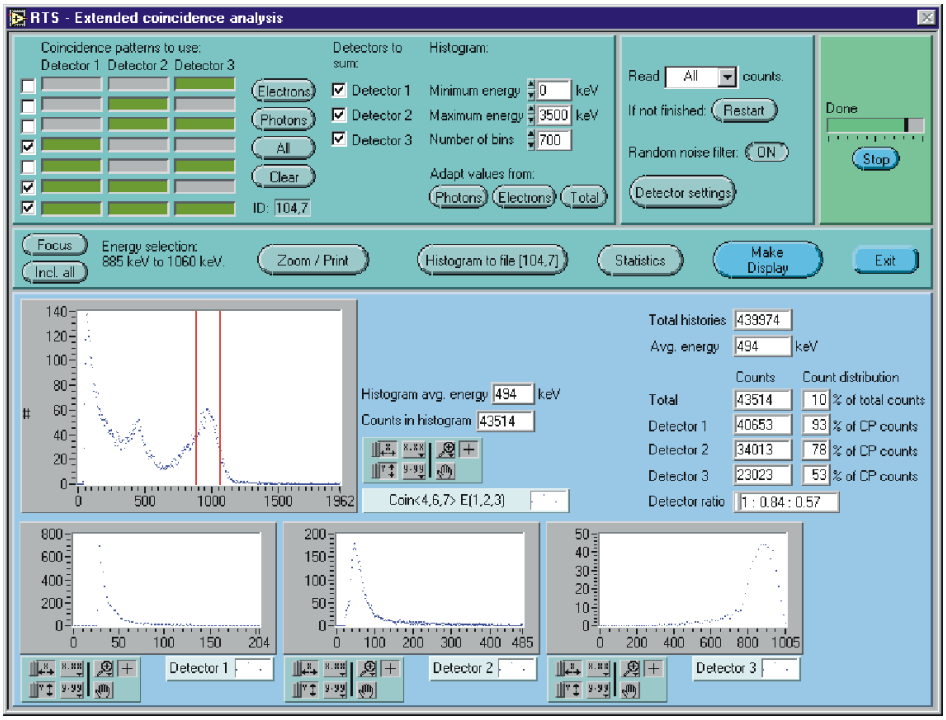

Figure 76. Detector analysis > Extended coincidence analysis

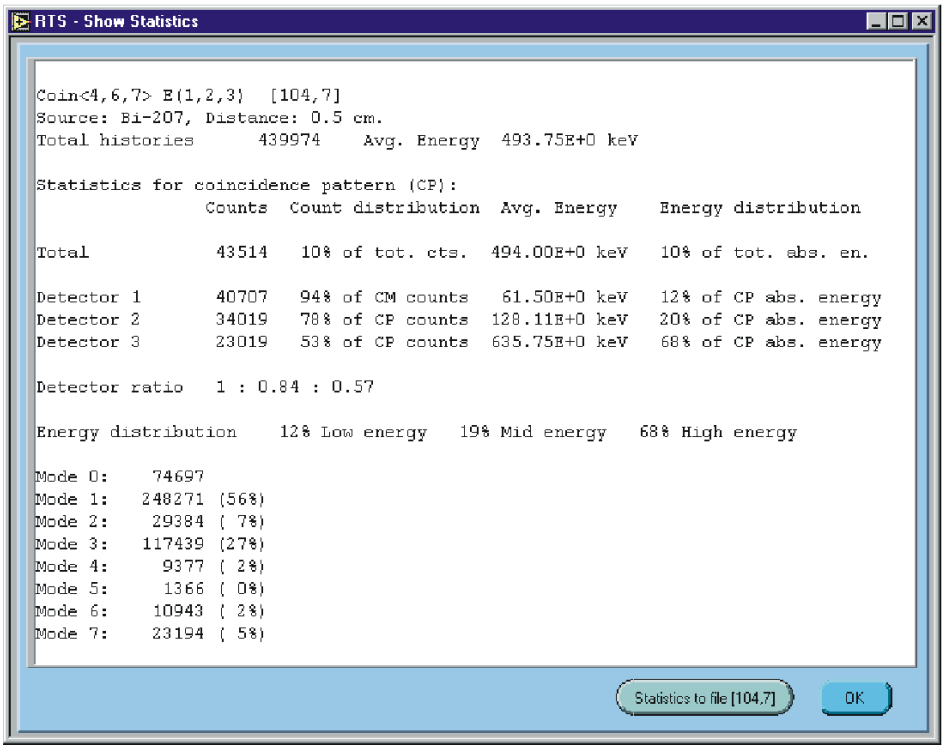

Figure 77. Detector analysis > Extended coincidence analysis > Show statistics

References

[1] Andreo, P., Medin, J. and Bielajew, A.F. (1993) Constraints on the multiple scattering theory of Molière in Monte Carlo simulations of the transport of charged particles. *Med. Phys.*, **20**, 1315-1325.

[2] Ashcroft, N.W. and Mermin, N.D. (1979) Solid State Physics, International edition. W.B. Saunders Company. ISBN 0-03-049346-3.

[3] Berger, M.J. (1963) Monte Carlo calculation of the penetration and diffusion of fast charged particles. *Methods Comput. Phys.*, **1**, 135-215.

[4] Berger, M.J. and Wang, R. (1989) Multiple-scattering angular deflections and energy-loss straggling in electron transport calculations. *In* 'Monte Carlo Transport of Electrons and Photons Below 50 MeV' (W.R. Nelson, T.M. Jenkins, a. Rindi, A.E. Nahum and D.W.O. Rogers, eds.) pp. 21-56. Plenum, New York.

[5] Bethe, H.A. (1953) Molière's theory of multiple scattering. *Phys. Rev.*, **89**, 1256-1266.

[6] Bielajew, A.F. (1994) Plural and multiple small-angle scattering from a screened Rutherford cross section. *Nucl. Instr. and Meth. B*, **86**, 257-269.

[7] Bielajew, A.F. and Rogers, D.O.W. (1987) PRESTA: The Parameter Reduced Electron-Step Transport Algorithm for Electron Monte Carlo Transport. *Nucl. Instr. and Meth. B*, **18**, 165-181.

[8] Borg, J. (1996) Dosimetry of Low-Energy Beta Radiation. Risø-R-907(EN). Department of Neuclear Safty Recearch. Risø National Laboratory, Roskilde, Denmark.

[9] Borg, J. and Helt-Hansen, J. (1997) EGS4 Monte Carlo Calculations of Energy Deposition in Silicon Detectors of a Triple Telescope Beta Spectrometer from Exposure to Electrons and Photons. Risø-I-1209(EN). Department of Neuclear Safty Recearch. Risø National Laboratory, Roskilde, Denmark.

[10] Böhm, J. (1986) The National Primary Standard of the PTB for Realizing the Unit of the Absorbed Dose Rate to Tissue for Beta Radiation. PTB-Dos-13. Physikalisch Technische Bundesanstalt. ISSN 0172-7095.

[11] Böhm, J., Alberts, W.G., Swinth, K.L., Soeares, C.G., McDonald, J.C., Thompson, I.M.G. and Kramer, H.M. (1999) ISO Recommended Reference Radiations for the Calibration and Proficiency Testion of Dosemeters and Dose Rate Meters Used in Radiation Protection. Radiat. Prot. Dosim. **86**(2), 87-105.

[12] Charles, M.W. (1986) The Biological Bases of Radiological Protection Criteria for Superficial, Low Penetrating Radiation Exposure. Radiat. Prot. Dosimetry, **14**(2), 79-90.

[13] Cross, W.G., Ing, H. and Freedman, N. (1983) A short Atlas of Beta-Ray Specra. *Phys. Med. Biol.*, **28**, No. 11, pp. 1251-1260.

[14] Duane, S., Bielajew, A.F. and Rogers, D.W.O. (1989) Use of ICRU-37/NBS Collision Stopping Powers in the EGS4 System. *National Research Council of Canada report PIRS-0177.*

[15] England, J.B.A. and Hammer, V.W. (1971) A New Type of Non-injecting Back Contact for Totally Depleted Silicon Surface Barrier Detectors. *Nucl. Instr. and Meth.*, **96**, 81-83.

[16] Personal communication. England, J.B.A. March 23 1997. Fax from Q-par Angus Ltd.

[17] Personal communication. England, J.B.A. March 4 1999. Fax from Q-par Angus Ltd. 'Commercial in Confidence' due to information about method of manufacture.

[18] Evans, R.D. (1958) Handbuch der Physik. Band XXXIV. Corpuscles and Radiation in Matter II. Sect. 15. 'Compton Effect'. Ed. Flügge. Springer-Verlag.

[19] Grosswendt, B. and Chartier, J.-L. (1994) Fluence-to-Absorbed-Dose Conversion Coefficients and Angular-Dependence Factors for 4-Element ICRU Tissue, Water and PMMA Slab Phantoms Irradiated by Broad Electrons beams. PTB-Dos-24. Physikalisch Technische Bundesanstalt. ISSN 0172-7095. ISBN 3-89429-496-5.

[20] Heinzelmann, M. (1991) Experiences and Problems of Skin Irradiation at Workplaces in Germany. *Radiat. Prot. Dosimetry*, **39**, No. 1/3. 173-181.

[21] Helt-Hansen, J. (1997) Beta-spectroscopy with silicon semiconductor detectors. Masterthesis in Danish. University of Copenhagen.

[22] Helt-Hansen, J., Larsen, H.E. and Christensen, P. (1999) Portable triple silicon detector telescope spectrometer for skin dosimetry. *Nucl. Instr. and Meth. A*, **438**, 523-539.

[23] Hirayama, H. (1993) Calculation of Absorbed Dose at 0.07, 3.0 and 10.0 mm Depths in a Slab Phantom for Monoenergetic Electrons. *Radiat. Prot. Dosimetry*, **51**, No. 2. 107-124.

[24] Horowitz, Y.S. (1993) Characterization of Beta Radiation Fields at CANDU Power Stations, Report COG-I-93-158, CANDU Owner's Group.

[25] Horowitz, Y.S., Hirning, C.R., Yuen, P. and Aikens, M. (1994) Beta ray spectroscopy based on a plastic scintilation detector / silicon surface barrier detector coincidence telescope. *Nucl. Instr. and Meth. A*, **338**, 522-533.

[26] Horowitz, Y.S., Weizman, Y. and Hirning, C.R. (1996) Measurements of Beta Ray Spectra in Candu Nuclear Generating Stations Using a Silicon Detector Coincidence Telescope. *Radiat. Prot. Dosimetry*, **66**, No. 1-4. 97-100.

[27] Hsu, H.-H., Chen, J., Ing, H., Clifford, E.T.H. and McLean, T. (1998) Skin dose measurement wit microspec 2™. *Nucl. Instr. and Meth. A*, **412**, 155-160.

[28] Hubbell, J.H. (1969) Photon Cross Sections, Attenuation Coefficients and Energy Absorption Coefficients from 10 keV to 100 GeV. NSRDS-NBS29. National Bureau of Standards, Washington, D.C.

[29] Hubbell, J.H. (1982) Mass attenuation and energy-absorbing coefficients. *Int. Appl. Radiat. Isot.*, **33**, 11.

[30] Hubbell, J.H. and Øverbo, I. (1979) Relativistic atomic form factors and photon coherent scattering cross sections. *J. Phys. Chem. Ref. Data*, **8**, 69-105.

[31] ICRP Report 38. (1983) Energy and Intensity of Emissions. The International Commission on Radiological Protection. Pergamon Press.

[32] ICRP Report 60. (1991) Recommendations of the International Commission on Radiological Protection. The International Commission on Radiological Protection. Annals of the ICRP, **20**(4). Pergamon Press.

[33] ICRU Report 37. (1984) Stopping Powers for Electrons and Positrons. International Commission on Radiation Units and Measurements. ICRU Publications.

[34] ICRU Report 47. (1992) Measurements of Dose Equivalents from External Photon and Electron Radiations. International Commission on Radiation Units and Measurements. ICRU Publications.

[35] ICRU Report 56. (1997) Dosimetry of External Beta Rays for Radiation Protection. International Commission on Radiation Units and Measurements. ICRU Publications.

[36] Jeraj, R., Keall, J. and Ostwald, P.M. (1999) Comparisons between MCNP, EGS4 and experiment for clinical electron beams. *Phys. Med. Biol.*, **44**. 705-717.

[37] Kawrakow, I. and Bielajew, A.F. (1998) On the representation of electron multiple elastic-scattering distributions for Monte Carlo calculations. *Nucl. Instr. and Meth. B*, **134**, 325-336.

[38] Kawrakow, I. and Bielajew, A.F. (1998) On the condensed history technique for electron transport. *Nucl. Instr. and Meth. B*, **142**, 253-280.

[39] Personal communication. Kawrakow, I. (Marts 1999) National Research Council of Canada.

[40] Kawrakow, I. (2000) Accurate condensed history Monte Carlo simulation of electron transport, I. EGSnrc, the new EGS4 version. *Med. Phys.*, **27** 485-498.

[41] Kawrakow, I. (2000) Accurate condensed history Monte Carlo simulation of electron transport, II. Application to ion chamber response simulations. *Med. Phys.*, **27** 499-513.

[42] Kawrakow, I. and Rogers, D.W.O. (2000) The EGSnrc Code System: Monte Carlo simulation of electron and photon transport. Technical Report PIRS-701, National Research Council of Canada, Ottawa, Canada. (http://www.irs.inms.nrc.ca/inms/irs/EGSnrc/EGSnrc.html)

[43] Knoll, G.F. (1979) Radiation detection and measurement. John Wiley & Sons, Inc. 1st ed.

[44] Kramer, H.M., Böhm, J., Iles, W.J. and Thompson, I.M.G. (1994) On the Current Status of an ISO Working Document on the Calibration and Type Testing of Radiation Protection Dosemeters for Photons. Radiat. Prot. Dosimetry, **54**(3/4), 267-272.

[45] Larsen, H.E. (1999) Portable Silicon Beta Spectrometer. Technical System Description. Optics and Fluid Dynamics Department. Risø-R-907(EN). Risø National Laboratory, Roskilde, Denmark.

[46] Molière, G.Z. (1948) Theorie der Streuung schneller geladener Teilchen II Mehrfach- und Vielfachstreuung. *Z. Naturforsch. A*, **3A**, 78-97.

[47] Nelson, W.R., Hirayama H., and Rogers, D.O.W. (1985) The EGS4 Code System, SLAC-Report-265.

[48] EG&G Ortec (1985) The whys and wherefores of charged particle detector spectrometry. Available throug EG&G sales offices.

[49] Osanov, D.P., Kruchkov, V.P. and Shaks, A.I. Determination of Beta Radiation Doses Received by Personnel Involved in the Mitigation of the Chernobyl Accident. IN Merwin, S.E. and Balonov, M.I. (eds). The Chernobyl Papers. Volume 1. 313-346.

[50] Greif, N. und Schrepf, H. (1998) Informationstechnik - Richtlinien f/ur die Softwareentwicklung - Richtlinie f/ur die Softwaredokumentation. PTB-8.31-98-1. Physikalisch Technische Bundesanstalt, Braunschweig und Berlin.

[51] Regulla, D.F. (1986) Importance of Exposure to Beta Particles in Practical Radiation Protection. *Radiat. Prot. Dosimetry*, **14**, No. 2. 95-100.

[52] Personal communication. Rogers, D.W.O. (Marts 1999) National Research Council of Canada.

[53] Rogers, D.O.W. and Bielajew, A.F. (1990) Monte Carlo Tecniques of Electron and Photon Transport for Radiation Dosimetry. Chapter 5, Vol. III of: The Dosimetry of Ionizing Radiation. (Kase, K.R., Bjarngard, B.E. and Attix, F.H. eds.) Academic Press. pp. 427-539.

[54] Rogers, D.O.W., Faddegon, B.A., Ding, G.X., Ma, C.-M., Wei, J. and Mackie, T.R. (1995) BEAM: A Monte Carlo code to simulate radiotherapy treatment units. *Med. Phys.*, **22** 503-524.

[55] Rogers, D.W.O., Kawrakkow, I., Seuntjens, J.P. and Walters, B.R.B. (2000) NRC User Codes for EGSnrc. Tecnical Report PIRS-702, National Research Council of Canada, Ottawa, Canada. (http://www.irs.inms.nrc.ca/inms/irs/EGSnrc/EGSnrc.html)

[56] Siegbahn, K. (editor), (1965) α-, β- and γ-ray spectroscopy. Vol 1. North Holland Publiching Co.

[57] Storm, E. and Israel, H.E. (1970) Photon cross sections from 1 keV to 100 MeV for elements $Z = 1$ to $Z = 100$. *Nucl. Data, Sect. A*, **7**, 565-681.

Bibliographic Data Sheet **Risø-R-1216(EN)**

Title and author(s)

Development of a Portable Triple Silicon Detector Telescope for Beta Spectroscopy and Skin Dosimetry

Jakob Helt-Hansen

ISBN	ISSN
87-550-2769-5; 87-550-2770-9 (Internet)	0106-2840

Dept. or group	Date
Department of Nuclear Safety Research	November 2000

Pages	Tables	Illustrations	References
154	28	77	57

Sponsorship

Danish Research Agency; European Union under Contract FI4PCT960037.

Abstract (Max. 2000 char.)

It is now recognized that beta radiation can be a significant radiation problem for exposure of the skin. There is thus a need for a portable and rugged active beta dosemeter-spectrometer to carry out immediate measurements of doses and energies of beta particles even in the presence of photon radiation. The main objective of this report is to describe the development of such an instrument.

A beta-spectrometer has been developed consisting of three silicon surface barrier detectors with the thickness: 50μm/150μm/7000μm covered by a 2 μm thick titanium window. The spectrometer is capable of measuring electron energies from 50 keV to 3.5 MeV.

The spectrometer is characterized by a compact low weight design, achieved by digital signal processing beginning at an early stage in the signal chain. 255 channels are available for each of the three detectors. The spectrometer is controlled by a laptop computer, which also handles all subsequent data analysis.

By use of coincidence/anti-coincidence considerations of the absorbed energy in the three detector elements, counts caused by electrons are separated from those originating from photons.

The electron energy distribution is multiplied by a set of conversion coefficients to obtain the dose at 0.07 mm tissue. Monte Carlo calculations has been used to derive the conversion coefficients and to investigate the influence of noise and the design of detector assembly on the performance of the spectrometer.

This report describes the development of the spectrometer and its mode of operation, followed by a description of the Monte Carlo calculations carried out to obtain the conversion coefficients. Finally is the capability of the telescope spectrometer to measure beta and photon spectra as well as beta dose rates in pure beta and mixed beta/photon radiation fields described.

Descriptors

BETA DOSIMETRY; BETA SPECTROMETERS; MONTE CARLO METHOD; PORTABLE EQUIPMENT; SI SEMICONDUCTOR DETECTORS; SKIN; TELESCOPE COUNTERS

Available on request from:
Information Service Department, Risø National Laboratory
(Afdelingen for Informationsservice, Forskningscenter Risø)
P.O. Box 49, DK–4000 Roskilde, Denmark
Phone (+45) 46 77 46 77, ext. 4004/4005 · Fax (+45) 46 77 40 13
E-mail: risoe@risoe.dk

RISØ

Risø National Laboratory carries out research within science and technology, providing Danish society with new opportunities for technological development. The research aims at strengthening Danish industry and reducing the adverse impact on the environment of the industrial, energy and agricultural sectors.

Risø advises government bodies on nuclear affairs.

This research is part of a range of Danish and international research programmes and similar collaborative ventures. The main emphasis is on basic research and participation in strategic collaborative research ventures and market driven tasks.

Research is carried out within the following programme areas:

- **Industrial materials**
- **New functional materials**
- **Optics and sensor systems**
- **Plant production and circulation of matter**
- **Systems analysis**
- **Wind energy and atmospheric processes**
- **Nuclear safety**

Universities, research institutes, institutes of technology and businesses are important research partners to Risø.

A strong emphasis is placed on the education of young researchers through Ph.D. and post-doctoral programmes.

ISBN 87-550-2769-5
ISBN 87-550-2770-9 (Internet)
ISSN 0106-2840

Copies of this publication are available from

Risø National Laboratory
Information Service Department
P.O. Box 49
DK-4000 Roskilde
Denmark
Telephone +45 4677 4004
risoe@risoe.dk
Fax +45 4677 4013
Website www.risoe.dk